Combined influence of site and buildings effects on the surface seismic wave field

Ophélie Rohmer

UNIVERSITÉ CÔTE D'AZUR

ÉCOLE DOCTORALE
SCIENCES FONDAMENTALES ET APPLIQUÉES

THÈSE DE DOCTORAT

Influence combinée des effets de site et du bâti sur le champ d'ondes sismiques en surface

Ophélie ROHMER

CEREMA/REPSODY

Présentée en vue de l'obtention
du grade de docteur en Sciences de la Planète et de l'Univers
de l'Université Côte d'Azur
Devant le jury, composé de :
Céline Chesnais, ITPE, Université Gustave Eiffel
Françoise Courboulex, Directrice de recherche, GEOAZUR
Nathalie Glinsky, Chargée de recherche, CEREMA
Panagiotis Kotronis, Professeur, Ecole Centrale de Nantes
Christophe Larroque, Maitre de conférence, Université de Reims Champagne-Ardenne
Clotaire Michel, Maitre de conférence (Dozent), ZHAW School of Engineering
Maria Paola Santisi D'Avila, Maitre de conférence, Université Côte d'Azur, Polytech
Jean-François Semblat, Professeur, ENSTA – Institut Polytechnique de Paris

Dirigée par : Etienne Bertrand
Co-encadrée par : Julie Régnier
Soutenue le : 18 mars 2022

RÉPUBLIQUE FRANÇAISE
Liberté
Égalité
Fraternité

Cerema
CLIMAT & TERRITOIRES DE DEMAIN

Influence combinée des effets de site et du bâti sur le champ d'ondes sismiques en surface

Combined influence of buildings and lithological site effect on seismic ground motion

Jury:

Présidente du jury

Françoise Courboulex, Directrice de recherche, GEOAZUR

Rapporteurs

Panagiotis Kotronis, Professeur, Ecole Centrale de Nantes

Clotaire Michel, Maitre de conférence (Dozent), ZHAW School of Engineering

Examinateurs

Céline Chesnais, ITPE, Université Gustave Eiffel

Christophe Larroque, Maitre de conférence, Université de Reims Champagne-Ardenne

Jean-François Semblat, Professeur, ENSTA – Institut Polytechnique de Paris

Invitées

Nathalie Glinsky, Chargée de recherche, CEREMA

Maria Paola Santisi D'Avila, Maitre de conférence, Université Côte d'Azur, Polytech

Résumé

Depuis plusieurs années, les problématiques portant sur l'interaction sol-structure (ISS) sont étudiées afin d'affiner l'évaluation du risque sismique à l'échelle locale. Cette thèse s'intéresse particulièrement à la quantification des effets de la présence du bâti sur l'aléa sismique local dans une vallée sédimentaire et à la caractérisation de paramètres dynamiques sensibles à l'interaction sol-structure à partir de données expérimentales de vibrations ambiantes et de modèles numériques 3D.

Elaboré dans le cadre du projet Ritmica soutenu par l'IDEX JEDI de l'Université Côte d'Azur, l'objectif de ce travail de thèse, financée par le Cerema, est d'évaluer l'impact respectif de la stratigraphie du site, de la géologie et du bâti sur l'aléa sismique. Pour cela, une des zones les plus sismiques et à enjeux forts en France métropolitaine est choisie pour cas d'étude : la basse vallée du Var. De nombreuses expérimentations y ont été réalisées depuis plusieurs années, incluant des instrumentations de bâtiments, d'ouvrages d'art et de sol qui ont permis de définir et décrire la configuration géologique de la vallée et le comportement dynamique de certaines des structures environnantes.

Dans l'objectif de mieux caractériser l'aléa sismique dans la vallée du Var en prenant en compte la présence des constructions existantes, plusieurs campagnes de mesures de vibrations ambiantes ont été réalisées sur le bassin et sur le rocher de la vallée et également, au niveau et au sein des plus hauts bâtiments de la zone. Ces données permettent d'une part, de définir le modèle géotechnique 3D de la vallée à partir des données géotechniques et géophysiques disponibles et d'autre part, de calibrer un modèle numérique simplifié de bâtiment dans le but d'établir un modèle 3D en élément finis de la vallée intégrant le bâti en surface. Ce modèle sert ensuite à simuler numériquement la propagation des ondes sismiques dans la vallée du Var en utilisant un séisme simulé. Le modèle de sous-sol de la vallée permet de mieux délimiter l'interface bassin-substratum et les vitesses d'ondes sismiques qui constituent des éléments importants dans l'étude des effets de site. Ce modèle montre que l'épaisseur du bassin augmente du Nord vers le Sud allant de 50 m d'épaisseur à plus de 100 m sous l'aéroport de Nice avec des vitesses Vs moyennes aux alentours de 400 $m.s^{-1}$. Une étude numérique réalisée à partir de cinq modèles de bâtiment en éléments finis (4 de faible hauteur et un de grande hauteur, en béton armé et maçonnerie) montre que les effets de l'ISS sont plus importants pour les bâtiments de type cantilever et que les irrégularités horizontales de rigidité jouent un rôle majeur

Mots-clés : risque sismique, dynamique des structures, interaction sol-structure, interaction structure-sol-structure, interaction site-ville, modèle de sol 3D, effets de site, vallée du Var

dans l'ISS. Les campagnes d'instrumentation de bâtiments dans la vallée du Var ont permis d'obtenir un large jeu de données pour l'identification des comportements dynamiques des bâtiments, l'étude de l'ISS et la caractérisation de la variabilité spatiale du mouvement du sol. Ces campagnes denses permettent de vérifier que le premier mode de déformée des bâtiments, par la suite utilisé dans la calibration de modèle simplifiés à partir d'une relation simple, correspond à un mode de flexion. L'analyse du spectre de basculement et des fonctions du décrément aléatoire est utile pour la caractérisation de l'ISS à partir des séries temporelles verticales à la base des structures. Afin d'étudier l'influence combinée des effets de site et du bâti sur le champ d'ondes sismiques en surface, la propagation des ondes sismiques a été numériquement simulée dans cinq modèles 3D en éléments finis différents calibrés à partir d'enregistrements de vibration ambiante et incluant ou non plusieurs types de configurations de villes.

Mots-clés : risque sismique, dynamique des structures, interaction sol-structure, interaction structure-sol-structure, interaction site-ville, modèle de sol 3D, effets de site, vallée du Var

Abstract

For several years, the problematic about soil-structure interaction (SSI) have been studied in order to refine the evaluation of the seismic risk at local scale. This thesis particularly focuses on the quantification of the effects induced by the presence of buildings on the local seismic hazard in a sedimentary valley and on the characterization of dynamic parameters sensitive to soil-structure interaction from experimental ambient vibration data and 3D numerical models.

Developed within the framework of the Ritmica project supported by the IDEX JEDI of the University Côte d'Azur, the objective of this thesis is to assess the respective impact of the site stratigraphy, of the geology and of the building on the seismic hazard. To do this, one of the highest seismic risk area in France mainland is chosen as study case: the lower Var valley. Many experiments have been carried out there for several years, including instrumentation of buildings, engineering structures and free field sites which have made it possible to define and describe the geological configuration of the valley and the dynamic behavior of some of the surrounding structures.

In the aim of better characterize the seismic hazard in the Var valley taking into account the presence of existing buildings, multiple campaigns of ambient vibration measurements were performed on the basin and on the rock of the valley and also, at the level and inside the highest buildings in the valley. These data allow first, to define the 3D geotechnical model of the valley from available geotechnical and geophysical data and second, to calibrate simplified numerical model of building in order to establish a 3D finite element model of the valley including building at the top. This model is used to numerically simulate the seismic wave propagation in the Var valley using simulated earthquake. The soil model of the valley permits to better delimit the basin-bedrock interface and the seismic wave velocities that constitute important elements in the study of site effect. This model shows that the basin thickness increases from North to South from 50 m deep to more than 100 m under the Nice airport with average Vs velocity around 400 $m.s^{-1}$. A numerical study done on five finite element models of building (4 low-rise and one high-rise, reinforced concrete and masonry) shows that bending type buildings are the most prone to SSI and that stiffness horizontal irregularities play a major role in SSI. The instrumentation campaigns of buildings in the Var valley allow to get a large set of data for the identification of the dynamic behavior of buildings, the study of SSI and the characterization of the spatial variability of the ground motion. These dense instrumentation

Keywords : seismic risk, structure dynamic, soil-structure interaction, structure-soil-structure interaction, site-city interaction, 3D soil model, site effect, Var valley

campaigns allow to check that the first mode shape of building, thereafter used in the calibration of simplified model through simple relationship, corresponds to a bending mode. The analysis of the rocking spectral ratio and of random decrement functions is useful for the characterization of SSI from vertical temporal series at the base of buildings. To study the influence of lithological site effect and buildings on the surface ground motion, seismic wave propagation has been numerically simulated in five different 3D finite element site-city models characterized using ambient vibration recordings and including various city configurations.

Keywords : seismic risk, structure dynamic, soil-structure interaction, structure-soil-structure interaction, site-city interaction, 3D soil model, site effect, Var valley

AKNOWLEDGMENTS

Des années assez étranges ont ponctué cette thèse avec notamment la pandémie du Covid dès la fin 2019. Une succession de confinements et de périodes de doutes difficiles à gérer et qui auraient été encore plus compliquées sans un bon entourage.

En premier lieu, je tiens à remercier les membres de mon jury de thèse. Mme Françoise Courboulex pour avoir accepté de présider ce jury ainsi que le Professeur Panagiotis Kotronis et M Michel Clotaire qui se sont acquittés de la délicate tâche de rapporteur sur cette étude. Je remercie également Mme Céline Chesnais, M Christophe Larroque et le Professeur Jean-François Semblat qui ont accepté de faire partie de ce jury de thèse. Sans oublier Mme Nathalie Glinsky et Mme Paola Santisi d'Avila pour leur participation scientifique, ainsi que le temps qu'elles ont consacré à ma recherche.

En deuxième lieu, je remercie mes encadrants qui m'ont particulièrement soutenu tout au long de ma thèse. A l'écoute et toujours disponible, je souhaite à tout doctorant de pouvoir profiter d'une aussi bonne direction. Etienne, merci de m'avoir fait confiance et de m'avoir accompagné dès mon stage de fin d'étude (déjà 4 ans qu'on travaille ensemble !). Je tiens spécifiquement en mémoire le délicieux ramen partagé à la gare de Lyon après mon audition de thèse et le fantastique voyage à Seattle où j'ai découvert le croissant cheddar et les frites cheddars. My god… Grâce à toi, j'ai beaucoup appris tant du monde de la recherche que du management d'équipe. Un clin d'œil aux CeremaGirlzzz, Marie-France, Nathalie et Julie, le pouvoir féminin de l'équipe de Sophia avec qui je partage avec plaisir anecdotes, sujets de discussion variés, pique-niques et pâtisseries. Egalement aux anciens, Simon, Florent et Matthieu qui m'ont tant appris sur le café, la confection du pain, python, la photographie, le Mercantour, le cyclisme, le trail et tant d'autres choses… Je pense à vous.

Merci aux doctorants (et ex-doc, félicitations) de Géoazur, Nico, Lionel, Flo, Caro, Albane et tellement d'autres… pour nos incroyables soirées jeux de société, pizza, raclette. Tout pour un esprit sain dans un corps sain ! Gracias Coloccito pour avoir eu le courage de te lancer dans une colocation atypique avec deux princesses. Quelle folle idée ! Un vrai bonheur de partager avec toi un verre de vin devant Friends et de raconter nos déboires.

Je remercie aussi chaleureusement ma famille qui m'a toujours appuyé dans mes choix et dans mon parcours. Merci beaucoup, encore et encore. Par ailleurs, elle ne lira sûrement jamais ce texte mais je tiens à l'inclure dedans. Ma précieuse Orphée m'a été d'un support essentiel lors de ma thèse et l'est toujours dans mon quotidien. Une boule de douceur qui remonte le moral dès qu'elle ronronne. Quelle chance j'ai eu de t'avoir. Enfin, je terminerais par saluer mon ange dont le soutien m'a porté jusqu'à la fin de ma thèse. Tu as su éclairé mes horizons et donner un nouveau souffle à ma vie. Un grand merci, je t'aime mon petit sucre.

“Parmi les milliers de touristes qui défilent chaque année sur la Côte d’Azur, combien en est-il qui manquent de s’arrêter à Nice et d’y gravir, pour contempler le radieux panorama de la Baie des Anges, les pentes du Mont Boron ou de la colline du Vieux Château ? Au-delà de la courbe harmonieuse de la plage, du fourmillement des maisons et des hôtels de la grande ville, [la vue] est marquée par le profil singulièrement rectiligne des collines derrière lesquelles le Var débouche dans la mer. » (Martonne, 1923).

CONTENTS

LIST OF FIGURES

LIST OF TABLES

Introduction

The 1985 Mexico earthquake is now a textbook case, as it is a key testimony of human casualties and material damages during strong seismic event in sedimentary basin (e.g. Bataillon, 1988). This earthquake is the first to notably show that the seismic wave field undergoes important modifications going through superficial soil layers that can damage structures. Actually, most of the time, these modifications result in amplification of the surface seismic motion compared to close-by rock sites related to the impedance contrast, multiple reflection phenomena between the basin surface and the basin-bedrock interface and to diffraction at the edge of the valley (Bard and Bouchon, 1980a, 1980b; Campillo et al., 1989). Those phenomena called lithological site effects are now well-known and still studied (e.g. Cetin et al., 2022). For seismic hazard assessment, they are integrated in the estimation of the seismic ground motion together with topographic site effect, source effects, large scale wave propagation effects and regional attenuation with distance. On the contrary, the presence of buildings or cities is never taken into account in the definition of the seismic solicitation (Figure 1).

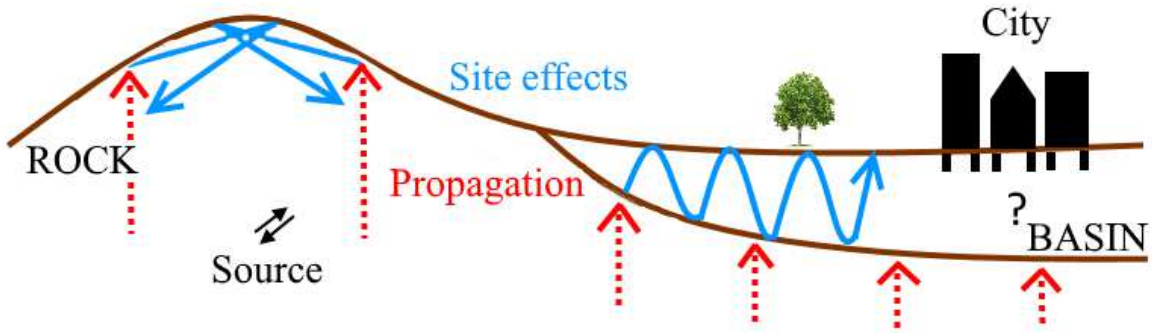

Figure 1: Scheme of the effects taken into account in the local seismic risk evaluation and uncertainty related to site-city interaction.

However, it has been shown that the city organization itself has an influence on the superficial wave field (e.g. Guéguen, 2000). It is called the site-city interaction (SCI) or the structure-soil-structure interaction (SSSI). Seismologists and civil engineers combine their knowledge to better understand the dynamic behavior of buildings in their environment. The objective is to improve the current building code and the resilience of the building taking into account the environmental conditions where the building is located in order to save lives and prevent additional costs when damage occur. According to the history of the soil-structure interaction

(SSI) experimental studies from Trifunac et al. (2001), it is only in the 70's that the term « soil-structure interaction » is published. Later, the term « Engineering Seismology » appears for the first time in the article of Kanai (1983) to designate the application of seismic methods to investigate and even monitor civil engineering structures. Kausel (2010) completed the review of the empirical SSI studies from the 1900s to the 2010s.

There were many observations of the SSI on earthquake and ambient vibration recordings (i.e. vibration induced by the wind, the anthropic activity, the sea tides…) as presented in the Table 1. Contrary to earthquake recordings that are rare, in-situ ambient vibration are a powerful tool to investigate a structure since they require little money, little time and can be distributed punctually to quickly cover a large area. These passive non-invasive measurements are used in many studies for different applications. They helped indeed to characterize not only the geological structure (e.g. Seht and Wohlenberg, 1999; Delgado et al., 2002; Parolai et al., 2002; Guéguen et al., 2007; Haefner et al., 2010; Mascandola et al., 2019), the shear wave velocity profiles and the site response characteristics (amplification factor and fundamental resonance frequency) (e.g. Raptakis et al., 2005; Roten et al., 2006; Barnaba et al., 2010; Manakou et al., 2010; Stephenson et al., 2019), but also the dynamic behavior of the buildings. It was shown that these types of data are also commonly used in the identification of the dynamic parameters of engineering structure and give reliable results (e.g. Carder, 1936; Kanai, 1950; Ward and Crawford, 1966; Guéguen, 2000; Dunand, 2005; Michel, 2007).

According to the Table 1 and other numerical studies, the main effects of SSI observed on recordings are an increase of the spatial variability of the seismic ground motion (e.g. Housner, 1957; Kashima and Kitagawa, 1988; Safak and Celebi, 1992; Guéguen, 2000; Kim and Stewart, 2003; Bradford et al., 2004; Castellaro et al., 2014; Sotiriadis et al., 2019) and the modification of the building response (e.g. Merritt and Housner, 1954; Kanai, Kiyoshi and Yoshizawa, 1961; Bard, 1988; Veletsos and Prasad, 1989; Muria-Vila and Alcorta, 1992; Paolucci, 1993; Ganev et al., 1993; Meli et al., 1998; Kitada et al., 1999; Guéguen, 2000; Gallipoli et al., 2004; Guéguen and Colombi, 2016) especially in double resonance condition, meaning that the first natural frequency of the building is close to the soil fundamental frequency (e.g. Kitada et al., 1999; Tobita et al., 2000; Kim and Stewart, 2003; Kumar and Narayan, 2018). Radiated waves from the structure to the ground have been observed up to a certain distance (e.g. Jennings, 1970; Wong et al., 1977; Kitada et al., 1999; Guéguen, 2000; Cornou et al., 2004; Castellaro et al., 2014). For example, using a single degree-of-freedom (SDOF) model and the discrete wave number technique using strong ground motion, Bard et al. (1996) found a distance up to 30 m

from the structure and Wirgin and Bard (1996) noted a distance equals to 10 times the size of the building base based on time domain and transfer functions analysis.

Several authors observed that SSI can be beneficial to the dynamic response of a structure using numerical models of building. For example, Sarrazin et al. (1972) analyzed SSI effects on a SDOF system using a probabilistic approach, spring method and seismic excitation. They concluded that the structural response amplification is less than 20% of the case of the fixed base (FB) structure. The same tendency is retrieved in the study of Veletsos and Prasad (1989) using an analytical linear model of cylindrical foundation and analysis in time domain or in the work of Saez et al. (2011) based on nonlinear finite element model of simple linear SDOF through time domain analysis.

Other authors observed that SSI effects can be detrimental to the structure response, notably by studying real cases as 1985 Mexico earthquake, 1998 Kobe earthquake or 1998 Adan-Ceyhan earthquake through numerical simulations. Several studies showed that the building response tends to increase with SSI. For instance, through time domain analysis, by using an analytical model of building (Naserkhaki and El-Rich, 2013), lumped mass model of building (Naserkhaki et al., 2014, 2012), or 2D numerical models solicited by strong motion through time domain analysis (e.g. Farghaly, 2017; Kontoni and Farghaly, 2018; Aden et al., 2019). In 2008, Nakhaei and Ali Ghannad (2008) showed using a bilinear SDOF model of structure subjected to strong motion, that SSI generally increases the damage index (equal to the ratio between the initial and the reduced resistance capacity of a building) before a natural period close to the fundamental period of the ground, especially in the case of high-rise building located on soft soil. The authors concluded that after this specific period, the trend in reversed and SSI induces a decrease of the damage index in the building. According to Wolf (1985), the natural frequency of a SDOF model with flexible base (SSI taken into account) decreases compared to the one of a SDOF model with fixed base condition. This is also observed in the study of numerical linear model of structure subjected to strong motion (Veletsos and Meek, 1974) and in the analytical study of Mylonakis and Gazetas (2000) based on displacement and acceleration spectra analysis.

The SSSI, meaning that structure vibration are transmitted to the ground and to neighboring structures, has been observed through seismic and vibration recordings in free field. An unusual observation was made during the impact of the Columbia space shuttle in the atmosphere. Kanamori et al. (1991) observed the propagation of seismic waves at a large distance on acceleration time series coming from the vibration of a group of high-rise buildings in Los

Angeles. Even more surprising, Erlingsson and Bodare (1996) and Erlingsson (1999) observed, through 3D modeling of the structure and the analysis of the displacement time series, the transmitted vibration by the structure during a rock concert in a stadium. The audience jumped in the rhythm of the music, generating waves that were transmitted into the soil and then reflected in the clay layer. The trapping of the waves induced then the structure vibration to such an extent that people felt the vibration.

The observations of the influence of one or several structures on the ground motion lead to interest in the interaction of the dynamic behavior of a group of structures and the ground motion (SCI), as for example a city lying on a sedimentary basin. Wong and Trifunac (1975) showed that, through 2D modeling of rigid semi-circular foundation subjected to shear horizontal waves (SH), the amplitude modification of the ground motion, particularly at the level of light structures, is caused by the reflection and the diffusion of incident waves on foundations of building groups.

All these observations show that complex interactions occur when buildings or a city, lie on soft soil, especially like a sedimentary basin. Actually, SSI impacts not only the building response but also the ground motion up to a certain distance from the structure, affecting the motion amplitude of the soil and buildings, the natural frequency, the damping of the structure, the rocking motion at the base and also the high frequency content of the ground response. The SSI estimation presents various dependent factors that make the study of the interaction effects quite difficult. It has been shown that SSI effects depend on geometrical (foundation and buildings type), mechanical (soil and structural properties) and spatial (distribution of buildings in a city, localization in the basin) features. Taking into account the phenomenon at the scale of the building and of the basin is challenging whatever the dimension of the numerical model adopted.

Numerous numerical studies for the characterization of SSI and SCI effects have already been performed using 2D models (e.g. Wirgin and Bard, 1996; Guéguen, 2000; Tsogka and Wirgin, 2003; Kham et al., 2006; Semblat et al., 2008). However, these models have limits, notably in the building representation using homogeneous block models. Indeed, the 2D configuration implicitly considers that these elements are infinite in the horizontal direction perpendicular to the profile. The finite dimension of buildings and their spatial organization within the city need a three-dimensional approach allowing to better take into account the interaction between waves, soil and buildings.

The objective of this thesis is to improve the quantification of the influence of lithological site effect and buildings on the surface seismic motion using numerical simulations. A realistic 3D geometry of a sedimentary basin is developed including or not different city configurations composed of simplified building models. One of the major contributions of this thesis is the calibration of the models based on in-situ recordings of vibration (soil and buildings).

For this purpose, we were inspired by the lower Var valley close to Nice, which constitutes a natural laboratory for the study of seismic risk in the South of France. This valley presents indeed high stakes, high-rise buildings and an increasing urbanization which has already been the subject of previous risk studies.

The manuscript is articulated according to the following chapters:

- Chapter 1 gives the basic knowledge related to the seismic risk and to the SSI. It also gathers the methods used in this thesis in signal processing and details how the data were analyzed.
- Chapter 2 presents the parametric study of the SSI impacts on the dynamic response of buildings. This study is based on 3D numerical finite element models of different structural types. The response of identical fixed and flexible base buildings is compared in order to identify the building types and dynamic parameters the most sensitive to SSI effects. The knowledge of relevant and measurable in-situ parameters will guide the instrumentation protocol of structures for the study of SSI in the Var valley.
- Chapter 3 details the dense in-situ ambient vibration instrumentations performed in various buildings in the Var valley. These temporary non-invasive measurements allow for the quick characterization of a large number of structures. A focus is made on the structure dynamic and the SSI characterization. In particular, the measures allow to obtain the dynamic parameters of the real buildings which will enable to calibrate the simplified models in the form of equivalent homogeneous blocks in the realistic 3D site-city models.
- Chapter 4 presents the development of the subsurface model of the Var valley through the combination of geotechnical borehole and ambient vibration data already available. Additional active and passive non-invasive in-situ instrumentation campaigns completed this database and thus enable to characterize the valley bedrock, and define

an average velocity zonation in the basin. The accuracy of the basin geometry helps to better estimate the site effect in the area.

- Chapter 5 combines all the elements presented in the previous chapters to build the realistic 3D site-city model for the SSI and SCI study. The seismic wave propagation is simulated using the Discontinuous Galerkin finite element method. A parametric study is performed in the time and frequency domain to quantify the influence of lithological site effect and buildings on the ground motion in the valley.

Table 1: Examples of building instrumentations for the observation of the soil-structure interaction.

Studies	Data	Methods	Main conclusions
(Merritt and Housner, 1954)	In-situ earthquake recordings	Analytical expressions, time domain (base shear forces)	The rocking motion of the building plays an important role in SSI.
(Kanai, Kiyoshi and Yoshizawa, 1961)	Ambient vibration benchmark	Statistical approach	More the shear wave velocity increases in the soil, more the building vibrates. The damping structure depends mainly on the kinematic effects.
(Housner, 1957)	In-situ earthquake recordings	Time domain (signal amplitude) , acceleration response spectra	The structure causes measurable effects on the ground motion.
(Jennings, 1970)	Forced vibration	Time domain	The interaction between the building and the soil motions is not only observed close to the structure but also up to several kilometers away.
(Wong et al., 1977)	Forced vibration	Time domain (signal amplitude)	SSI disturbs the ground motion up to distances of more than one time the size of the foundation.
(Kashima and Kitagawa, 1988)	Acceleration time series	Analytical model, time domain (coherence functions)	SSI induces a bad correlation of the high frequency content of the ground motion with distance.
(Bard, 1988)	Earthquake recordings	Time domain, frequency domain (Fourier spectra, transfer functions)	The rocking motion may represent 25 to 50% of the total transverse motion of the roof with respect to the structure base.
(Muria-Vila and Alcorta, 1992)	Earthquake recordings + in-situ ambient vibration	Analytical model, time domain, frequency domain (Fourier spectra, transfer functions)	SSI decreases the first natural frequency of buildings by 4 with respect to the fixed base model.
(Safak and Celebi, 1992)	Earthquake recordings	Frequency domain (Fourier spectra, response spectra)	The structural resonance is retrieved at high frequency on the free field motion.
(Ganev et al., 1993)	Acceleration time series + ambient vibration	Frequency domain (Fourier spectra, transfer functions)	SSI causes sway and rocking motions leading to decrease the first natural frequency of the structure.
(Paolucci, 1993)	Earthquake recordings	Analytical 3DOF spring model, time domain, frequency domain (Fourier spectra, transfer functions)	SSI effects are stronger in the rocking motion than in the torsional one.
(Meli et al., 1998)	Earthquake recordings + ambient vibration	Time domain, frequency domain	Buildings located on soft soil undergo more tilting effects due to SSI, even for structures with deep foundations.
(Kitada et al., 1999)	Forced vibration + earthquake recordings	Frequency domain	The first natural frequency of the solicited building is modified as function of its neighborhood. In some cases, the structure may significantly modify the ground motion up to a certain distance away from the buildings, especially if there is double resonance condition.

Studies	Data	Methods	Main conclusions
(Tobita et al., 2000)	Earthquake recordings + ambient vibration	Time domain (damping ratio), frequency domain (transfer functions)	The double resonance condition causes an increase of the SSI effects.
(Guéguen, 2000)	Earthquake recordings + ambient vibration	Time domain (kinematic energy ratio), frequency domain, 2D finite element model (*CESAR* code)	The soil class appears as an important parameter in the study of SSI. The effects tend to decrease the first natural frequency of the structure. The rocking motion may be more than 10% of the pure bending behavior, even for structure with foundation piles. Free oscillation of buildings were recorded to a distance of 2 to 10 times the size of the structure base, the ground motion corresponded to 25 to 5% to the one of the structure.
(Kim and Stewart, 2003)	Acceleration time series	Frequency domain (transfer functions)	SSI causes the modification of the surrounding ground motion of building.
(Cornou et al., 2004)	Ambient vibration	Spatial domain (back-azimuth), frequency domain (Fourier spectra, Horizontal-to-Vertical spectral ratio), apparent velocity, discrete wave number modeling	In the case of double resonance condition, the wave trains present high amplitude up to long distance.
(Gallipoli et al., 2004)	In-situ ambient vibration	Frequency domain (microtremor Horizontal-to-Vertical spectral ratio)	The microtremor Horizontal-to-Vertical spectral ratio method enables to estimate the presence of SSI with respect to the natural frequency of a structure. A shift of the fundamental frequency and a decrease in the ratio amplitude are observed.
(Bradford et al., 2004)	Forced vibration	Time domain (damping), frequency domain	The seismic waves are radiated from the building base to the ground.
(Castellaro and Mulargia, 2010)	Ambient vibration	Frequency domain (microtremor Horizontal-to-Vertical spectral ratio)	The SSI influence is negligible on microtremor Horizontal-to-Vertical spectral ratio.
(Castellaro et al., 2014)	Ambient vibration	Frequency domain (spectral ratio, modal characterization), boundary element method	The ground motion is influenced by the presence of structures up to 40 m away from them.
(Guéguen and Colombi, 2016)	Earthquake recordings	Time domain, frequency domain (Fourier spectra, mode shapes characterization, transfer functions), spectral element method (*SPECFEM3D* code)	Variations in the seismic response of buildings depend on the azimuth of the seismic excitation. A splitting of the fundamental frequency and a decrease of the vibration is observed with SSI.
(Sotiriadis et al., 2020, 2019)	Acceleration time series	Analytical expressions, frequency domain (transfer function), time domain (coherence function, peak ground acceleration)	SSI induces a decrease of the ground motion intensity. And it causes also the filtering of the high frequency content of the ground motion response compared to the free field.

Chapter I. General concepts and Methods

This chapter introduces the general aspects of seismic risk related to this thesis with a focus on site effect and soil-structure interaction. Then, we present the methods to model the building using analytical methods with simplified models and more advanced techniques involving numerical simulations. Finally, we describe the signal processing methods used in temporal and frequency domains applied to the motion at the top of the building (building response) and at the basin surface (site response) to extract the impulse response of the building (using transfer functions), modal parameters and to study the effects of the soil-structure interaction.

I.1. Seismic risk

Risk is the combination between hazard and vulnerability of the elements at stake. For example, if a Mw 8 earthquake hits a place where no structures are built, no damages can be induced, and the risk will be therefore inexistent. In probabilistic seismic hazard assessment (PSHA), the hazard is defined as the probability, for a given region, to be struck by a certain ground motion level during a given period of time. The level of seismic hazard notably depends on the magnitude, on the distance from the seismic sources and on the local site configuration (geology and topography). The vulnerability is an intrinsic parameter of the construction related to the degree of loss or damages due to the occurrence of the hazard. For example, when the structures are built in the compliance with the seismic building code, the seismic response of the structure is satisfactory. Nowadays, the world population continues to concentrate in urban areas, especially close to active seismic zones as subduction zones (West side of Asia, East coast of the United States, India and the Mediterranean zone) (Figure 2). This leads automatically to an increase of the risk in these areas. Populated sedimentary basins are numerous all over the world (Alpine valleys, Sichuan basin, Mexico D.F. valley, Los Angeles basin…). Indeed, they allow the development of large urban centers because of their topography and localization, generally close to the sea or a large river that facilitates goods and people transportation and supports the development of trade exchange. Unfortunately, this kind of location is also prone to site effect that is responsible of the seismic ground motion amplification as presented in Bard and Bouchon (1980a, 1980b) and in Bard and Bouchon (1985) for instance.

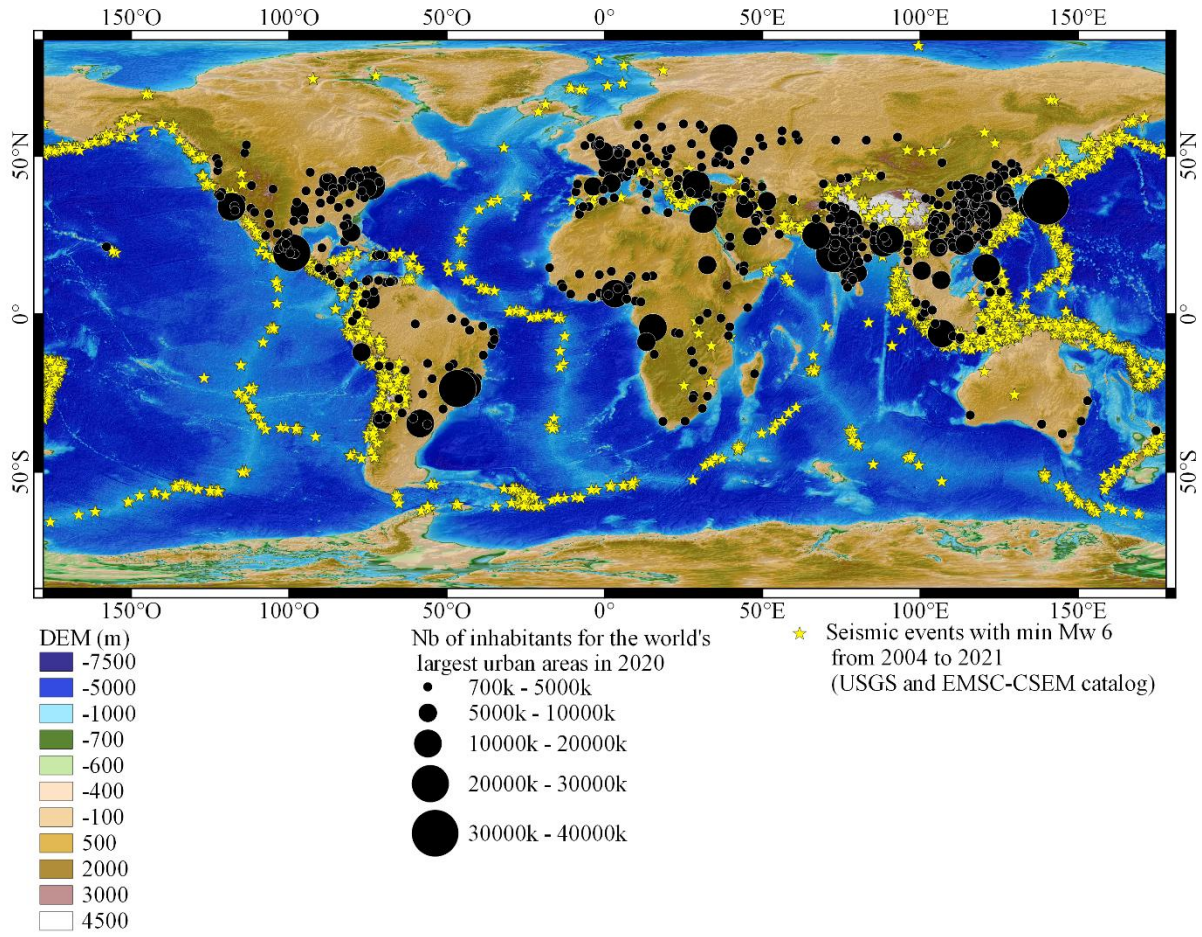

Figure 2: Exposure of the world's largest urban areas to seismic hazard in 2020. Population data are extracted from the database creating by Nordpil and the UN Population Division. The database originally represents the historic, current and future estimates and projections with number of inhabitants for the world's largest urban areas from 1950-2050 ("Nordpil," 2021).

The major destructive seismic events showed that it is not the earthquake that kills people but direct effects of the seismic vibration on structures and infrastructures (building collapse, severed infrastructure, electricity network shutdown…) and indirect effects (rock falls, landslides, liquefaction phenomenon, flooding, tsunami, pollution, homeless people, diseases…). For example, the 2015 25th April Mw. 7.8 earthquake in Nepal caused around 20k injuries directly due to the building collapse but also more than 8k of deaths related to avalanche, landslides, mudslides and network shutdown. These tragic events increasingly raise the question of how to protect people from direct and indirect damages of earthquakes and so, how to prevent structures from collapsing during an earthquake.

Seismic hazard studies at regional scale consist in the estimation of the seismic ground motion that depends on the source effects, for example, the type of faults and source mechanisms, the rupture direction, the propagation of waves in the underground medium and particularly the

attenuation with the distance considering a homogeneous medium. At local scale, the ground motion recorded on a soft or stiff soil, or on a topography, is different from the one recorded at a flat rocky outcrop.

I.2. Site effect

Increase in the vibration duration and amplification of the ground motion at certain site-specific frequencies suggest the presence of site effect. In this case, the seismic hazard estimation is not only based on source, propagation and attenuation effects, but also take into account this particular effect (Figure 3).

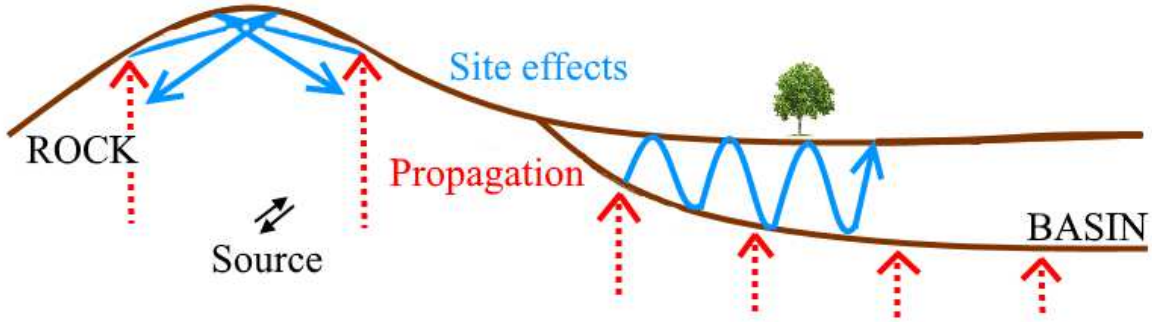

Figure 3: Scheme of the effects taken into account in the local seismic risk evaluation.

Topographic site effect is due to diffraction phenomena of seismic waves because of topographic irregularities. This effect is controlled by the wave type, the geometry and the heterogeneities within the soil. Amplifications of seismic waves may result from constructive interferences due to irregular topography like crests, hills or canyons (i.e. Boore, 1972; Gaffet and Bouchon, 1989). The examples of the 1909 earthquake in Rognes (France) or the 1695 earthquake in Civita di Bagnoregio (Italy) illustrate well the devastating effects that can be generated by this kind of site effect (e.g. Paolucci, 2002; Duval et al., 2009). In this thesis, we will only address lithological site effect due to the sedimentary filling in an alluvial valley.

Lithological site effect is function of the structure and the nature of the soil. It is due to the strong impedance contrasts between the superficial sedimentary layers where the seismic wave velocities are low, and deep soil layers where the velocities are higher. Constructive interferences of waves may result from this effect. According to the Snell-Descartes law, when the waves travel through, for example, a 1D heterogeneous bilayer media where the velocity in

the upper layer V_1 is low and in the underlying one V_2 is higher, and reach the free surface, the waves undergo modifications of their incident angle at the interfaces because of the strong impedance contrast between the free surface and the interface between the two layers. Three primary waves are induced by this phenomenon at the free surface that are the direct wave, the reflected wave and the refracted wave (Aki and Richards, 1980). The direct wave travels in a straight line to the free surface. The reflected and the refracted waves radiate back in the ground medium and reach the interface between the two layers with a certain incident angle. If this angle is lower than the critical angle i_c defined by Eq.(1), then all the waves are trapped in the upper layer. If the incident angle is higher than i_c, the refracted wave can travel back in the below layer being totally reflected toward the free surface. In the case of V_1 is higher than V_2, there is no critical angle and the refracted wave is directed to the free surface following the vertical

$$\sin(i_c) = \frac{V_1}{V_2}. \tag{1}$$

In reality within 2D and 3D domains, diffractions at the edges of the sedimentary basin and multiple reflections in the various sedimentary layers lead to additional constructive interferences between the different waves resulting in an increase in the amplitude and duration of the surface ground motion as it was the case during the 1985 Michoacan earthquake in Mexico city (Campillo et al., 1989).

Lithological site effect is characterized by a transfer function depending on the frequency. This function describes how the seismic vibration is modified by the travel of the seismic waves in the sedimentary layers. Under the hypothesis of elastic soil behavior lying on a rigid rock substratum, this function tends to reach infinite amplification at site-specific frequencies. For a soil profile composed of a unique soil layer with thickness *H* and shear wave velocity V_s, we found the well-known formula for the resonance frequencies as indicated in Eq.(2)

$$f_n = (2n-1)\frac{V_s}{4H}. \tag{2}$$

The estimation of the transfer function can be made using numerical or experimental methods. Numerical methods group together numerical models and simulations of seismic waves propagation whereas experimental methods consist in the use of seismic noise or earthquake

recordings to retrieve the characteristics of surface waves and/or more directly of the transfer function, for example using the Horizontal-to-Vertical spectral ratio (HVSR) or the Site to Reference spectral ratio (*Site/Reference*). The HVSR computes the ratio between the mean of the horizontal components of motion and the vertical one. It enables to define the frequency content of the ground response and then, to estimate the fundamental resonance frequency of the medium. The simplicity and rapidity of its application make the method common for the study of site effect. The *Site/Reference* ratio is computed from the ratio of the Fourier spectra of signal recorded on the studied site generally on soft soil site (*Site*) and the Fourier spectra of signal recorded on the *Reference* site that is generally close to a rock site where no site effect is observed. This method allows to quantify the transfer function of a site in terms of amplification and frequency because it normalizes the signal recorded at the site by the source and the regional propagation effects to only consider the impulse site response. However, the need to have a proper reference site not too far away from the considered site and to have sufficient time to record earthquakes make difficult the application of the *Site/Reference* technique. Lithological site effect is spatially variable (e.g. Olsen, 2000; Lebrun et al., 2001) and can induce heavy damages to buildings and fatalities (e.g. Bataillon, 1988; Bertrand et al., 2007). Parameters controlling the 1D, 2D or 3D resonance inside a sedimentary basin had been investigated through numerical simulations by Moczo et al. (2018). They showed that the key structural parameters controlling the resonance phenomenon are the aspect ratio of the valley that is the height-width basin ratio, the overall geometry of the sediment-bedrock interface, impedance contrast at the sediment-bedrock interface, and attenuation in sediments. It is then important to well know the basin geometry and the mechanical properties of sediments to better understand seismic hazard and prevent associated risk in dense urbanized valleys.

Besides, it is now well-recognized that the site effect can be significantly different during strong events as compared with small ones. It has been first demonstrated using laboratory tests such as cyclic triaxial press and resonant columns device on soil samples (Hardin and Drnevich, 1972; Dobry and Vucetic, 1987). Since the 80's, the seismological community has been working hard to demonstrate that non-linear soil behavior has a significant impact on site responses and consequently on the prediction of strong ground motions (e.g. Tang, 1989; Aki, 1993; Beresnev et al., 1995; Field et al., 1997).The main effects of non-linear soil behavior are a reduction of its shear modulus and an increase in its attenuation properties with strain level. The main impacts of these changes on site responses are a shift of the resonance frequencies towards lower values together with a reduction in the associated amplifications. Recently

studies have shown that these impacts are significant even at a moderate level of vibration (Régnier et al., 2013). In this thesis, nonlinearity properties are not taken into account.

I.3. Soil-structure interaction effects

The current estimation of seismic hazard at the local scale does not describe completely the surface seismic wave field in urban areas as it does not yet consider the building stock as illustrated in Figure 4. In this section, we present the soil-structure interaction (SSI) effects on the seismic response of a structure.

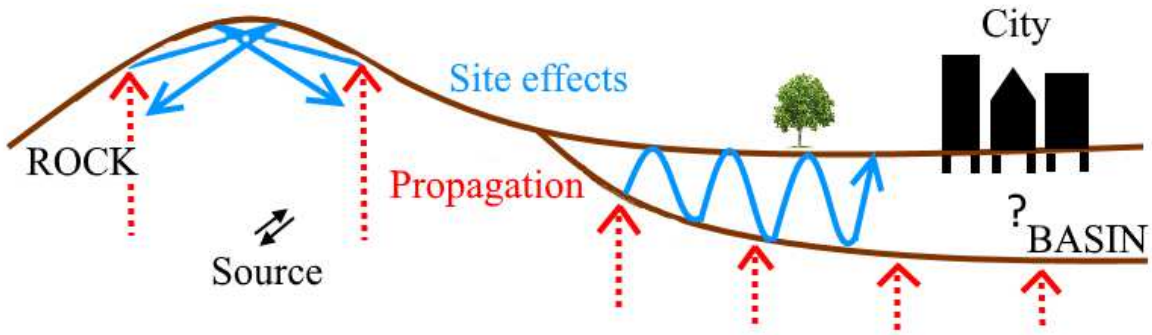

Figure 4: Scheme of the effects taken into account in the local seismic risk evaluation and uncertainty related to site city interaction.

Borghei and Ghayoomi (2019) showed that kinematic and inertial effects are at the origin of the difference between the foundation and the free field motions (Figure 5). Inertial interaction represents the transmission of inertial forces of the structure into the foundation caused by the soil-structure system oscillation under seismic excitation. Kinematic interaction is due to the relative stiffness of the foundation (Mita and Luco, 1986) compared to the embedding soil, that may alter transferred motion from the free field to the foundation, creating reflection or refraction of the propagating waves. We present both effects in this section.

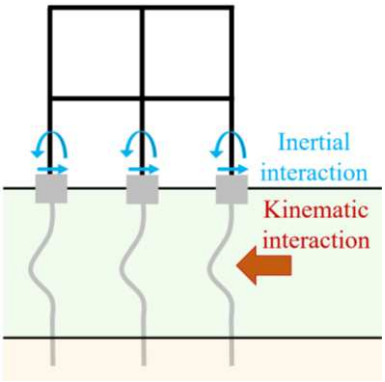

Figure 5: Scheme of inertial and kinematic effects (modified from AFPS report n°38).

I.3.1. Inertial effects

Structural vibration lead to relative displacements between foundation and free field. As this effect is caused by structural inertia, it is called inertial interaction (Apsel and Luco, 1987; Borghei and Ghayoomi, 2019). Oscillation of the structure induces waves that propagate from the structure to the soil passing through the foundation slab. This phenomenon leads to dissipate some of the deformation energy of the structure (i.e. Wirgin and Bard, 1996; Veletsos and Prasad, 1989; Stewart and Fenves, 1998; Guéguen, 2000; Dunand, 2005). With SSI, variations of the stiffness in the building can be interpreted as the results of the inertial effects. Therefore, the building impulse response can be modified and a rocking motion at the base of the building may be expected. Stewart et al. (1999) studied, through analytical model and earthquake recordings, the frequency ratio and damping factors to estimate SSI effects. The authors noted that the inertial interaction may be stronger than the kinematic interaction due to the strong impedance contrast between the soil and the structure, the aspect ratio (defined as the height-width structure ratio (Stewart et al., 1999)) and the type of foundation. From 2D linear SSI analysis using strong motion, Bárcena and Esteva (2007) defined, through displacement, acceleration time series analysis and Fourier spectra, dynamic amplification functions that illustrate inertial effects of SSI. These effects may produce an elongation of the first natural frequency of the structure and the increase or decrease of the structure response. Variations of the structure response are related to translated or rocking motion of the foundation that depend on the damping radiation.

I.3.2. Kinematic effects

Kinematic interaction is defined by the scattering and the reflection of incident wave field by the foundation. These effects produce not only an important modification of the seismic response of structures but also, change the wave field in the vicinity of buildings (Housner, 1957; Wong and Trifunac, 1975). They are at the origin of the structure-soil-structure interaction (SSSI) and site-city interaction (SCI).

Two mechanisms can explain the kinematic interaction that are the foundation effects and the embedding condition (Housner, 1957; Iguchi, 1982; Veletsos and Prasad, 1989). Kinematic effects can be neglected in the case of superficial foundations. Tang and Zhang (2011) explained that the foundation may move and undergo a rotation during an earthquake. This movement induces the modification of the input motion from the foundation to the building (kinematic effects) and changes the dynamic features of the soil-structure system (inertial effects).

I.4. Modeling of simplified buildings

Because, it is technically not possible yet to consider detailed buildings in numerical models including a large soil domain, simplified equivalent models of building are generally defined by simple relationships. These models are developed either in the form of lumped mass model, or in the form of equivalent homogeneous block. Although the lumped mass model is interesting to estimate the building response, it is difficult to integrate in numerical model when the degree-of-freedom increases. The equivalent block model can be related to a parallelepiped medium defined by an equivalent Young modulus. In this case, we deal with a 3D element contrary to the lumped mass model that is 1D. It is this type of model that we use in the finite element (FE) mesh.

Many authors used 2D solid equivalent block element for 2D numerical modeling of SSI (e.g. Wirgin and Bard, 1996; Tsogka and Wirgin, 2003; Kham et al., 2006; Semblat et al., 2008). These elements are considered having infinite extension in one horizontal direction. Guéguen (2000) notably used this technique but mentioned that this numerical model may underestimate SSI because of the low degree-of-freedom of the equivalent building element. Recently, 3D soil-structure system have been developed to estimate SSI effects. Through time domain

analysis, several studies stated that the building response increases with SSI (Ghandil and Aldaikh, 2017; Li et al., 2017).

I.4.1. Fixed base condition

The simplification of fixed base (FB) condition, currently used for building design in engineering practice, does not consider the environment in which the structure is built. The FB condition assumes thus that the building is placed on a rock site whereas the flexible base take into account the SSI (Figure 6).

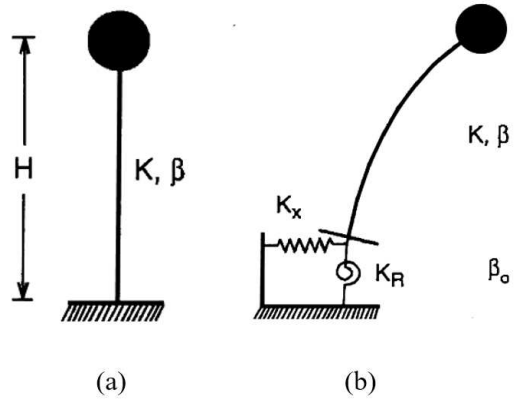

Figure 6: Simple models of (a) fixed base building and (b) flexible base building (with soil-structure interaction) from Mylonakis and Gazetas (2000). H is the height of the building. K is the stiffness of the ramp and β is the associated damping in fixed base condition. K_x and K_R are respectively the axial stiffness and the rotational stiffness induced by a flexible soil. β_0 is the effective damping of the whole system.

I.4.1.1 Harmonic oscillators

Equivalent model of building is presented as a single (SDOF) or multi (MDOF) degrees of freedom oscillator with an attributed damping. The SDOF oscillator is composed of a lumped mass model with a mass *m* hanging on a massless stem of equivalent stiffness *k* generally fixed at the base (Figure 7). For the MDOF model, each equivalent mass corresponds to the mass of each floor of the real building.

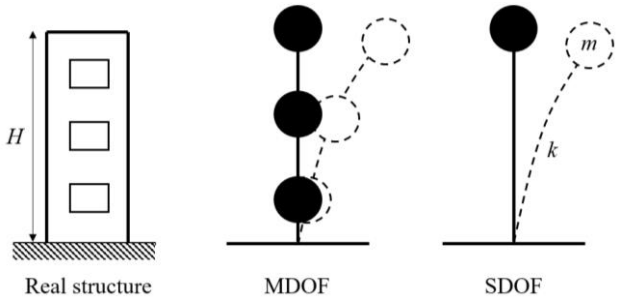

Figure 7. Representation of equivalent model of building using multi-degrees of freedom (MDOF) or single-degree of freedom (SDOF). *H* is the height of the building, *m* and *k* are respectively the equivalent mass and stiffness of each floor.

The equation of the equivalent system for a SDOF model considering free oscillation is Eq.(3)

$$m\ddot{u}(t) + ku(t) = 0 \tag{3}$$

where *m* [kg] is the equivalent mass, *k* [N.m^{-1}] is the equivalent stiffness, $\ddot{u}(t)$ is the acceleration time series and $u(t)$ is the displacement time series. The first term $m\ddot{u}(t)$ represents the inertial force. The second term $ku(t)$ represents the elastic force.

The mass and the stiffness are linked by the natural pulsation of the equivalent system ω_0 [rad.s^{-1}] by Eq.(4)

$$\omega_0 = \sqrt{\frac{k}{m}}. \tag{4}$$

And the natural pulsation is linked to the natural frequency of the equivalent system f_0 [Hz] by Eq.(5)

$$f_0 = \frac{\omega_0}{2\pi}. \tag{5}$$

Therefore, it is also linked to the natural period of the equivalent system T_0 [s] using Eq.(6)

$$T_0 = \frac{2\pi}{\omega_0}. \tag{6}$$

Introducing the damping coefficient in Eq.(3), the equation of the equivalent system becomes Eq(7)

$$m\ddot{u}(t) + c\dot{u}(t) + ku(t) = 0 \quad (7)$$

where $\dot{u}(t)$ is the velocity time series and c [kg.s^{-1}] is the damping coefficient. The added term $c\dot{u}(t)$ represents the viscous force.

The damping coefficient c indicates the energy loss due to friction and how evolves and decreases the oscillation of a SDOF system subjected to excitations. This parameter is often described by the damping ratio ξ [%] (Eq.(8))

$$\xi = \frac{c}{2m\omega_0}. \quad (8)$$

where c [kg.s^{-1}] is the damping coefficient, m [kg] is the equivalent mass and ω_0 [rad.s^{-1}] the natural circular frequency of the equivalent system.

Damping is mainly related to the mass and stiffness of a structure. These features are generally depending on the building materials but also on a combination of multiple factors linked to the structural configuration and to the connections between the structural elements. Material with high heterogeneities and low-quality connections between structural elements can lead to decrease non-linearly the stiffness of the structure and so, increase the damping (Jeary, 1997). Factors can also be of physical type: scattering effects of waves inside the building (Dunand, 2005), SSI at the foundation level leading either to radiated waves in the soil or diffracted waves in the building (Wolf, 1994; Guéguen, 2000). Many studies showed that the damping is depending on the building frequency and on the amplitude of the vibration (e.g. Jeary, 1986; Lagomarsino, 1993; Tamura and Suganuma, 1996; Satake et al., 2003; Dunand, 2005). Mikael (2011) presented an overview of several methods of determination of damping and frequency in structures in temporal or frequency domain. The author concluded that, for long ambient vibration recording (several days), these methods are convenient to estimate the frequency and the damping of a building. Mucciarelli and Gallipoli (2007) notably developed a method for the estimation of damping using short ambient vibration recordings (~6h), however this method only gives a first approximation of the damping value and is less accurate than the traditional random decrement (RD) technique.

From Eq.(7), the equation of the equivalent system considering damping and forced oscillation is defined as Eq.(9)

$$m\ddot{u}(t) + c\dot{u}(t) + ku(t) = -m\ddot{u}_g(t) \quad (9)$$

where the term $-m\ddot{u}_g(t)$ is the force applied at the base of the equivalent system. This equation is valid for shear deformation in building that means to assume that the floor is rigid and the columns or walls are flexible.

I.4.1.2 Beam models

Boutin and Hans (2009) developed criteria for the homogenization of real structures by defining theoretical models of beam based on ambient vibration, harmonic excitation and shocks recordings. Three of them are presented in the Figure 8: shear type, bending type also called Euler-Bernoulli beam and Timoshenko beam.

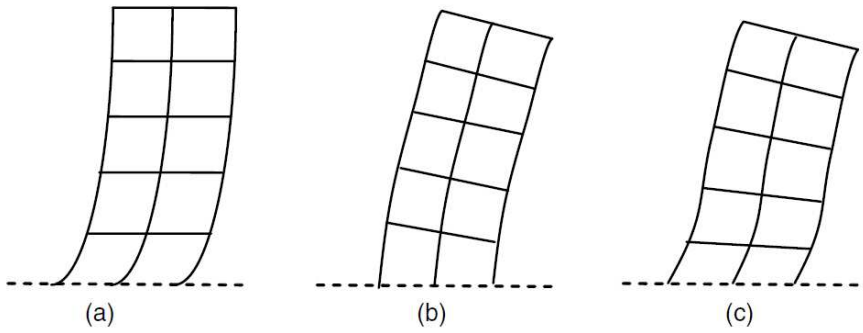

Figure 8: Framed structure with (a) shear behavior, (b) framed-wall structure with bending behavior (Bernoulli-Euler beam system) and (c) framed-wall structure with combined shear and bending behavior feature of the Timoshenko beam. Models are in fixed base condition (from Cheng and Heaton (2015)).

Shear type system is composed of rigid floors and embedded columns at the top and the bottom. The vertical elements undergo deformation. The mass is concentrated on the floors. The expression defining the free oscillation of the shear type beam model without damping is presented in Eq.(10).

$$\bar{M}\ddot{X} + \bar{K}X = 0 \quad (10)$$

where $\overline{M}$ and $\overline{K}$ are respectively the mass and stiffness matrix of the beam, $\ddot{X}$ and X are respectively the acceleration and the displacement of the beam. The solution of this equation is described in Eq.(11)

$$X(t) = \phi(x)e^{i\omega t} \tag{11}$$

where ϕ is the signal phase and ω is the pulsation. The global solution of Eq.(10) equals to Eq.(12)

$$(\overline{K} - \overline{M}\omega^2)\phi(x) = 0\,. \tag{12}$$

Considering equivalent mass and stiffness all along the shear type model, the eigenmodes and mode shape are described in Eq.(13) and Eq.(14)

$$\omega_i = 2\sin\left(\frac{2i-1}{2n+1}.\frac{\pi}{2}\right)\sqrt{\frac{k}{m}} \tag{13}$$

$$\phi_i^j = 2\sin\left(\frac{2i-1}{2n+1}.j\pi\right) \tag{14}$$

where j is the node number, n is the total node number, i is the considered mode, k is the equivalent stiffness and m is the equivalent mass of the beam.

Bending type system is composed of columns and walls where walls are more rigid than floors. The connection between both structural elements remains rigid during the deformation. The mass and the inertia module are homogeneously distributed all along the structure height. The free oscillation of the bending type model is defined by the Bernoulli equation in Eq.(15)

$$EI\frac{d^4v(x,t)}{dx^4} + m\frac{d^2v(x,t)}{dt^2} = 0 \tag{15}$$

where EI is the bending stiffness composed of E the elastic modulus and I the inertia, m is the equivalent mass and $v(x,t)$ describes the oscillation.

The solution of Eq.(15) is presented in Eq.(16) as well as the general solution in Eq.(17)

$$v(x,t) = \phi(x)e^{i\omega t} \tag{16}$$

$$\phi^4 = a^4\phi \; with \; a^4 = \frac{\omega^2 m}{EI} \tag{17}$$

where ϕ is the mode shape defined by Eq.(18)

$$\phi(x) = A_1 \cos ax + A_2 \sin ax \; + A_3 \cosh ax + A_4 \sinh ax \; . \tag{18}$$

The boundary condition of the beam represents the embedding condition described by $\phi(0) = 0$, $V(H) = 0$ and $M(H) = 0$ with M the moment, V the shear force and H the beam height. This leads to develop Eq.(19) which have roots defined in Eq.(20), Eq.(21), Eq.(22) and Eq.(23)

$$\cos aH = -\frac{1}{\cosh aH} \tag{19}$$

$$aH_1 = \frac{1.194\pi}{2}, aH_2 = \frac{2.990\pi}{2} \tag{20}$$

$$aH_n = \frac{(2n-1)\pi}{2} \; pour \; n \geq 3 \tag{21}$$

$$\omega_n = (aH_n)^2 \sqrt{\frac{E}{mH^4}} \tag{22}$$

$$\begin{aligned} \phi_n(x) = [\sin aH_n + \sinh aH_n]\left[\cosh\frac{aH_n x}{H} - \cos\frac{aH_n x}{H}\right] \\ - [\cosh aH_n + \cos aH_n]\left[\sinh\frac{aH_n x}{H} - \sin\frac{aH_n x}{H}\right]. \end{aligned} \tag{23}$$

For a sufficiently large number of nodes, the expressions Eq.(13) and Eq.(22) can be approximated by introducing the relationships between high modes frequency f_n (n >1) and the first natural frequency f_1 (for shear type (24) and for bending type (25)).

$$f_n \approx (2n-1)f_1 \qquad \text{for shear type (24)}$$

$$f_n \approx 0.7(2n-1)^2 f_1 \qquad \text{for bending type (25)}$$

The Euler-Bernoulli beam model neglects shear deformation whereas the Timoshenko beam model considers shear and bending deformation together. Complex model of Timoshenko beam have been developed to take into account the non-linear behavior of multi material beam like multi fiber wall (Kotronis et al., 2003). The equation of the behavior of the Timoshenko beam model in a horizontal motion and harmonic regime is described in Eq.(26) (Hans, 2002; Boutin et al., 2005)

$$EIU^4(x) + \frac{EI}{K} m\omega^2 U^2(x) = -m\omega^2 U(x) \tag{26}$$

where $U(x)$ describes the oscillation, EI is the bending stiffness composed of E the elastic modulus and I the inertia, K is the shear stiffness, m is the mass and ω is the pulsation .

The global solution of Eq.(26) is presented in Eq.(27)

$$U(x) = a.\cos\delta_1 \frac{x\pi}{2H} + b.\sin\delta_1 \frac{x\pi}{2H} + c.\cosh\delta_1 \frac{x\pi}{2H} + d.\sin\delta_2 \frac{x\pi}{2H} \tag{27}$$

where H is the beam height and coefficients δ_1 and δ_2 are respectively described in Eq.(28) and Eq.(29)

$$\delta_1^2\delta_2^2 = \frac{m\omega^2}{EI}\left(\frac{2H}{\pi}\right)^4 \tag{28}$$

$$\delta_1^2 - \delta_2^2 = \frac{m\omega^2}{K}\left(\frac{2H}{\pi}\right)^2 . \tag{29}$$

The dimensionless Timoshenko parameter is defined from Hans (2002) by the Eq.(30). It indicates if the structure has a behavior close to the bending type when C goes to 0 or of shear type when C is very high (Boutin et al., 2005) (Figure 9).

$$C = \frac{EI\pi^2}{4KH^2} \tag{30}$$

where H is the height of the beam and K is the shear stiffness.

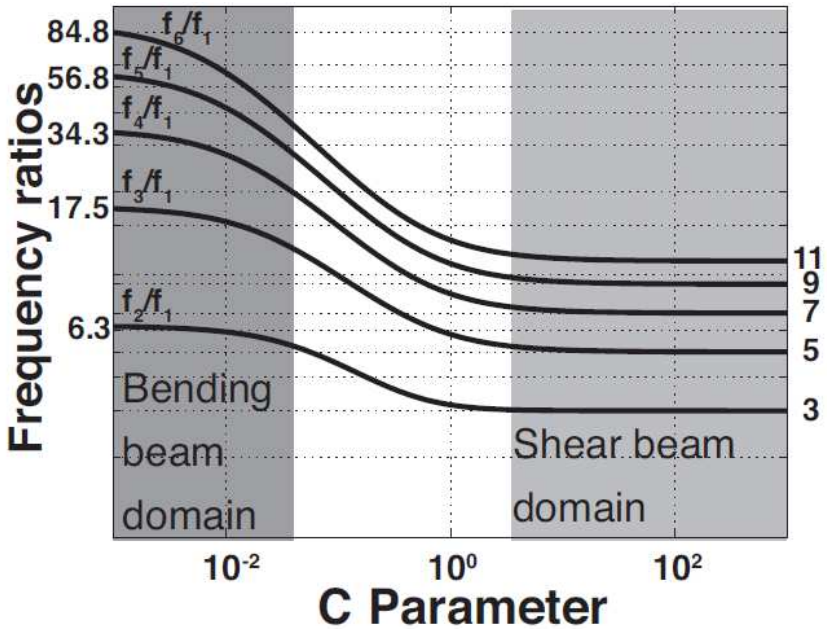

Figure 9: Estimation of the Timoshenko parameter using natural frequency ratio of the building from Michel (2007).

Parameters $\delta_1$and δ_2 are related to the Timoshenko parameter C by Eq.(31)

$$\delta_2 = \frac{\delta_1}{\sqrt{1 + C\delta_1^2}}. \tag{31}$$

As in the case of the Euler-Bernoulli beam model, the boundary condition for the Timoshenko beam is represented by the embedding condition meaning that $\phi(0) = 0,$ and $\dot{\phi}(0) = 0,$ $V(L) = 0$ and $M(L) = 0$. Parameters $\delta_1$and δ_2 are then defined by Eq.(32)

$$\begin{aligned} 2\delta_1^2\delta_2^2 + \delta_1\delta_2(\delta_1^2 - \delta_2^2)\sin\left(\frac{\delta_1\pi}{2}\right)\sinh\left(\frac{\delta_2\pi}{2}\right) \\ + (\delta_1^4 + \delta_2^4)\cos\left(\frac{\delta_1\pi}{2}\right)\cosh\left(\frac{\delta_2\pi}{2}\right) = 0\,. \end{aligned} \tag{32}$$

Eigenmodes and eigenfrequency of the considered beam model are respectively given by Eq.(33) and Eq.(34)

$$f_n = \frac{1}{4H} - \frac{\delta_{1n}^2}{\delta_{11}^2}\frac{\sqrt{1 + C\delta_{11}^2}}{\sqrt{1 + C\delta_{1n}^2}} \tag{33}$$

$$\phi_n(x) = \delta_{1n}^2\delta_{2n}^2\left[\delta_{1n}\sin\frac{\delta_{1n}\pi}{2} + \delta_{2n}\sin\frac{\delta_{2n}\pi}{2}\right].\left[\cosh\frac{\delta_{2n}\pi x}{2H} - \cos\frac{\delta_{1n}\pi x}{2H}\right] - \left[\delta_{1n}^2\cosh\frac{\delta_{2n}\pi}{2} + \delta_{2n}^2\cos\frac{\delta_{1n}\pi}{2}\right].\left[\delta_{2n}^3\sinh\frac{\delta_{2n}\pi x}{2H} - \delta_{1n}^3\sin\frac{\delta_{1n}\pi x}{2H}\right]. \quad (34)$$

Recently, Michel and Guéguen (2018) proposed a new simple formulation that links the shear wave velocity (V_s) to the natural frequency of the system taking into account the Timoshenko beam behavior. This formulation is well suited in Timoshenko-like structure for ambient vibration data and the results better fit the measured velocity. According to Michel and Guéguen (2018), the V_s in the building can be found using the Timoshenko correction factor χ_j :

$$f_j = \frac{Vs}{4H}\chi_j(C) \quad (35)$$

where f_j is the natural frequency [Hz] in the direction j, V_s is the shear wave velocity [m.s^{-1}], H is the height of the building and $\chi_j(C)$ is a numerical factor depending on the Timoshenko parameter and estimated by graphic reading.

I.4.2. Flexible condition: soil-structure interaction

Several analytical and numerical methods exist to study the SSI. Makrypidi et al. (2017) compared different methods for the modeling of SSI from direct methods to hybrid methods. They emphasized the spring method and the coupling of the FE and beam element methods (FEM-BEM). In the framework of this thesis, we focus on the numerical modeling of the SSI using FE method.

The FE method (Day, 1977) and the BEM (Bonnet, 1999) represent the most commonly used approaches for seismic simulation in continuum domain.

The BEM enables to create infinite or semi-infinite complex domain and to obtain precise solution in each node (Sanchez-Sesma and Luzon, 1995; Beskos, 1997; Semblat and Dangla, 2005; Semblat et al., 2000, 2008). This method is convenient for weak heterogeneities and linear models. The disadvantage of this method is found in the high computation time for large

models. Improvements are proposed in the studies of Chaillat et al. (2008, 2009) and tested in the application for sedimentary basin (Meza-Fajardo et al., 2016).

The FE method (Bielak et al., 2003) allows to study complex geometries by discretizing spatially and temporally the domain and to consider the non-homogeneous soil properties (Chin-Joe-Kong et al., 1999; Bielak et al., 2005). It often allows a high accuracy in the result but requires high computation time. A brief presentation about other numerical methods for the modeling of seismic wave propagation is proposed in Appendix 1. This approach is commonly used in the engineering and seismologist community to study fluid or structural dynamics. Moreover, this method displays many advantages to model specific structure like building or bridge. To model FE structures, different software exist like *SAP2000* (https://www.csiamerica.com/ [last access: 02/11/2021]), *ABAQUS* (https://www.3ds.com/products-services/simulia/products/abaqus/) [last access: 10/04/2020]), *Cast3M* (http://www-cast3m.cea.fr/index.php [last access: 02/11/2021]) or *ASTER* code (Levesque, 1998), *CESAR* (https://www.cesar-lcpc.com/fr/ [last access: 03/11/2021]) or *OpenSees* (https://opensees.berkeley.edu/ [last access: 03/11/2021]), all showing their advantages and drawbacks.

To study the SSI, several software can be employed like *LAYER* (Rukos, 1971), *SLAVE* (Constantino and Miller, 1979), *SHAKE* (Schnabel et al., 1972), *FLUSH* (Lysmer et al., 1975), *SASSI* (Lysmer et al., 1988), *CARES* (Xu et al., 1990) or *CLASSI* (Wong and Luco, 1980). They are computer programs that allow to model a soil column and foundation matrix to compute impedance functions. In the framework of this thesis, we chose to use the *ABAQUS* software to model 3D buildings using the FE method. This software proposes a very intuitive interface for the user such as it gives the impression to “draw” the structure. It is often used by civil engineering student and experts (Helwany, 2007; Lubineau and Ladevèze, 2008; Giner et al., 2009; Sinaei et al., 2012; Barbero, 2013; Khennane, 2013; Genikomsou and Polak, 2015). Practically, the software computes the displacement, the related deformation and the constraint for each node of the FE model. It also allows to directly compute the impulse response of the building to find the modal parameters. The whole system is considered linear with only small constraints.

The discrete dynamic equilibrium equation is solved directly for the soil domain and the structure, including compatibility conditions, 3D linear constitutive relation and the imposed boundary conditions. It is expressed in the matrix form as presented in Eq.(36)

$$M\Delta D^{"} + C\Delta D' + K\Delta D = \Delta F \tag{36}$$

where M, C and K are the mass, damping and stiffness matrix of the building-soil system, respectively. ΔD, $\Delta D'$ and $\Delta D^{"}$ are the increments of the absolute displacement, velocity and acceleration vectors respectively. The load vector F derives from the adopted absorbing boundary condition.

From Eq.(9), the numerical dynamic equilibrium equation for SDOF model solicited by seismic loading F can be resolved at each time knowing the Eq.(37) and Eq.(38)

$$y_i = \theta(\Delta t) y_{i-1} + \gamma_0(\Delta t)\mathrm{v}F_{i-1} + \gamma_1(\Delta t)\mathrm{v}F_i \tag{37}$$

$$\dot{y}_i = D y_i + \mathrm{v}F_i \tag{38}$$

where i is the iteration step and the terms y_i, v, θ(Δt), D, $\gamma_0(\Delta t)$ and $\gamma_1(\Delta t)$ are respectively defined by Eq.(39), Eq.(40), Eq.(41), Eq.(42), Eq.(43) and Eq.(44) considering the resting initial conditions $u(0) = 0$ and $\dot{u}(0) = 0$.

$$y_i = \begin{bmatrix} u(t_i) \\ \dot{u}(t_i) \end{bmatrix} \tag{39}$$

$$\mathrm{v} = \begin{bmatrix} 0 \\ 1 \end{bmatrix} \tag{40}$$

$$\theta(\Delta t) = \begin{bmatrix} -\omega_0^2 g(\Delta t) & h(\Delta t) \\ -\omega_0^2 h(\Delta t) & h(\dot{\Delta} t) \end{bmatrix} \tag{41}$$

$$D = \begin{bmatrix} 0 & 1 \\ -\omega_0^2 & -2\xi\omega_n \end{bmatrix} \tag{42}$$

$$\gamma_0(\Delta t) = \left(\theta(\Delta t) - \frac{1}{\Delta t} L(\Delta \mathrm{t}) - \mathrm{I}\right) D^{-1} \tag{43}$$

$$\gamma_1(\Delta t) = \left(\frac{1}{\Delta t} L(\Delta t) - I\right) D^{-1} \tag{44}$$

where ω_0 is the angular frequency, ξ is the damping ratio, I is the identity matrix, the functions $L(\Delta t)$, $g(\Delta t)$, $h(\Delta t)$ and $\dot{h}(\Delta t)$ are given in Eq.(45), Eq.(46) and Eq.(47)

$$L(\Delta t) = (\theta(\Delta t) - I)D^{-1} \tag{45}$$

$$h(\Delta t) = g(\Delta t) = \frac{1}{\omega_0^2} e^{-\xi\omega_0\Delta t}\left(\cos(\omega_D \Delta t) + \frac{\xi\omega_0}{\omega_D}\sin(\omega_D \Delta t)\right) \tag{46}$$

$$\dot{h}(\Delta t) = e^{-\xi\omega_0\Delta t}\left(\cos(\omega_D \Delta t) - \frac{\xi\omega_0}{\omega_D}\sin(\omega_D \Delta t)\right) \tag{47}$$

where $\omega_D = \omega_0\sqrt{1-\xi^2}$ is the damped angular frequency of vibration.

The dynamic properties of the FB structure are obtained in the FE scheme by solving the eigenvalue problem using Eq.(48)

$$K_{FB}\Phi = M_{FB}\Phi\Omega^2 \tag{48}$$

where M_{FB} and K_{FB} are respectively the mass and stiffness matrix of the FB building. Φ is the modal matrix. The terms of the diagonal matrix Ω are the natural pulsations of the building. Natural pulsations are the real non-zero values in ascending order obtained by solving Eq.(49)

$$\det(K - \lambda M) = 0 \tag{49}$$

where λ is the vector of eigenvalues such as $\lambda_i = \omega_i^2$.

The modal matrix Φ is orthonormalized with respect to mass matrix, such as $\Phi^T M_{FB}\Phi = I$, where I is the identity matrix. The columns of the modal matrix Φ represent the mode shapes of the building. It gives the displacements associated to each degree-of-freedom in the mode shape.

I.5. Estimation of dynamic properties of building and soil from seismic signals

In this thesis, several temporal and frequency domain methods are used to investigate dynamic parameters of buildings and soil. We use results from numerical FE models and experimental data recordings in the Var valley. For numerical models, synthetic seismic signal and white

noise are considered as signal input motions. Experimental records are composed of earthquake and ambient vibration recordings.

To empirically characterize SSI, we are looking at dynamic parameters of buildings that are the resonance frequencies, the mode shapes, the damping and the seismic wave velocity propagating in the structure. The rocking motion at the base of buildings and the motion intensity parameters are also investigated. Besides, we review the methods to obtain the fundamental resonance frequency of the soil. Results are compared using a variation coefficient (%) described in Eq.(50)

$$\frac{|x_A - x_B| \times 100}{x_A} \tag{50}$$

where x_A is the variable of reference and x_B is the variable to be compared.

I.5.1. Modal parameters

To estimate the resonance frequency of a structure, the Fourier spectra, the transfer function and the RD method are used. We apply operational modal analysis (Brincker et al., 2001; Zhang and Brincker, 2005) on numerical and experimental signals to study also the mode shapes and the damping coefficients of structures (e.g. Trifunac et al., 2001; Dunand, 2005; Michel et al., 2008; Lorenzo, 2016; Athanasiou et al., 2020). The frequency domain decomposition (FDD) method is used in accordance with the vectorial RD method to precise the determination of building mode shapes.

I.5.1.1 Resonance frequency

- *Fourier spectrum*

The Fourier spectrum *S(w)* describes signal time series by equivalent functions in the frequency domain (Eq.(51)). It is computed based on integral relationships composed of harmonic terms applicable to a random signal *s(t)* (Eq.(52)).

$$S(w) = |A(w)|e^{i\phi(w)} = \int_{-\infty}^{\infty} s(t)e^{-i\omega t}dt \quad (51)$$

where *w* is the angular frequency, *A(w)* is the amplitude of each harmonic component, $\phi(w)$ is the phase shift and

$$s(t) = \frac{1}{2\pi}\int_{-\infty}^{\infty} S(w)e^{i\omega t}d\omega\,. \quad (52)$$

The Fourier spectrum is computed based on the discrete Fourier transform of an arbitrary signal time series using the Fast Fourier Transform technique (FFT).

- *Frequency response function*

The frequency response function is the function that modifies the input signal going through a system. In the temporal domain, this function represents the impulse response of the system, also called Green function in seismology. In the case where the transfer function is defined as the ratio of the Fourier spectrum of the motion at the building roof level $U(f)$ and the Fourier spectrum of the motion at the building ground level $S(f)$, the function provides information about the frequency content of the building impulse response and not of the global system response that is, in the case of SSI, the building and the soil domain (Figure 10).

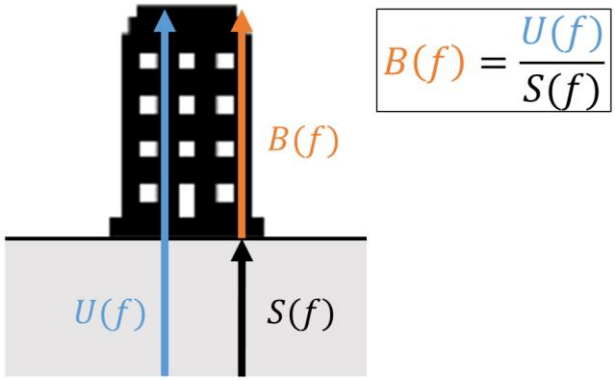

Figure 10: Scheme and equation of the frequency response function for application in building.

- *Earthquake Horizontal-to-Vertical ratio and Standard Spectral Ratio*

The HVSR technique can be applied on earthquake recordings (e.g. Lermo and Chavez-Garcia, 1993; Theodulidis and Bard, 1995; Yamazaki and Ansary, 1997). In the thesis, this method is used to estimate site effect in the lower Var valley from several earthquake recordings and to compare the results with the one of the Standard Spectral Ratio (SSR) approach (Borcherdt, 1994; Duval and Vidal, 2003; Duval et al., 2013) that is similar to the *Site/Reference* ratio presented before. For both methods and for each earthquake recordings, the condition of the signal windows selection is that the signal to noise ratio should be above 3. The earthquake HVSR is defined by the ratio between the mean of the horizontal components and the vertical one of one seismic signal whereas the SSR is based on the ratio between the Fourier spectra recorded at a considered site (for example on a sedimentary basin) and the one of a reference site (for example a close by rock site) for one component of motion.

- *Microtremor Horizontal-to-Vertical ratio*

The HVSR approach is also used for microtremor data (Nakamura, 1989) through the *Geopsy* open source software (Wathelet et al., 2020) to estimate the depth of the different impedance contrasts in the soil at the studied site. First, we select the time windows, with an overlapping coefficient of 5%, where the signal is stationary which is one of the requirements for microtremor HVSR analysis. The number of selected windows varies according to each measurement. A 5% cosine taper is applied on both ends of the windows. The ratio between the mean of the horizontal components and the vertical component of each selected signal windows is computed using the FFT. A Konno and Ohmachi (1998) smoothing is applied to the ratio using a b-parameter equals to 40. The HVSR curves are computed by averaging all individual smoothed ratios. The origin of ambient vibration data is then studied to identify natural or anthropic sources. Natural origin of these data is characterized by the SESAME (site effects assessment using ambient excitations) European project (European Commission, 2004) and must satisfy the followings criteria:

- A flat noise spectrum for all frequencies and on the 3 components (north, east and vertical).
- The amplitude of the rotation spectrum as function of the azimut is the same for all azimut.

- The noise auto correlation for east and north components has the shape of an attenuation with time, not the shape of a sweep (maintained noise).

According to this project, a clear peak is well distinguished on HVSR curves when site effect is present. The first peak of HVSR curves is assumed to indicate the resonance frequency of the soil column. This assumption is applied for curves with well-defined and single sharp peak with amplitude level above than 3 and additional criteria detailed in the SESAME European project (European Commission, 2004).

I.5.1.2 Mode shape

➢ *Frequency Domain Decomposition*

The FDD is a non-parametric method in the frequency domain introduced by Brincker et al. (2001). It is commonly used in operational modal analysis of structures. In fact, the method provides information about the natural frequencies, damping, and the mode shapes of the system. The equation of the response of a structure is defined as the sum of its modal deformations by Eq.(53)

$$y(t) = \Phi_1 q_1(t) + \Phi_2 q_2(t) + \cdots + \Phi_{n_c} q_{n_c}(t) = \Phi q(t) \tag{53}$$

where n_c is the number of sensors, Φ is the modal matrix and $q(t)$ is the modal vector. They are defined by:

$$\Phi = [\Phi_1\ \Phi_2 \dots\ \Phi_{n_c}] \tag{54}$$

$$q(t) = [q_1(t)\ q_2(t) \dots\ q_{n_c}(t)]^T \tag{55}$$

where *T* is complex conjugate and transpose.

The FDD method allows to decompose the cross-correlation between all simultaneous recordings, in independent degree-of-freedom by means of the singular values decomposition (SVD) (Prevosto et al., 1982). In order to keep the phase information of the waves, it is

important that the recordings are simultaneous. The correlation functions matrix is given in modal coordinates by Eq.(56)

$$R_y(k) = E[y(t)y^T(t+k)] = \Phi E[q(t)q(t+k)]\Phi^T = \Phi R_q(k)\Phi^T \quad (56)$$

where $R_y(k)$ is the correlation matrix, $E[\bullet]$ is the mathematical Esperance function, $y(t)$ is the vector of the building response, Φ is the modal matrix and $R_q(k)$ is the matrix of the correlation functions in modal coordinates.

By applying the Fourier transform to Eq. (56), the spectral density matrix of the responses is obtained by Eq.(57)

$$G_y(f) = HG_q(f)H^T \quad (57)$$

where H is the frequency response function matrix and $G_q(f)$ is the power spectral density matrix (PSD) of the input.

H can be decomposed in partial fraction form (Brincker et al., 2001) by Eq.(60(58)

$$H(j\omega) = \sum_{k=1}^{n} \frac{R_k}{j\omega - \lambda_k} + \frac{\overline{R_k}}{j\omega - \overline{\lambda_k}} \quad (58)$$

where n is the number of modes, λ_k is the pole and R_k is the residue defined by Eq.(59). The poles indicate where the maximum of the cross-correlation are reached in the frequency domain

$$R_k = \phi_k \Upsilon_k^T \quad (59)$$

where ϕ_k and Υ_k are respectively the mode shape vector and the modal participation vector.

For each frequency, a decomposition of the cross-correlation matrix is performed, called the SVD (Prevosto et al., 1982). This process gives the best correlation between each component of each recorded signals and then, enables the modal decomposition of the PSD matrix.

The Eq. (57) is solved using the SVD technique:

$$G_y(f) = \Phi[diag\{g_{ii}^2(f), \dots, g_{n_c n_c}^2(f)\}]\Phi^T \quad (60)$$

where $g_{ii}^2(f)$ is a spectral cross-correlation function, one corresponding to one analyzed signal for one specific frequency.

Finally, the obtained singular values are depicted to define the modal parameters of the system. The singular values show maximum at mode frequency of the structure. If several singular value curves show maximum at the same frequency, this may mean that either the source of the excitation is artificial or the mode shapes in both horizontal directions are coupled or have close resonance frequencies.

- *Vectorial random decrement*

To describe the vectorial RD, we first explain the RD method applied to a single measurement.

Random decrement method: The RD method is used to extract the RD functions for each natural frequency of the structure and at any measurement location. This method was first introduced by Cole (1973) for the study of aerospace structure. The objective is to retrieve the impulse response of an equivalent SDOF oscillator. From the recording of stationary random excitation, a large number of time windows are selected using a specific triggering condition $T_{X(t)}$ and stacked to reduce the random part of the signal (Eq.(61)). More details about the definition of the triggering conditions can be found in Alvandi (2003). This method presents the advantage to be independent of the seismic source but is limited to one unique measurement.

$$RD(\tau) = \frac{1}{N}\sum_{i=1}^{N} X(t_i + \tau)\,|T_{X(t)} \quad (61)$$

where N is the number of windows in the mean of the signal and $X(t_i + \tau)$ defines the signal window.

For one mode n, the signal is filtered around the frequency f_n (identified on the SVD) using a Butterworth passband filter of order 3 from $0.95f_n$ Hz to $1.05f_n$ Hz. A triggering process is applied to the filtered signal, the condition to select the beginning of a window is the signal amplitude is over zero and the slope is positive:

$$T_{X(t)} = \left\{ X(t) = 0, \qquad \frac{dX(t)}{dt} > 0 \right\}$$

where $X(t)$ is the signal amplitude. The selected time windows have the same length than the one chosen for the FDD computation. At the end of the process, all windows are stacked and averaged to obtain the RD functions.

In this thesis, the method proposed by Clough and Penzien (1993) is adopted to precise the natural frequency of the building models. The idea is to retrieve the natural period that best fit the corresponding mode by computing the RD functions of the signal. Several authors already used this method to study the damping behavior of structures from ambient vibration recordings (e.g. Caughey and Stumpf, 1961; Vandiver et al., 1982; Ibrahim et al., 1998; Huerta et al., 1998; Huang and Yeh, 1999; Dunand et al., 2002; Dunand, 2005; Lorenzo, 2016).

In this process, each extremum of the RD functions is identified using the absolute value of the RD functions. The mean of the period between each extremum is computing according to a selected number of periods. This is this period that is used hereafter to precise the frequency value related to the modal deformation of the structures.

Vectorial random decrement method: Contrary to the traditional RD technique, the vectorial RD method enables to consider MDOF system. This method was developed by Ibrahim et al. (1998). Asmussen et al. (1999) notably showed that this technique is more efficient compared to the traditional RD method in terms of speed and accuracy to compute the frequencies, the damping and the mode shapes of a structure. It enables to keep the phase information of several recordings in the structure based on the vector triggering conditions $T_{\{X(t_i)\}}$ (Eq.(62)). In other terms, during the computing of the RD functions from the ambient vibration data, the phase relations between simultaneous records are maintained. Practically, the time windows picked on a reference signal are applied to other signals recorded simultaneously in order to keep the same initial time between all signals.

$$\{\widetilde{RD}(\tau)\} = \frac{1}{N}\sum_{i=1}^{N} \{X(t_i + \tau)\} \,|T_{\{X(t_i)\}} \tag{62}$$

where $\{\widetilde{RD}(\tau)\}$ designates the vector of the means of RD functions.

- *Modal assurance criterion*

According to Allemang and Brown (1982) and Pastor et al. (2012), the modal assurance criterion (MAC) is evaluated as a correlation coefficient of the mode shape on a frequency range around the picked frequency on SVD. It allows to compare structural mode of the structure using Eq.(63)

$$MAC(\{\varphi_r\},\{\varphi_s\}) = \frac{|\{\varphi_r\}^{*t}\{\varphi_s\}|^2}{(\{\varphi_r\}^{*t}\{\varphi_r\})(\{\varphi_s\}^{*t}\{\varphi_s\})} \quad (63)$$

where φ_r is the displacement in one direction of the mode *r* and φ_s is the displacement in one direction of the mode *s*. The resulting MAC value is between 0 and 1 where 1 means that the modes are identical between both conditions.

I.5.1.3 Damping

The evaluation of damping values is a difficult task and still debated among the engineering community, different approaches can be used. We first introduce the damping estimation using empirical relationships. Other approaches are based on the analysis of ambient vibration recordings and the use of RD functions. Finally, we briefly introduce the consideration of damping in numerical studies.

- *Empirical relationships*

The damping can be interpreted from empirical relations derived from numerical simulations (e.g. Barbieri et al., 2004) or previous ambient vibration measurements and linked the damping value to geometrical and/or modal parameters (e.g. Jeary, 1986; Lagomarsino, 1993; Satake et al., 2003; Dunand, 2005). Some authors have shown that the damping value reflect SSI by attributing the loss of energy in the building to the frequency dependent radiated waves from the structure to the soil (e.g. Guéguen, 2000; Mylonakis and Gazetas, 2000; Satake et al., 2003). They notably compared experimental results to numerical results to show that SSI could have an important role in the damping value of buildings (Dunand et al., 2002). This observation shows that the damping value extracted from experimental measurement informs not only on

the energy dissipation due to material constituting the structure but also on the energy dissipation in the surrounding environment.

Several authors provided empirical relationships to estimate the damping value. The empirical equation proposed by Jeary (1986) is applied for buildings having different dimensions at the building step. Based on the study of Ellis (1980), the author considered the first natural frequency of the studied buildings close to $\frac{46}{H}$ [Hz] where H [m] is the height of buildings. The empirical formula Eq.(64) is derived from the dynamic analysis of nine different buildings subjected to forced vibration and controlled conditions. Because forced vibration induce higher amplitude of motion than ambient vibration, the attenuation observed in structure may be related to non-linear and hysteretic behavior of material. This is generally the case when strong motions occur. Therefore, the assumption of linear elastic material is no more valid. Variations of damping value can also be expected if SSI is present.

$$\xi = \frac{46}{H} + e^{\frac{\sqrt{D}}{2}} \times \frac{x}{H} \tag{64}$$

where D is the dimension of the building in the direction of the maximal deformation of the first mode [m] and x is the maximum amplitude at the top of the building in the direction of the maximal deformation of the first mode.

Lagomarsino (1993) proposed another empirical law close to the Rayleigh formula. Based on a dataset of 185 mixed buildings in construction materials and structural elements subjected to different excitation conditions. The author highlighted three different analogous relationships between the natural period of buildings and their height depending on the building material (steel-framed, reinforced concrete (RC) and mixed type buildings). These relationships were found close to the one proposed by Ellis (1980). The equation proposed by Lagomarsino (1993) is presented in Eq.(65).

$$\xi = \frac{\alpha}{f} + \beta f \tag{65}$$

where f is the natural frequency of the building [Hz]. The associated coefficients to apply this empirical law for different types of building are given in the Table 2.

Table 2: Coefficient of the Lagomarsino's equation (Lagomarsino, 1993).

	Steel-framed building	Reinforced concrete building	Mixed type building
α	0.3192	0.7238	0.2884
β	0.7813	0.7026	1.2856

The author specified also the confidence range (50% and 80% of confidence) for the estimation of damping ratio. According to Satake et al. (2003), Lagomarsino's relationship (Lagomarsino, 1993) tends to overestimate damping ratio for high-rise structures. The equation of Satake et al. (2003) is applied for amplitude-height ratio $\left(\frac{x}{H}\right)$ lower than 2.10^{-5} with H between 10 m and 130 m (Eq.(66))

$$\xi = 1.4f + 47000\frac{x}{H} - 0.18 \tag{66}$$

where H is the building height [m], f is the first resonance frequency of the building [Hz], D is the dimension of the building in the direction of the maximal deformation of the first mode [m] and x is the maximum amplitude at the top of the building in the direction of the maximal deformation of the first mode.

Based on a catalog of 205 mixed buildings in construction materials subjected to vibration tests of low amplitude, Satake et al. (2003) showed that higher the building, lower the damping ratio for the first fundamental mode of deformation. They also studied the SSI effects and found that low-rise RC building undergo much stronger effects than high-rise building. They define an empirical relationship to estimate damping ratio according to certain geometrical criteria ($\frac{x}{H}$ < 2.10^{-5} and 10 < H < 130 m). These criteria give the limitations of application of its law.

More precisely, Dunand (2005) showed that the relationship proposed by Satake et al. (2003) overestimates the damping for low frequencies (< 1 Hz) and underestimates this parameter for high frequencies (> 4 Hz). Therefore, the author proposed another equation to compute the damping value of the structure (Eq.(67)) based on 26 different buildings instrumented in Grenoble using ambient vibration recordings.

$$\xi = e^{-0.22+0.42f} \tag{67}$$

The empirical laws presented in this thesis and the associated database are summarized in the Table 3.

Table 3: Summaries of the dataset used to develop empirical laws from the given literature.

	Jeary (1986)	Lagomarsino (1993)	Satake et al. (2003)	Dunand (2005)
Number of buildings	9	185	205	26
Height of buildings (m)	30 to 80	Unknown	10 to 130	9 to 85
Conditions of vibration	Forced vibration at the building step	Various	Forced vibration with low amplitude	In-situ ambient vibration recordings
Empirical law	$\xi = \frac{46}{H} + e^{\frac{\sqrt{D}}{2}} \times \frac{x}{H}$	$\xi = \frac{\alpha}{f} + \beta f$	$\xi = 1.4 * f + 47000\frac{x}{H} - 0.18$	$\xi = e^{-0.22+0.42f}$

Errors induced by measurement techniques, measurement conditions or modal interferences can lead to overestimate the damping value, but they are not the only ones. Not so often confidence intervals or error investigations are shown in damping assessment study. In fact, the limited number of tested buildings (that can be standard or specific buildings) constrained the application of the relationships. These laws still must be enriched with other experimental measurements and detailed structural information to be well constrained.

Another parameter that may lead to overestimate damping ratio value is the potential presence of SSI (i.e. Jeary, 1986, 1997; Dunand et al., 2002; Satake et al., 2003). It is known that SSI effects influence the whole system by changing the building response. Those phenomena are not taken into account in the empirical laws that only considered the geometrical characteristics of the structure.

- *From vibration recordings*

The basic method to estimate the damping from experimental data is called the half-power bandwidth which is a quick identification method of the damping in the frequency domain using the shape of the resonance peak of the building. Defined as the width of the peak at $\frac{1}{\sqrt{2}}$ of its amplitude level, the damping result is dependent of the good identification of the first natural frequency of the building. Jeary (1986) briefly presented the uncertainty existing in this method.

The method proposed by Clough and Penzien (1993) is presented in the following. After the computation of the logarithm of each extremum of the RD functions, a linear regression function is applied to the results (Figure 11).

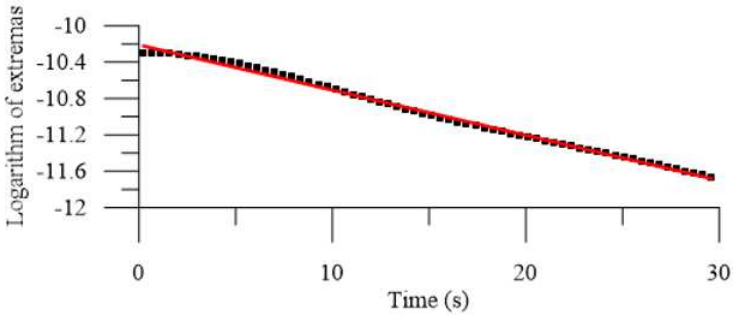

Figure 11: Damping estimation method by linear regression (red curve).

The slope coefficient of the linear regression is used in the formula proposed by Clough and Penzien (1993) to estimate the damping of the building:

$$\xi(\%) = \frac{1}{2\pi} log\left(\frac{|A_n|}{|A_{n+1}|}\right) 100 \tag{68}$$

where $|A_n|$ and $|A_{n+1}|$ are absolute values of the amplitude of two successive extremas of the RD functions. The Eq.(68) can be rewritten as Eq.(69).

$$\xi(\%) = \frac{-PT}{2\pi} \times 100 \tag{69}$$

where P is the slope coefficient of the linear regression and T is the mean of periods between two extrema.

Results from the *Geopsy* software (Wathelet et al., 2020) are also compared assuming that the method used in the software is the one proposed by Clough and Penzien (1993). We can note that no empirical relationships presented here consider SSI effects. That is why the comparison between the damping values from measurements compared with those from FB model can show possible existence of SSI.

- *In numerical study*

The viscous damping provided by structural (floor, beam, wall…) and non-structural (equipment, frame…) components is taken into account according to the Rayleigh approach (Clough and Penzien, 1993; Chopra, 2007). This also enables to attenuate numerical noise. The damping submatrix related to the building is assumed to be a linear combination of the mass and stiffness (Eq.(70)).

$$C = \alpha M + \beta K \tag{70}$$

where C is the Rayleigh damping, M and K are respectively the mass matrix and the stiffness matrix of the FB building. The factors applied to mass and stiffness matrix are respectively $\alpha = 2\xi_0(\omega_1\omega_2)/(\omega_1 + \omega_2)$ and $\beta = 2\xi_0/(\omega_1 + \omega_2)$ and depend on the first two natural pulsations (ω_1, ω_2) of the FB building and on the damping ratio ζ_0.

Generally, the Rayleigh damping is set to 5% for engineering conception of building according to the Eurocode 8 (CEN, 2003). This value is coherent with reinforced concrete buildings with masonry infill type that are not so numerous in metropolitan France. A lot of studies show that this value is overestimated and not retrieved in real buildings. It depend on the first natural frequency of the building as shown in Figure 12, the lower the first resonance frequency, the lower the damping ratio (i.e. Çelebi, 1996; Dunand et al., 2002; Satake et al., 2003; Gallipoli et al., 2009; Mikael et al., 2013).

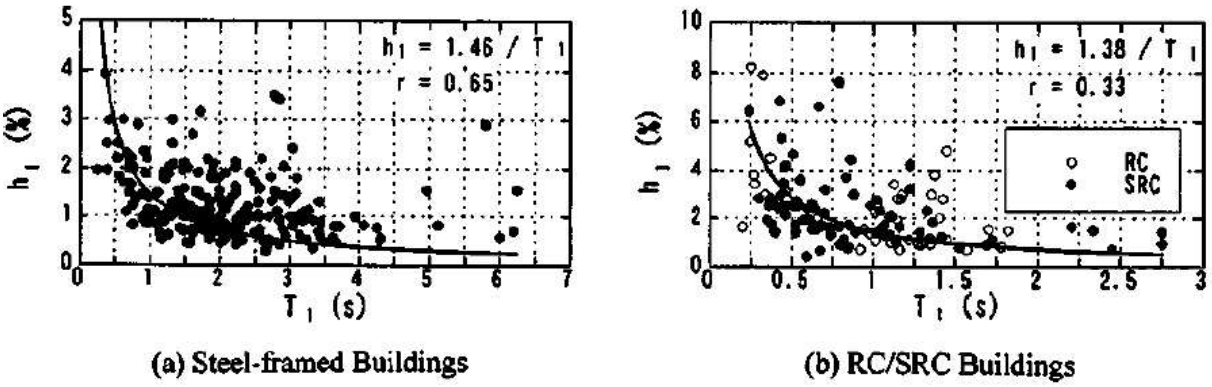

Figure 12: Damping ratio h_1 as function of the first natural period T_1 of different types of building: steel-framed buildings (a) and reinforced concrete and mixed steel-reinforced concrete buildings (b) from Satake et al. (2003).

I.5.1.4 Description of the FDDA code

To improve the modal frequency research and to apply this algorithm to buildings, a code (called FDDA) has been developed in the framework of this thesis to combine FDD and vectorial RD technique. The process can be summarized as follow:

- The modal frequency are first picked on the singular values plot from the FDD and then refined using the RD functions from the method proposed by Clough and Penzien (1993).
- The damping is estimated using the same RD technique.
- The mode shapes are computed from the vectorial RD method.

The flowchart in Appendix 2 presents the application of the combined algorithms (FDD and vectorial RD) to estimate the mode frequency, the damping ratio and the mode shapes of a structure.

To compute the FDD, we used the code developed by Keith Soal in 2016 using MATLAB® software based on the method proposed by Brandt (2011) and Brincker and Ventura (2015). Each signal is apodised using Hanning windows. Time windows of at least $10 \times 1/f_{min}$ seconds, where f_{min} is the minimal frequency considered for the analysis equals to $f_{sampling}/N_{samples}$, are selected from signal using an overlapping of 5%. This duration is chosen to be 10 times higher than the natural period of the building in order to obtain the global RD functions of the structure corresponding to the impulse response of the building (Mikael et al., 2013). The efficient cross spectral density is estimated using the welch method (Welch, 1967) with convolution and symmetry. It means that, for each time window, the signal is convolved with itself. The FFT of the convolution result is then computed in the frequency range f_{min} to f_{max} where $f_{max} = 15Hz$ that is convenient to study the global dynamic behavior of buildings. When all FFT are computed, they are convoluted one to another to obtain a PSD matrix. This matrix is then scaled in decibel and averaged. The extrema of the SVD are automatically identified in terms of frequency with a 95% range of confidence that corresponds to frequency where there is the maximum of correlation between signals, also called the modal frequency.

The vectorial RD method is implemented in a series of code developed under MATLAB® by Christian Cremona and Flavio de Souza Barbosa from the LCPC/IFSTAR/Université Gustave Eiffel (Crémona et al., 2001) originally intended for the monitoring of bridges using several

setups. At first, this algorithm aims to estimate the modal frequency through statistical results (histograms).

I.5.2. Seismic wave velocity in buildings

The interferometry computation is used to estimate the seismic wave velocity propagation in the building. According to Snieder and Şafak (2006), this method allows to separate the mechanical properties of the building from the excitation and the ground coupling by deconvolving the motion at all levels with respect to the motion at a given target level (Nakata et al., 2013). It can be applied to ambient vibration data in order to have an approximation of the impulse response of the building. However, some studies showed that the deconvolution process has difficulty to eliminate effects related to the rocking motion of the foundation (Todorovska, 2009a, 2009b).

The propagation velocity of the wave phase in the building is computed as follow:

$$V_{a-b}^{phase} = \frac{H}{t_{a-b}} \tag{71}$$

where H is the building height [m] and t_{a-b} is the time [s] taken by the causal (down going) waves to travel through the structure based on the deconvoluted seismograms filtered between frequencies a and b.

I.5.3. Torsion and rocking motions

Torsion in building is observed on horizontal components of the motion. It can be induced either by a difference in the mass center and the rigidity center of the building or by the non-symmetry of the foundation system or by both effects (Apsel and Luco, 1976; Trifunac and Todorovska, 1999). Todorovska and Trifunac (1989, 1990) showed that torsion can be important in the case of tall and slender structures.

Rocking represents a differential vertical motion between two distant points. Using analytical dynamic equations of rectangular rigid foundation subjected to oblique incident wave, Scanlan (1976) noted differences in the foundation motion whatever the direction of vibration. By

studying translational and rocking motions of a structure, Bonkowski et al. (2019) showed that torsion motion can induce either a maximal increase of 30% of the structure response or a decrease. Therefore analyzing these motions in buildings appears interesting for the study of SSI.

I.5.3.1 Classical approach in the time domain

Usually, the rocking and torsion motions are directly derived from accelerometric data of earthquake recordings (respectively for vertical and horizontal components) to find the differential displacement between two points sufficiently distant (respectively at the base and at the top of the building). However, integrating acceleration to obtain displacement should be performed with attention and requires to execute some data processing before the integration to avoid potential errors in the resulting displacement (i.e. Boore, 2001; Boore and Bommer, 2005; Javelaud, 2016). Furthermore, in the absence of rotational strong motion sensors, Trifunac et al. (2001) proposed to compute, at the foundation level, the average torsional motion of the structure in the time domain based on the differential motion between two distant sensors and earthquake recordings (Eq(72)).

$$T(t) = \frac{u_{h1}(t) - u_{h2}(t)}{d} \tag{72}$$

where $u_{h1}(t)$ and $u_{h2}(t)$ are the recordings of the earthquake in one of the horizontal component of the building (transverse or longitudinal) respectively at the sensor 1 and at the sensor 2, *d* is the distance between the both sensors [cm].

Guéguen (2000) suggested to compute the rocking motion at the foundation level based also on earthquake recordings and taking into account the height *H* of the building:

$$R(t) = \frac{u_{z1}(t) - u_{z2}(t)}{d} \times H \tag{73}$$

where $u_{z1}(t)$ and $u_{z2}(t)$ are the recordings of the earthquake in the vertical component of the building respectively at the sensor 1 and at the sensor 2, *d* is the distance between the both sensors [cm].

I.5.3.2 Torsion and rocking spectral ratio computation

The torsion spectral ratio was introduced by Dunand (2005) to estimate the torsion of a building from horizontal components of two synchronous recordings at the opposite sides of the top floor from ambient vibration recordings

$$T_{12_k}(f) = \left| \frac{FFT\ \ (u_{s1} - u_{s2})}{FFT\ \ (mean(u_{s1}, u_{s2}))} \right| \quad (74)$$

where T_{12_k} is the torsion spectrum defined as the ratio of the Fourier spectrum of the difference between the signal at the sensor 1 and the signal at the sensor 2 and of the Fourier spectrum of the mean of the both signals.

Based on the interpretations of Dunand (2005), a torsion motion of the building is expected when the torsion spectrum exceed the value of 2 and the torsion axis is more or less centered between the both sensors.

In the following of the thesis, we are also looking for the analysis of the rocking at the base of the building as a witness of the SSI. Based on Eq.(74), we will hereafter call “rocking spectral ratio” the torsion spectral ratio computed from the vertical components at the base of the building for ambient vibration and seismic data.

The rocking spectral ratio allows to precise at which frequency a vertical differential motion occurs between two points sufficiently distant. To compute this spectrum, the difference between the signals (numerator in Eq.(74)) and the mean of the signals (denominator in Eq.(74)) are calculated. Then, the Fourier spectrum of the numerator and the one of the denominator are computed. A whitening is applied to the Fourier spectrum of the denominator in order to avoid errors in the division by values close to zero. The coefficient associated to the whitening spectrum is equal to the maximum of the Fourier spectrum of the numerator divided by 100. When the Fourier spectrum of the denominator is below this coefficient, the value of the Fourier spectrum amplitude is replaced by the coefficient value.

The rocking spectral ratio is then computed using Eq.(74) for ambient vibration data. Finally, the mean rocking spectral ratio is computed as the average of the rocking spectral ratio of each time window on the same frequency range.

The analysis of the spectrum is performed in conjunction with the filtered seismic signal (if available) or RD functions from long ambient vibration recordings (a few hours) of the compared simultaneous signals. The rocking spectral ratio analysis highlights vertical differential motion in two conditions:

- The phases of the signals are opposed. The rocking spectral ratio shows infinite amplifications at some frequencies:

$$U_{s1} = -U_{s2}\ ;\ U_{s1} - U_{s2} = 2U_{s1}\ ;\ U_{s1} + U_{s2} = 0$$

$$T\ \neq 0$$

- The motion is different at both sensors. The rocking spectral ratio shows non-zero amplifications at some frequencies:

$$U_{s1} \neq U_{s2}\ ;\ \frac{U_{s1} + U_{s2}}{2} \gg (U_{s1} - U_{s2})$$

$$T \to 0$$

I.6. Intensity parameters of the seismic motion

Intensity parameters of the seismic motion can be investigated through Anderson criteria (Anderson, 2004). They are used to characterize the building response to a seismic solicitation for FB condition and with SSI in terms of cross-correlation, Arias intensity (AI), integral energy (EI), acceleration response spectra, peak acceleration, peak velocity, peak displacement and maximum relative displacement ratio.

Cross–correlation coefficient between seismic signals are computed to observe similarity between the seismic response of the FB and the flexible conditions in the temporal domain (in terms of amplitude, phase and duration). The equation of the cross-correlation coefficient is presented below:

$$C_{12} = 10\max[C^*(a_1(t), a_2(t)),0] \tag{75}$$

where the cross-correlation function is:

$$C^*(a_1, a_2) = \frac{\int a_1(t)a_2(t)dt}{[\int a_1^2(t)dt]^{1/2}[\int a_2^2(t)dt]^{1/2}} \quad (76)$$

$a_1(t)$ and $a_2(t)$ are acceleration time series.

In this research, AI and EI are calculated according to:

$$AI = I_{AI}(T_d) \quad (77)$$

where

$$I_{AI}(t) = \frac{\pi}{2g}\int_0^t a_i^2(\tau)d\tau \quad (78)$$

$$EI = I_{EI}(T_d) \quad (79)$$

where

$$I_{EI}(t) = \int_0^t v_i^2(\tau)d\tau \quad (80)$$

$a_i(t)$ is acceleration time series and $v_i(t)$ the corresponding velocity.

The acceleration response spectrum is the plot of the peak response (in terms of acceleration) of a series of oscillators of varying vibration period that are forced into motion by the same seismic solicitation.

The maximum relative displacement ratio indicates the difference of displacement between the top and the bottom of the building compared between FB condition and considering SSI. It is defined by the Eq.(81)

$$\frac{d_{SSI}}{d_{FB}} = \frac{\max(\left|d_{SSI_{top}} - d_{SSI_{bot}}\right|)}{\max(\left|d_{FB_{top}} - d_{FB\,bot}\right|)} \quad (81)$$

where $d_{SSI_{top}}$ is the displacement time series at the top of the building with SSI, $d_{SSI_{bot}}$ is the displacement time series at the bottom of the building with SSI, $d_{FB_{top}}$ is the displacement time series at the top of the building in FB condition, $d_{FB_{bot}}$ is the displacement time series at the bottom of the FB building.

Chapter II. Soil-structure characterization in a finite element numerical modeling

The Chapter II presents a numerical study of the soil-structure interaction (SSI) impact on the dynamic response of buildings. This study is based on 3D finite element models of different structural typologies as for example, shear type and bending type buildings. Five types of building are investigated: 1) shear type building having low-rise framed structure, regular in plan and elevation, 2) bending type building having low-rise frame wall system, regular in plan and elevation, 3) bending type building having low-rise frame wall system, regular in elevation but not in plan, 4) masonry low-rise building, regular in plan but not in elevation and 5) bending type building having high-rise wall system, regular in plan but not in elevation. Their seismic responses are compared between a fixed and flexible base condition in order to identify which building types and dynamic parameters are the most sensitive to SSI. We injected white noise and simulated earthquake at the base of the model and we obtained the seismic response of the building in the four corners and on all floors. The output signals of the soil-structure system are directly extracted from the numerical modeling.

Finally, a comparison between the different buildings is made as function of the modal parameters (natural frequency, mode shapes), motion intensity criteria (velocity of the seismic wave propagation in the building, acceleration peak, Arias intensity…) and we investigate rocking motion through the rocking spectral ratio.

In particular, the model of Nice Prefecture building has been first calibrated using the local soil stratigraphy, before been analyzed in the framework of the SSI investigation.

II.1. Building finite element modeling

In the framework of this thesis, we chose to use the *ABAQUS* software to model buildings using the finite element (FE) method. 3D numerical models of building present the advantage to study in detail the dynamic behavior of the structures knowing all the structural and mechanical features of them. Recently, 3D soil-structure system have been developed to estimate soil-structure interaction (SSI) effects. Through time domain analysis, several studies stated that the building response increases with SSI (Ghandil and Aldaikh, 2017; Li et al., 2017).

The structural response of the considered buildings is obtained by three-dimensional FE models of structure and soil, in the linear regime, assuming vertical propagation in horizontally layered and infinitely extended soil domain. The effect of irregularities in plan and in elevation, as well as the effect of rocking is considered for framed structures and frame-wall systems, having shallow foundation or underground floors with deep foundation.

SSI effects are studied first for different kind of buildings using a unique soil stratigraphy and second for the Nice Prefecture building using the local stratigraphy.

II.1.1. Building structural description

Four reinforced concrete (RC) buildings and one masonry building are analyzed. They are characterized by their geometry, height (Table 4) and mechanical features (Table 5):

- (ST) a low-rise framed structure, regular in plan and elevation according to the Eurocode 8 (CEN, 2003) (equivalent inertia, mass and stiffness distribution in all directions), conceived as a shear type building;
- (RBT) a low-rise frame wall system, regular in plan and elevation, conceived as a bending type building, it has concrete walls of same dimensions placed in the middle of the lateral;
- (IBT) a low-rise frame wall system, regular in elevation but not in plan, conceived as a bending type building, it has one offset RC staircase;
- (M) a low-rise masonry building, regular in plan but not in elevation, it has openings on the two longest walls, no floors are considered in order to reduce the stiffness of the building to better observe deformation through walls;
- (HR) a high-rise wall system, regular in plan but not in elevation, behaving as a bending

type building.

Table 4: Geometry of the buildings: low-rise shear type building (ST), low-rise regular bending type building (RBT), low-rise irregular bending type building (IBT), low-rise masonry building (M) and high-rise bending type building (HR). The aspect ratio is defined as the ratio between height and width (H/W) (Stewart et al., 1999).

Bldg	Floors	Height (m)	Length (m)	Width (m)	H/W	Foundation (m*m)	Soil area (m*m)
ST	4	12	15	9	1.3	16×10	40×24
RBT	4	12	15	9	1.3	16×10	40×24
IBT	4	12	15	9	1.3	16×10	40×24
M	1	8	20	10	0.8	21x11	40×24
HR	22	60	60	17	3.5	56×24	70×50

Table 5: Mechanical properties of the buildings. E is the Young modulus, v is the Poisson's ratio, ρ is the density and ζ_0 is the damping ratio.

Bldg	Structural part	E (N.m^{-2})	v	ρ (kg.m^{-3})	ζ_0 (%)
RC low-rise (ST, RBT, IBT)	All	3.122×10^{10}	0.20	2500	5
RC high-rise (HR)	All	3.300×10^{10}	0.20	2200	5
Masonry (M)	Wall	1.070×10^{9}	0.12	2500	5
	Lintel	9.000×10^{10}	0.20	2500	5

The column orientation and the floor plan dimensions are indicated in Figure 13. The FE models of the buildings is displayed in Figure 14. Special attention is paid to the orientation of the building columns in order to distribute homogeneously the stiffness in the model. Each node of the model is composed of 6 degrees-of-freedom: three of translation (x, y, z) and three of rotations (R_x, R_y, R_z).

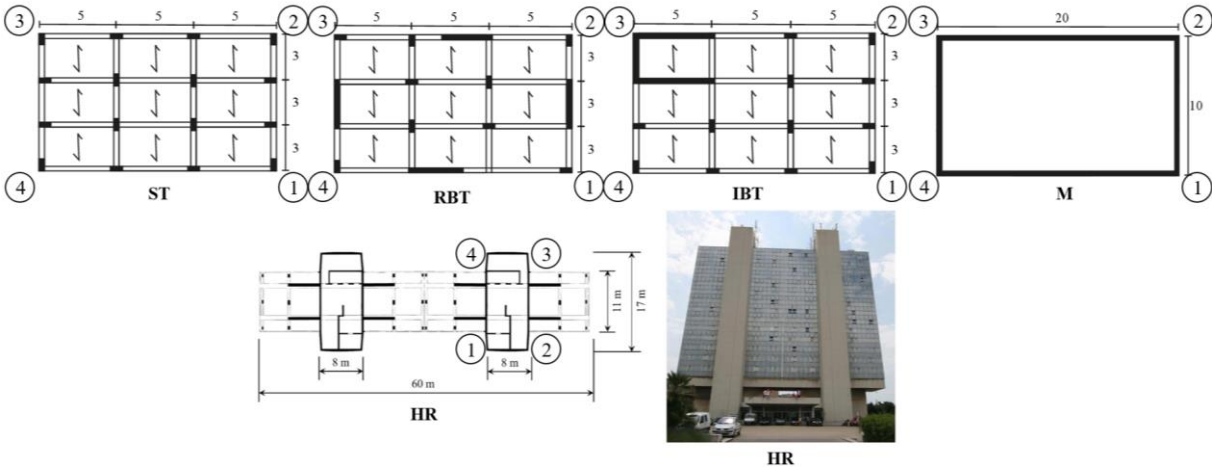

Figure 13: Plans of the analyzed reinforced concrete buildings: shear type (ST), regular bending type (RBT), irregular bending type (IBT), high-rise (HR) and masonry (M) buildings. For HR, the horizontal section is represented at +9 m above the ground and a front view of the Nice Prefecture building (southeastern France) is shown, on which the HR structure is based. The dimensions are given in meters. Corners are identified by numbers to help for the rocking motion analysis.

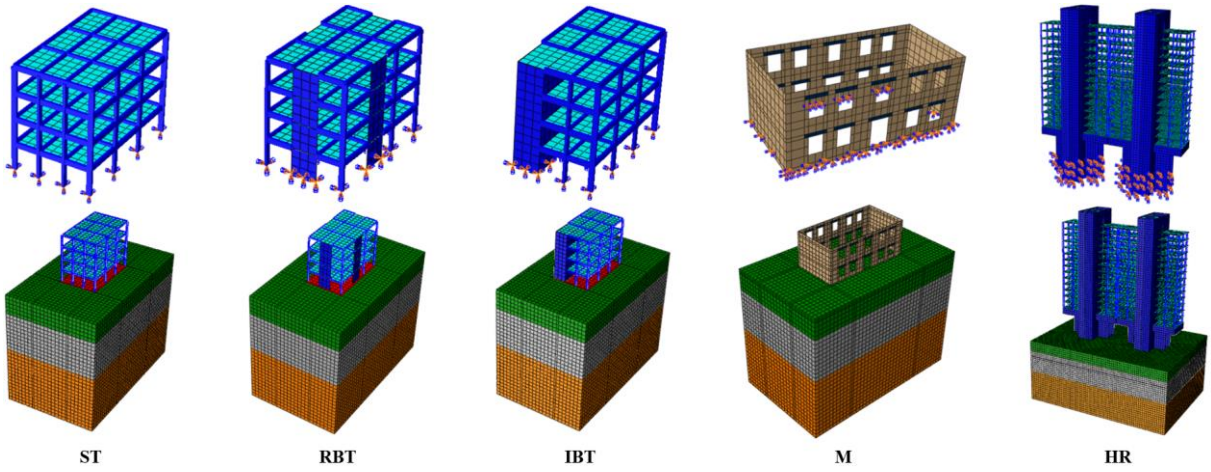

Figure 14: Finite element models of analyzed building-soil systems. Upper part are fixed base models with indicated seismic loading nodes. Lower part are soil-structure models. In the case of the masonry (M) model, the slab foundation is buried at 50 cm from the ground surface. The high-rise (HR) building is embedded in the soil domain.

The 3D framed structures are modeled using Timoshenko beam elements. The transverse shear stiffness of the beam cross-section is defined as χGA where χ is the shear correction factor (Kaneko, 1975) equal to $\chi = (5(1+\nu))/(6+5\nu)$ where ν is the Poisson's ratio, G is the shear modulus and A is the area of the cross-section of the beam. For RC buildings, the rectangular cross-section of beams elements is 30×60 cm, having shear correction factor $\chi = 0.857$. The sum of the considered dead and live loads is 800 kg.m^{-2}. This load is distributed uniformly on the beams in the longitudinal direction, according to their influence area, as mass per unit of

length. The damping ratio for all the models is $\zeta_0 = 5\%$ according to the recommendation of the Eurocode 8 (CEN, 2003).

The RC framed and frame-wall structures have an inter-story height equal to 3 m. The M model has only one storey and no floor. This building model has homogeneous building material. In reality, this kind of structure is composed of very heterogeneous material that is often weathered and replaced by new material. This leads to a complex medium that is difficult to integrate in numerical modeling in terms of computational costs. For all the FE building models, the material is considered in the linear range adopting a linear elastic model. The foundation is a rectangular RC slab that is 1 m deep and embedded in the soil. Its dimensions vary with the type of the structure (Table 4).

The analyzed HR model is based on the Nice Prefecture building (HR in Table 4). It is a complex building located in the Var valley (southeastern France, see Chapter IV). The building was built in 1979 according to the French PS69 seismic code, and is continuously monitored since June 2010 through 24 accelerometric sensors operated by the French permanent accelerometric network (Pequegnat et al., 2008; CETE, 2010a; Brunel and Bertrand, 2010). It is a 67.5 m high RC building having 20 stories and two underground levels. It is one of the highest buildings in the area. The structure is composed of two symmetric parts, each of them being a RC tower, connected by a box girder at the first floor (Figure 13e). Cantilever RC shells are fixed to the towers at each floor. Thin columns, not connected to foundation but laid on the box girder, connect the floors between them to limit deflection. The FE model of the FB HR model has been developed and discussed by Lorenzo et al. (2018).

II.1.2. Soil domain description

A 3D soil domain, assumed as horizontally layered and infinitely extended along the horizontal directions, with a building at the surface, is modeled in a FE scheme as a 3D three-components (3D-3C) model with embedding slab foundation and integrating in the *ABAQUS* software according to Fares (2018) (Figure 14). It means that the vertical propagation of shear and compressional waves from the top of the underlying elastic bedrock to the soil surface is numerically simulated in the three directions *x*, *y* and *z*, as well as the dynamic response of the

building, in the linear elastic regime. Continuity and homogeneity of materials is assumed for the structure and each soil layer.

One of the main advantages of considering a 3D soil model is that the dependence of rocking effect on the building aspect ratio is identified. Indeed, in the case of 1D soil column modeling, all displacements at the base of the building remain the same. Therefore, the 1D model does not allow to observe any rocking phenomenon.
SSI is described by the combination of kinematic and inertial interactions and rocking effects. The kinematic interaction results from the strong impedance contrast between the soil and the building where radiation phenomenon and reflection of waves in the ground due to boundary conditions can take place. The inertial interaction comes from the vibration of the building itself changing the seismic wave field at the base of the structure compared to the case in free field. In this Chapter, the kinematic interaction is considered negligible according to the horizontal layered soil domain and for vertical propagation (Betbeder-Matibet, 2008). However, this interaction is included in the 3D site-city models to study the site-city interaction in the Chapter V. Here, SSI can be analyzed in terms of inertial interaction and rocking effects. SSI in liquefiable soil is not addressed.

II.1.2.1 Mechanical characteristics

Numerical modeling of soil-structure system is sensitive to the aspect ratio that is defined here as the ratio between the length of the building and the length of the soil domain. A 1D soil column composed of the interested sedimentary layers is defined to estimate the free field soil fundamental frequency (f_{s0}). To retrieve this value in the FE soil-building model, it is necessary that the building is placed far away enough of the model boundaries. In fact, the further the building from the boundaries and the lower the influence on the f_{s0}. Therefore, the soil domain area is selected by checking that both horizontal dimensions are enough to guarantee that the obtained soil fundamental frequency is equivalent to the free field case. This frequency is evaluated through the soil surface to bedrock transfer function for the building-soil model.

The five analyzed buildings are assembled with the 30 m deep soil profile described in Table 6.

Table 6: Stratigraphy and mechanical properties of the soil domain. ρ is the density and V_p is the compressional wave velocity and V_s is the shear wave velocity.

					Element Mesh	
Depth (m)	**Thickness (m)**	**ρ (kg/m^3)**	**V_p (m/s)**	**V_s (m/s)**	**Min number**	**Max Height (m)**
0	5	1930	1330	200	4	1.3
5	10	1930	1400	240	7	1.4
15	15	1926.4	1500	300	8	1.9

The soil is modeled using 8-nodes solid FE having three translational degrees-of-freedom per node, with consequent constant strain in each element. Soil properties are assumed constant in each FE and soil layer. To accurately represent the dynamic response of the soil-structure system, the minimum number of solid elements per layer is defined as $(p \times h_i)/\lambda_{min}$ where p is the minimum node per wavelength equals to 10, h_i is the thickness of the i-th layer, λ_{min} is the minimum wavelength of the seismic signal defined by the ratio V_{si}/f_{max} where V_{si} is the shear wave velocity in the i-th layer and f_{max} is the maximum frequency assumed corresponding to 15 Hz. When the number of solid elements per layer reaches a decimal value, the result is round to the upper integer.

Stratigraphy and mechanical parameters of the soil profile, having increasing shear wave velocity (V_s) with depth, are given in Table 6. The soil profile is arbitrarily fixed to obtain a selected f_{s0} of 2.37 Hz (Figure 15).

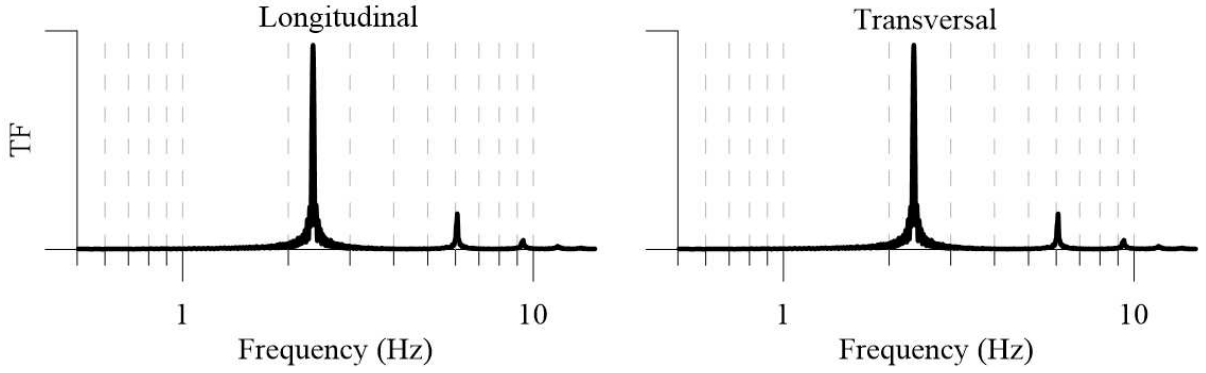

Figure 15: Transfer functions (TF) of the soil column on both horizontal components, computed considering the spectral ratio between the signal at the top and the bottom of the soil model and normalized by the maximum amplitude of the horizontal TF.

The first natural frequency of the ST model (2.4 Hz) is closed to the f_{s0}. Therefore, the double resonance condition is obtained for this model ($f_{0building} = f_{s0}$). According to the literature, the double resonance condition favor and even amplify SSI effects (e.g. Wirgin and Bard, 1996; Gallipoli et al., 2004; Kham et al., 2006; Semblat et al., 2008; Castellaro et al., 2014; Sahar et

al., 2015).

The compressional wave velocity V_p [km.s^{-1}] and the soil density ρ [kg.m^{-3}] are deduced according to the following relationships discussed by Boore (2015):

$$V_p = 0.9409 + 2.094V_s - 0.82V_s^2 + 0.2683V_s^3 - 0.0251V_s^4 \quad (82)$$

where:

$$\begin{array}{cc} V_p < 1.5\ km.s^{-1} & \rho = 1930 \\ 1.5 < V_p < 6\ km.s^{-1} & \rho = 1.74V_p^{0.25} \\ V_p > 6\ km.s^{-1} & \rho = 1.6612V_p - 0.4721V_p^2 + 0.0671V_p^3 - 0.0043V_p^4 + 0.000106V_p^5 \end{array}$$

Then, the elastic shear and P-wave moduli ($G_0 = \rho V_s^2$ and $M_0 = \rho V_p^2$, respectively) are estimated for each soil layer. The Poisson's ratio is evaluated as a function of V_p to V_s ratio, according to the relation $\nu = (0.5V_p^2/V_s^2 - 1)/(V_p^2/V_s^2 - 1)$.

II.1.2.2 Boundary conditions

We assume that the FB buildings are placed on rock site numerically defined by the embedding and the blocked rotations of the beam or walls at the base of the buildings. In the soil-structure model, the base of the building is rigidly connected to the slab foundation: translational degrees-of-freedom (x, y, z) are tied and rotational degrees-of-freedom (R_x, R_y, R_z) are blocked. The building shallow foundation is rigidly connected to the soil, node-by-node. This model induces a strong hypothesis on the dynamic behavior of the foundation because the degrees-of-freedom are limited and the foundation is considered rigid.

In order to better represent the soil domain, periodic conditions are applied on the lateral sides of the model. No strain variation is considered in horizontal directions. This is obtained by imposing a tie constraint between parallel lateral surfaces. This condition allows the use of a limited soil domain maintaining a horizontal wave front. The oedometric condition M_0 is then used to represent a compression without lateral deformation.

The soil column is bounded at the bottom by a semi-infinite bedrock having elastic behavior. Viscous dashpots are localized at the nodes of the soil-bedrock interface as absorbing boundary

condition (Joyner and Chen, 1975; Fares et al., 2019) to take into account the finite rigidity of the bedrock and allow energy to be radiated back into the soil column. Consequently, the seismic loading is first applied at the bottom of the soil column. When the energy comes back in the bedrock, a part of it is absorbed and the other part is radiated back in the soil domain.

Absorbing boundary are used at the soil bedrock interface, the shear and normal stresses at the soil column base are: $\rho_b V_{s_b}(V_x - 2V_{b_x})$, $\rho_b V_{sb}(V_y - 2V_{by})$ and $\rho_b V_{pb}(V_z - 2V_{bz})$ where ρ_b is the density of the bedrock, V_{s_b} is the shear wave velocity in the bedrock (V_{s_b}> 800 m.s^{-1} and should be large enough to avoid trapping of numerical waves), V_{b_x}, V_{by} and V_{bz} are the three components of the incident seismic motion at the bedrock level in terms of velocity in *x*-, *y*- and *z*-direction that, respectively, correspond to the halved outcropping motion $(2V_{bx}, 2V_{by}, 2V_{bz})$. The three terms V_x, V_y and V_z are the unknown velocities (incident and reflected motions) at the soil-bedrock interface, in *x*-, *y*- and *z*-direction, respectively, that are evaluated during the process.

The dissipation coefficient is defined as $C_b = \rho_b V_{s_b}$. In *ABAQUS*, the dissipation is modeled as viscous dashpots placed at each node at the soil bedrock interface of the model for the three translational degrees of freedom:

$$\delta C_x = \frac{\rho_b V_{sx} A}{N b_{nodes}} \qquad \delta C_y = \frac{\rho_b V_{sy} A}{N b_{nodes}} \qquad \delta C_z = \frac{\rho_b V_p A}{N b_{nodes}} \tag{83}$$

where $\rho_b V_{sb} A$ is applied in the horizontal directions and $\rho_b V_{pb} A$ is applied in the vertical direction. A/Nb_{nodes} represents the influence area of each node and Nb_{nodes} is the number of nodes at the base of the soil domain, having area A. The components of dynamic loading, applied at the bottom of the soil column in terms of force, are $(\rho_b V_{sb} A) 2V_{bx}$, $(\rho_b V_{sb} A) 2V_{by}$ and $\left(\rho_b V_{pb} A\right) 2V_{bz}$.

In the *ABAQUS* software, the dynamic process is solved step-by-step by the implicit Hilber-Hughes-Taylor algorithm (Hughes, 1987). This algorithm helps to control the numerical damping in high frequencies induced by the derivation of Eq.(36). The three parameters $\alpha = 0$, $\beta = 0.25(1 - \alpha)^2 = 0.25$ and $\gamma = 0.5 - \alpha = 0.5$ are used to guarantee an unconditionally numerical stability of the time integration scheme. The choice of $\alpha = 0$, meaning that we do not add numerical damping to reduce the non-physical high frequency content numerically

generated, is considered suitable in the linear elastic regime. The time step is fixed from the sampling frequency of the input signal.

II.2. Input

In order to analyze the FE models in frequency and time domain, two different dynamic loadings are injected at the base. The first one is a seismic record of the 6th April 2009 L'Aquila earthquake. The second one is a synthetic white noise showing flat envelope amplitude of the Fourier spectrum in the interested frequency band for building monitoring (0.5 – 15 Hz).

II.2.1. Synthetic white noise

A synthetic white noise is used as three-component dynamic input motion in the FE models. Inverse analysis is applied to the numerical building response to identify the natural frequencies and shape modes.

A white noise sequence of zero mean unit variance is generated, having acceleration amplitude of 1 mm/s² (Figure 16) (it is ten times larger than commonly measured ambient vibration amplitude nearly equivalent to 10^{-5} g), a duration of $t_{WH} = 300$s and a time step of $dt_{WH} = 0.02$s to ensure a maximum frequency of $f_{\max\_WH} = \frac{1}{2dt_{WH}} = 25$ Hz and a frequency step of $df_{WH} = \frac{1}{t_{WH}} = 0.0033$ Hz for the singular value decomposition (SVD) spectra of the frequency domain decomposition (FDD) analyses. The signal is subsampled to $dt_{WH} = 0.002$s to improve the discretization for the deconvolution interferometry. The Fourier spectrum of the synthetic white noise is flat in the frequency range of 0.5 to 15 Hz that is convenient for building studies (Figure 16).

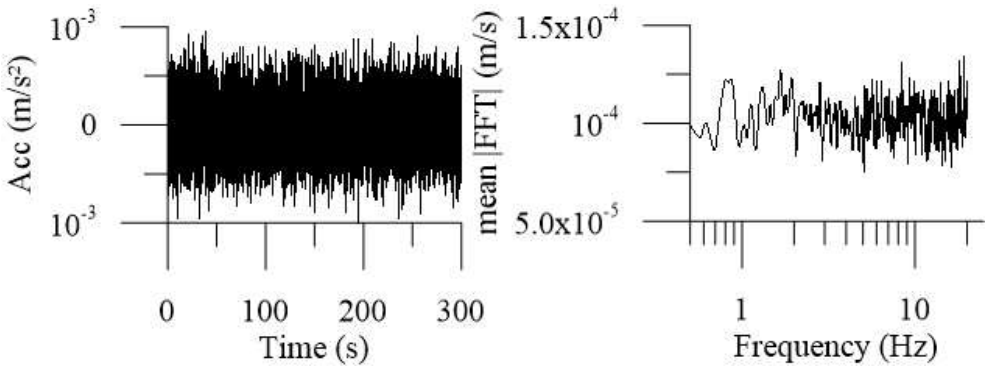

Figure 16: Synthetic white noise input (left) and mean of the absolute value of the Fourier spectrum (right).

II.2.2. Seismic record

In order to better observe SSI effects, the seismic signal injected at the base of the model should have a frequency content in good accordance to the one of the building impulse response. In that way, two options are possible for the simulation. First, a synthetic seismic signal can be chosen which have the required frequency content. This kind of signal has the advantage to be clear of any noise. Second, a real earthquake recording can be used with care to the location of recording. In fact, the best location is in the rock directly through borehole recording for example or on rock outcropping in order to limit the site response contained in the signal. Then, the frequency content of the signal can be analyzed after filtering. In this thesis, one earthquake recording is considered sufficient to take into account in the linear elastic model. A recorded signal of the 6 April 2009 M_w 6.3 L'Aquila earthquake is used as input motion to apply signal processing tools in frequency and time domain. The signal is recorded at the Sulmona station (SUL) of the Italian strong motion network, localized in Abruzzo region (Italy), at an epicentral distance of 53.7 km (Figure 17). The peak ground acceleration (PGA) is 0.34 m.s^{-2} in the East-West direction, 0.27 m.s^{-2} in North-South direction and 0.24 m.s^{-2} in vertical direction (Figure 17). The low amplitude guarantees its applicability in a linear elastic regime. The sample rate of the recorded signal is 0.005s. SUL is a free field station on stiff soil (having $V_{s30} > 800$ m.s^{-1} (https://doi.org/10.13127/SD/X0FXnH7QfY [last access: 10/05/2020])). Consequently, the record is considered as a rock outcropping motion and it is used at the base of the horizontally multilayered soil, in terms of three-component velocity. The data have been post processed by the INGV using a Butterworth filter of order 2 between 0.04 Hz and 40 Hz. According to the

Fourier spectrum in Figure 17, the seismic input has energy on a large frequency content (0.3 – 4 Hz) and, consequently, it is able to excite the natural frequencies of all the analyzed buildings.

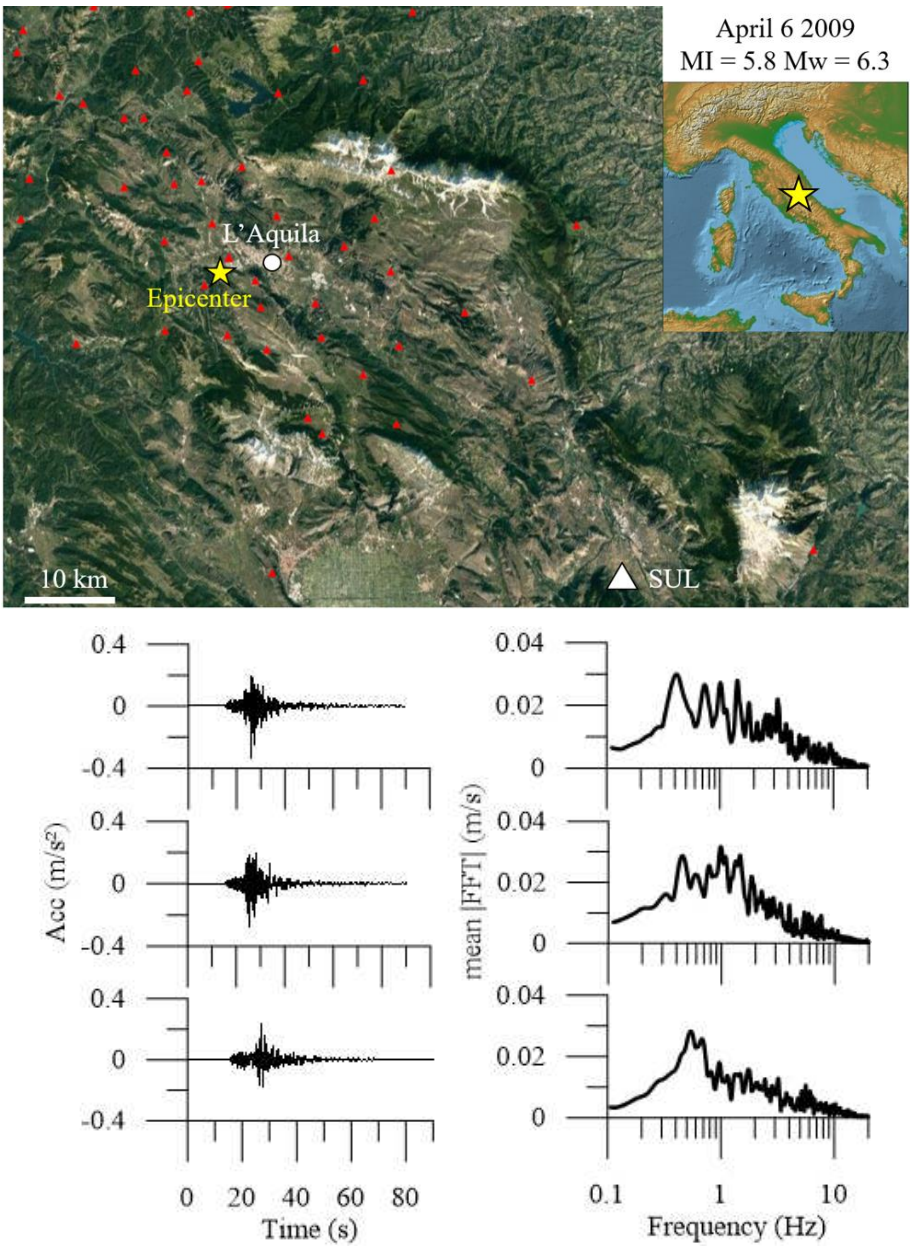

Figure 17: Acceleration time series and mean of the Fourier spectra (FFT) amplitude of the 2009 L'Aquila earthquake recorded at the Sulmona station (SUL) in Italy located on rock site for East-West (top), North-South (middle) and vertical (bottom) components (map from IPGP and FDSN). Red triangles are permanent stations of the INGV Seismological Data Centre.

II.3. Analysis of the building response

The results obtained for the five building-soil systems are presented in this section and compared with the FB condition. The objective is to identify key dynamic parameters of building sensitive to SSI effects. A three-component loading is applied in all the analyzed cases. The frequency range between 0.5 to 15 Hz is considered because it includes the frequency content of the impulse response of the most all the studied building. The FE mesh has been built accordingly to the frequency content of the loading. A large set of node points have been selected to extract signals from the model (20 for low-rise RC buildings, 22 for M building and 24 for HR building together with 72 points extrapolated). This allows, among other things, to observe detailed mode shapes and additional modes in higher frequencies.

First, the time series are analyzed for each model and compared between the FB and flexible conditions. Signal amplitude, phase and duration are notably studied using cross-correlation. The intensity parameters of the seismic motion are computed to emphasize the building response differences of each model for both conditions through Arias intensity (AI), energy integral (EI) and acceleration spectra (SA). SSI is also tracked in the frequency domain based on the noise recordings through Fourier and elastic response spectra, mode shapes and natural frequency analysis. The effective modal mass is used to understand the participation of mode in the deformation of the structure for both conditions. Rocking motion at the base of the buildings is also characterized in the frequency domain through the rocking spectral ratio and using both types of data: seismic and noise. Finally, the V_s is estimated by deconvolution interferometry for the Nice Prefecture model and compared to the velocity measured through real ambient vibration recordings (Lorenzo, 2016).

II.3.1. Signal amplitude, phase and duration

The seismic signal output at each considered points has a time step of 0.005s and 90s of duration, similar to the seismic record. The shape of the signal at the top of each FE building models is studied in terms of amplitude, phase and duration.

It is observed that the signal amplitude (Figure 18) slightly varies between both conditions for the ST, RBT and IBT models. For ST model, the signal amplitude decreases on horizontal components and increases on vertical one with SSI effects. For RBT model, it increases on all

components. For IBT building, the amplitude increases only on the vertical component with SSI effects and decreases on the horizontal components. For HR structure, the signal amplitude strongly decreases on the horizontal components, but SSI is negligible on vertical component. Finally for M model, the signal amplitude slightly increases on vertical component but shows negligible variations on horizontal components.

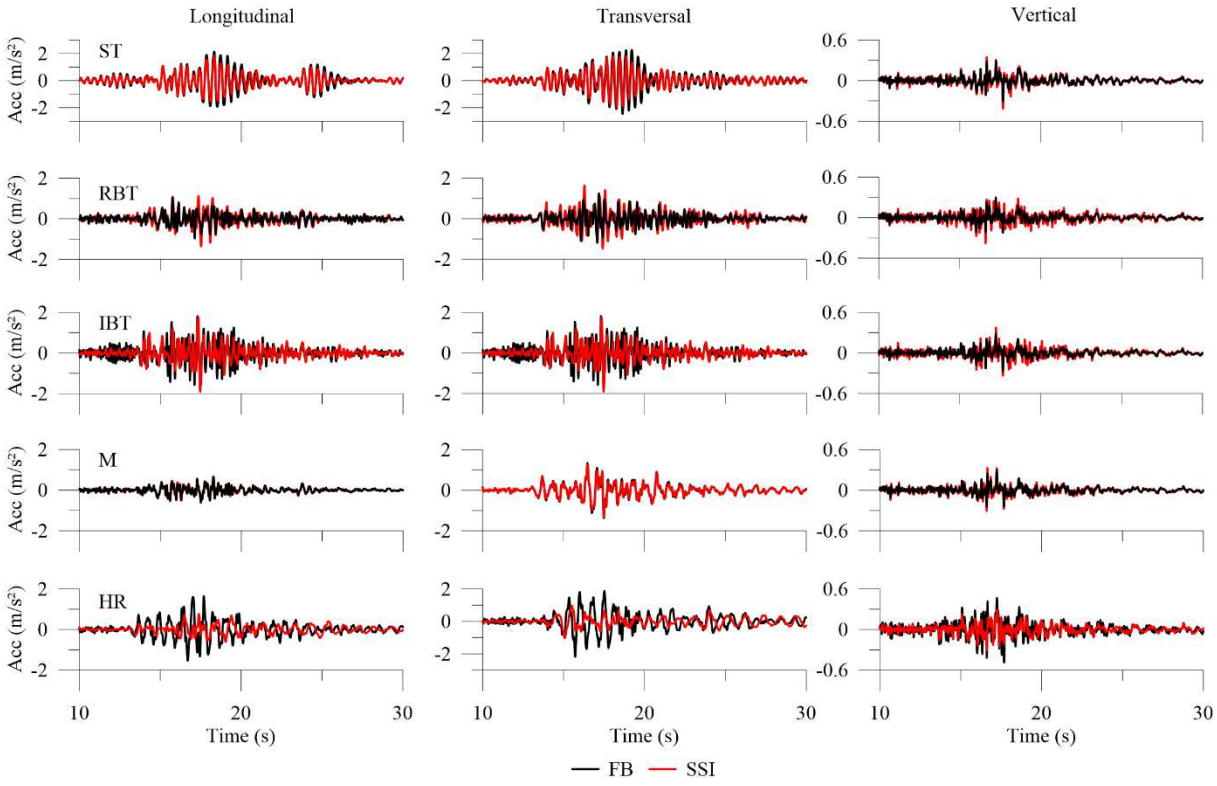

Figure 18: Zoom on the acceleration time series for fixed base condition (FB) and with soil-structure interaction (SSI) at the top of each building for the longitudinal, transversal and vertical components.

The cross-correlation analysis of signals (Figure 19) shows that SSI effects do not change the phase of the signal much for ST and M models. However, for RBT, IBT and HR structures, the phase is different between both conditions on all components (under 70% of similarity for low-rise RC buildings and less than 25% on horizontal components for HR building). For this kind of buildings, the phase seems to be a parameter sensitive to SSI effects. In a general point of view, the phase is modified on the vertical component for all the models.

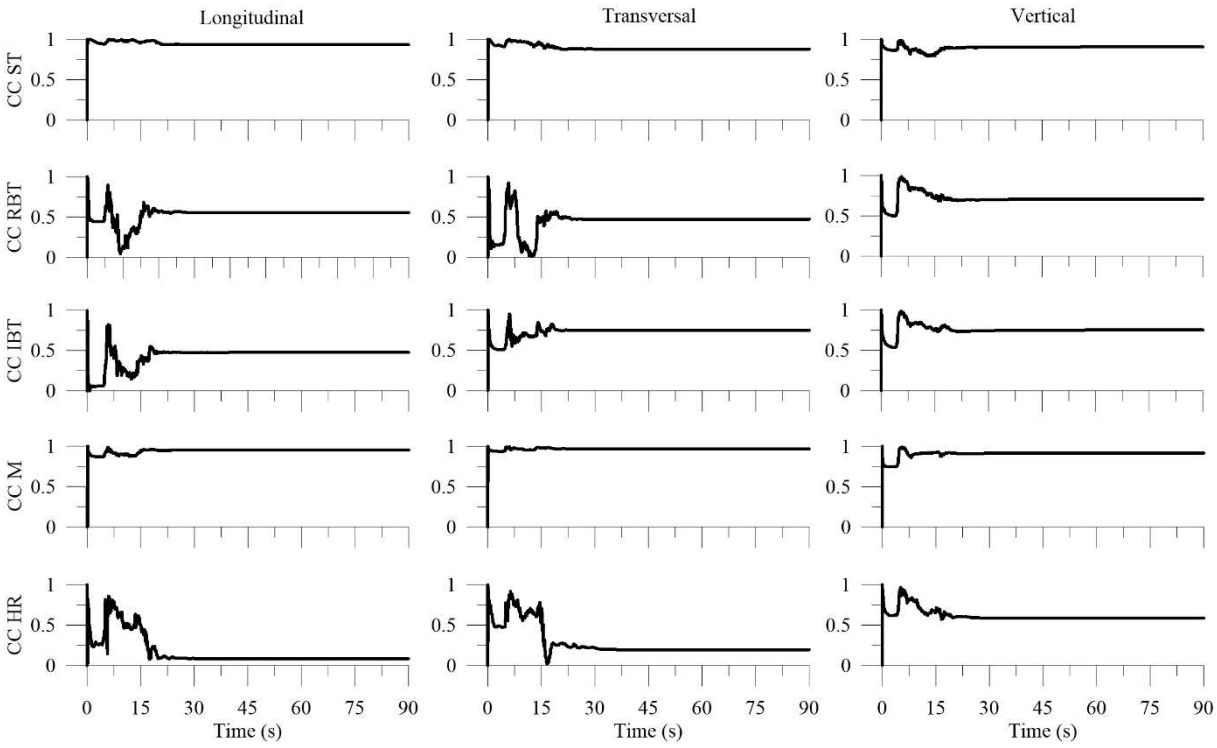

Figure 19: Cross-correlation (CC) of the signals between the fixed base (FB) and soil-structure (SSI) models at the top each building for the longitudinal, transversal and vertical components.

The duration of the signal (Table 7) exhibits negligible variations on all components for M model with SSI and slight decrease for ST and IBT models. Lengthening of the signal is observed at the top of the HR structure (from 24% to 55% on horizontal components) with SSI. However, the signal duration shows no significant changes at the bottom of these buildings. For RBT model, the duration is shortened on vertical component whatever the sensor position (top or bottom) and on the longitudinal component at the top of this building. For other components and sensor positions, negligible variations are observed between both conditions.

Table 7: Duration of signals in seconds at the top and at the bottom of each building for the fixed base (FB) and soil-structure (SSI) models for the longitudinal (L), transverse (T) and vertical (V) components. The condition applied to define the duration of the signal is that the amplitude is between 5% and 95% of the maximum amplitude of the Husid integral (squared acceleration integral of the signal).

	TOP														
	ST			RBT			IBT			M			HR		
	L	T	V	L	T	V	L	T	V	L	T	V	L	T	V
FB	10.2	9.5	19.3	14.3	10.8	20.3	11.5	11.5	20.2	11.0	15.6	20.6	10.2	10.7	14.3
SSI	10.0	10.8	17.3	10.1	12.0	16.4	10.9	10.3	17.2	11.0	16.1	19.2	22.8	17.5	18.8
Diff (%)	2	12	12	42	10	24	6	12	17	0	3	7	55	39	24
	BOTTOM														
	ST			RBT			IBT			M			HR		
	L	T	V	L	T	V	L	T	V	L	T	V	L	T	V
FB	12.1	12.5	21.8	12.1	12.5	21.8	12.1	12.8	18.4	12.1	12.5	21.8	12.5	12.1	21.8
SSI	12.2	13.2	19.0	12.1	12.9	16.7	12.1	12.5	21.8	12.0	12.6	20.0	13.4	12.5	19.9
Diff (%)	1	5	15	0	8	27	0	2	16	1	1	9	7	3	10

II.3.2. Intensity parameters of the seismic motion

Each model shows different AI and EI variations as function of the considered component (Figure 20 and Figure 21). For AI parameter, the ST building shows an important decrease on horizontal components (more than 60%) and slight increase on vertical component (less than 30%) with SSI. For RBT model, AI exhibits an important increase on all components (more than 35%) with SSI. Slight effects are observed on horizontal components for IBT model with SSI (7% in the transverse direction and 32% in the longitudinal one) but a significant increase of AI on the vertical component is noted (43% of increase). The HR building presents an important decrease of AI on all components (more than 100%) with SSI. The M structure does not show significant changes of AI parameter with SSI.

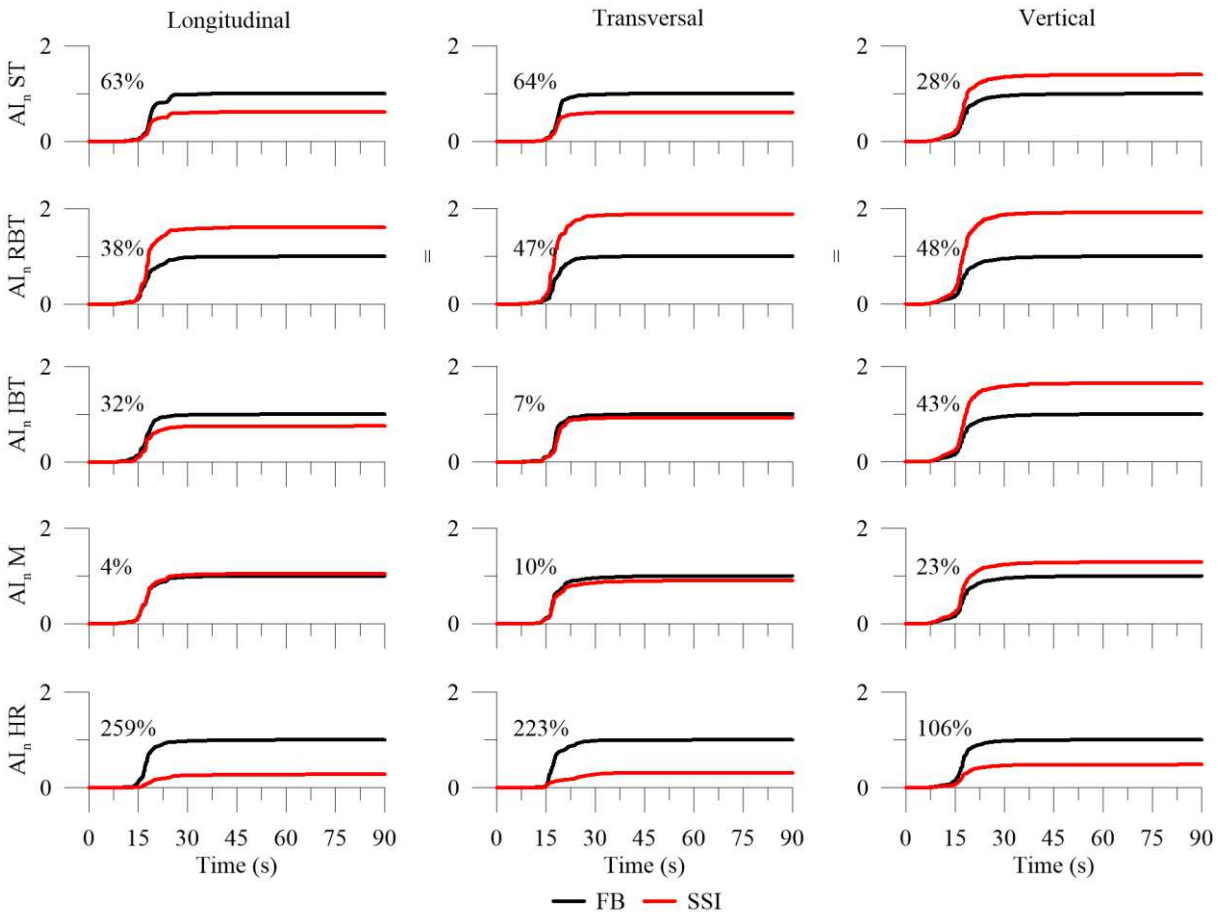

Figure 20: Normalized Arias intensity (AI_n) at the top of each building for the longitudinal, transversal and vertical components for fixed base (FB) and soil-structure (SSI) models represented with the relative difference between both conditions. AI_n is normalized using the FB condition as reference.

For EI parameter, the ST building shows an important decrease on horizontal components (more than 50%) and negligible modification on vertical component (less than 3%) with SSI. For RBT model, an important increase of EI is observed on the horizontal components (more than 40%) with SSI. No variations are noted on the vertical component. The HR structure presents an important decrease of EI on the horizontal components (above 80%) with SSI. The vertical component exhibits negligible modifications. No strong effects are observed on all components for IBT and M models with SSI (under 25% of difference between both conditions).

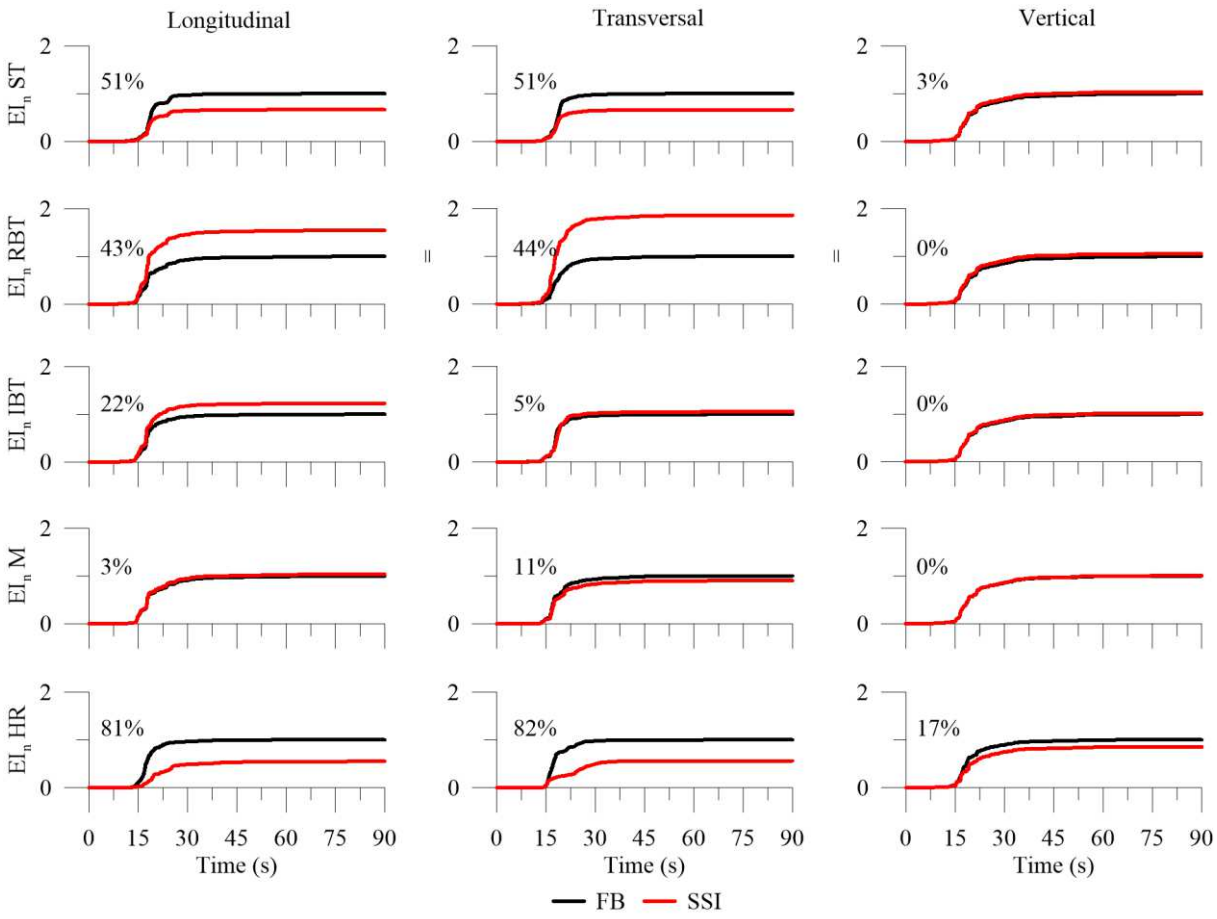

Figure 21: Normalized integral of energy (EI_n) at the top of each building for the longitudinal, transversal and vertical components for fixed base (FB) and soil-structure (SSI) models represented with the relative difference between both conditions. EI_n is normalized using the FB condition as reference.

Peak acceleration (PA), peak velocity (PV) and peak displacement (PD) values at the top and at the bottom of buildings for FB and with SSI, and for the three directions for the ST, RBT, IBT, M and HR models can be found respectively in Table 8, Table 9, Table 10, Table 11 and Table 12. SSI effects seem to have insignificant influence on PA, PV and PD value for most of the models (ST, RBT, IBT and M show values under 30% of relative difference). Only the HR structure shows major differences of these values for both conditions. PA is affected by a decrease of more than 110% at the top of the building with SSI, PV is affected by a decrease of more than 55% and PD by a decrease of more than 10% on the horizontal components. Therefore, these parameters appear to be sensitive to SSI effects only in the case of HR building.

Table 8: PA, PV and PD for FB and soft soil conditions at the top and the bottom of the shear type (ST) model and for the three directions. The relative discrepancies between the both conditions is also indicated.

	TOP								
	Longitudinal			Transverse			Vertical		
	PA (cm/s²)	PV (cm/s)	PD (cm)	PA (cm/s²)	PV (cm/s)	PD (cm)	PA (cm/s²)	PV (cm/s)	PD (cm)
FB	2.13	0.17	0.02	2.47	0.16	0.01	0.31	0.03	0.01
SSI	1.87	0.15	0.02	1.94	0.12	0.01	0.42	0.03	0.01
Diff.	14%	11%	0%	27%	28%	0%	25%	0%	0%
	BOTTOM								
	Longitudinal			Transverse			Vertical		
	PA (cm/s²)	PV (cm/s)	PD (cm)	PA (cm/s²)	PV (cm/s)	PD (cm)	PA (cm/s²)	PV (cm/s)	PD (cm)
FB	0.58	0.06	0.01	0.57	0.04	0.01	0.27	0.03	0.01
SSI	0.56	0.06	0.01	0.55	0.04	0.01	0.33	0.03	0.01
Diff.	4%	0%	0%	3%	0%	0%	17%	0%	0%

Table 9: PA, PV and PD for FB and soft soil conditions at the top and the bottom of the regular bending type (RBT) model and for the three directions. The relative discrepancies between the both conditions is also indicated.

	TOP								
	Longitudinal			Transverse			Vertical		
	PA (cm/s²)	PV (cm/s)	PD (cm)	PA (cm/s²)	PV (cm/s)	PD (cm)	PA (cm/s²)	PV (cm/s)	PD (cm)
FB	1.03	0.06	0.01	1.24	0.07	0.01	0.30	0.03	0.01
SSI	1.35	0.08	0.02	1.63	0.09	0.01	0.38	0.03	0.01
Diff.	24%	23%	7%	24%	25%	0%	22%	0%	0%
	BOTTOM								
	Longitudinal			Transverse			Vertical		
	PA (cm/s²)	PV (cm/s)	PD (cm)	PA (cm/s²)	PV (cm/s)	PD (cm)	PA (cm/s²)	PV (cm/s)	PD (cm)
FB	0.58	0.06	0.01	0.57	0.04	0.01	0.27	0.03	0.01
SSI	0.58	0.06	0.01	0.53	0.04	0.01	0.37	0.03	0.01
Diff.	0%	0%	0%	8%	0%	0%	26%	0%	0%

Table 10: PA, PV and PD for FB and soft soil conditions at the top and the bottom of the irregular bending type (IBT) model and for the three directions. The relative discrepancies between the both conditions is also indicated.

	TOP								
	Longitudinal			Transverse			Vertical		
	PA (cm/s²)	PV (cm/s)	PD (cm)	PA (cm/s²)	PV (cm/s)	PD (cm)	PA (cm/s²)	PV (cm/s)	PD (cm)
FB	1.81	0.09	0.01	2.62	0.15	0.01	0.29	0.03	0.01
SSI	1.92	0.11	0.01	2.19	0.13	0.02	0.38	0.03	0.01
Diff.	5%	20%	0%	20%	17%	13%	24%	0%	0%
	BOTTOM								
	Longitudinal			Transverse			Vertical		
	PA (cm/s²)	PV (cm/s)	PD (cm)	PA (cm/s²)	PV (cm/s)	PD (cm)	PA (cm/s²)	PV (cm/s)	PD (cm)
FB	0.58	0.06	0.01	0.57	0.04	0.01	0.27	0.03	0.01
SSI	0.54	0.06	0.01	0.54	0.04	0.01	0.34	0.03	0.01
Diff.	7%	0%	0%	6%	0%	0%	20%	0%	0%

Table 11: PA, PV and PD for FB and soft soil conditions at the top and the bottom of the masonry (M) model and for the three directions. The relative discrepancies between the both conditions is also indicated.

	TOP								
	Longitudinal			Transverse			Vertical		
	PA (cm/s²)	PV (cm/s)	PD (cm)	PA (cm/s²)	PV (cm/s)	PD (cm)	PA (cm/s²)	PV (cm/s)	PD (cm)
FB	0.66	0.06	0.01	1.37	0.13	0.02	0.30	0.03	0.01
SSI	0.68	0.06	0.01	1.32	0.13	0.02	0.34	0.03	0.01
Diff.	3%	0%	0%	4%	0%	0%	13%	0%	0%
	BOTTOM								
	Longitudinal			Transverse			Vertical		
	PA (cm/s²)	PV (cm/s)	PD (cm)	PA (cm/s²)	PV (cm/s)	PD (cm)	PA (cm/s²)	PV (cm/s)	PD (cm)
FB	0.58	0.06	0.01	0.57	0.04	0.01	0.27	0.03	0.01
SSI	0.58	0.06	0.01	0.56	0.04	0.01	0.30	0.03	0.01
Diff.	0%	0%	0%	3%	0%	0%	9%	0%	0%

Table 12: PA, PV and PD for FB and soft soil conditions at the top and the bottom of the high-rise (HR) model and for the three directions. The relative discrepancies between the both conditions is also indicated.

	TOP								
	Longitudinal			Transverse			Vertical		
	PA (cm/s²)	PV (cm/s)	PD (cm)	PA (cm/s²)	PV (cm/s)	PD (cm)	PA (cm/s²)	PV (cm/s)	PD (cm)
FB	1.64	0.15	0.02	2.18	0.19	0.03	0.49	0.03	0.01
SSI	0.76	0.09	0.02	1.04	0.13	0.03	0.31	0.04	0.01
Diff.	114%	60%	0%	110%	55%	0%	60%	11%	0%
	BOTTOM								
	Longitudinal			Transverse			Vertical		
	PA (cm/s²)	PV (cm/s)	PD (cm)	PA (cm/s²)	PV (cm/s)	PD (cm)	PA (cm/s²)	PV (cm/s)	PD (cm)
FB	0.57	0.04	0.01	0.58	0.06	0.01	0.27	0.03	0.01
SSI	0.37	0.04	0.04	0.39	0.05	0.01	0.23	0.03	0.03
Diff.	55%	0%	0%	49%	13%	0%	18%	0%	0%

PA ratio represents the difference of the structure ability to endure a specific displacement at one period between FB and with SSI (Table 13). It is observed that this ratio is higher on the vertical component than on the horizontal components for all the FE models. It means that SSI increases the value of PA on this component and so, can induce stronger vertical displacements in the building. Only the HR building exhibits ratio under 1 for all components that means that SSI effects produce lower displacement in the building whatever the component.

Table 13: Summary of the peak acceleration (PA) ratio between the soil-structure system (SSI) and fixed base (FB) condition at the top of each building.

	PA_{SSI} / PA_{FB}		
Bldg	**Longitudinal**	**Transverse**	**Vertical**
ST	0.88	0.79	1.35
RBT	1.31	1.31	1.27
IBT	1.06	0.84	1.31
M	1.03	0.96	1.13
HR	0.46	0.48	0.63

The analysis the RBT, IBT and M models show no specific influence of SSI on the SA on the horizontal components (Figure 22). Only the vertical one presents an increase of SA generally at the first natural frequency of the building (and in higher frequencies for RBT and IBT buildings). The ST model exhibits slight difference of SA value on the three components between both conditions. The horizontal one shows a decrease of the spectrum amplitude whereas the vertical component shows an increase of SA. Lower amplitude of SA is observed for the HR structure on the horizontal components. SA on vertical component does not present

significant variations. With SSI, there is no energy for lower periods than the one characteristic of the SA of the soil domain (from 0.5s).

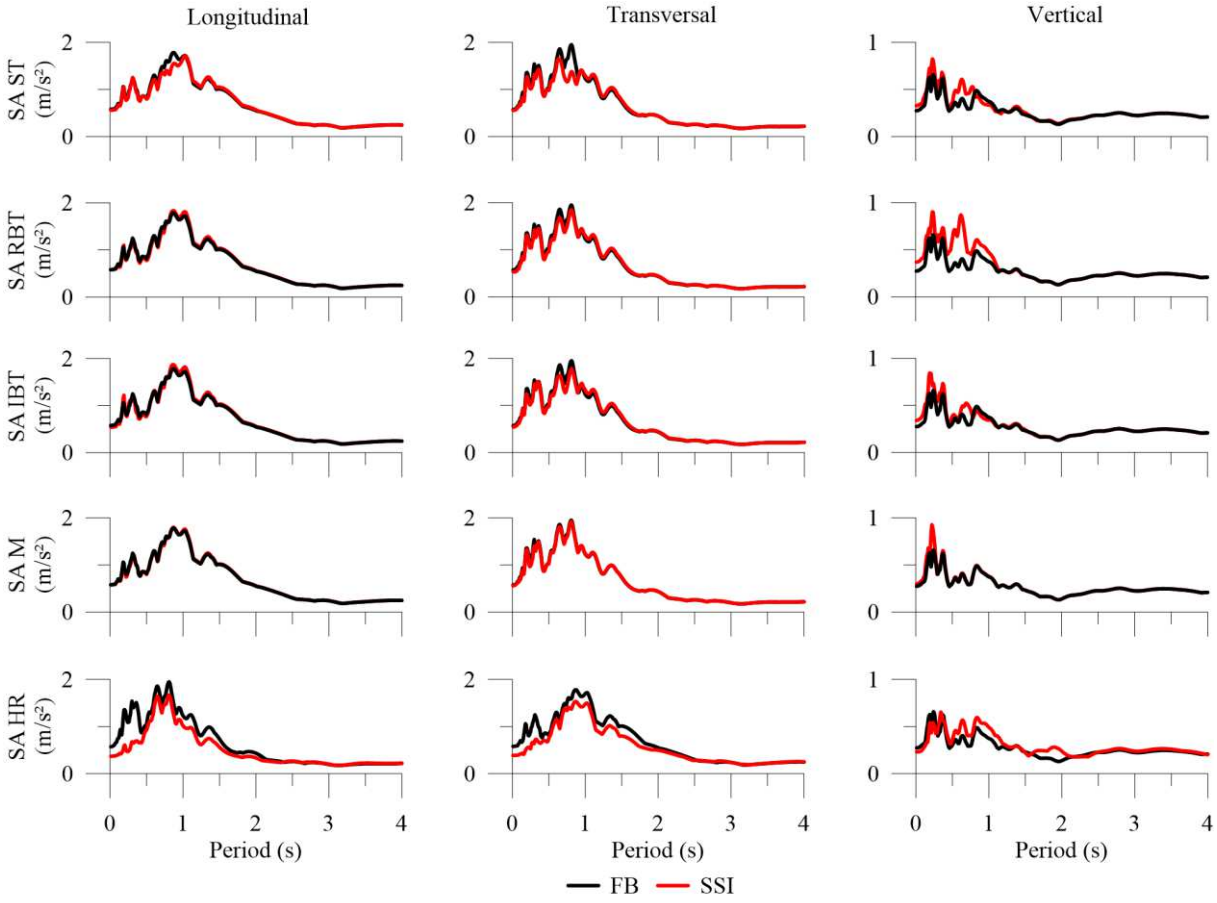

Figure 22: Acceleration spectra (SA) at the base of each building for fixed base (FB) and soil-structure (SSI) models for the longitudinal, transversal and vertical components.

II.4. Modal parameters

The modal parameters from the FE models are compared to the ones obtained from the numerical noise output at each level and each corner of the FE building models using the *FDDA* code that combines FDD and vectorial random decrement (RD) technique (Figure 23, Figure 24, Figure 25, Figure 26 and Figure 27). Signal output from white noise excitation has a time step of 0.02s and 300s of duration, similarly to the input signal. The effects of SSI on each FE model are studied as function of the natural frequency and the mode shapes through the effective mass of each mode and the modal assurance criterion (MAC).

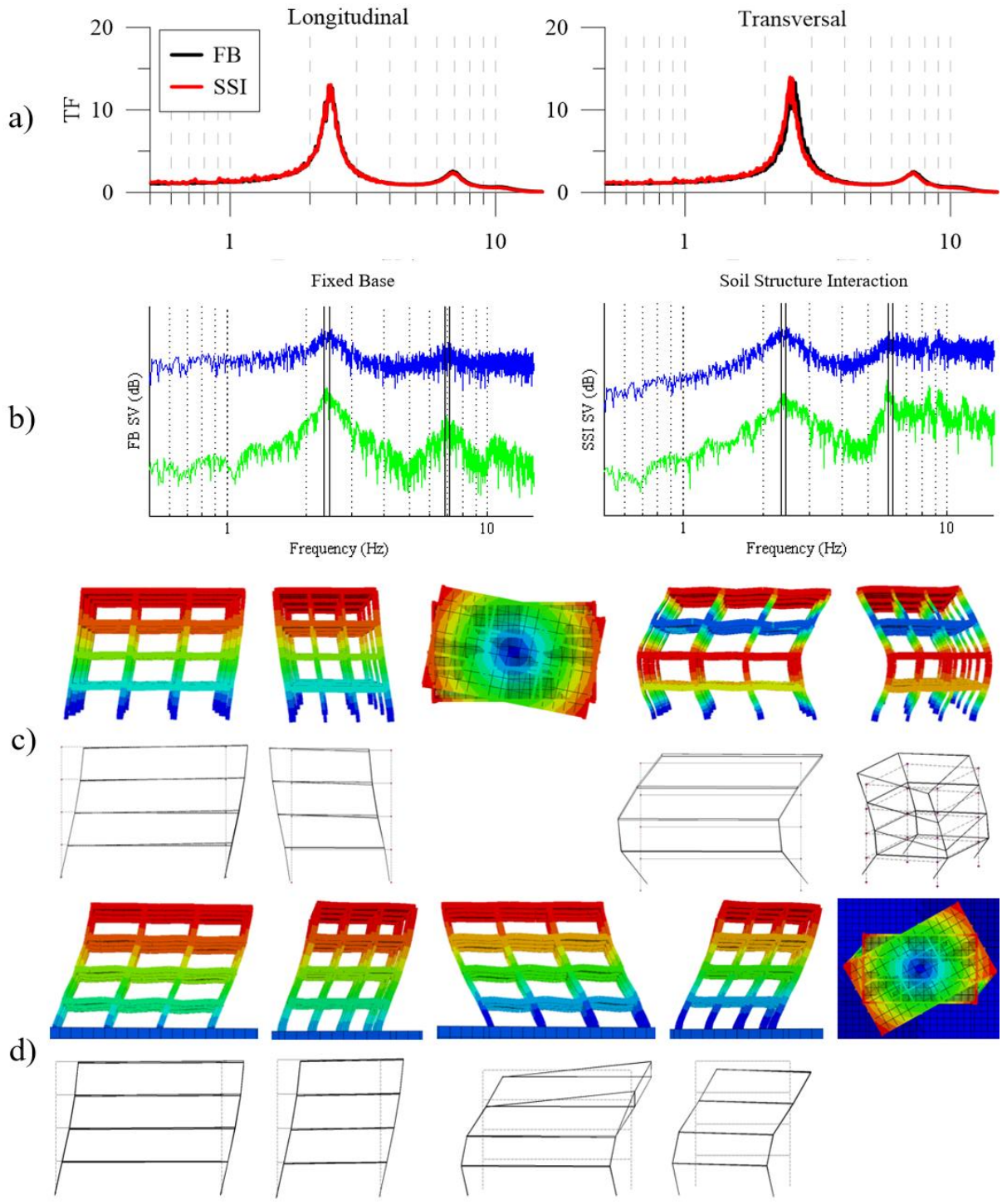

Figure 23: Dynamic features of the shear type (ST) model: (a) top to bottom transfer functions (TF) for the longitudinal and transversal component of motion; (b) first (blue) and second (green) singular value (SV) spectra obtained from the *FDDA* code for fixed base (FB) condition and with soil-structure interaction (SSI); mode shapes obtained by modal analysis in a finite element scheme and from the *FDDA* code for the (c) FB and (d) SSI models.

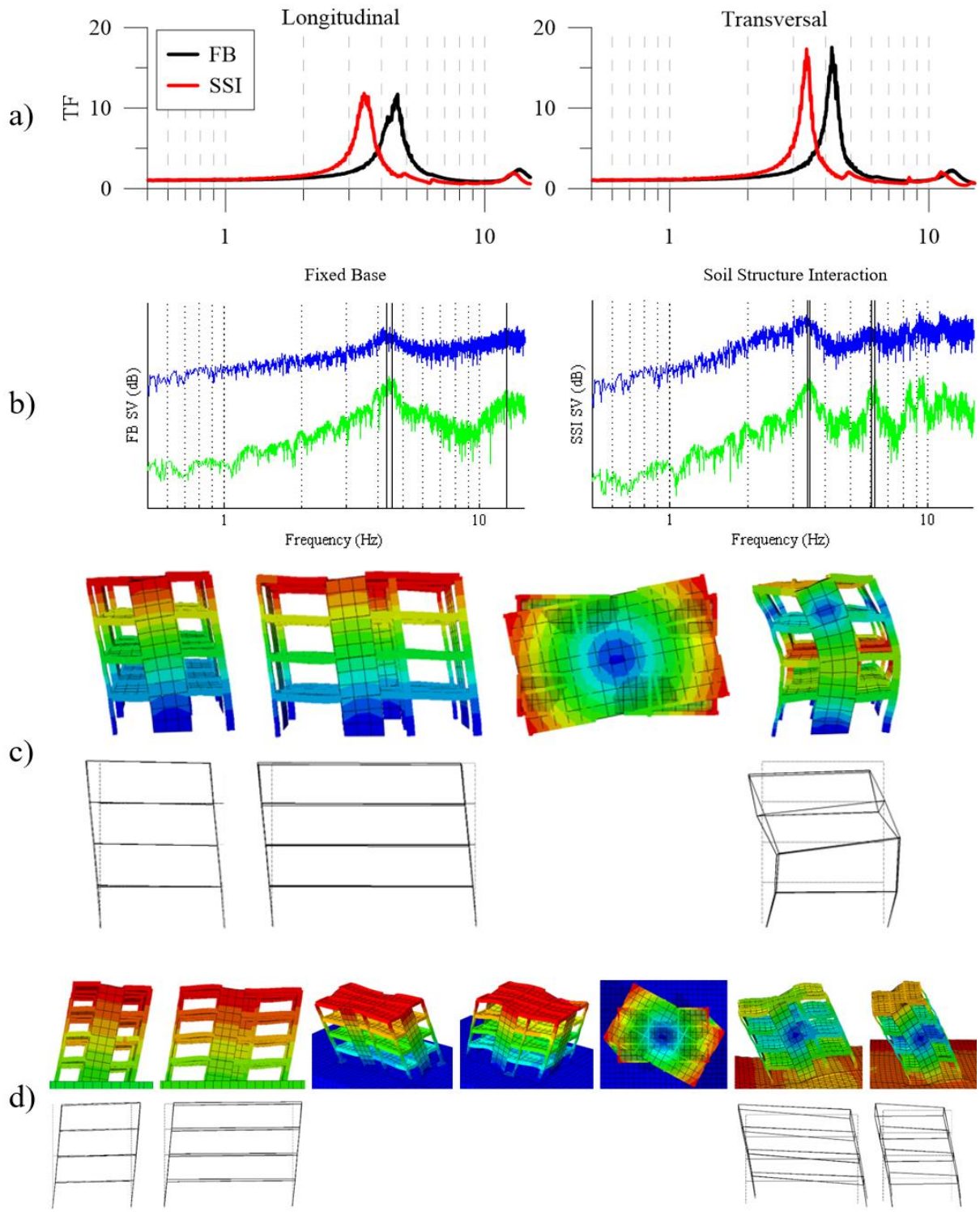

Figure 24: Dynamic features of the regular bending type (RBT) model: (a) top to bottom transfer functions (TF) for the longitudinal and transversal component of motion; (b) first (blue) and second (green) singular value (SV) spectra obtained from the *FDDA* code for fixed base (FB) condition and with soil-structure interaction (SSI); mode shapes obtained by modal analysis in a finite element scheme and from the *FDDA* code for the (c) FB and (d) SSI models.

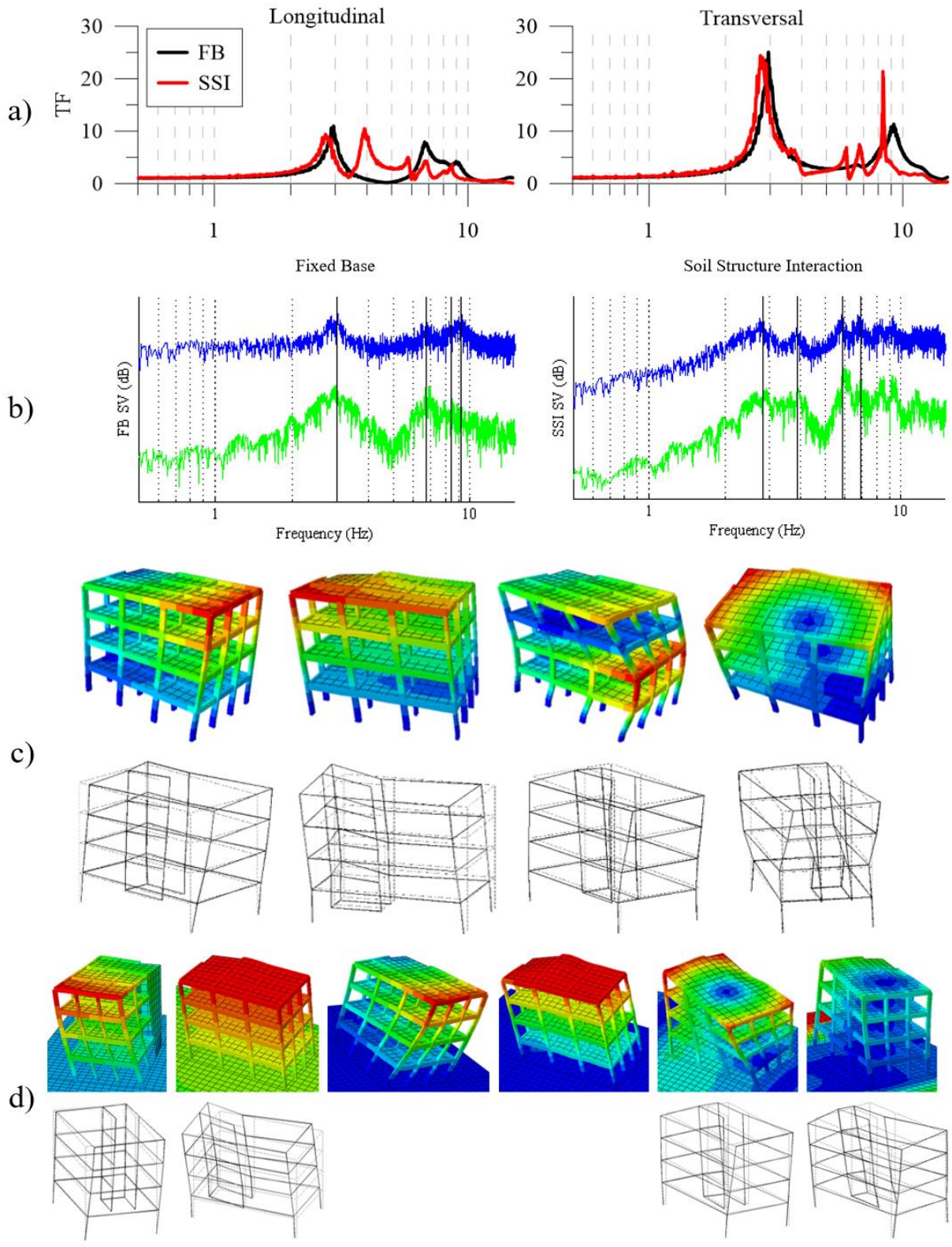

Figure 25: Dynamic features of the irregular bending type (IBT) model: (a) top to bottom transfer functions (TF) for the longitudinal and transversal component of motion; (b) first (blue) and second (green) singular value (SV) spectra obtained from the *FDDA* code for fixed base (FB) condition and with soil-structure interaction (SSI); mode shapes obtained by modal analysis in a finite element scheme and from the *FDDA* code for the (c) FB and (d) SSI models.

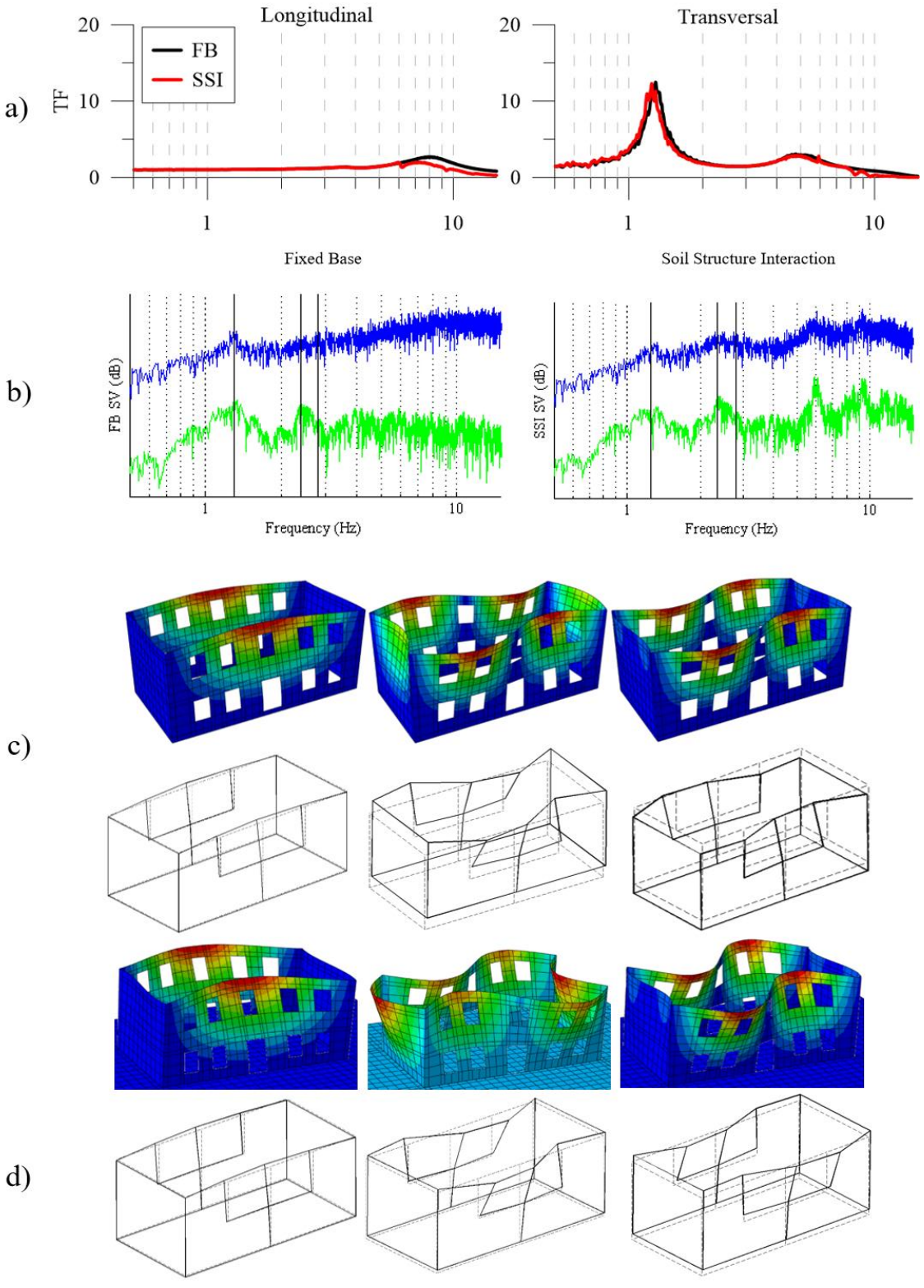

Figure 26: Dynamic features of the masonry (M) model: (a) top to bottom transfer functions (TF) for the longitudinal and transversal component of motion; (b) first (blue) and second (green) singular value (SV) spectra obtained from the *FDDA* code for fixed base (FB) condition and with soil-structure interaction (SSI); mode shapes obtained by modal analysis in a finite element scheme and from the *FDDA* code for the (c) FB and (d) SSI models. A peak is observed on the SV plot with SSI around 6 Hz but not compared in this analysis because the FE model found this mode after more than 200 modes (both global and local).

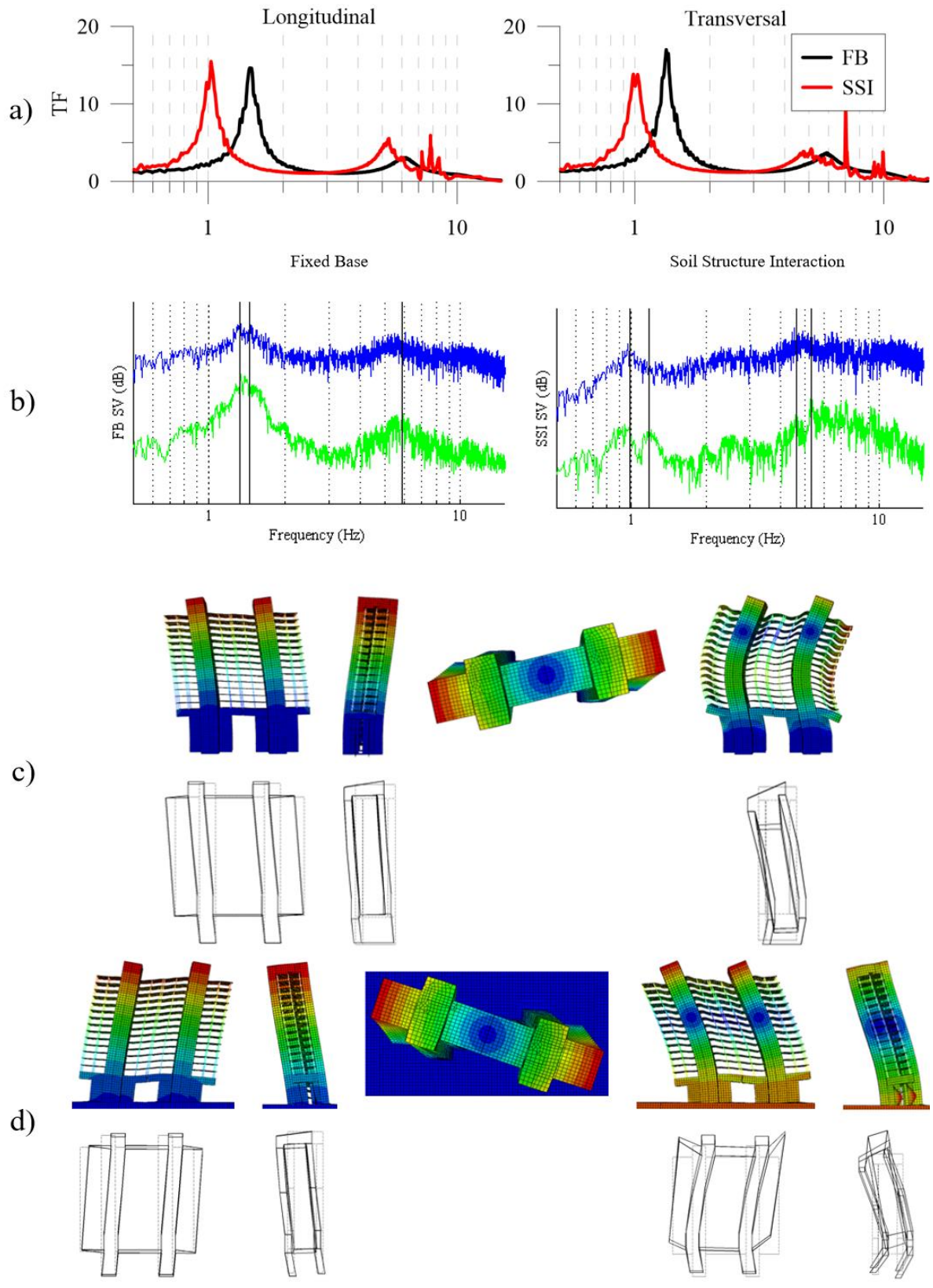

Figure 27: Dynamic features of the high-rise (HR) model: (a) top to bottom transfer functions (TF) for the longitudinal and transversal component of motion; (b) first (blue) and second (green) singular value (SV) spectra obtained from the *FDDA* code for fixed base (FB) condition and with soil-structure interaction (SSI); mode shapes obtained by modal analysis in a FE scheme and from the *FDDA* code for the (c) FB and (d) SSI models.

II.4.1. Natural frequency

The natural frequency of each building and the mode shapes are obtained from the FE models, the transfer functions analysis and the *FDDA* code. They are computed from 30s signal duration in the frequency range 0.5 – 15 Hz. To smooth even more the SVD curves, 20s time windows are chosen in the *FDDA* process. The short term average (STA) and long term average (LTA) used to compute the transfer functions are respectively equal to 3s and 10s. The minimum ratio STA/LTA is set to 0.2 and the maximum is put at 2.5. Results are presented in Table 14. Results for both transfer function and *FDDA* approach are discussed.

Table 14: Natural frequencies *f*, direction of the related mode shape and effective mass ε obtained from the fixed base (FB) and soil-structure (SSI) models from the finite element (FE) models, transfer function (TF) analysis and *FDDA* code.

		FB					SSI				
		FE			TF	FDDA	FE			TF	FDDA
Bldg	**Mode**	**Dir**	***f* (Hz)**	**ε (%)**	***f* (Hz)**	***f* (Hz)**	**Dir**	***f* (Hz)**	**ε (%)**	***f* (Hz)**	***f* (Hz)**
ST	1	L[+]	2.40	83.5	2.4	2.3	L	2.19	46.0	2.4	2.3
	2	T[++]	2.59	84.1	2.5	2.5	T	2.23	55.8	2.5	2.4
	3	Tor[+++]	2.98	0.0	-	-	L	2.56	31.9	-	-
	4	L2	7.50	10.4	6.9	6.8	T	2.63	22.1	-	-
	5	T2	7.96	10.5	7.3	7.1	Tor	2.97	0.0	-	-
	6	Tor	9.22	0.0	-	-	L2	6.37	10.6	6.9	6.0
	7	-	-	-	-	-	T2	6.39	9.1	7.3	6.2
RBT	1	T	4.36	71.1+4.4	4.2	4.4	T	2.31	64.5+10.6	3.4	3.4
	2	L	4.70	72.3+4.4	4.5	4.6	L	3.22	65.0+10.7	3.4	3.5
	3	Tor	6.55	0.1	-	-	T	3.44	2.5	-	-
	4	T2	16.04	16.2	12.4	12.6	L	3.60	2.1	-	-
	5	L2	19.26	13.5	13.5	-	Tor	4.99	0.0	-	-
	6	-	-	-	-	-	L2	6.40	10.0	6.2	6.0
	7	-	-	-	-	-	T2	6.41	10.5	6.2	6.2
IBT	1	T+L	2.98	56.3+5.5	2.9	3.0	T+L	2.28	61.6+7.9	2.8	2.7
	2	L+T	7.23	58.2+12.6	6.8	6.7	L+T	2.31	67.6+8.7	2.8	3.9
	3	T2	9.22	4.5	9.1	8.5	T	2.84	7.4	-	-
	4	Tor	10.45	14.7+11.4	-	9.3	L	3.94	1.7	3.9	-
	5	-	-	-	-	-	Tor	6.15	2.6+0.1	5.9	5.9
	6	-	-	-	-	-	T2	6.16	2.6	6.8	6.9
	7	-	-	-	-	-	L2	6.42	9.8	6.8	-
M	1	T	1.29	31.7	1.2	1.3	T	1.24	0.0	1.2	1.3
	2	T+L	2.50	2.8	3.6	2.4	T+L	2.36	0.0	3.6	2.4
	3	T2	2.70	0.0	8.1	2.8	T2	2.65	0.0	6.0	2.8
HR	1	T	1.34	57.7	1.3	1.3	T	0.97	7.2	1.0	0.9
	2	L	1.48	63.1	1.4	1.4	L	0.98	7.9	1.0	1.1
	3	Tor	1.86	0.0	-	-	Tor	1.37	0.0	-	-
	4	T2	6.19	18.4	5.9	6.0	T2	2.40	70.6	4.9	4.6
	5	L2	7.10	0.0	6.1	-	L2	2.42	70.6	5.3	5.3

[+] Longitudinal bending; [++] Transverse bending; [+++] Torsion mode

Both methods show similar results for all models. It is observed that the SVD of all FE models contains more peaks with SSI than in FB condition.

The comparison of the transfer functions shows that the first natural frequency of FE models tends to decrease with SSI. The variation of frequency observed for the ST and M models seems negligible from one condition (FB) to another (SSI) contrary to other types of building. RBT, IBT and HR models, specifically, show differences between the natural frequency values of the first three modes for both conditions (up to 140% for the IBT building observed on the transfer function of the mode 2).

II.4.2. Mode shape

The mode shapes of each FE building are analyzed and compared between the FB and soil-structure condition. The effective modal mass and the MAC are notably introduced and used to quantify the modal comparison.

II.4.2.1 Effective modal mass

The linear dynamic analysis of the FB model gives the effective mass for each mode and each component through the numerical modeling. The effective modal mass indicates how much the total mass of the system contributes to a specific mode of deformation. In other words, the effective modal mass is a kind of measure of the energy contained within each resonant mode (Finkelstein, 2019). This parameter associated to each mode shape is estimated as:

$$\varepsilon_i = 100\left(\frac{p_i^2}{M_{FB}}\right)[\%] \tag{84}$$

where $M_{FB} = p^T p$ is the total mass of the building, p_i is the modal participation factor, term of the modal participation vector $p = \Phi^T M_{FB} \tau$, where τ is the influence vector of dynamic loading.

In analytical approaches, the effective modal mass is defined as the mass needed to be added to the true mass to correctly predict the behavior of the system. In the Eurocode 8 (CEN, 2003), the modes where the effective modal mass is greater than 5% is generally considered as

dominant modes in the dynamic response of the system. Low effective modal mass suggests either the presence of local mode of deformation or symmetric mode shape with respect to the center of gravity of the system.

II.4.2.2 Comparison of modes between fixed base and soil-structure models

The comparison of mode shapes using MAC value is presented in Table 15. An example of comparison is explained to help the reader to interpret the table. For the ST building, the MAC is computed between the first mode shape identified in FB and the first mode shape identified with SSI for the longitudinal direction. The obtained MAC value is close to 1 that means that the first mode shape in both conditions, and for this specific direction, are quite similar. On the contrary, the MAC computed between the 4th mode shape identified in FB and the 6th mode shape identified with SSI for the longitudinal direction gives a result close to 60% that means that the mode shapes differ.

Table 15: Difference in mode shapes between fixed base (FB) and soil-structure (SSI) models: effective modal mass ε and cross-modal assurance criterion (MAC).

		FB			SSI			
Bldg	**Dir**	**Mode**	***f* (Hz)**	**ε (%)**	**Mode**	***f* (Hz)**	**ε (%)**	**MAC (%)**
ST	L	1	2.40	83.5	1	2.19	46.0	99.9
	T	2	2.59	84.1	2	2.23	55.8	99.1
	L2	4	7.50	10.4	6	6.37	10.6	62.6
	T2	5	7.96	10.5	7	6.39	9.1	59.8
RBT	T	1	4.36	71.1+4.4	1	2.31	64.5+10.6	99.3
	L	2	4.70	72.3+4.4	2	3.22	65.0+10.7	98.7
	T2	4	16.04	16.2	6	6.40	10.0	0.7
IBT	T+L	1	2.98	56.3+5.5	1	2.28	61.6+7.9	99.0
	L+T	2	7.23	58.2+12.6	2	2.31	67.6+8.7	95.3
	T2	3	9.22	4.5	6	6.16	2.6	30.7
M	T	1	1.29	31.7	1	1.24	0.0	99.9
	T+L	2	2.50	2.8	2	2.36	0.0	99.7
	T2	3	2.70	0.0	3	2.65	0.0	17.9
HR	T	1	1.34	57.7	1	0.97	7.2	99.8
	L	2	1.48	63.1	2	0.98	7.9	99.7
	T2	4	6.19	18.4	4	2.40	71.3	84.8

T=transverse direction, L=longitudinal direction

In the first place, it is observed that mode shapes observed from the FE model are generally well retrieved through the *FDDA* analysis. Missing modes in the *FDDA* analysis may results

from modes that have low effective modal mass value and so, low contribution in the whole system. Therefore, this kind of modes are not distinguished in the SVD. One other possibility of the absence of modes in *FDDA* analysis may be the proximity of several peaks in the SVD. This can lead to interpret the existence of a unique mode whereas there are several or maybe to the presence of only one mode that contributes in the deformation of both horizontal directions. This uncertainty also exists during the interpretation of real data through *FDDA* analysis. For ST, RBT and HR models, torsion mode shows low participation of the mass of the buildings in FB condition (0% on the longitudinal and transverse components). This deformation is however well observed on the FE models. M building presents negligible effective mass value in its deformation behavior. But in contrast, IBT structure shows high effective modal mass in the torsion mode (11% on the longitudinal component and 15% on the transverse component).

The analysis of the FE building model shows that SSI induces a change in the order of appearance of modes compared to the FB condition. For low-rise RC structures, torsion mode always appears at higher frequency with SSI than in FB condition. For ST and RBT buildings, the mode goes to the 5th place with SSI whereas it was in 3rd place in FB condition. For IBT building, the torsion mode is shifted from the 4th to the 5th position with SSI.

The comparison of modes using the MAC shows that the first two mode shapes are generally highly correlated between both conditions for all buildings (above 95% of similarity). The difference between the mode shapes increases with higher modes.

For the IBT model, it is observed that the center of rotation of the torsion mode is localized at the center of the building with SSI contrary to the off-center position in FB condition. Also, the torsion is observed in the *FDDA* analysis because the effective modal mass is relevant in this deformation.

We can note that the deformation of the building seems to be concentrated in the floors instead of the beams for the 3rd and the 4th modes of the FE models of ST, RBT and IBT with SSI.

For the M model, SSI seems to have negligible effects on the dynamic behavior of this building compared to the FB condition, notably in the longitudinal direction of deformation (the most rigid direction). The deformation is concentrated in the transverse direction, in longer walls where openings are placed. The *FDDA* analysis have difficulty to show details of local modes. It will need more control points to represent well the deformation. Notably on the shorter walls (instead of zero at present) and more on the longer ones (instead of the current 22 points).

Furthermore, SSI seems to have also negligible effects on the deformation of the foundation for ST, IBT and M models. On the contrary, RBT and HR structures show slight deformation of the foundation in higher modes.

II.5. Soil-structure interaction of the Nice Prefecture building

II.5.1. The soil-structure finite element model

The Nice Prefecture building represents a detailed complex case study of an important HR building located in the Var valley (Nice, France). In 2018, Lorenzo et al. (2018) studied the dynamic behavior of the complex building through ambient vibration data. They compared the results of the building modeling to the results of the inverse analysis based on recordings. The authors found that the dynamic analysis of only one tower does not allow to retrieve the measured natural frequency of the building (1.21 Hz). Only the complete model of the building under low excitation and with no consideration of the seismic joint between the towers is able to give the measured natural frequency in FB condition. The Nice Prefecture building in FB condition is represented as the HR model (Table 4). In this thesis, the calibration of the building model is updated by assembling the structure with the local stratigraphy and adding the foundation composed of RC foundation slab and rigid inclusions (Figure 28). The building is supported by 140 rigid inclusions located in the ground having a diameter equals to 0.73 m, height of 5 m and inter-distance equals to 3 m. 1D elements and 3D elements have been used and compared to represent the inclusions in the soil domain. The results show that 1D elements have no effects on the dynamic behavior of the building contrary to the 3D elements that have local impact. The white noise signal is injected at the base of the model.

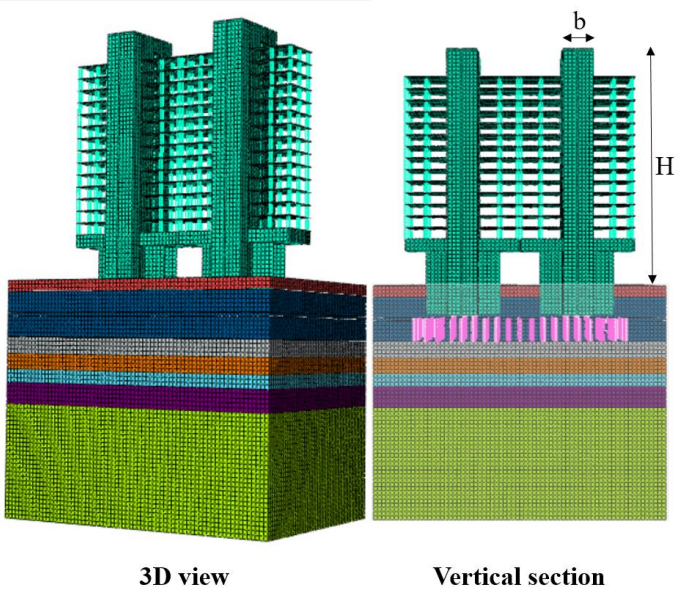

Figure 28: Finite element model of the Nice Prefecture building assembled with a 3D soil domain representing the local stratigraphy. The vertical section shows the soil domain with excavation, the two underground floors (lighter green parts of the building) and rigid inclusions (pink elements). The effective height H and the length of the structural wall b in the direction of the first mode shape are indicated.

The soil stratigraphy of the lower Var valley is added to the building model using the last geotechnical model of the valley (Rohmer et al., 2020) in order to study the SSI effects. At the location of the Nice Prefecture building, the soil profile is composed of seven soft sedimentary layers with different properties and thickness (Table 16). The estimated f_{s0} of this profile is 2 Hz (Figure 29) and corresponds to the measured frequency in the field at this place (1.96 Hz according to Rohmer et al. (2020)). The building model is calibrated to reproduce the natural frequency obtained by FDD using recorded signals (1.21 Hz). Instead of changing the dimension of the beams to fit the measured frequency (as in the study of Lorenzo et al., 2018), we calibrate the structural properties. Imposing the structure dimensions declared in the construction plans and soil stratigraphy, the building model is calibrated using 800 kg.m^{-2} as sum of dead and live loads. The mechanical properties of RC are used: the elastic modulus $E_c = 3.30 \times 10^{10}$ N.m^{-2}, Poisson's ratio $\nu_c = 0.2$, density $\rho_c = 2200$ kg.m^{-3} and damping ratio $\zeta_0 = 5\%$. The effective structure height is 60 m (Table 4) and the length of the RC wall in the direction of the first mode shape is 8 m (Figure 28). This building has thus a large aspect ratio compared to the others (Table 4).

Table 16: Geometrical properties of the local soil stratigraphy under the Nice Prefecture building. H is the mesh element height.

		Element Mesh	
Depth (m)	**Thickness (m)**	**Min nb**	**Max H (m)**
0	2.7	2	1.4
2.7	10.6	4	2.7
13.3	4	2	2.0
17.3	3.7	2	1.9
21	3.1	2	1.5
24.1	5.1	3	1.7
29.2	27	9	3.0

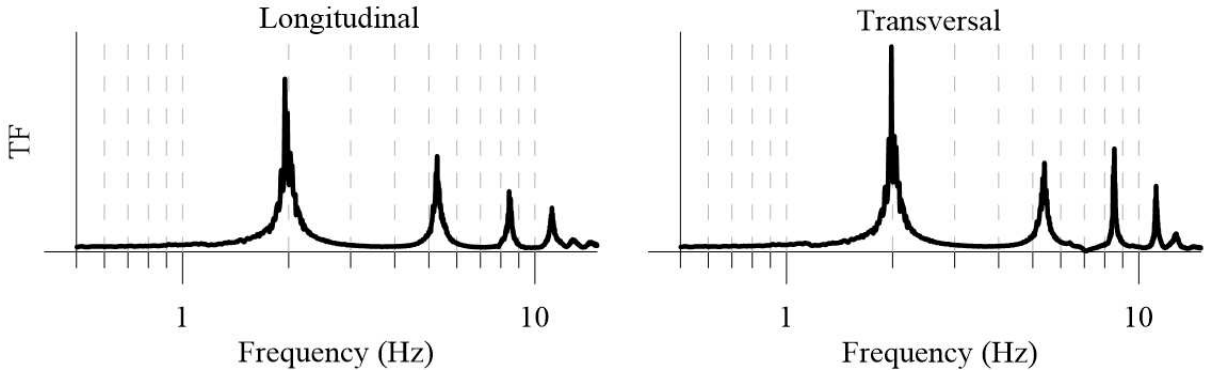

Figure 29: Transfer functions (TF) of the soil column on the both horizontal components, computed considering the spectral ratio between the signal at the top and the bottom of the local soil model and normalized by the maximum amplitude of the horizontal TF.

II.5.2. Natural frequency

The transfer functions between the top and the bottom of the Nice Prefecture building are computed for each model and presented in Figure 30. The results show that the SSI tends to decrease the first natural frequency of the building by almost 20% respectively from 1.37 Hz to 0.99 Hz and from 1.5 Hz to 0.98 Hz on the longitudinal and transversal components. Moreover, higher modes appear to have a lower natural frequency value with SSI.

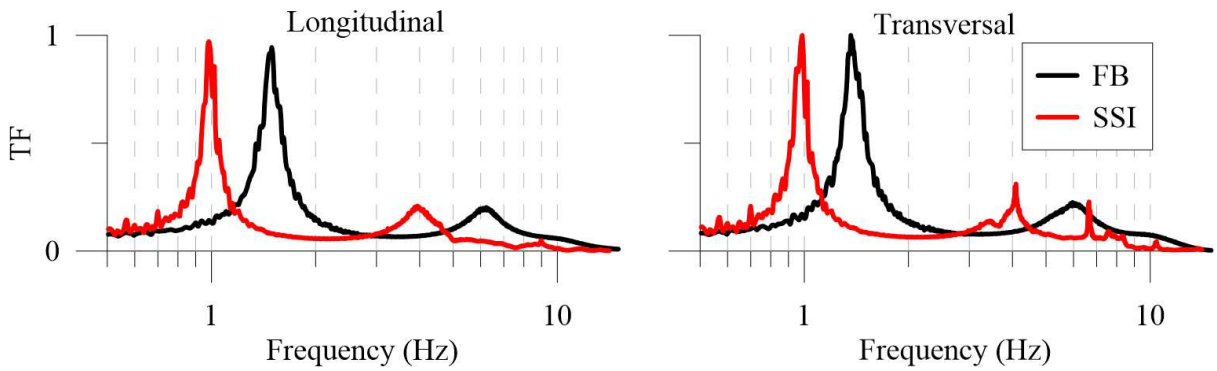

Figure 30: Transfer functions (TF) of the longitudinal and transversal components computed between the top and the bottom of the Nice Prefecture finite element model.

II.5.3. Seismic wave propagation velocity

The deconvolution interferometry method (Snieder and Şafak, 2006) is used to estimate the V_s through the Nice prefecture building. The duration of signals is 100s with high frequency sampling equals to 500 Hz to better observe the seismic wave propagation through the building. The signals are first filtered between 0.5 and 10 Hz using a Butterworth bandpass before applying the deconvolution process (Figure 31).

The wave trains are picked at the maximum of the wavelet at the top of the building. The large width of the wavelet at the bottom of the building is taken into account to estimate a confidence range for the V_s estimation. Results are summarized in Table 17.

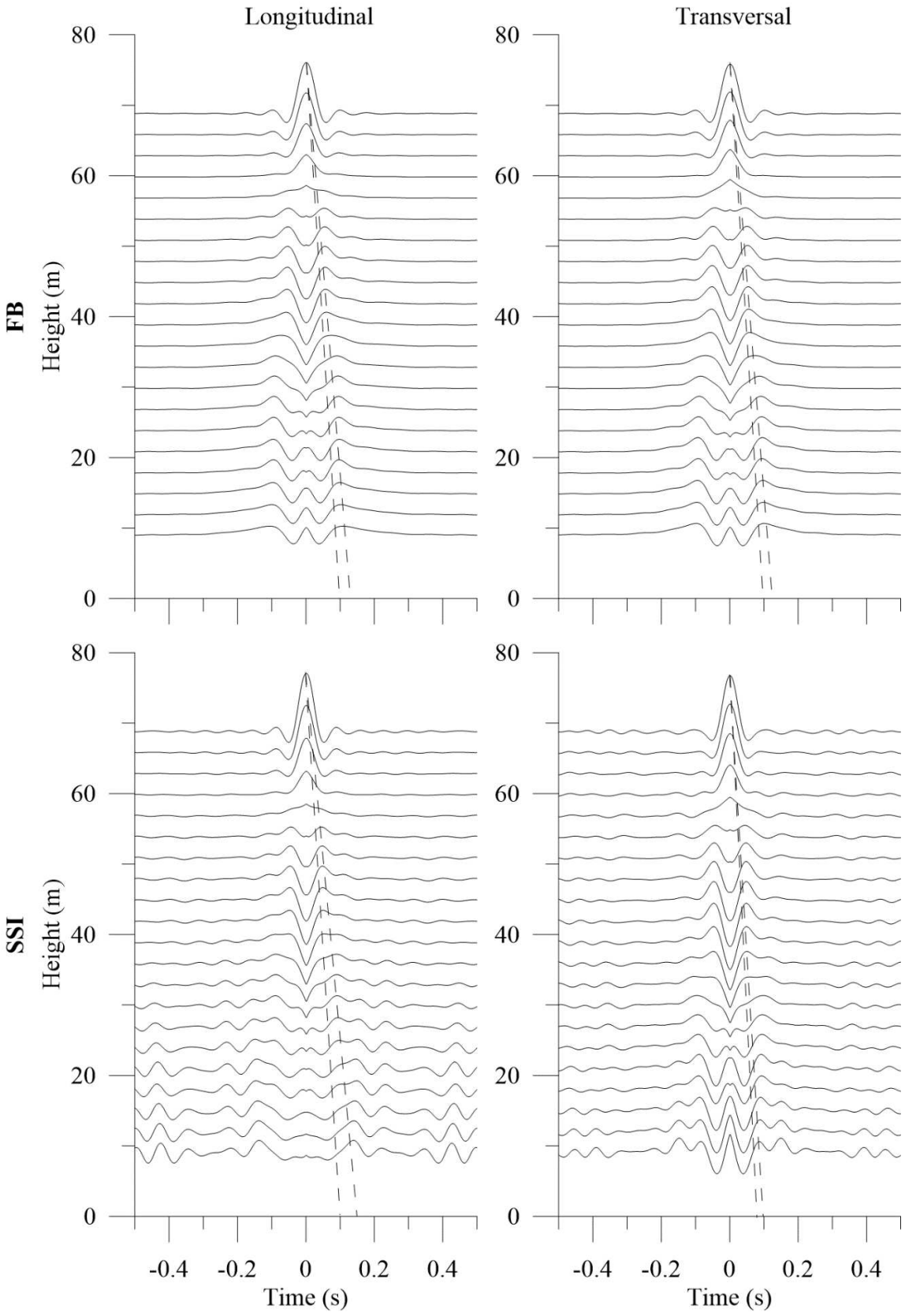

Figure 31: Impulse response function for each floor on the horizontal component for fixed base (FB) and with soil-structure interaction (SSI). The virtual source station is at the bottom. The signals have been filtered between 0.5 and 10 Hz before deconvolution process. Dashed lines indicated the picked propagation velocity.

Table 17: Estimated shear wave velocity (V_s) from impulse response functions in the model and relative difference between the both conditions.

	V_s mean (m/s)		Uncertainty (m/s)	
	Longitudinal	**Transverse**	**Longitudinal**	**Transverse**
FB	610	640	180	140
SSI	600	770	200	130
Relative diff.	2%	17%	/	/

The application of the relationship proposed by Michel and Guéguen (2018) (presented in the Chapter I) to the Nice Prefecture building is presented below (Eq.(85)). The first and second bending modes have very close natural frequencies, therefore, the velocity tends to be the same in both directions of the building.

$$V_s = \frac{f \times 4H}{\chi(C)} = \frac{1.2 \times 4 \times 66}{0.7} = 452.6\, m.s^{-1} \quad (85)$$

The result shows that the velocity value is very close to the one found by Lorenzo (2016) from ambient vibration data (490 to 540 m.s^{-1}) whereas the result from the deconvolution interfererometry present larger velocity value with high uncertainty. The equation proposed by Michel and Guéguen (2018) appears suitable to investigate the V_s in this building.

II.6. Rocking motion analysis

SSI effects are now investigated through the study of the rocking motion at the base of the buildings. The rocking spectral ratio presented in Chapter I is used to put in evidence the presence of rocking motion on a large frequency range. The analysis is first applied on the FE building model using a single horizontal component of seismic loading and white noise input. Second, the method is applied to real earthquake recordings and ambient vibration data obtained from accelerometric sensors at the base of the Nice Prefecture building. For noise data, vertical components are compared in the frequency range 0.1 – 8 Hz and using 30s overlapping (5%) time windows. The investigation of rocking motion is performed up to 8 Hz because the observed mode frequency of the FE buildings did not exceed this frequency in the FDD analysis. The STA and LTA are respectively set to 3s and 10s. The minimum STA/LTA ratio is 0.2 and the maximum is 2.5.

II.6.1. From numerical data

We choose to propagate seismic waves in the horizontal component corresponding to the direction of the first mode shape of each FE building in order to observe potential vertical differential motions. Here, the displacement is directly extracted from the *ABAQUS* software and filtered using a Butterworth passband filter of order 3 with a central frequency equals to the first natural frequency of each building. Only the RC buildings are studied. Indeed, the M model is considering too low and stiff to show significant differential displacements at the base of the building.

From the Figure 32, differential displacements on the vertical component, interpreted as rocking motion, is clearly observed between the points aligned in the direction of vibration for all buildings. Therefore, the analysis of the displacement time series gives a first insight of the rocking phenomenon in the buildings. We can note that the amplitude of motion in ST building is negligible compared to the other buildings. Consequently, we consider that the differential displacement at the base of this building is negligible and, thus, do not consider it in the following analysis.

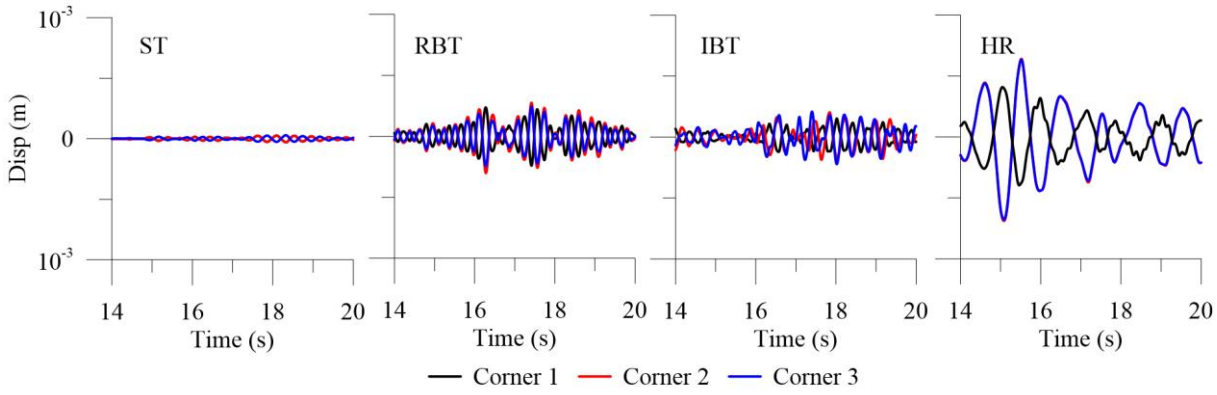

Figure 32: Zoom on the displacement time series of the vertical component at three corners at the base of the reinforced concrete buildings with soil-structure interaction.

The rocking spectral ratio are then computed for the RBT, IBT and HR buildings in order to investigate more deeply the rocking motion and identified at which frequency this motion occurs (Figure 33, Figure 35 and Figure 37). The seismic response of the buildings are filtered around the frequency ranges highlighted by the rocking spectral ratio analysis in order to confirm the presence of rocking motion at the considered frequency (Figure 34, Figure 36 and Figure 38). The Table 18 summaries the results of this analysis.

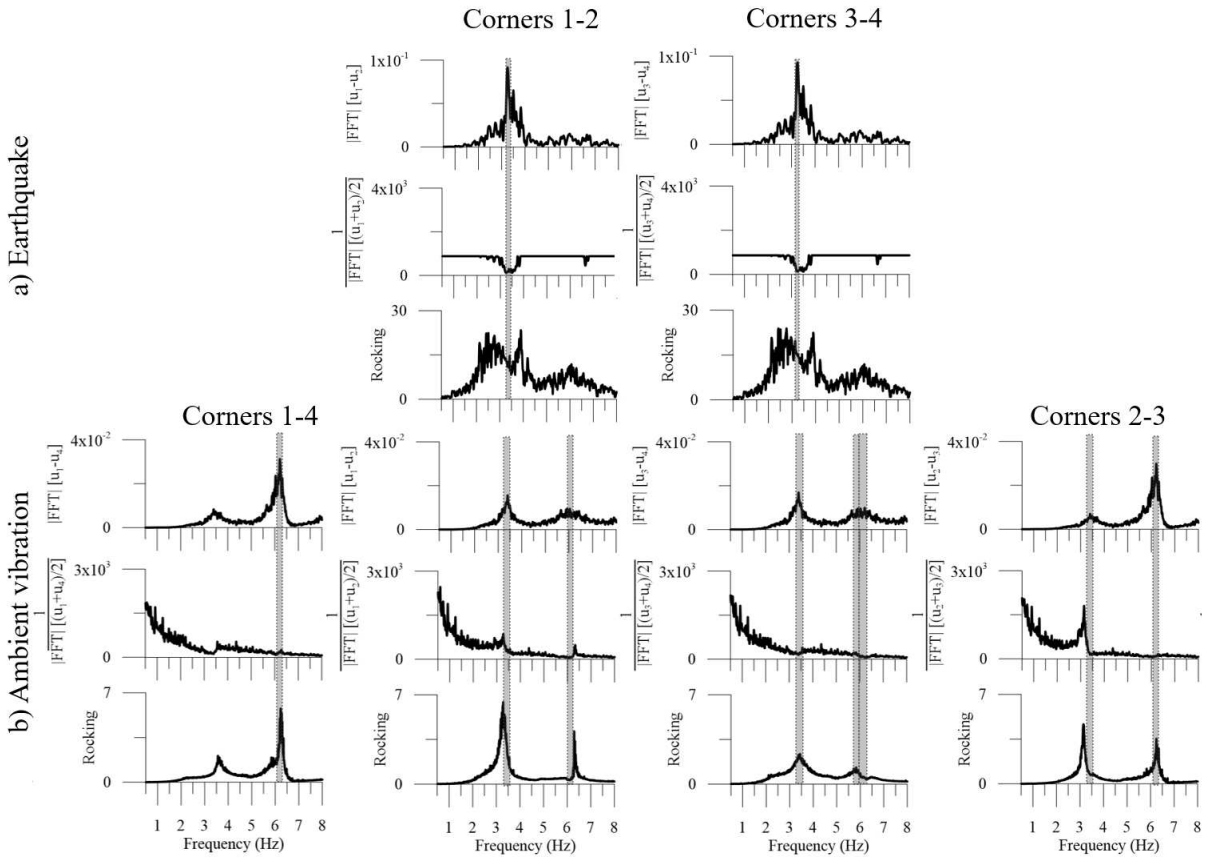

Figure 33: Rocking spectral ratio of the regular bending type (RBT) building computed from a) seismic signal between corners 1 – 2 and 3 – 4 in the direction of the vibration and b) ambient vibration data between corners 1 – 2, 3 – 4, 1 – 4 and 2 – 3. The rocking effect is highlighted at 3.2 – 3.6 Hz for couples 1 – 2, 3 – 4, 2 – 3; at 5.6 – 6 Hz for couples 3 – 4 and at 6.2 – 6.6 Hz for all couples.

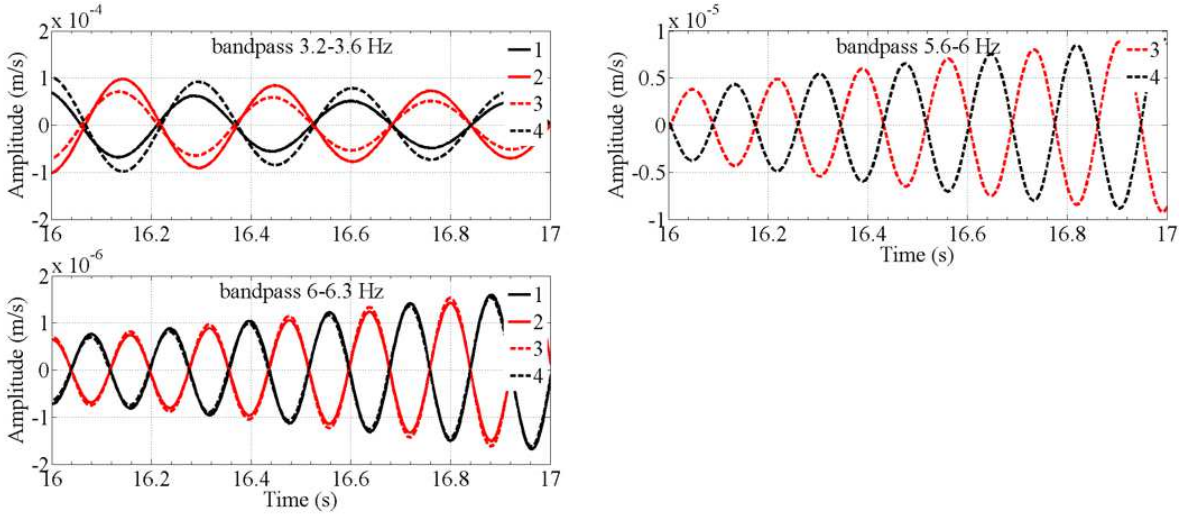

Figure 34: Zoom on the filtered velocity time series of the seismic signal at each corner computed for the highlighted frequency bands in the rocking spectral ratio of the regular bending type building (RBT).

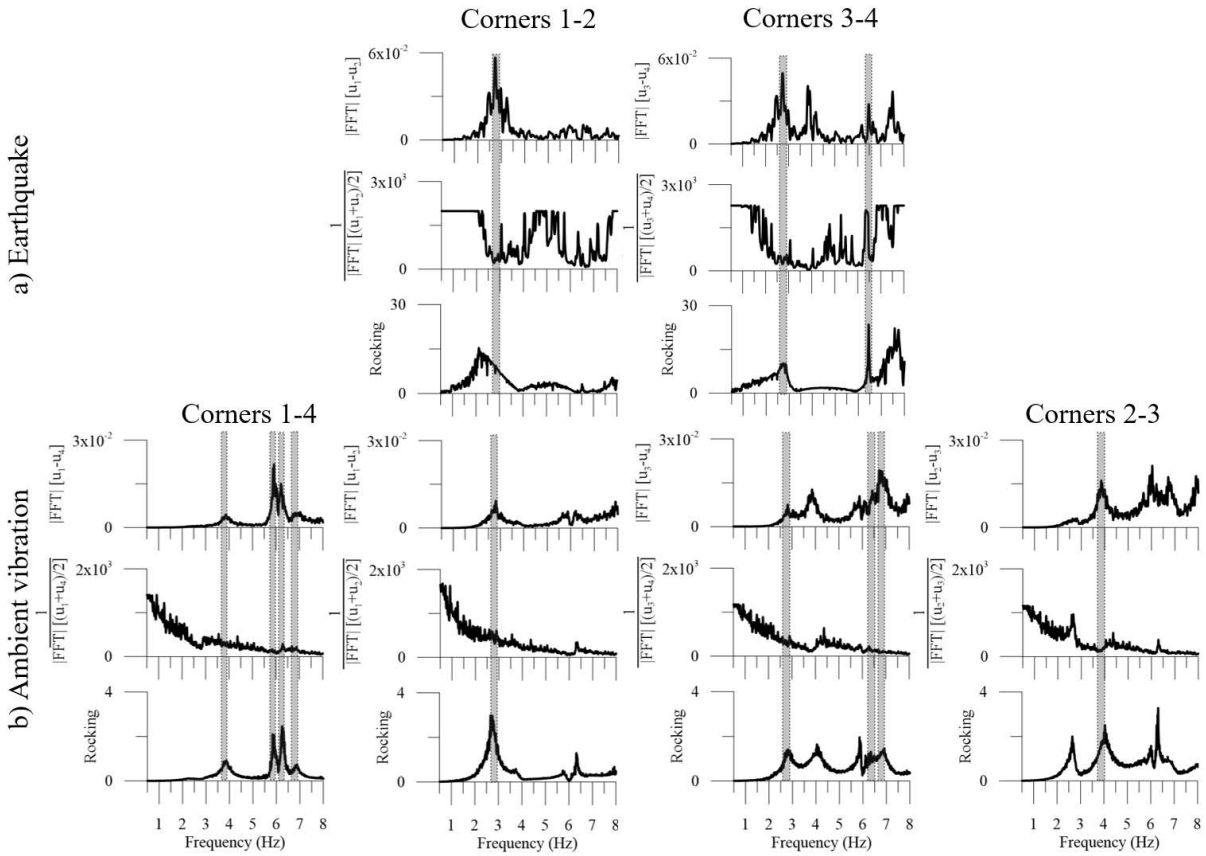

Figure 35: Rocking spectral ratio of the irregular bending type (IBT) building computed from a) seismic signal between corners 1 – 2 and 3 – 4 in the direction of vibration and b) ambient vibration data between corners 1 – 2, 3 – 4, 1 – 4 and 2 – 3. The rocking effect is highlighted at 2.6 – 3 Hz for couples 1 – 2 and 3 – 4; at 3.7 – 4 Hz for couples 1 – 4 and 2 – 3; at 5.6 – 6 Hz for couple 1 – 4; at 6.1 – 6.5 Hz for couples 1 – 4 and 3 – 4; at 6.7 – 7 Hz for couples 1 – 4 and 3 – 4.

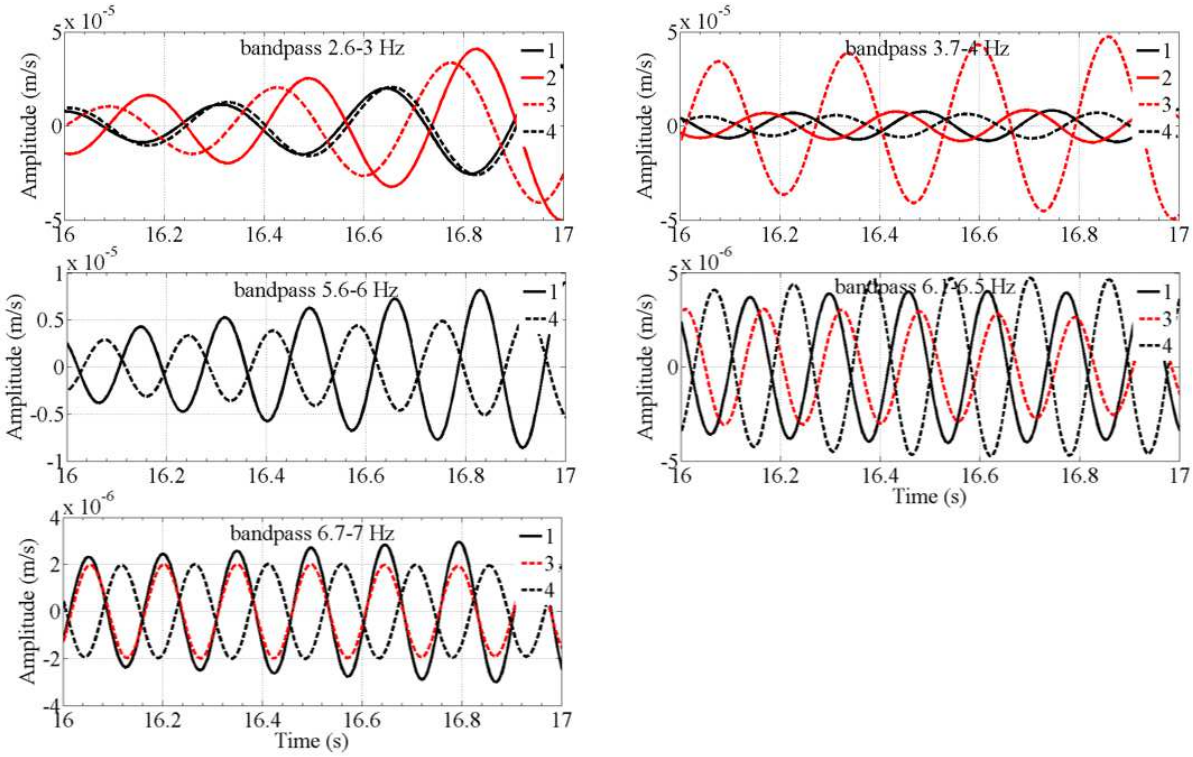

Figure 36: Zoom on the filtered velocity time series of the seismic signal at each corner computed for the highlighted frequency bands in the rocking spectral ratio of the irregular bending type building (IBT).

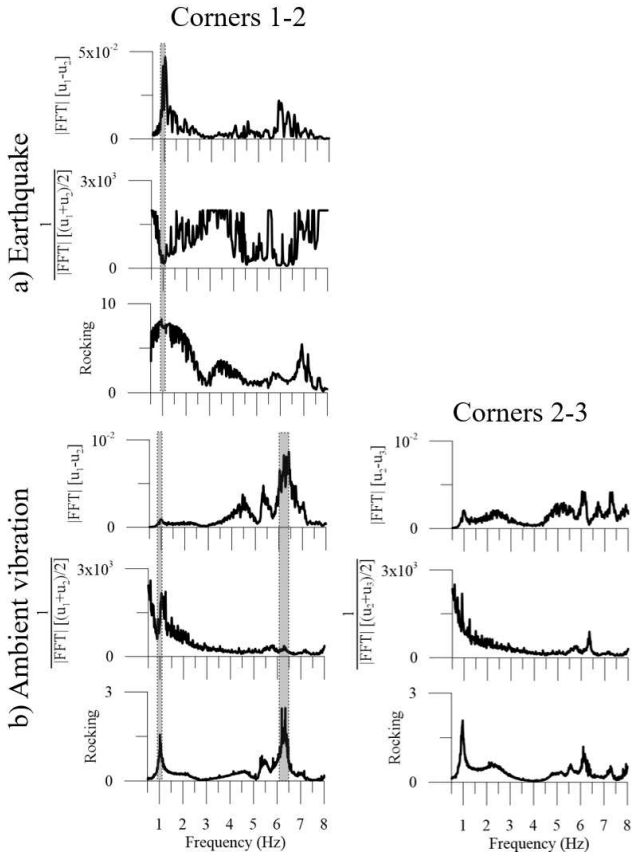

Figure 37: Rocking spectral ratio of the high-rise bending type (HR) building computed from a) seismic signal between corners 1 – 2 in the direction of vibration and b) ambient vibration data between corners 1 – 2 and 2 – 3. The rocking effect is highlighted at 0.9 – 1.1 Hz and at 6 – 6.5 H for couple 1 – 2.

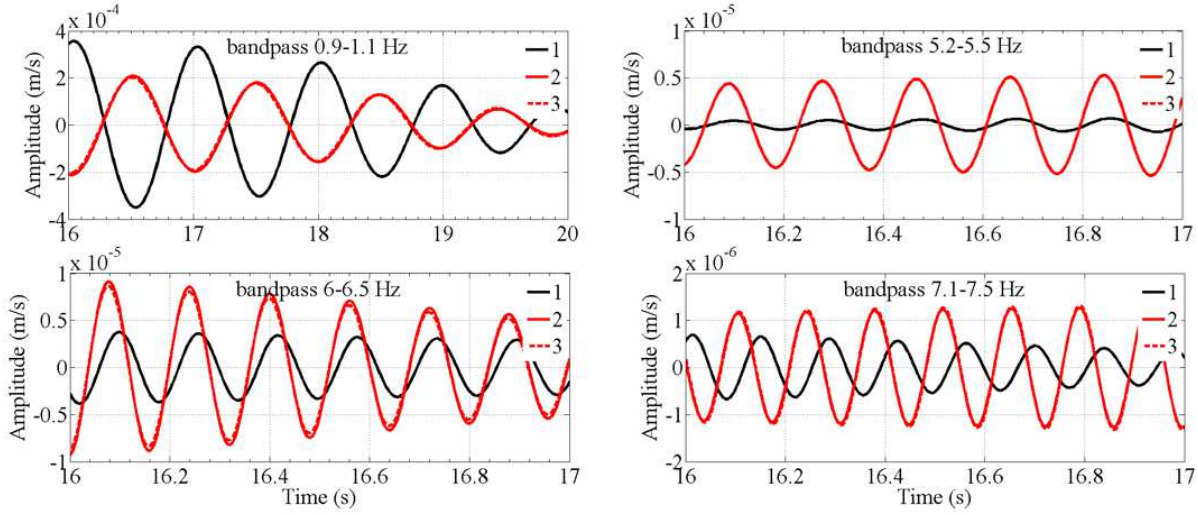

Figure 38: Zoom on the filtered velocity time series of the seismic signal at each corner computed for the highlighted frequency bands in the rocking spectral ratio of the high-rise bending type building (HR). The rocking effect is put in evidence at 0.9 – 1.1 Hz and at 6 – 6.5

Hz for couple 1 – 2. Other frequency bands are presented to show that peak on rocking spectral ratio may not represent rocking motion but transient motion.

Table 18: Frequency band highlighted by high amplitude peaks on the rocking spectral ratio for each building and validation of the presence of rocking motion based on the filtered seismic signal.

		Rocking spectral ratio		
		Direction of sensor alignment where differential vertical motion is observed		Validation of the rocking motion assumption
Bldg.	**Frequency range (Hz)**	**Seismic data**	**Noise data**	**Filtered seismic signal**
RBT	3.2 – 3.6	T^{+}	$T+L^{*}$	Yes
	5.6 – 6.0	/	T	Yes
	6.2 – 6.6	/	T+L	Yes
IBT	2.6 – 3.0	T	T	Yes
	3.7 – 4.0	/	L	Yes
	5.6 – 6.0	/	L	Yes
	6.1 – 6.5	T+L	T+L	Yes
	6.7 – 7.0	/	T+L	Yes
HR	0.9 – 1.1	T	T	Yes
	5.2 – 5.5	/	T+L	No
	6.0 – 6.5	/	T+L	Yes
	7.0 – 7.4	/	T+L	Yes for T No for L

T^{+}=transverse direction, L^{*}=longitudinal direction

For the RBT, IBT and HR models, the rocking motion is observed by a clear out of phase on the displacement time series.

For the RBT model (Figure 33), a peak is observed on the differential motion computed from both type of data (seismic and noise) at 3.4 Hz corresponding to the first natural frequency of the building. One can notice that close to this frequency, the rocking spectral ratio from seismic data indicate two peaks, one below and another above 3.4 Hz, whereas on the rocking spectral ratio from noise data the peak is well defined. The analysis of the filtered seismic signals at the sensors (Figure 34) clearly shows that, for the frequency range 3.2 – 3.6 Hz, the motions are in phase opposition for three couples of sensors in both horizontal direction of the building. The amplitude is similar at corners 2 – 3 and at corners 1 – 4. But it differs between corners 1 – 2 and 3 – 4. Peaks are also distinguished on the rocking spectral ratio at 5.6 – 6 Hz and at 6.2 – 6.6 Hz on both horizontal directions of the building only using the noise data. Signals in phase opposition are observed for the both frequency ranges between the corners in the transverse direction and only for the higher frequency range between the corners in the longitudinal direction.

The complex spatial distribution of the stiffness in the IBT building caused by the offset staircase induces high amplitude in the rocking spectral ratio at different frequency band as function of the considered direction of motion (Figure 35). Peak on the rocking spectral ratio is observed at 2.6 – 3 Hz for couple of sensors aligned in the transverse direction of the building for the seismic and ambient vibration data. This vertical differential motion is found at the first natural frequency of the IBT building (2.8 Hz) but also in higher frequencies. From seismic data, the rocking spectral ratio also presents peak at 6.1 – 6.5 Hz for couple of sensors in both horizontal directions. From noise data, peaks are observed at 3.7 – 4 Hz, 5.6 – 6 Hz, 6.1 – 6.5 Hz and 6.7 – 7 Hz mainly for couple of sensors that include the sensor localized in the staircase. For all these frequency ranges and considered couples of sensors, the filtered seismic signals are in phase opposition (Figure 36).

For the HR building (Figure 37), vertical differential motions are observed for both type of data (seismic and ambient vibration) at 0.9 – 1.1 Hz corresponding to the first natural frequency of the HR structure (0.98 Hz). This motion appears between sensors aligned in the transverse direction of the building. Higher frequency peaks at 5.2 – 5.5 Hz, 6 – 6.5 Hz and at 7 – 7.4 Hz are noted on the rocking spectral ratio computed from noise data. The analysis of the filtered seismic signal between these frequency ranges (Figure 38) shows that they all testify of rocking motion by phase differences, except for the frequency range 5.2 – 5.5 Hz where the only difference between signals is the amplitude level and at 6 – 6.5 Hz for sensors aligned in the longitudinal direction where signal phases are identical. Those examples present the limitation of the rocking spectral ratio interpretation.

II.6.2. From real data

The rocking spectral ratio is applied to real data in order to 1) compare rocking spectral ratio obtained from earthquake recording and ambient vibration data and to 2) validate the interpretation of the spectrum. The 7th April 2014 5.3 M_w Barcelonnette earthquake has been recorded by permanent accelerometric sensors placed in one of the RC tower of the Nice Prefecture building (Pequegnat et al., 2008; Brunel and Bertrand, 2010; CETE, 2010a). The epicenter was located 100 km away at the North of the building. The acceleration time series have been integrated according to the process proposed by Boore (2001) to find the displacement time series at the base of the building during the seismic event. The signals are

then filtered around the first natural frequency of the building (1.20 Hz according to Lorenzo et al. (2018)) to have first insight of potential rocking motions and to compare with the rocking spectral ratio (Figure 39). In the following, the rocking spectral ratio is first computed from earthquake recording taking into account the strong phase of the signal after the first seismic wave arrival. The duration of the selected signal is 90s. Secondly, the rocking spectral ratio computed from ambient vibration recording at the same sensors is compared to the one of from the seismic signals (Figure 40) and the interpretation is validated according to the RD functions at the considered frequency and sensor couple (Figure 41). The duration of the ambient vibration data is 1h.

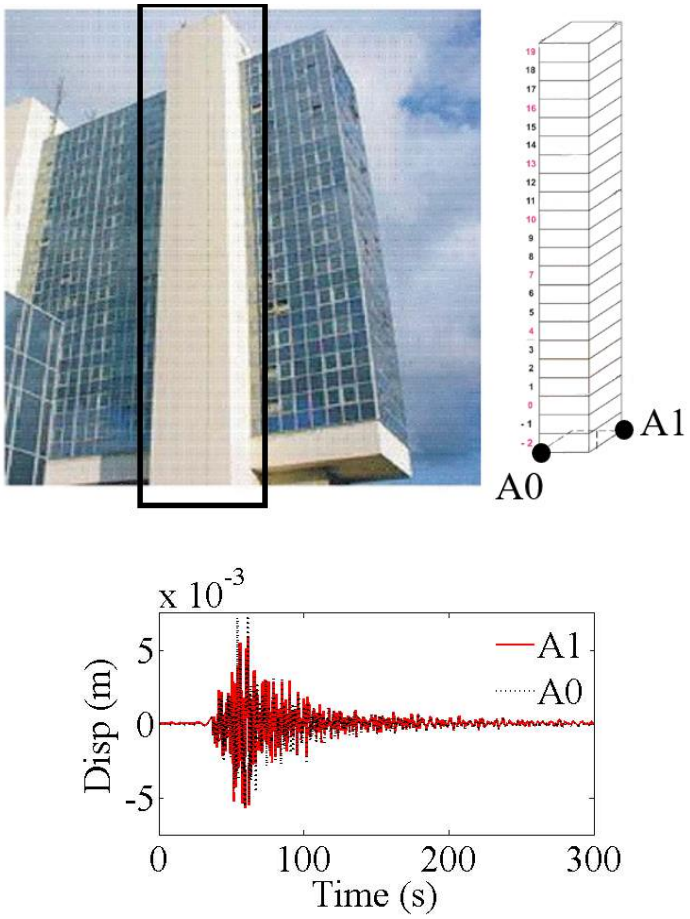

Figure 39: Displacement time series on the vertical component at the base of the Nice Prefecture building record during the 7th April 2014 5.3 M_w Barcelonnette earthquake: zoom on 300s.

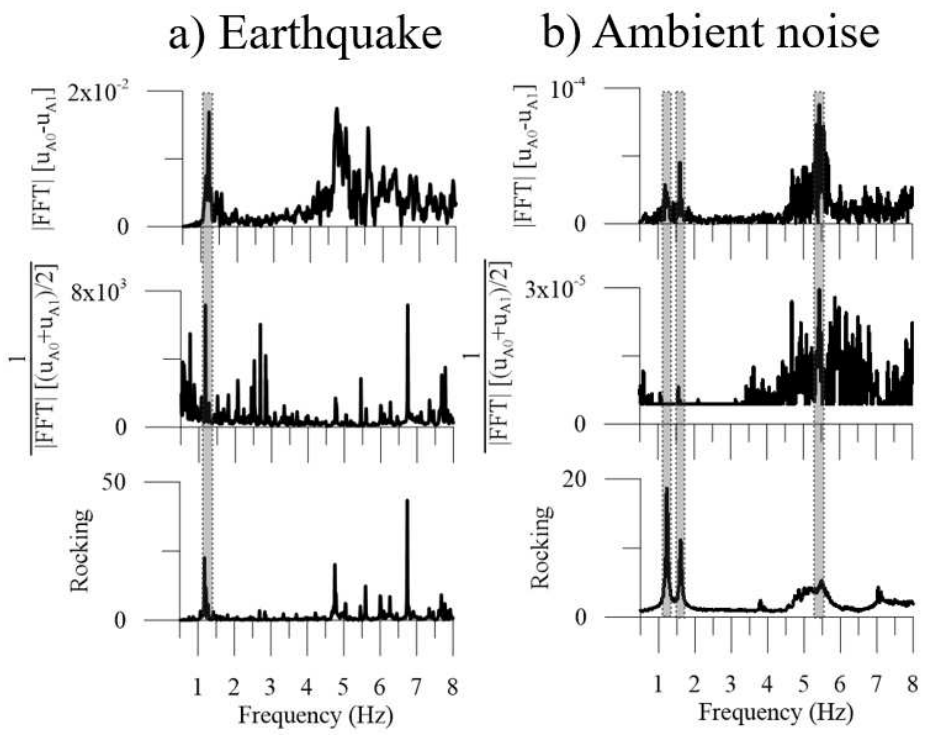

Figure 40: Rocking spectral ratio of the Nice Prefecture building computed from a) the 7th April 2014 5.3 M_w Barcelonnette earthquake recording (90s of duration from the time of the first seismic wave arrival) and b) using ambient vibration recording (3600s of duration with 30s windows) between sensors A0 and A1 located at the base of one reinforced concrete tower. The rocking effect are highlighted at 1.1 – 1.4 Hz, 1.5 – 1.7 Hz and 5.4 – 5.6 Hz.

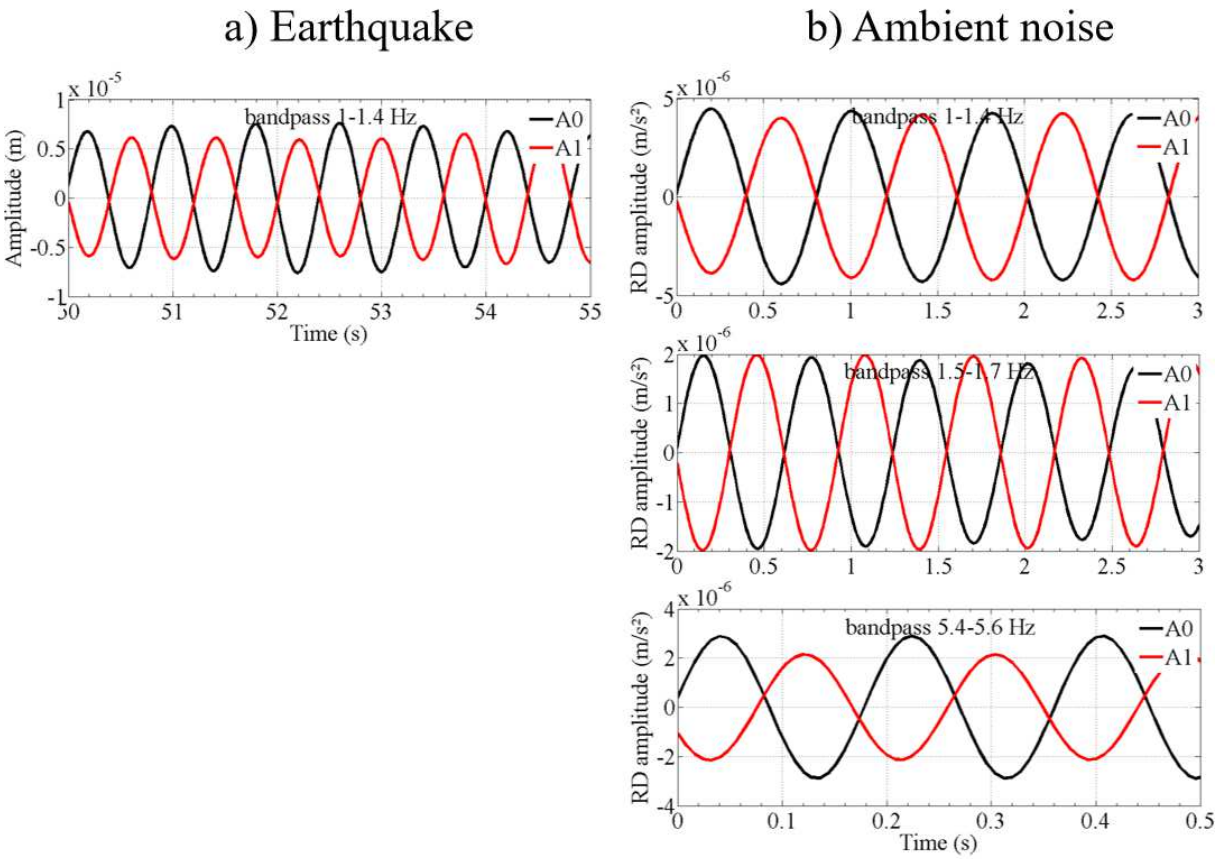

Figure 41: a) Zoom on the filtered displacement time series of the seismic signal and b) random decrement functions at sensors A0 and A1 computed for the highlighted frequency bands in the rocking spectral ratio of the Nice Prefecture building from earthquake recording. The rocking effect is put in evidence at 1.1 – 1.4 Hz, 1.5 – 1.7 Hz and 5.4 – 5.6 Hz.

The comparison of rocking spectral ratio based on earthquake recording and ambient vibration data (Figure 40) shows that both spectra highlight high amplitude around the first natural frequency of the building (1.2 Hz). It appears that ambient vibration allows to put in evidence a second peak of amplitude around 1.5 Hz that is either hidden with earthquake recording or not excited by the earthquake. The filtered displacement time series of the seismic signal and the RD functions computed from noise data (Figure 41) valid a potential rocking motion around the first natural frequency of the building by the opposition of signal phases between both sensors.

The application of rocking spectral ratio on numerical and experimental data shows that this method is suitable to investigate SSI effects when two distant sensors are recording simultaneously the vertical motion at the base of the building. For all the FE building models, a rocking motion is noticed at the first natural frequency in the low stiffness direction of the

building. Moreover, this motion can be retrieved in higher frequencies that do not necessarily correspond to mode frequency of the buildings.

The comparison of rocking spectral ratio computed from seismic or noise data exhibits that the interpretation of the ratio is easier when the signal duration is large, increasing then the number of windows considered in the computation. In fact, the increase of the number of windows leads to smooth the rocking spectral ratio curve and to highlight and refine high amplitude peak. For the analysis at the first natural frequency of building, both type of data can be used. However, rocking motion is better investigated in high frequency range using long ambient vibration recording than earthquake recording (Table 18).

II.7. Sensitive dynamic parameters to soil-structure interaction effects

Through the detailed analysis of the dynamic behavior of different types of building, key parameters of the structural response sensitive to SSI effects have been put in evidence. The Table 19 summaries the results of the analysis.

Table 19: Soil-structure interaction effects as function of the dynamic parameters for each building models.

	Time domain analysis									**Frequency domain analysis**			
	Amplitude	Phase	Duration	AI	EI	SA	PA	PV	PD	Order of modes	f1	Mode shapes	Rocking
ST													
RBT													
IBT													
M													
HR													

Negligible effects	**Slight effects**	**Major effects**

Signal time series at the top of the building:

SSI causes negligible effects on the signal of M buildings and on the signal phase of ST building. Slight changes are observed on the signal amplitude for ST, RBT and IBT models especially on the vertical component where it increases with SSI.

Major effects occur with SSI on the signal time series of the HR building by drastically decrease the signal amplitude on horizontal components and by causing the extension of the signal duration at the top of the building. For the case of low-rise RC buildings, the signal duration tends to decrease.

SSI effects tend to change the phase of the signal for RBT, IBT and HR models compared to the FB condition, in a stronger way on the vertical component.

Anderson criteria at the top of the building:

Major effects of SSI are observed for HR building. The analysis of AI, EI, SA, PA, PV and PD criteria shows that SSI effect are beneficial to the building response by decreasing all of this parameter, mainly on the horizontal components.

PA, PV and PD criteria appear to be not sensitive to SSI effects in the case of low-rise buildings whatever the building material. However, the PA ratio demonstrates that SSI effects can be beneficial or detrimental to the building response and the deformation modes depending on the building type. Mylonakis and Gazetas (2000) also found that the displacement spectra of a structure under SSI shows that this interaction is not always favorable for the structure. The study of the SA highlights an increase of this parameter on the vertical component for low-rise buildings with SSI. Only for ST model, the horizontal components show a significant decrease of the spectrum amplitude at some frequencies.

For ST, RBT and IBT buildings, the influence of SSI effects on AI and EI depends on the building type. The effects are not the same as function of the component, these parameters can increase or decrease with SSI.

Except for SA parameter, the M model does not present variations induced by SSI.

Natural frequency:

The first natural frequency of most of the FE models tends to decrease with SSI and this is stronger for HR building. No changes are observed on ST and M buildings between the both base conditions.

Mode shape:

The analysis of the FE building model shows that SSI induces a change in the order of appearance of modes compared to the FB condition. For low-rise RC structures, torsion mode always appears later with SSI than in FB condition.

The comparison of modes using the MAC shows that the first two modes shapes are generally highly correlated between both conditions for all buildings. The difference between the mode shapes increases with higher modes.

For the M model, SSI seems to have negligible effects on the dynamic behavior of this building compared to the FB condition.

Rocking:

The analysis of the rocking motion highlights the fact that this motion occurs not only at the first natural frequency of the building but also in higher frequencies. Rocking effect appears to be negligible in the case of ST or M buildings whereas this motion is well observed for bending type buildings.

II.8. Discussion

Our analysis shows that SSI impacts the dynamic behavior of buildings in many different ways. Not all parameters are equally sensitive to SSI effects depending on the building type.

In several studies, the response of the building generally tends to increase with SSI (in terms of displacement and forces applied at the base of the structure). This was also observed in many other studies (e.g. Naserkhaki et al., 2012; Mahmoud et al., 2013; Madani et al., 2015; Ghandil and Aldaikh, 2017; Miari et al., 2019). As in Rahmani et al. (2015), the first natural frequency of the HR building decreases drastically with SSI.

Bárcena and Esteva (2007) brought out a relationship between the aspect ratio of the structure and the increase or decrease of the motion amplitude of the whole system with SSI. For low value of the ratio, the building response tends to be lower with SSI than the FB one. We observed that it is not only the shape of the building that controls the seismic response but also the structural configuration. Actually, for the same dimensions, ST and bending type buildings

undergo different SSI effects. In the case of ST building, the motion tends to decrease with SSI while it is not so simple in the case of IBT building. Indeed, the non-uniform distribution of the stiffness in the building (here the staircase) can lead to decrease or increase the building response with SSI.

The detailed study of the sensitivity of dynamic features of the M model shows that only SA is sufficiently sensitive to put in evidence SSI effects. Cavalieri et al. (2021) based their study on this parameter and on the acceleration time series to study SSI effects on a numerical model of masonry building with basement. They conclude that SSI does not impact the recordings at the base of the building.

The rocking spectral ratio combined with filtered seismic signal or RD functions from long ambient vibration recordings appear to be useful to detect rocking motion at the base of the building in a considered frequency band. This method does not require the integration of acceleration or velocity signals that can be troublesome (Boore, 2001; Boore and Bommer, 2005; Javelaud, 2016). Knowing that the presence of rocking motion witnesses an important variation of the first natural frequency of building with SSI, attention should be paid during the instrumentation set up.

Large uncertainty exists in the definition of the mechanical properties of the considered FE buildings. Indeed, these FE models are theoretical models used to understand SSI effects and not used to monitor the vulnerability of the buildings. Assumptions made to develop simple FE models do not take into account effects linked to meteorological conditions, reinforcement of the structure, mechanism to improve the damping capacity of the structure, pre-existing damages in materials that can be, for all of these examples, strong factors of the disturbance of the global stiffness of the soil-structure system (i.e. Hans, 2002; Dunand, 2005; Michel, 2007). Consequently, the nonlinearity of the structures has not been considered here.

Moreover, the consideration of a soil domain of three homogeneous sedimentary layers is also a strong simplification of the real case. In fact, it is known that the superficial soil, especially in valley, is rarely constituted of homogeneous material. It is often filled with different sedimentary deposits from different sources due to the passage of a river or even anthropogenic filling in the case of dense urbanization of the area. The Var valley is a typical example of the mixing of both cases and in addition, presents marine deposits.

The observed SSI impact on the considered seismic response parameters may be underestimated because of some effects have not been taken into account in this analysis. For example, the energy amplification at some frequencies with SSI can be explained by different phenomena occurring in a sedimentary basin such as 2D/3D resonance effects, the proximity of topography or basin edge inducing the generation of surface waves, seismic waves trapping in sedimentary layers, all depending on the shape and the depth of the basin (i.e. Kumar and Narayan, 2018), the mechanical properties of the sedimentary basin (V_s, ρ, G,…) including the non-linear soil behavior. Closer to the building, the stiffness ratio and damping ratio between the foundation and the soil are also involved in the solicitation of SSI (i.e. Ghannad and Jahankhah, 2007).

II.9. Conclusion

Several building types and their dynamic parameters have been investigated to find which of them are the most sensitive to SSI effects. Five different types of building, high and low-rise, some having reinforced concrete or masonry materials, have been considered and subjected to white noise and simulated earthquake.

We show that the impact of the SSI on the building response is depending on the aspect ratio of the structure and also on the non-uniform distribution of rigidity in the structure. The low-rise M and ST buildings appear to be the less sensitive to SSI effects whereas bending type buildings show changes in several dynamic parameters. We note that even if the first natural frequency of the ST building is closed to the soil fundamental frequency and induced a double resonance condition, the influence of SSI effects on the response of this building remains lower than the one of the bending type buildings.

Building dynamic parameters the most sensitive to SSI are presented in the following. Their variations are described in the case of the flexible base condition compared to the fixed base condition.

- A decrease of the first natural frequency is observed for all the reinforced concrete buildings.
- The mode shapes and the order of apparition of the modes differ in the case of low-rise reinforced concrete buildings.

- The amplitude and the phase of the signal are modified by the SSI for all the reinforced concrete buildings. For ST, IBT and HR models, the amplitude decreases at the top of the building whereas it increases for the RBT model.
- The signal duration decreases in the case of low-rise reinforced concrete buildings but increases for HR building.
- The motion intensity in high and medium frequencies tends to decrease for ST and HR buildings whereas it increases for the RBT model.
- A rocking motion is highlighted at the base of the reinforced concrete bending type buildings at their first natural frequency but also in higher frequencies.

For experimental studies, we show that the analysis of mode shapes does not give obvious information about SSI effects. However, the rocking spectral ratio analysis constitutes a powerful tool to identify SSI effects. This analysis is possible using sensors at all corners/extremities of the base of the instrumented building. Therefore, in-situ experiments involving the recordings of ambient vibration with synchronized sensors could be used to characterize the SSI in structures taking into account its environment and its complexity and irregularity. For numerical studies of SSI, it is relevant to know which dynamic parameter of the targeted building is the most sensitive to SSI effects. Knowing these parameters, computational costs of the numerical analysis is reduced by directly selecting the proper method in time or frequency domain to study SSI effects. Also, attention should be paid before the integration of the building in numerical models for engineering studies (shear type ≠ bending type).

Chapter III. Soil-structure interaction observations on high-rise structures in the Var valley

In the previous chapter, we found that the bending type buildings were most sensitive to the soil-structure interaction (SSI) and that rocking spectrum could help to recognize SSI effects. In this Chapter, we propose to verify that observation with in-situ recordings of ambient vibration. These temporary non-invasive measurements allow for the quick characterization of a large number of structures. The numerical investigation of SSI was performed on simplified structure types, one of the main advantages of in-situ measurements is that the analysis is specific to the building with its intrinsic complexity and in its environment.

Several studies showed that SSI effects are more important on soft soil site than on rock site (e.g. Bard, 1988; Kanai, Kiyoshi and Yoshizawa, 1961; Paolucci, 1993; Meli et al., 1998; Nakhaei and Ali Ghannad, 2008; Salameh et al., 2016). The same conclusion was observed for the structure-soil-structure interaction (SSSI) studies (e.g. Vicencio and Alexander, 2018; Bybordiani and Arici, 2019). High-rise and slender structures are generally more flexible than low-rise structures. The high difference in signal between the top and the bottom of the tall building and the possibility to perform detailed investigation of the mode shape allows to better observe SSI and SSSI effects.

The Var valley is densely urbanized with the tallest buildings in Nice and is subjected to site effect (see Chapter IV). In addition to the instrumentation of the Nice prefecture in 2010 (Brunel and Bertrand, 2010; CETE, 2010b; Lorenzo, 2016), a single tower and a residential compound composed of high-rise and low-rise buildings have been temporally instrumented in the framework of the thesis. These high-rise structures (including the Nice prefecture) constitute the tallest buildings in the Var valley. They reach 57 m high and have rectangular cross-section. They are among the classical constructions in France composed of reinforced concrete walls.

This chapter describes the dense in-situ ambient vibration instrumentation performed in various buildings in the Var valley. Here, we focus on the characterization of the modal parameters of the instrumented buildings, the identification of SSI effects on ambient vibration recordings and on the quantification of these effects compared to the free field ground motion. The modal parameters are solid basis for the calibration of realistic simplified 3D numerical models of

building because they have the advantage to take into account the real stiffness of the structures and to include the SSI. The simplified building model calibrated in the form of equivalent homogeneous block will be added in the realistic 3D site-city models (see Chapter V).

III.1. Description of the buildings

III.1.1. Localization

The instrumented buildings are located on the eastern part of the sedimentary basin of the lower Var valley (LVV) close to the hills of Nice (Figure 42). They are all located next to the Nice Prefecture building. The structures are surrounded by the A8 highway and the Var River to the west, the upper Var valley to the north, Nice Côte d'Azur airport to the south and the Pliocene hills to the east. They are located 2 km away from the Mediterranean Sea. According to the 3D geotechnical model of the LVV (Rohmer et al., 2020), the buildings are built on the recent quaternary sedimentary basin of the valley mainly filled with sand, gravel and mix clays. At the building positions, the basin depth goes from 45 m to 50 m, the average shear wave velocity (V_s) in the basin at the building positions is estimated between 200 and 400 m.s^{-1} and the soil fundamental frequency (f_{s0}) varies from 1.8 to 2.1 Hz. The single tower (Figure 42b) presents the same geometry as the four identical towers (A, B, C and D) (Figure 42c-d). The low-rise buildings (E and F) have irregular shape (Figure 42c-d).

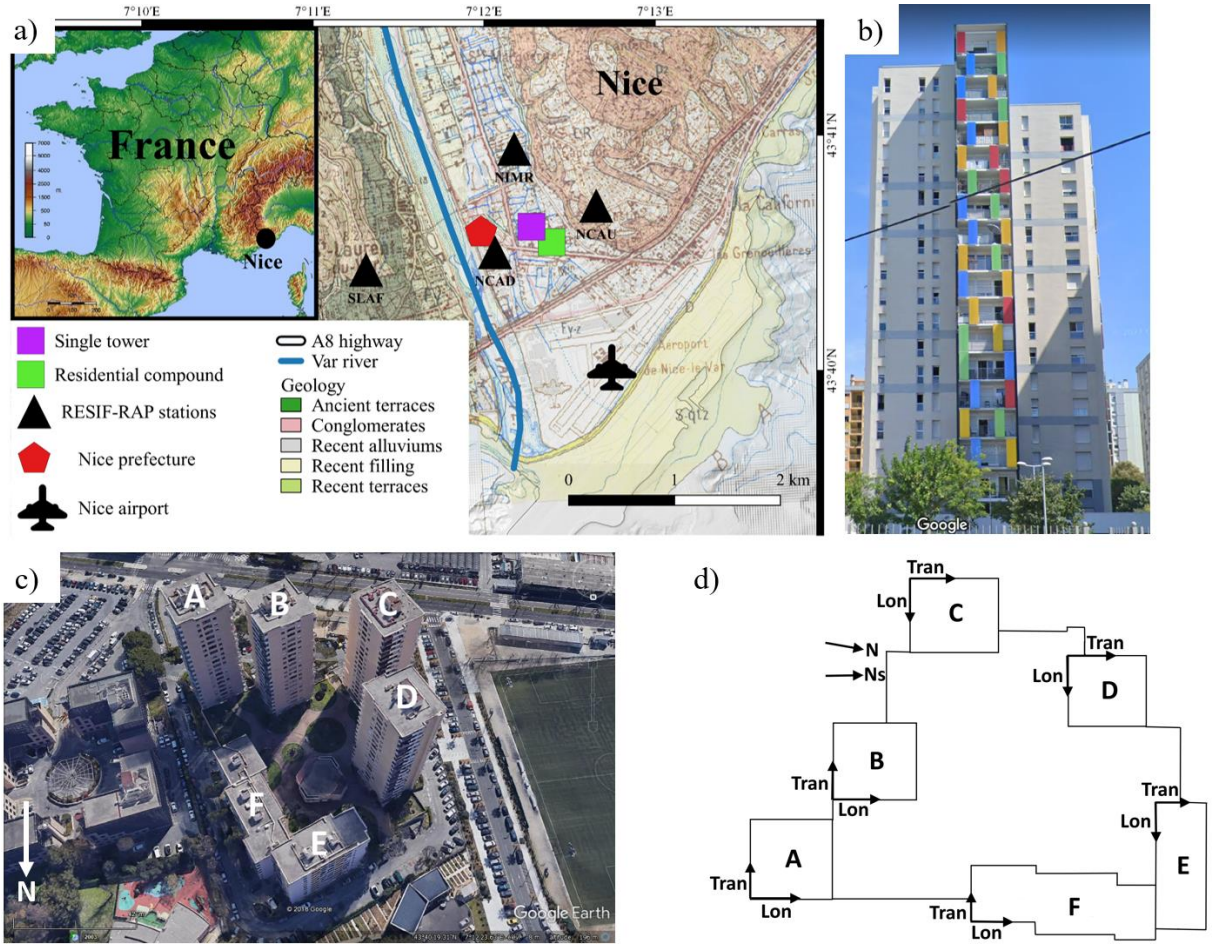

Figure 42: a) Localization of the instrumented buildings in the Var valley. The background map is the 1/50000e geological map from the French Geological Survey (BRGM), b) Front view of the single tower, c) Top view of the residential compound, d) Simplified plan of the residential compound, the north orientation of the sensors "Ns" is close to the geographic north "N".

III.1.2. Structural characteristics

III.1.2.1 The single tower

The single tower was built in 1974 and has benefited of recent renovations in 2015, notably on the facades, the common areas and the surroundings of the building. This structure presents an irregular rectangular shape having dimensions 27x35x52 m (Figure 42b) but for sake of simplification, we consider a regular rectangular shape in the dynamic analysis. The tower is composed of 18 floors where the last one is only distributed on the half floor surface. 106 apartments, 2 elevator shafts and one staircase composed the building. Other structural features can be found on the collaborative PSS database (https://www.pss-archi.eu/immeubles/FR-06088-27698.html [last access: 12/11/2021]).

III.1.2.2 The residential compound

The group of structures is composed of four very similar and tall towers (called here « tower A », « tower B », « tower C » and « tower D » and one irregular in shape low-rise building. This last building is irregular in elevation and forms a « L » in plan. It is composed of a succession of four structures separated by empty joints. We assumed only two buildings (called here « building E » for the part with eight floors and « building F » for the part with six floors) (Figure 42c-d).

The set of buildings was constructed in several steps. The buildings E and F were the first to be built in 1974. The second one is the tower D dating 1975. The tower B was built in 1976, the tower A in 1978 and the tower C in 1980. The towers were the tallest buildings of Nice until the construction of the Nice Prefecture in 1981. The chronology of the construction suggests that the two underground levels, linking all the buildings, were built after. There is currently no available information about the join between the slab and the structures and the nature of the foundations.

The slab area is around 12 000 m². Two parking lots compose two underground levels that are shared by all the structures. The first underground level has half of its area embedded in an embankment. The parking exit is between the tower A and the building F at the same altitude of the road. The second underground level is completely embedded in an embankment. The parking exit is between the towers A and B (Figure 43).

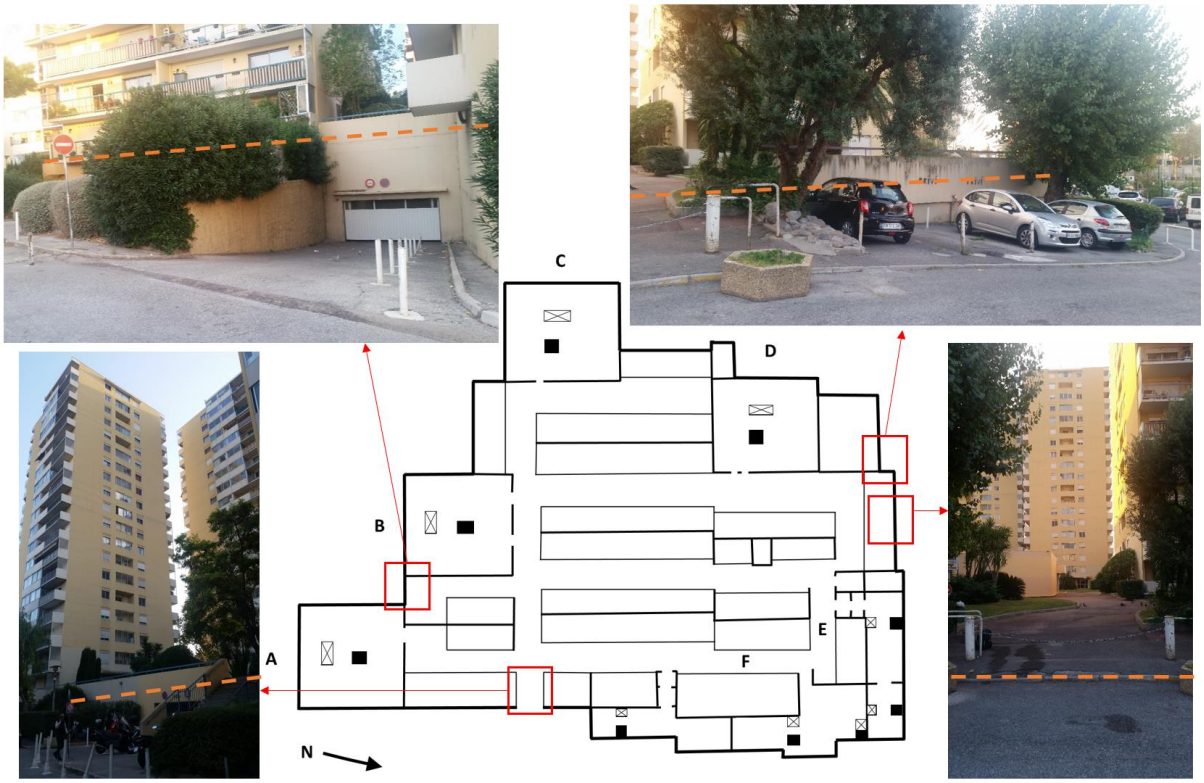

Figure 43: Detailed scheme of the instrumented residential compound in the Var valley (view at the first underground level). The geographic north is indicated by the arrow. Black rectangles are the staircases and crossed-out rectangles are elevator columns. Illustrations of the embedding condition of the superstructure. Orange dot lines indicate the slab level.

The four towers have similar rectangular shape with a section of 18x18 m. They also have similar height of 57 m with 18 floors (above the slab). The height between each floor is about 3 m (2.5 m in the underground levels). There are 2 elevator shafts situated in the center of each tower. The elevators link all the floors and the underground levels except for one elevator in building F. The layout of the corridors and apartments is the same in each tower. Only the orientation of the towers differs. In fact, the entrances of the towers A and B are oriented toward the geographic north whereas the ones of the towers C and D are oriented toward the geographic east. Therefore, it is important to consider the building orientation during the recording setup so that sensors have the same orientation and comparison between recordings is possible. The low-rise building is composed of four structures separated by dilatation joints. The northern part (shorter part of the “L” shape) called building E is the highest part. It is composed of 8 floors whereas building F, the longer part of the L shape has only 6 floors. The heights of the different parts are 27 m and 21 m for the buildings E and F respectively, with a height between each floor around 3 m (2.5 m in the underground levels). There are 6 elevator shafts on either side of the building. Other characteristics and information about these buildings can be found

on the website of the collaborative database PSS (http://www.pss-archi.eu/resultats/FR,,,,06088,,99,2,0-0,0-0,50,1,2,0,,,,,,3,1,1,,bois+boulogne [last access: 12/11/2021]).

Due to their geometrical features and proximity, the set of the five buildings represents an ideal configuration to study the SSI and SSSI.

III.2. Instrumentation setup

The analysis of the dynamic behavior of the different buildings is performed using ambient vibration recordings. Cityshark and Minishark recorders (Chatelain et al., 2000) as well as 3-components CMG-40 broadband velocimeters have been deployed. During the instrumentation setup, sensors have been placed directly on the floor. Their north component corresponds to the direction at 20° from the geographic north along one horizontal direction of the building (transverse or longitudinal depending on the building). Sensors show flat instrumental response between 0.5 Hz and 50 Hz. The Table 20 presents the material and the measurement settings used to record ambient vibration data for each set of instrumented buildings.

Table 20: Summary of the recording material for the instrumentation campaigns.

	Recorders	Nb of CMG-40 stations	Frequency sampling (Hz)	Recording duration/setup	Nb of setups
Single tower	1 Cityshark	8	200	11 days	1
Residential compound	1 Cityshark 3 Minishark	15	250	30 min	12

III.2.1. Single tower

In the single tower, the data were continuously recorded during 11 days from the 20th of November 2018 to the 31st of November 2018. To characterize a structure with ambient vibration recordings, only few hours of recordings are needed. However, at the time of the instrumentation, a large seismic campaign was led on the Ligurian Sea for 11 days. Therefore, to take advantage of the possible impacts of the seismic shots on the structure response, we increase the duration of the recordings. Unfortunately, the seismic shots were not seen in the recordings.

Eight sensors were installed: half of them at each corner on the ground floor and the other half at each corner on the rooftop (Figure 44). At the rooftop level, two seismological sensors are installed at the last floor (18th) and two are placed at the 17th level. This is due to the configuration of the last floor which is extend only on the half surface of the floor (Figure 42b).

The setup configuration allows to identify differential motions between horizontal and vertical components of all sensors. Therefore, the presence of torsion at the top of the tower and rocking motion at the building base can be clearly analyzed.

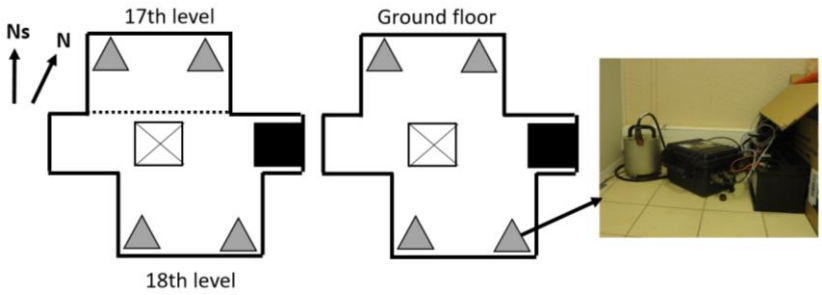

Figure 44: Setup layout in the single tower. Staircases are black boxes and elevator shafts are represented by crossed-out rectangles. On the scheme, the arrow “N” indicates the geographic north and the arrow “Ns” indicates the north component of the sensors and corresponds to the transverse direction of the building.

III.2.2. The residential compound

The instrumentation campaign of the residential compound lasted three days in October 2019. The layouts of the different setups are shown in Figure 45. In total, 12 setups were performed including 11 setups with simultaneous measurements in pairs of towers (AB and CD) and in buildings E and F (color themes in Figure 45a). The last setup was performed outside the structures (Figure 45b). The layouts of the setups are similar within each tower. For each setup, two sensors were installed per floor to analyze torsional modes. Due to the limited available space in the corridor of towers, the maximum distance between sensors at one floor is 7 m (Figure 45c-d). The reference sensor remained at the last floor (18th) during the entire building instrumentation. One of the main interests to densely place sensors at several floors is to study in detail the mode shapes of the building and to compare modes to the theoretical ones (shear beam, cantilever beam, or Timoshenko beam).

As the configuration of the buildings E and F differs from the towers, the setups layout is different (Figure 45e). The only access to dispose sensors was in front of the elevator shafts. The sensors positions have been chosen to well discretize spatially each building deformation. Moreover, the reference sensors for building E and F were respectively placed at the last floor (8^{th} for E, 6^{th} for F).

Moreover, one setup was performed outside the structures (yellow filled triangles in Figure 45b). Three sensors were installed above the two underground levels on the slab and three sensors were installed around the parking lots at the soil level. This layout was performed to study the influence of the slab on the nearby ground motion. For this instrumentation campaign, the Cityshark recorders were used to record vibration in the structures. Two Minishark recorders were used to record vibration outside the structure. No rain or wind disturbed the outdoor recordings.

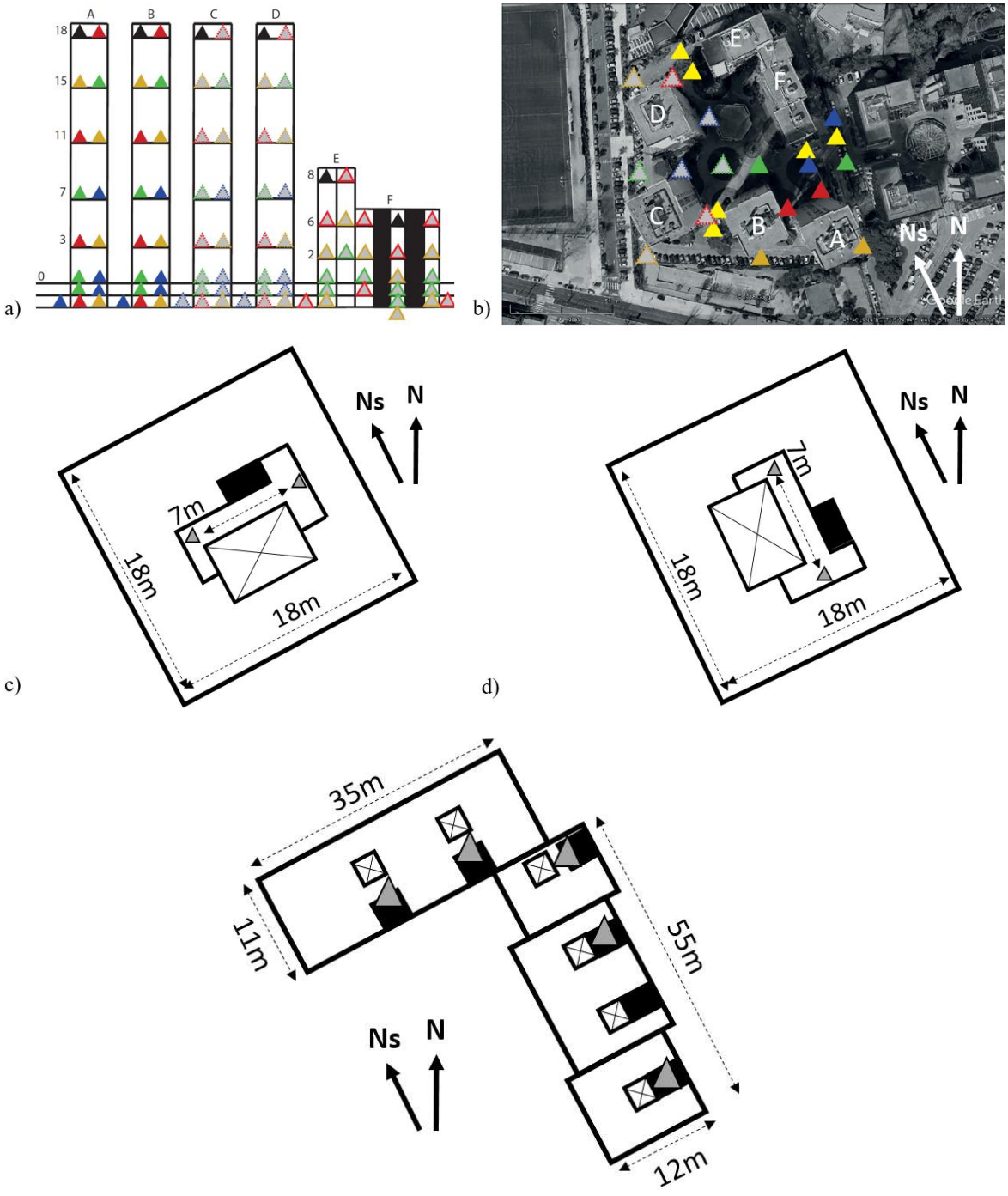

Figure 45: Setup layout in (a) and around (b) the buildings. Triangles are the sensors: black ones are the reference sensors, colored ones indicate sensors in each setup (for example, full red triangle are sensors of one setup simultaneously realized in tower A and B taking the black triangle in tower A as the reference sensors for tower A, and the black triangle in tower B as the reference sensor in tower B). Positions of sensors at the floor levels are represented in the towers A and B (c), in the towers C and D (d) and in buildings E and F (e). Elevator shafts are represented by crossed-out rectangles and staircases by black boxes. On the scheme, the arrow "N" indicates the geographic north and the arrow "Ns" indicates the north component of the sensors.

In order to isolate the impulse response of the structure, the localization of the seismological stations must be carefully chosen. According to Trifunac et al. (2001), in-situ recordings of buildings with rotational sensors enable to refine soil-structure models. Indeed, these sensors allow not only to define the center of torsion of a structure but also to separate the contribution of the foundation rocking motion and the structural deformation from the building response. For this instrumentation campaign, we did not benefit of this kind of material to perform the instrumentation. However, the presence of couple of sensors at each floor allows to study torsion and rocking motions.

For the signal analysis, the beginning of each signal is cut so that they start exactly at the same time. Therefore, the maximal signal duration is equal to 25min for all records. This duration is considered sufficiently long to apply general operational modal analysis methods like Fast Fourier Transform (FFT) or the frequency domain decomposition (FDD) but also for torsion and rocking estimation or Horizontal-to-Vertical spectral ratio (HVSR) to estimate the f_{s0}. The damping parameter is also investigated, however damping assessment methods strongly depend on the signal duration and show more accurate results when the signal is sufficiently long (at least 6h according to Mucciarelli and Gallipoli (2007)).

III.3. Dynamic analysis of the single tower

The dynamic behavior of the single tower is analyzed in terms of natural frequency, mode shape and rocking motion to compare the obtained modal parameters to the other towers of the residential compound and to investigate SSI. The main objective of this instrumentation is to show that for structures having similar geometry (50 m high rectangular towers) the modal deformations can be different. Since the simplified representation of buildings in numerical simulation is done by equivalent homogeneous blocks based on the first natural frequency of the structure and its height, the calibration of these models from real data can only be done if the first mode of deformation corresponds to a flexion.

The FFT is calculated on the stationary part of the signal. To select time windows, we use an anti-triggering process based on the calculation of the ratio between the short term average (STA) and the long term average (LTA) of the signal. 30s signal windows duration, the STA and the LTA length are respectively equal to 1s and 30s and minimum STA/LTA ratio of 0.2

and maximum one of 2.5 are used. The mean of the FFT is computed from all sensors located at the top of the single tower. The *FDDA* analysis used the same time windows durations.

III.3.1. Modal parameters

Results highlights the mode frequencies up to the 6th mode (Figure 46). We observe that the first three modes have very close natural frequencies (only 0.1 to 0.3 Hz of difference) (Table 21).

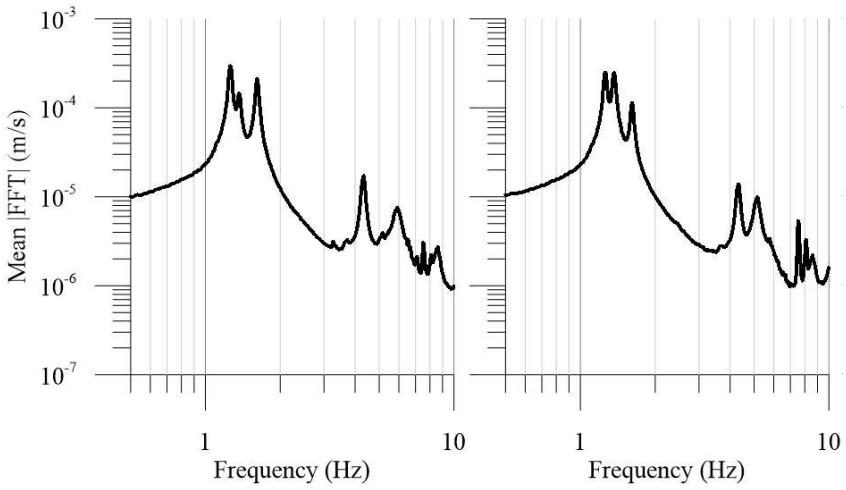

Figure 46: Mean of the absolute value of Fourier spectra at the top of the single tower for the transverse (left) and longitudinal (right) components.

Table 21: Mode shape and related frequency of the single tower.

Mode	1	2	3	4	5	6
Frequency	1.2 Hz	1.3 Hz	1.6 Hz	4.4 Hz	5.1 Hz	5.9 Hz
Direction	Torsion	Longitudinal	Transverse	Torsion	Longitudinal	Transverse

The singular value decomposition (SVD) plot computed from all recordings for the three components clearly exhibits the six modes up to 6 Hz (Figure 47). From the *FDDA* analysis, it appears that the building has a first torsion mode, a second bending mode in the longitudinal direction and a third mode of bending in the transverse direction (Figure 48).

In this specific case, the fundamental resonance frequency should not be used to calibrate the simplified structure models but an average between the second and third modes, corresponding to the first bending modes on the two horizontal components should be used instead.

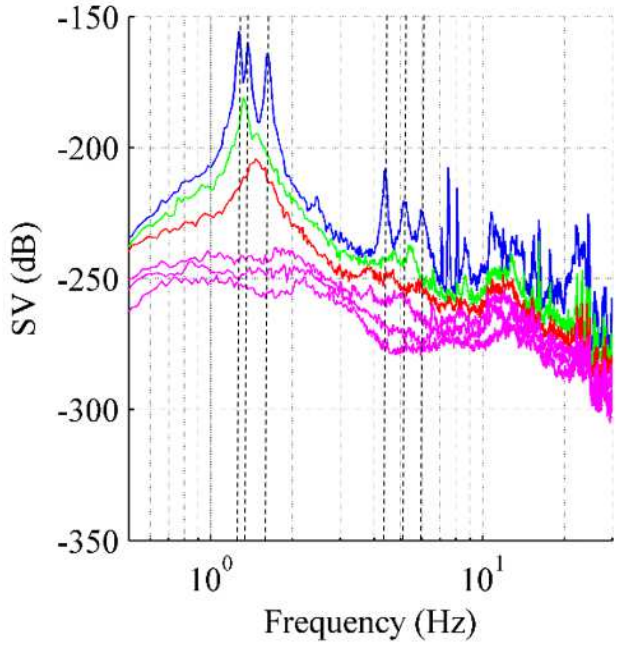

Figure 47: Singular values from the single tower recordings. Dashed lines indicate observed modes.

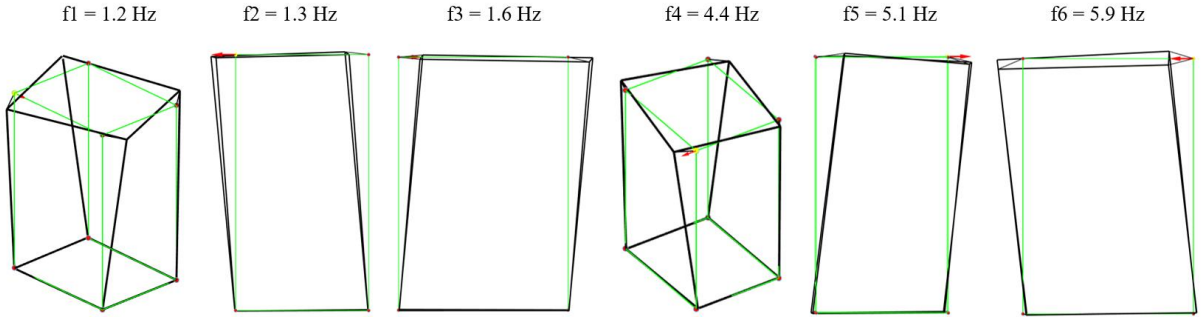

Figure 48: Mode shapes of the single tower. Green lines indicate initial position of the building. Dark lines describe the mode shapes. The red arrow is the direction of normalization of the mode.

III.3.2. Rocking motion

The rocking of the foundations is one of the characterizations of SSI effects. In this paragraph, we propose to analyze the rocking motion at the base of the single tower using the rocking spectral ratio presented in the Chapter I. The rocking spectrum is defined as the ratio of the Fourier spectrum of the signals difference and the Fourier spectrum of the signals average. The objective is to highlight frequency excited by a potential rocking motion of the slab. A couple

of sensors is chosen such as the two sensors recorded simultaneously the motion and are located at opposite sides of the building.

For all data, vertical components are compared in the frequency range 0.5 – 8 Hz and using 30s overlapping (5%) time windows. The STA and LTA are respectively set to 1s and 30s. The minimum STA/LTA ratio is 0.2 and the maximum one is 2.5. The rocking spectral ratio is estimated based on the average of rocking spectral ratio computed from 21 ambient vibration recordings of one hour duration at the base of the single tower. To compute the random decrement (RD) functions at each sensor, the ambient vibration recording of the 2018 November 17th at 1h00 AM with one hour duration have been used based on 2s overlapping time windows.

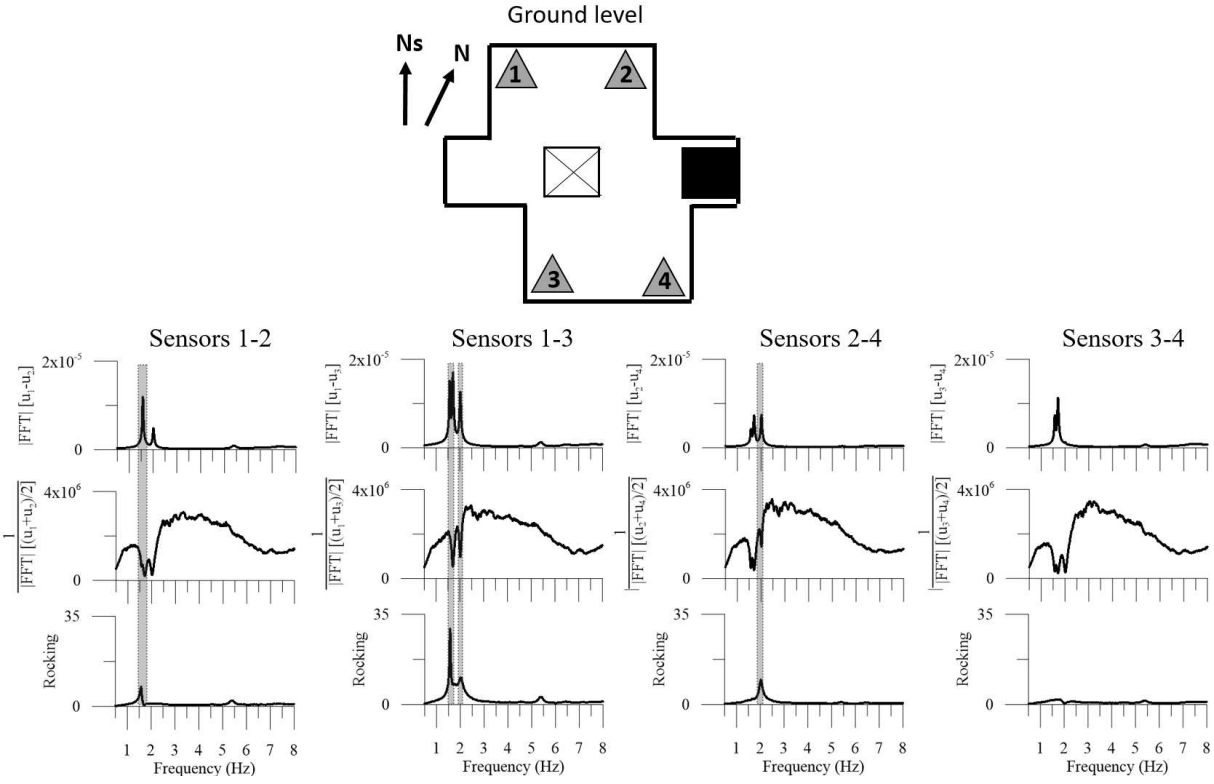

Figure 49: Rocking spectral ratio of the sensors located at the base of the single tower computed between sensors 1 – 2, 1 – 3, 2 – 4 and 3 – 4. The rocking effect is highlighted at 1.6 Hz for the couple of sensors 1 – 2 and 1 – 3; at 2 Hz for the couple 1 – 3 and 2 – 4. On the scheme, the arrow "N" indicates the geographic north and the arrow "Ns" indicates the north component of sensors and corresponds to the transverse direction of the building.

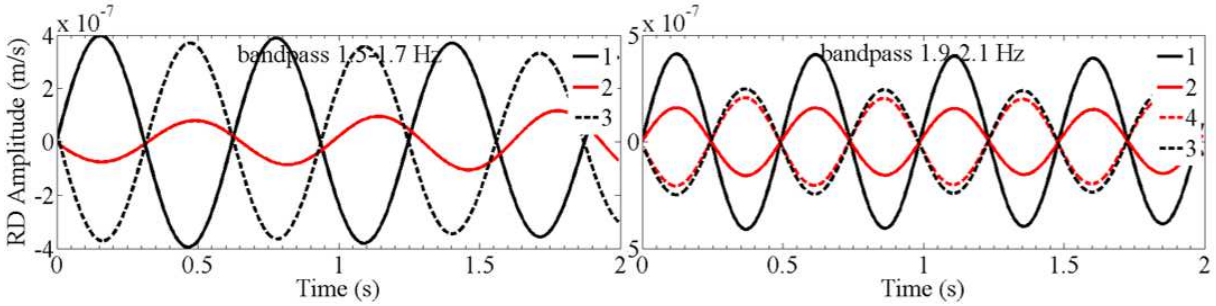

Figure 50: Random decrement functions at sensors 1, 2, 3 and 4 computed for the highlighted frequency bands in the rocking spectral ratio of the single tower from ambient vibration recordings.

The analysis of the rocking spectral ratio shows evident peaks at 1.6 Hz and 2 Hz depending on the couples of sensors. Both peaks are also clearly observed in the Fourier spectrum of the average and the difference of the signals for all the couple of sensors. The first one is closed to the 3rd mode frequency of the single tower corresponding to the first transverse mode (f_3=1.6 Hz) while the second one is closed to the f_{s0} (2.1 Hz at 130 m from the single tower) according to Rohmer et al. (2020). However, these two peaks are not always visible on the rocking spectral ratio depending on the couple of sensors. In fact, the peak at 1.6 Hz is only observed for the couple of sensors 1 – 2 while, the peak at 2 Hz is only observed for the couple of sensors 2 – 4. In the rocking motion between the couple 1 – 3, both peaks are observed and for the sensors 3 – 4 no clear peak is identified on the rocking spectral ratio. These differences are well distinguished in the RD functions where opposite phases are shown for couple indicating rocking effect. For example, the RD functions of the data filtered between 1.5 and 1.7 Hz present opposite phase between the RD functions of the sensor 1 and the sensor 3 that is a couple of sensors which shows clear peak in the rocking spectral ratio at 1.6 Hz. For all couples of sensors, the rocking spectral ratio differs. The high irregularity in plan of the single tower and the embedding condition may explained the spatial difference in rocking motion at its base. This is similar to the case of the irregular low-rise bending type building studied in the Chapter II where rocking spectral ratio are different depending on the considered couples of sensors.

Therefore, rocking motion is put in light at the base of the single tower and witnesses the presence of SSI effects.

III.4. Dynamic analysis of the residential compound

The set of the five buildings are analyzed in terms of modal parameters (natural frequency, mode and damping), seismic wave propagation within the towers, rocking and torsion motions and variability of the ground motion within the residential compound in order to characterize the dynamic properties of each building, the SSI and the SSSI.

Then, we will address the case of the low-rise buildings E and F. We can see on Figure 43b-e that buildings E and F are separated by a seismic joint. The resonance frequencies, modes and damping of these structures are computed considering that (1) both are independent structures and (2) both are linked structures to improve our understanding of the dynamic behavior of this irregular low-rise building.

We used the same calculating parameters than in the modal analysis of the single tower.

III.4.1. Modal parameters

III.4.1.1 Natural frequency

The analysis of SVD spectra (Figure 51 and Table 22) of the five buildings shows that the first natural frequency of the towers is between 1.03 Hz and 1.12 Hz and the first frequency of the low-rise buildings is between 2.33 Hz and 2.49 Hz. In details, the tower B has the lowest first resonant frequency (1.03 Hz) then comes, in increasing order, the first resonant frequency of the tower D (1.06 Hz), then the one of tower A (1.10 Hz), tower C (1.12 Hz), building E (2.35 Hz) and building F (2.36 Hz). Higher modes are well observed up to the 8^{th} mode.

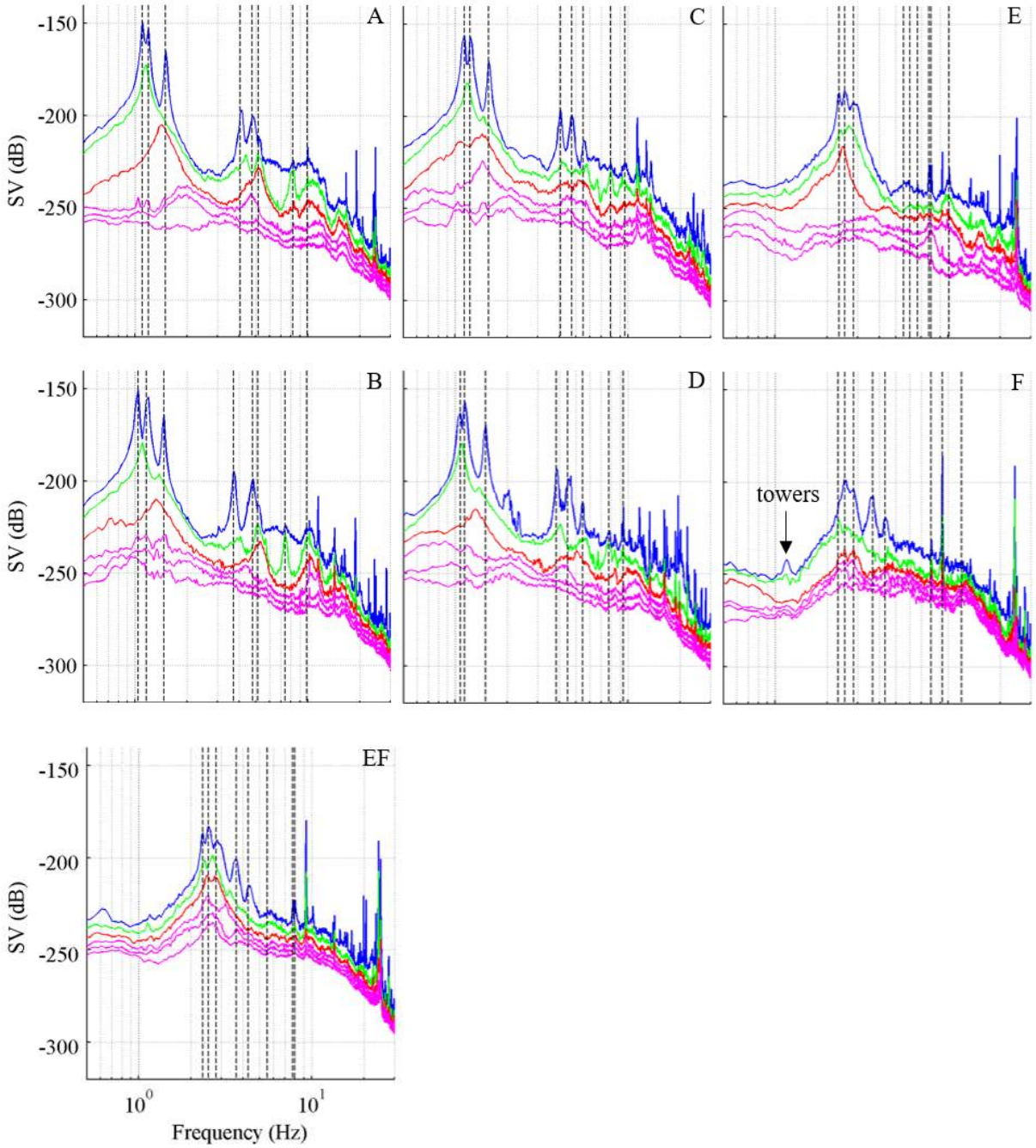

Figure 51: Singular values of the five buildings and for the low-rise pair of buildings instrumented simultaneously. Dashed lines indicate observed modes.

Singular values curves of building F show very low peak around 1 Hz on the first curve that corresponds to the influence of the towers. Moreover, the building E shows a first bending mode in the transverse direction at 2.35 Hz. Here, we conclude that there is SSSI effects between close buildings of different height. This conclusion was also found in Bybordiani and Arici (2019). These authors indeed noted that SSSI effects are important on the resonant peak of structures located on soft soil and sharing different natural frequency and that the resonant peak

of high-rise structure is not significantly modified. However, it is difficult to say, based only on the natural frequencies, if there is SSSI effects between the towers because of their very similar frequency content. More investigation of these effects are presented in the section III.6.

Considering the coupled system linking buildings E and F, we notice that the resonant frequency of each building is retrieved in the frequency content of the system response.

III.4.1.2 Mode shape

The mode shapes and the related frequency of the buildings of the residential compound are summarized in (Table 22). The mode shapes of each tower are presented in Figure 52. The high-rise structures present similar deformation modes. The 8 first mode shapes are: 1) the 1st transverse bending mode, 2) the 1st longitudinal bending mode, 3) the 1st torsion mode, 4) the 2nd transverse bending mode, 5) the 2nd longitudinal mode, 6) the 2nd torsion mode, 7) the 3rd transverse bending mode, 8) the 3rd longitudinal bending mode. Contrary to the single tower, for this set of building, the first mode is a bending mode.

Table 22: Natural frequencies of observed modes on the singular values spectra of the five buildings. The first resonant frequency is highlighted in bold for each building.

Building	Longitudinal	Transverse	Torsion
A	f2 = 1.18 Hz f5 = 4.82 Hz f8 = 10.02 Hz	**f1 = 1.10 Hz** f4 = 4.10 Hz f7 = 8.21 Hz	f3 = 1.50 Hz f6 = 5.11 Hz
B	f2 = 1.17 Hz f5 = 4.80 Hz f8 = 9.95 Hz	**f1 = 1.03 Hz** f4 = 3.73 Hz f7 = 7.39 Hz	f3 = 1.46 Hz f6 = 5.06 Hz
C	f2 = 1.23 Hz f5 = 4.70 Hz f8 = 9.54 Hz	**f1 = 1.12 Hz** f4 = 4.04 Hz f7 = 7.86 Hz	f3 = 1.56 Hz f6 = 5.54 Hz
D	f2 = 1.13 Hz f5 = 4.56 Hz f8 = 9.54 Hz	**f1 = 1.06 Hz** f4 = 3.85 Hz f7 = 8.42 Hz	f3 = 1.49 Hz f6 = 5.45 Hz
E	f2 = 2.56 Hz f4 = 5.56 Hz f6 = 6.67 Hz f8 = 7.95 Hz	**f1 = 2.35 Hz with torsion** f3 = 2.82 Hz f5 = 6.03 Hz f7 = 7.84 Hz f9 = 10.04 Hz	
F	**f1 = 2.36 Hz** f2 = 2.54 Hz f6 = 7.98 Hz f7 = 9.27 Hz	f3 = 2.81 Hz f4 = 3.65 Hz f5 = 4.35 Hz f8 = 11.99 Hz	
EF	f2 = 2.55 Hz f6 = 5.60 Hz f8 = 7.94 Hz	**f1 = 2.36 Hz with torsion** f3 = 2.81 Hz f4 = 3.65 Hz with torsion f5 = 4.35 Hz f7 = 7.86 Hz	

Despite of their geometrical and similar aspect, the impulse responses of the towers show small differences. The difference is less than 0.9 Hz. The gap between the frequency values of the same mode tends to increase with higher modes. This may result either from their various structural stiffness due to the different distribution of what we called the live load in engineering problems (as furniture, light walls, superficial renovations) or it can be related to the presence of SSI effects (Mikael, 2011).

Some modes, especially in the high frequency band, show a non-zero motion at the base of the building (Figure 52 A-f4, A-f7, B-f7, B-f8, C-f5, C-f6, C-f7, C-f8, D-f6, D-f7, D-f8). According to Michel (2007), this motion can be explained by the recording of the global soil-structure system and not only of the building impulse response. The torsion modes (mode 3 and mode 6) are characterized by the participation of bending modes on both horizontal directions.

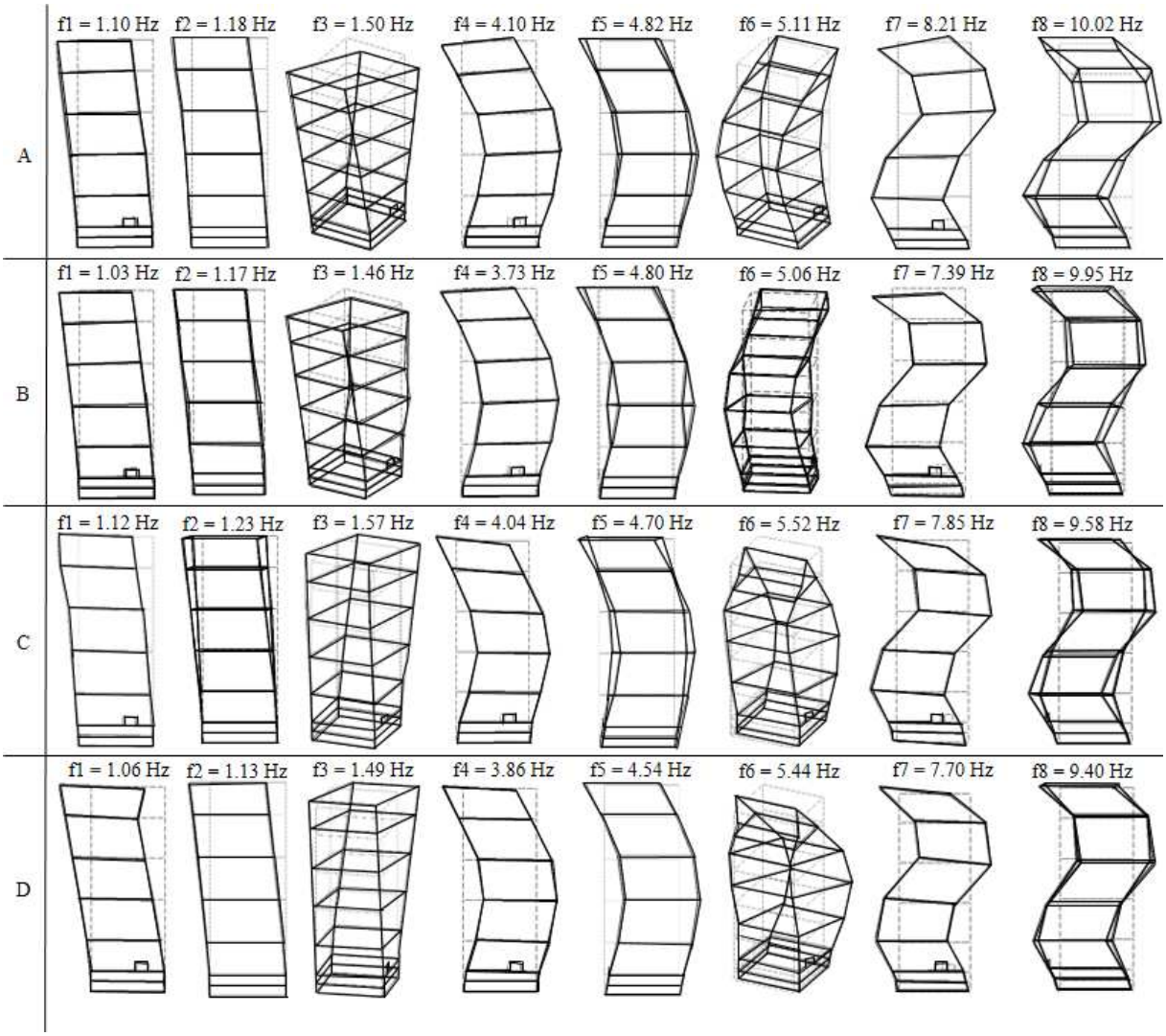

Figure 52: Observed mode shapes for the towers A (top line), B (second line), C (third line) and D (bottom line) of the residential compound.

Considering the building E alone (top part in Figure 53), the structure shows complex mode shapes combining bending and torsion behaviors. These behaviors are expected for a building having irregularities in plan as in the case of the connected buildings E and F. Considering the building F alone (middle part in Figure 53), the structure seems to have only bending deformation in the longitudinal direction with slight torsion in higher modes. Compared to the towers, the embedding of the underground levels for both buildings are clearly observed by a zero-displacement of this section for most of the mode shapes.

When the buildings are studied together considering that the two structures are linked (seismic joint not playing its role), the mode shape interpretation gets easier. The mode of the coupled system occurs at the same frequency than the ones of the independent structures (Table 23). For example, the first mode occurs at 2.36 Hz that corresponds as well to the first mode of the

buildings E and F. Comparing the modes between the different systems, we obtain similar mode shapes for the most of them between the ones of the independent building E and the ones of the coupled system with value close to 100% of similarities (Figure 53 and Table 23). On the contrary, the deformation is different for the building F with lower modal assurance criterion (MAC) value not exceeding 50% for all modes. In fact, even if the first mode of the building F seems to coincide with the first mode of the coupled system considering only this building, the difference in motion appears to reach only 0.3%. This suggests that there is a strong interaction between the low-rise buildings (at least under ambient vibration) and that the highest building (E) controls part of the deformation of the building F.

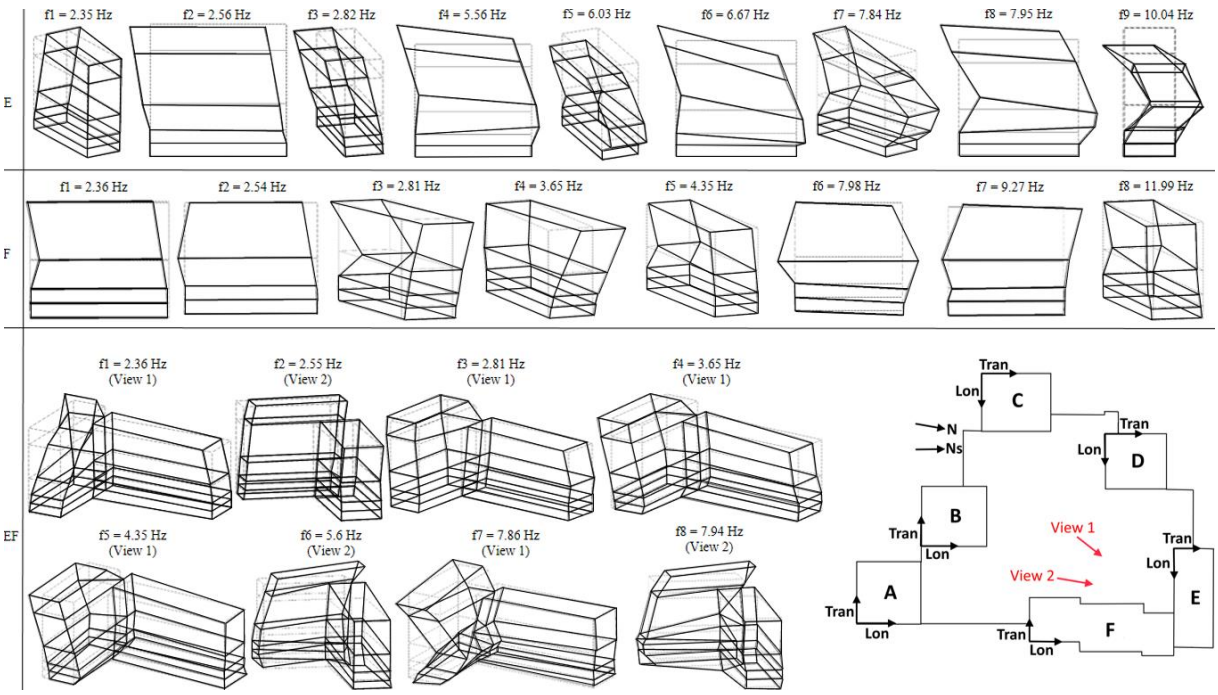

Figure 53: Observed mode shape for building E (top part), building F (middle part) and both buildings rigidly connected considering the sensor at the top of the building E as reference (bottom part). On the scheme, the arrow "N" indicates the geographic north and the arrow "Ns" indicates the north component of the sensors.

Table 23: Difference in mode shapes between independent buildings E and F and the coupled system and cross-modal assurance criterion (MAC).

	E		F		Coupled system EF				MAC (%)	
Mode	***f* (Hz)**	**Dir**	***f* (Hz)**	**Dir**	**Mode n°**	***f* (Hz)**	**Dir. (E)**	**Dir. (F)**	**E/EF**	**F/EF**
1	2.35	T	2.36	L	**1**	2.36	T	T	99.9	0.3
2	2.56	L	2.54	L	**2**	2.55	L	L	100.0	13.8
3	2.82	T	2.81	T	**3**	2.81	T	T	99.9	31.0
4	5.56	L	3.65	T	**4**	3.65	L	L	48.6	13.1
5	6.03	T	4.35	T	**5**	4.35	L	T	8.0	47.1
6	6.67	L	/	/	**6**	5.60	T	/	8.1	/
7	7.84	T	/	/	**7**	7.86	T	/	100	/
8	7.95	L	7.98	L	**8**	7.94	L	T	100	33.4

III.4.1.3 Real data versus theoretical modes

The comparison of the empirical mode shapes with the theoretical ones can provide a first idea on how the building behaves: is it a shear type or a bending type? The type of behavior has influence on the SSI. The bending beam model mainly differs from the shear beam model as the SSI is greater when the slenderness decrease. This was also observed in the Chapter II. The comparison of the theoretical modes to the observed ones are presented in Figure 54 and quantified in Table 24. According to the MAC values, the first and second modes of the towers present high similarities with the three theoretical models with MAC value more than 90%. The difference between modes tends to increase with higher mode for all the comparisons. However, since the fourth mode, the difference increases drastically for the shear beam and Timoshenko beam comparisons going from MAC values of 90% to 70% whereas the ones for the cantilever beam remains mostly above 80%. Therefore, the cantilever beam mode shape seems to be the closest theoretical mode of the observed modes of the towers (Table 24).

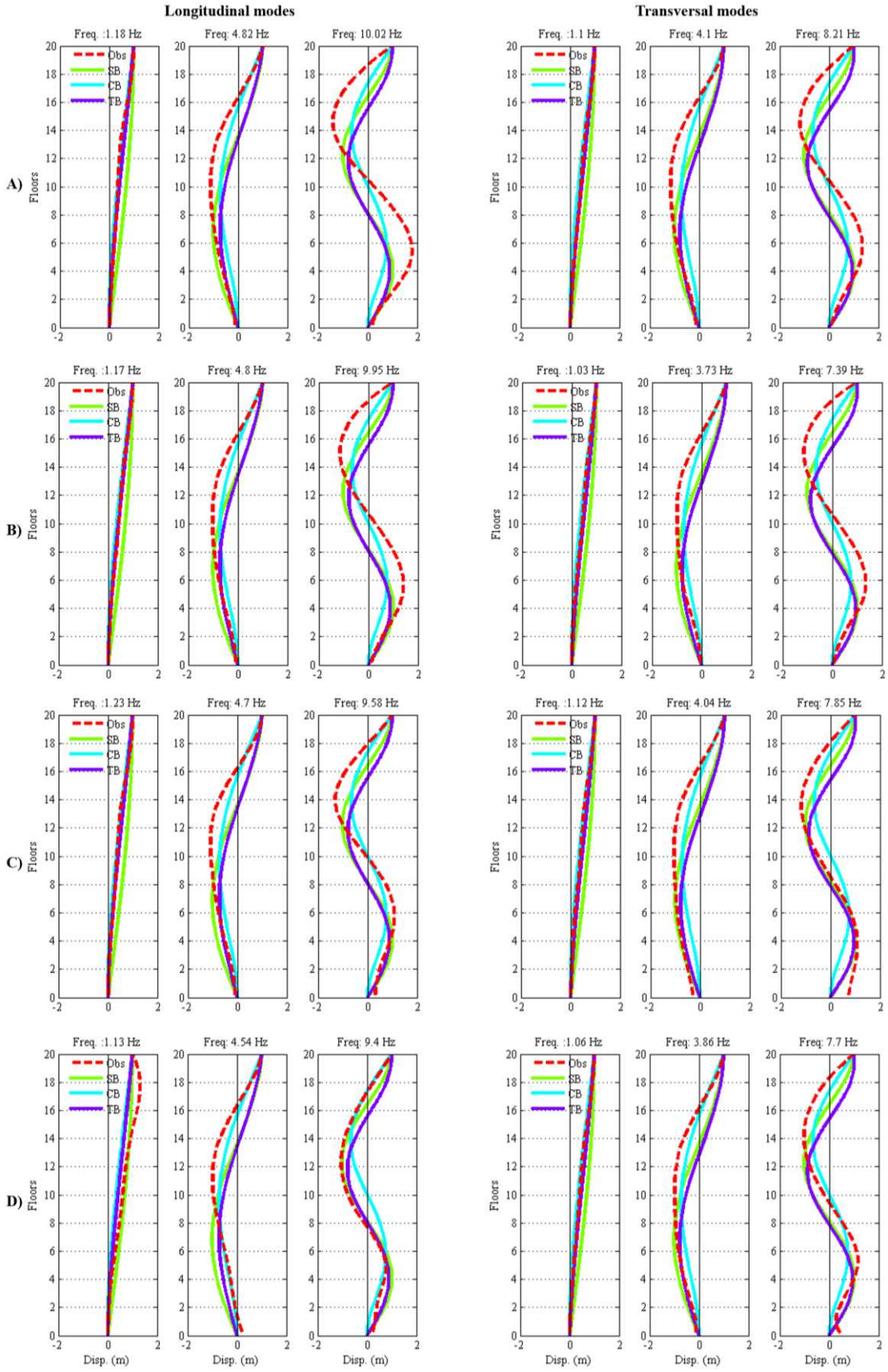

Figure 54: Theoretical mode shapes (shear beam (SB), cantilever beam (CB), Timoshenko beam (TB)) compared to the observed one of towers A, B, C and D of the residential compound for the first three longitudinal (left) and transverse (right) modes.

Table 24: Cross-modal assurance criterion (MAC) for the comparison between theoretical modes and observed modes of the instrumented towers of the residential compound (shear beam (SB), cantilever beam (CB), Timoshenko beam (TB)).

			MAC (%)		
	Mode	**Dir.**	**SB**	**CB**	**TB**
A	1	T	96.0	99.1	99.7
	2	L	93.1	99.0	98.9
	4	T	70.2	94.0	53.2
	5	L	70.8	93.9	62.2
	7	T	52.0	88.6	30.0
	8	L	51.1	84.8	34.2
B	1	T	95.3	99.4	99.6
	2	L	95.7	99.3	99.9
	4	T	67.5	94.8	51.2
	5	L	68.4	95.0	60.8
	7	T	43.1	83.1	22.2
	8	L	45.1	83.0	29.0
C	1	T	94.6	99.6	99.4
	2	L	93.5	99.4	99.3
	4	T	71.9	90.4	54.5
	5	L	67.7	95.4	61.0
	7	T	81.4	73.4	58.4
	8	L	68.1	92.7	49.1
D	1	T	95.2	99.4	99.5
	2	L	96.0	98.1	99.1
	4	T	74.5	96.0	58.5
	5	L	56.4	92.5	52.0
	7	T	68.9	89.3	44.6
	8	L	91.4	65.1	77.0

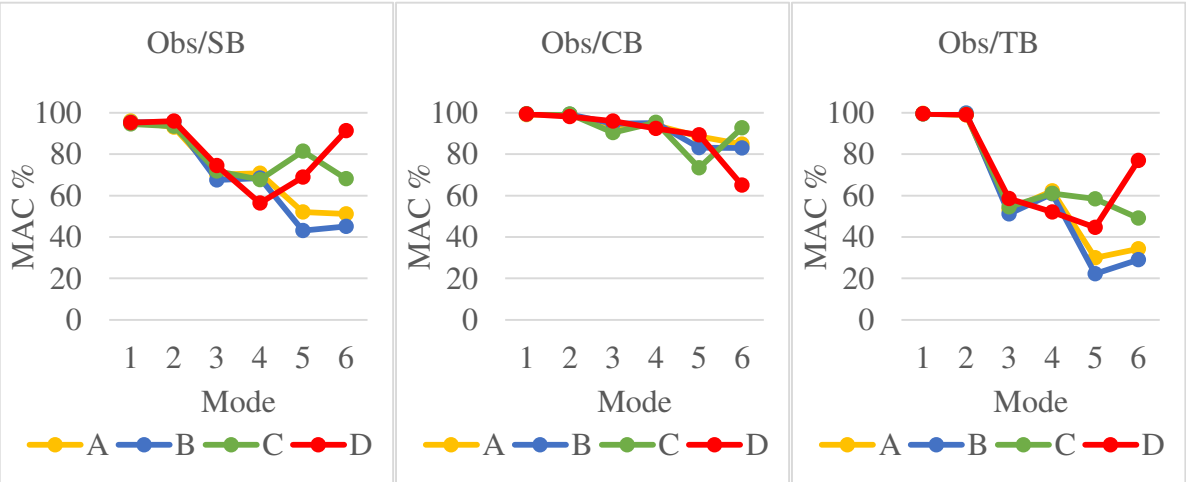

III.4.1.4 Damping

The damping of each building of the residential compound is computed for one setup at the first natural frequency using the RD computation scheme proposed by Clough and Penzien (1993) (see Chapter I). The obtained results are compared with the damping computed using the literature relationships to observe possible SSI. These empirical methods all consider either the shape of the building or the frequency of the first mode shape.

Jeary (1986) and Dunand (2005) advise to have at least 500 signal time windows to obtain the complete RD functions of the building and to better estimate the damping value. Here the number of windows varies among the different setups but is between 1513 and 1651 windows for towers and 3428 and 3719 windows for buildings E and F.

One limitation of the method proposed by Clough and Penzien (1993) is the definition of the linear regression. The coefficients are indeed depending on how many periods (T) are considered and vary also according to the first periods considered for the computation. A detailed study of the possible errors of this method is presented below considering the results of the five buildings (Figure 55). The error is computed as $2 * \Delta P$ where ΔP is the standard deviation of the linear regression.

Figure 55 presents the study of the sensitivity of the damping value to the number of periods considered in the linear regression and obtained from 30s overlapping time windows. It is shown that the damping values increase with the number of periods in the case of the towers. The errors of the linear regression remain low (under 0.2). For low-rise buildings, the variation of the damping values with larger number of periods shows that the damping values decrease drastically after a maximum of 1.98% (30T) for building E and 2.74% (20T) for building F. Compared to the high-rise buildings, the errors of the linear regression tend to exponentially increase with the number of periods considered for low-rise structures.

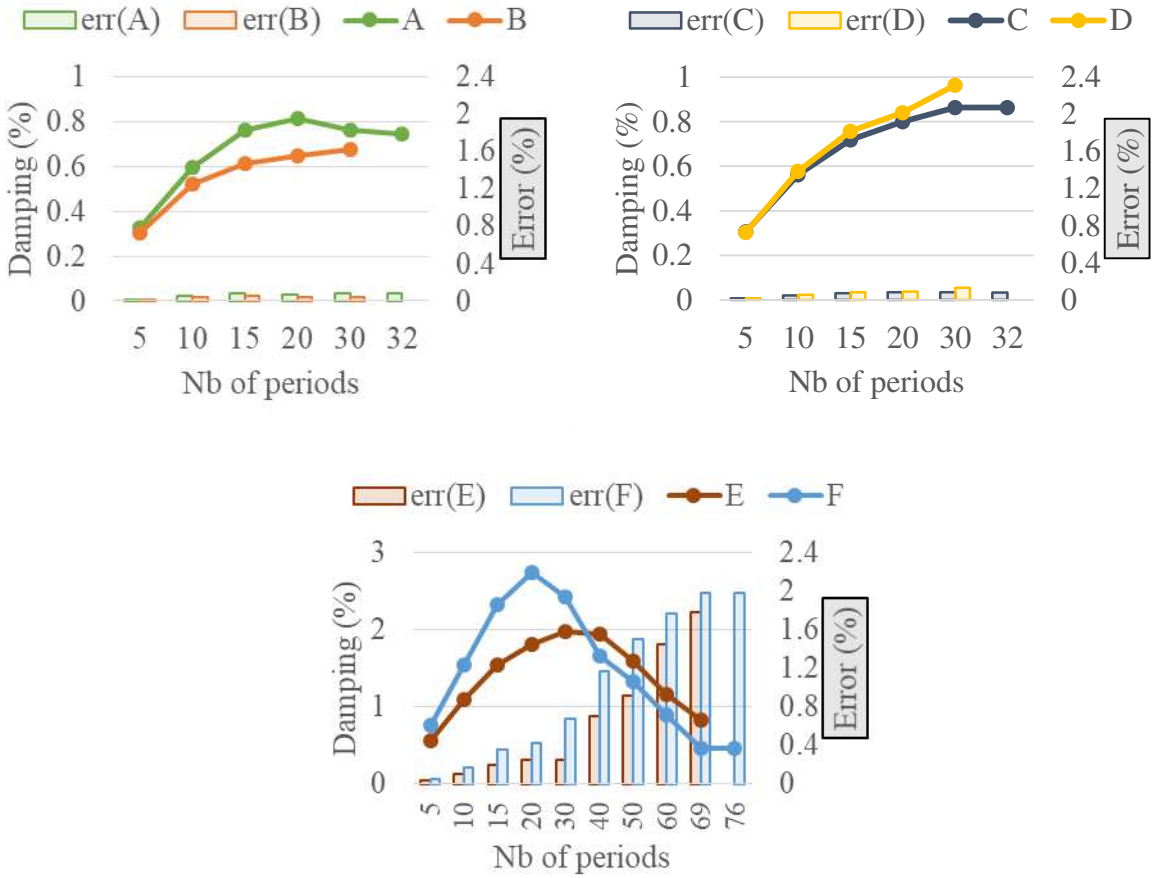

Figure 55: Damping estimation and linear regression error from the relation proposed by Clough and Penzien (1993) as function of the number of periods selected in the random decrement functions for one setup.

Maximal values of damping found using the Clough and Penzien (1993) method (Table 25) are compared to damping estimations based on empirical relationships and *Geopsy* software (Table 26). We can note that, compared to the 5% value considered in the Eurocode 8 building regulation code (CEN, 2003), the damping value of the buildings are very low, especially for high-rise buildings. This leads in an overestimation of the damping value in the construction of new buildings.

Table 25: Maximal damping estimations (ζ) for each building of the residential compound using the Clough and Penzien (1993) technique. The relative error of the linear regression and the number of period (T) considered to estimate the damping value are also indicated.

	A	B	C	D	E	F
Max ξ (%)	0.81	0.67	0.86	0.97	1.98	2.74
Err (%)	0.07	0.04	0.08	0.13	0.25	0.42
Nb of T	20	30	32	30	30	20

Table 26: Comparison of the damping values estimated from different empirical relationships for one setup in the instrumented residential compound. ΔP is the standard deviation from the linear regression in the method of Clough and Penzien (1993).

			Empirical relationships				From in-situ measurements in Nice	
	Building		**Jeary (1986)**	**Lagomarsino (1993)**	**Satake et al. (2003)**	**Dunand (2005)**	**Geopsy**	**Clough and Penzien (1993)**
ξ (%)	**High-rise**	**A**	0.81	1.42	1.36	1.27	0.57	0.81
		B	0.81	1.42	1.28	1.24	0.64	0.67
		C	0.81	1.43	1.40	1.29	0.97	0.86
		D	0.81	1.42	1.32	1.26	0.64	0.97
	Low-rise	**E**	/	1.95	3.11	2.15	4.98	1.98
		F	/	1.93	3.07	2.13	2.72	2.74

The analysis of recordings in the towers shows that the damping value varies between 0.5% and 1%. The damping of the building E is slightly different than the one of the building F and both values are higher than the damping of the towers.

The Table 26 shows that the damping estimations are depending on the method. For the towers, the damping varies between 0.57% and 1.47% and for the low-rise buildings, the damping varies between 1.93% and 4.98%. Depending on the method, the results vary at the maximum from 39% in accordance with the maximum obtained damping for the studied group of buildings. Considering the variety of the dataset used to define each empirical law for the estimation of damping, the variation in the damping results is assumed to be negligible.

Jeary's formula (Jeary, 1986) provides the same damping value for all towers. The method is only valid for high-rise structures that is why there is no information for buildings E and F in the Table 26. Lagomarsino's formula (Lagomarsino, 1993) provides similar damping value for the towers and very close damping value for low-rise buildings. Standard error in the damping estimation for A, B, C, D, E and F instrumented buildings can be estimated according to the proposed confidence range in Lagomarsino (1993) and is equal to $^{+}/_{-}$ 1% for having 50% of

confidence. The same trend is observed for Satake et al.'s formula (Satake et al., 2003) and Dunand's formula (Dunand, 2005).

All methods show that the damping values of the towers are close. The same observation is found for the buildings E and F except from the in-situ measurement (results from *Geopsy* and those from the Clough and Penzien's formula). Moreover, the estimation of damping values of slender and high structures is well constrained whatever the empirical relationship. It is interesting to note that, for the towers, the damping values found with Jeary's formula is the closest to the one found with the Clough and Penzien's method. The characteristic of the Jeary's formula is that the resulting damping is not linked to specific SSI. Therefore, the damping parameter is not a significant parameter to study SSI for these buildings.

Damping estimation for the low-rise buildings shows that this parameter is always higher than the ones of the towers. These results are surprising in the way that lower buildings are generally stiffer than higher buildings. Moreover, buildings E and F have a larger surface embedded in the slab and they are linked making these two elements even stiffer. Then, the expected damping values should be lower. This observation raises a question about the relevancy of the procedures presented above for low-rise buildings. The study of the damping sensitivity to the number of the considered periods showed that, in the case of low-rise buildings, the total number of periods selected in the RD functions should not be taken into account in the assessment of the damping. This error may lead to underestimate this parameter.

The estimation of the damping in structures is variable and presents a lot of uncertainty regardless the approach used. First the quality of recordings is significant for the precision of the parameter evaluation. Recordings need to be stationary and long enough to ensure a large number of signal windows to better approach the true value of the damping ratio (Jeary, 1986; Dunand, 2005).

Second the analysis should be performed with care to select the right frequency of each mode. Indeed, this parameter is needed in some empirical laws for the damping estimation (e.g. Clough and Penzien, 1993; Lagomarsino, 1993; Satake et al., 2003; Dunand, 2005). The coupling of resonance modes can be source of error as well. Close resonance modes can lead to overestimate damping ratio value. It was shown also that the number of periods selected in the RD functions can lead to underestimate the damping value of the building.

III.4.2. Seismic wave velocity

The seismic wave velocity is estimated in the towers of the residential compound using the deconvolution interferometry approach (Snieder and Şafak, 2006). The length of the signals is 1800s with 250 Hz frequency sampling. The signals are first filtered between 0.5 and 10 Hz using a Butterworth bandpass before applying the deconvolution process (Figure 56).

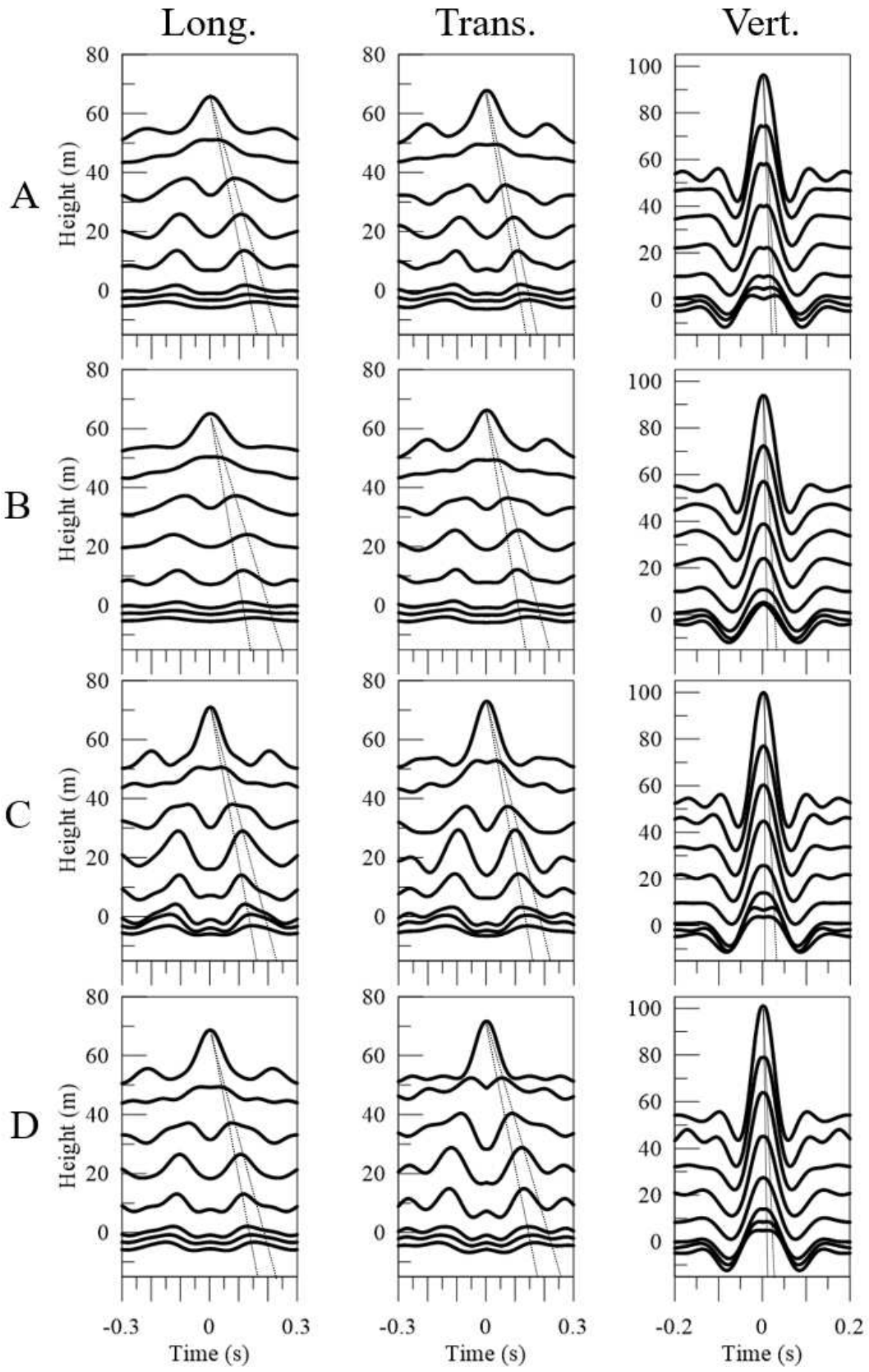

Figure 56: Impulse response functions from recordings in the towers of the residential compound for the transversal, longitudinal and vertical components for all setups. Dashed lines indicated the picked propagation velocity.

The average V_s in both directions are estimated between 300 m.s^{-1} and 320 m.s^{-1} for the longitudinal component and between 270 and 370 m.s^{-1} for the transversal component depending on the towers. The standard deviation of the V_s is well constrained between 100 m.s^{-1} and 130 m.s^{-1}. The estimated V_s in the towers is lower than the one found by Fernandez Lorenzo (2016) for the Nice Prefecture building from ambient vibration records (V_s = 540 m.s^{-1} in the transverse direction and V_s = 490 m.s^{-1} in the longitudinal direction). The compressional seismic wave velocity (V_p) is about 3350 m.s^{-1} with a standard deviation of 2800 m.s^{-1}.

These results are compared to the seismic wave velocity computed from the formula proposed by Michel and Guéguen (2018) presented in Chapter I, for the same structures. The height H and the $\chi_T(C)$ coefficient are the same for all towers and equals to 57 m and 0.5 respectively. The V_s is computed for each horizontal component and for the minimal and maximal first natural frequency among all the towers. The computation of the V_s using this formula shows that the velocity value is higher than the one found by deconvolution interferometry method from ambient vibration data (around 300 m.s^{-1}) (Table 27).

Table 27: Estimated V_s from impulse response functions from recordings in the towers and from the relationship proposed by Michel and Guéguen (2018).

	From IRF		From Michel and Guéguen (2018)			
	Transversal	Longitudinal	Transversal		Longitudinal	
	V_s (m/s)	V_s (m/s)	f (Hz)	V_s (m/s)	f (Hz)	V_s (m/s)
Minimal	270	300	1.03	470	1.13	515
Maximal	370	320	1.12	510	1.23	560

III.5. Soil-structure interaction investigation

III.5.1. Rocking motion at the base of the residential compound

As for the single tower, we propose to analyze the rocking motion of the slab of the residential compound using the rocking spectral ratio presented in the Chapter I. The parameters used to calculate the rocking spectral ratio are the same than the ones used in the analysis of the single tower (30s overlapping (5%) time windows and same value for STA/LTA ratio).

The spectrum is computed from the vertical component, first at the 2nd underground level and second between the sensors on the slab. Two couples of sensors recorded simultaneously ambient vibration at the 2nd underground level as shown in Figure 57. A couple is chosen such

as the two sensors are located at opposite sides of the underground. The setup performed outside the structures (yellow filled triangles in Figure 45) made possible the computation of three rocking spectral ratio at the slab level. The results are presented in Figure 57 and Figure 58.

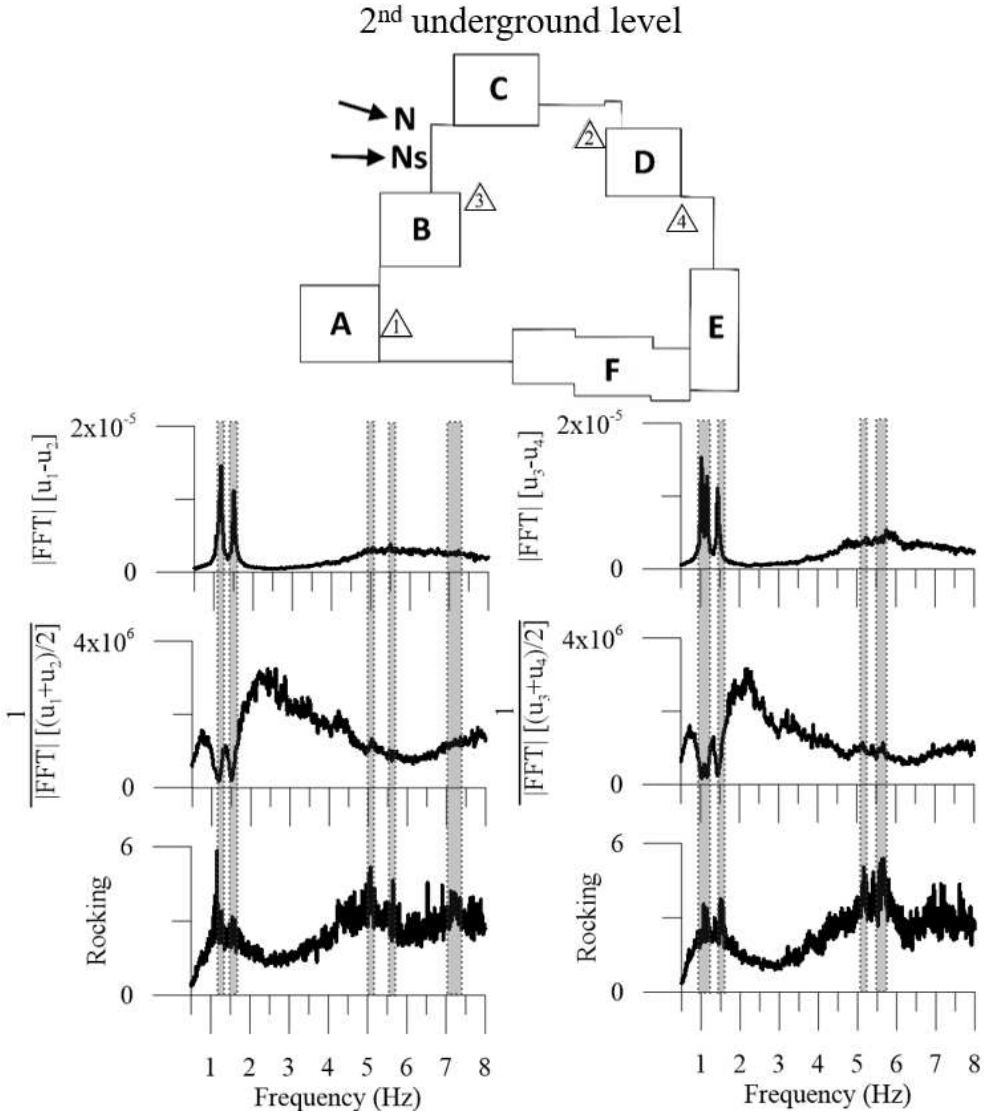

Figure 57: Rocking spectral ratio of the sensors located at the 2nd underground level computed between sensors 1 – 2 and 3 – 4. The rocking effect is highlighted at 1 – 1.4 Hz, 1.4 – 1.6 Hz, around 5 Hz, at 5 – 5.2 Hz and at 5.5 – 5.8 Hz for the couples of sensors; at 7.1 – 7.3 Hz for the couple 1 – 2. On the scheme, the arrow "N" indicates the geographic north and the arrow "Ns" indicates the north component of the sensors.

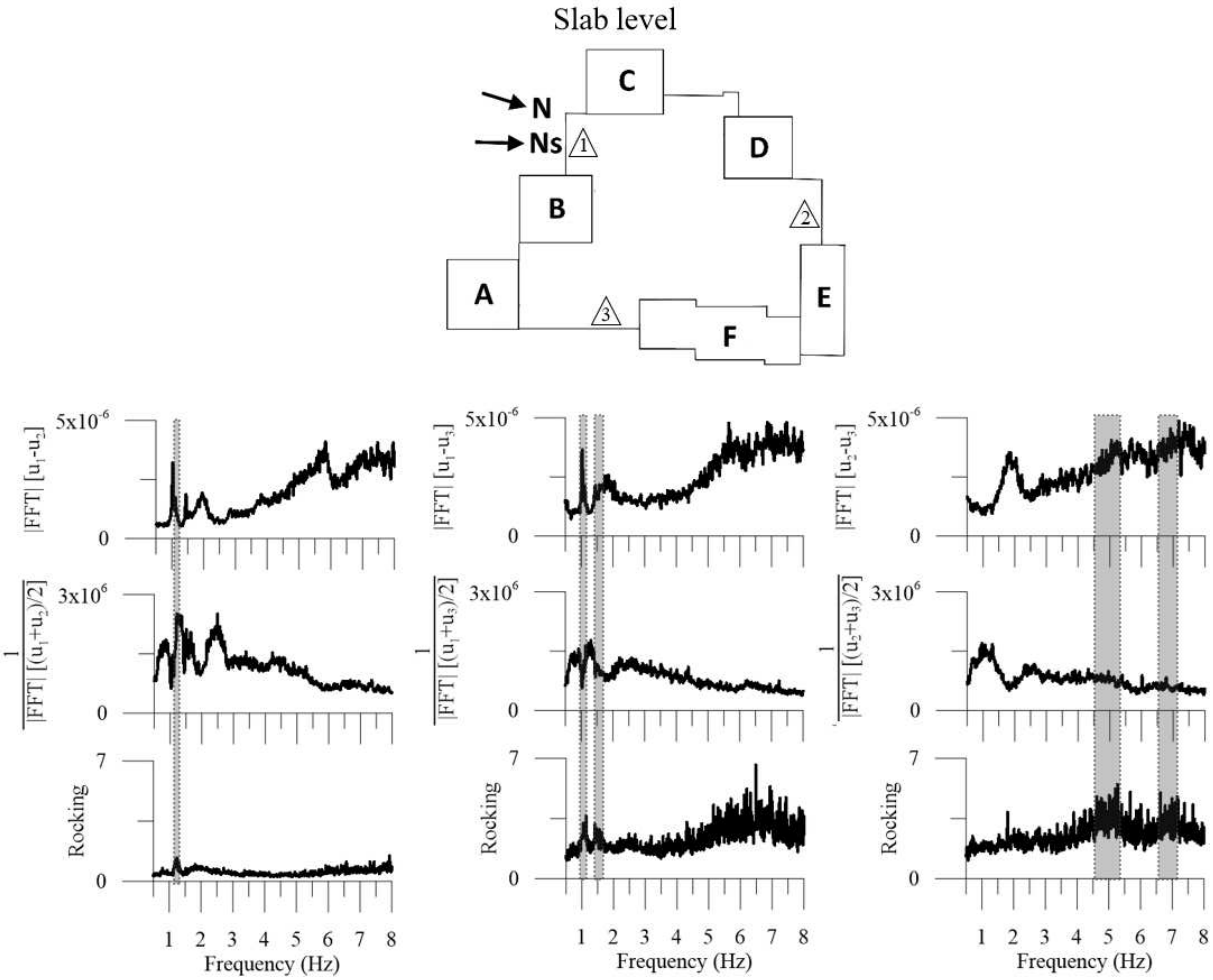

Figure 58: Rocking spectral ratio of the sensors located on the slab outside the buildings computed between sensors 1 – 2, 1 – 3 and 2 – 3. The rocking effect is highlighted at 1 – 1.4 Hz for couples 1 – 2 and 1 – 3; at 1.4 – 1.6 Hz for couples 1 – 3. On the scheme, the arrow "N" indicates the geographic north and the arrow "Ns" indicates the north component of the sensors.

The analysis of the rocking spectral ratio at the 2nd underground level (Figure 57) shows, for all the couples of sensors, clear peaks at 1 – 1.4 Hz and 1.4 – 1.6 Hz and several close peaks are observed at 5 – 5.2 Hz and 5.5 – 5.8 Hz. For the sensors 1 – 2, a supplementary peak is noted at 7.1 – 7.3 Hz. The first two peaks are also clearly observed in the Fourier spectrum of the average and of the difference of the signals and are closed to the fundamental frequencies of the towers A, B, C and D (f_1=1 Hz, f_2=1.1 Hz, f_3=1.5 Hz). The other peaks in higher frequencies are not well distinguished in the Fourier spectrum of the average and of the difference of the signals. However, we may identify them on the rocking spectral ratio. At the slab level (Figure 58), peaks are observed at 1 – 1.4 Hz for couples of sensors 1 – 2 and 1 – 3 and at 1.4 – 1.6 Hz for the pair of sensors 1 – 3. These peaks are also identified in both Fourier spectra of the rocking spectral ratio. For the comparison of sensors 2 – 3, large peaks are highlighted at 4.7 – 5.3 Hz and 6.5 – 7.3 Hz on the rocking spectral ratio. We note that the Fourier spectra of the

average and of the difference of the signals show high peak amplitude around 1.8 Hz (corresponding to the f_{s0} measured at this position (Rohmer et al., 2020)) but no peak is observed on the rocking spectral ratio.

Looking at the results, we can easily link the peaks of the rocking spectral ratio between 1 and 1.6 Hz to the first three modes of the towers (1 Hz, 1.1 Hz and 1.5 Hz the first mode of torsion). Therefore, we may expect differences in vertical motions on either side of the slab in phase opposition. It means that, for example, when the vertical motion at sensor 1 reaches a maximum amplitude, at the same time, the vertical motion at sensor 3 is reaching a minimum. These observations support the presence of SSSI within the residential compound. The other observed modes of the towers and of the low-rise buildings are not well distinguished in the rocking spectral ratio. As seen in the analysis of the rocking motion at the base of the Nice prefecture (see Chapter II) and in the single tower, the identification of peaks may be easier with longer signal duration (a few hours) because of the smoothing of the mean curve.

Large peaks observed at high frequency range between 4.7 – 5.3 Hz and 6.5 – 7.3 Hz are not related to any observed building modes. These peaks are noted, for 4.7 – 5.3 Hz at the slab level only, and for 6.5 – 7.3 Hz at both levels. Consequently, we suppose that the vertical differential motions identified at these frequencies express rocking effects of the slab translating a strong SSI with the surrounding soil.

III.5.2. Ground motion

The free field is generally considered as a site far enough from constructions to not feel their effects on the recorded vibration. These free field recordings can thus be interpreted in term of the ground motion without being perturbed by the buildings nor the presence of any foundations. Wong and Trifunac (1975) showed that the scattering of incident waves due to the foundation can induce a significant modification in the free field motion. The coupling effect between SSI and the trapping of the surface waves in the superficial soil layers may induce kind of wave packages in the shape of spindle up to about a hundred meters away from the structures (Bard et al., 1996). In 2004, the SESAME project (European Commission, 2004) studied through microtremor HVSR the SSI effects and concluded that high-rise structures may modify the HVSR curves by adding frequency peaks induced by the SSI. In that way, we analyze the spatial variability of the ambient vibration data performed all around the residential compound.

We used the same calculating parameters than in the modal analysis of the single tower. The microtremor HVSR computed at each measurement point are spatially presented in Figure 59. Figures of each HVSR with better image resolution can be found in Appendix 3. Here, we are looking in detail at the frequency content of the recordings and the shape of HVSR. However, for some recordings, only few stationary windows are found and analyzed leading in some uncertainties in the result at these points (curves 3, 12, 15 and 17 on the Figure 59).

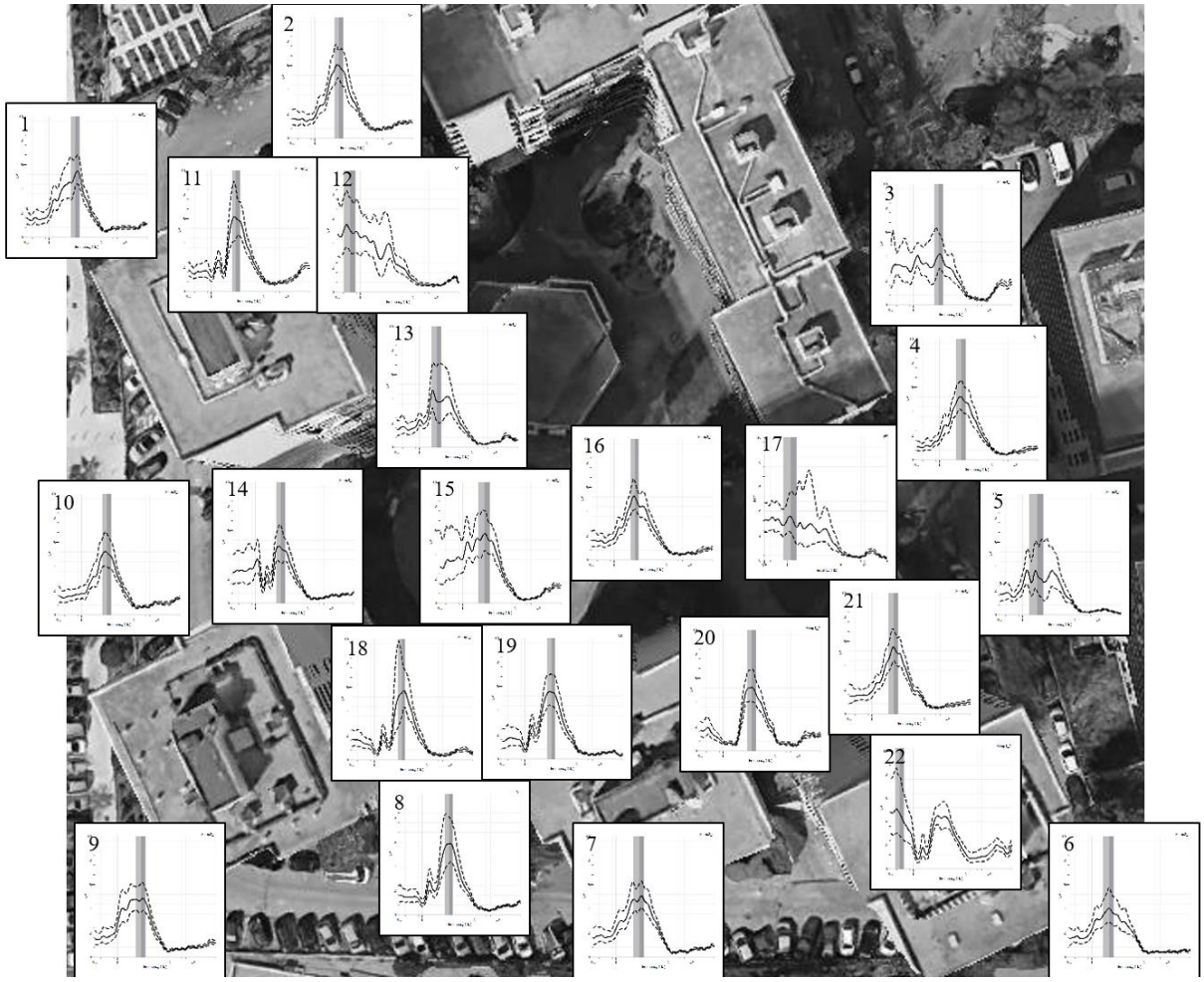

Figure 59: Spatial distribution of HVSR computed at each measurement point on the slab of the residential compound and around.

Thanks to a dense and large instrumentation campaign, we studied the influence of the presence of buildings on the HVSR in terms of the frequency (Figure 60), the frequency gap between two peaks (Figure 61), the peak width (Figure 62) and the maximum amplitude of the peak (Figure 63). In the data analysis, we will see that all HVSR present double peaks. Thus, we called f_1 the first frequency peak and f_2 the second one. The frequency peak width is evaluated as function of the half of the maximum amplitude of f_2 in HVSR. The frequency peak gap is estimated between the maximum of both peaks. The curves computed using only a few of

windows are classify as “NaN” result on the different figures and are not considered in the further analysis.

We expect to see the influence of the towers around 1 Hz, the influence of the low-rise building around 2.3 Hz and the ground motion should vary from 1.5 to 2.5 Hz from west to east and from south to north according to the measured f_{s0} in the LVV (Rohmer et al., 2020) (Figure 59).

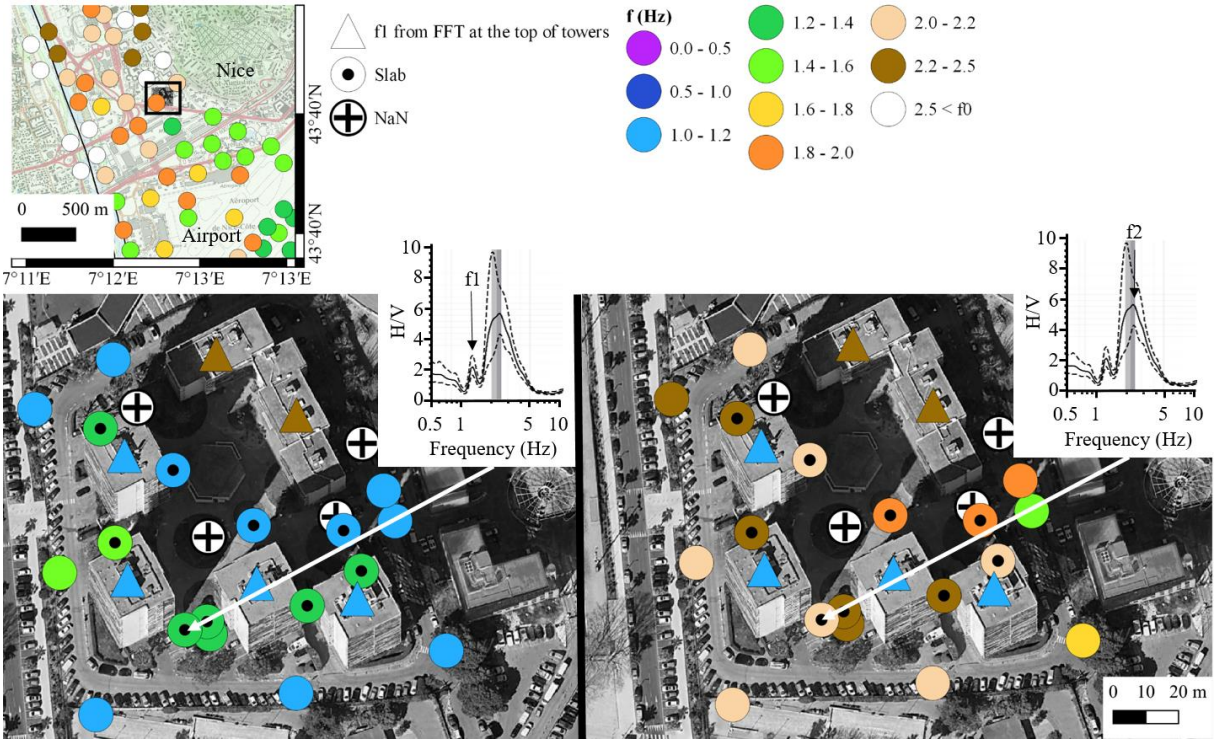

Figure 60: Spatial variability of the frequency peak of the HVSR in the residential compound. The first natural frequency of the towers is indicated in triangle for comparison. The frequency values indicated in the map (top left) come from the ambient vibration campaign performed to build the 3D geotechnical model of the LVV (Rohmer et al., 2020).

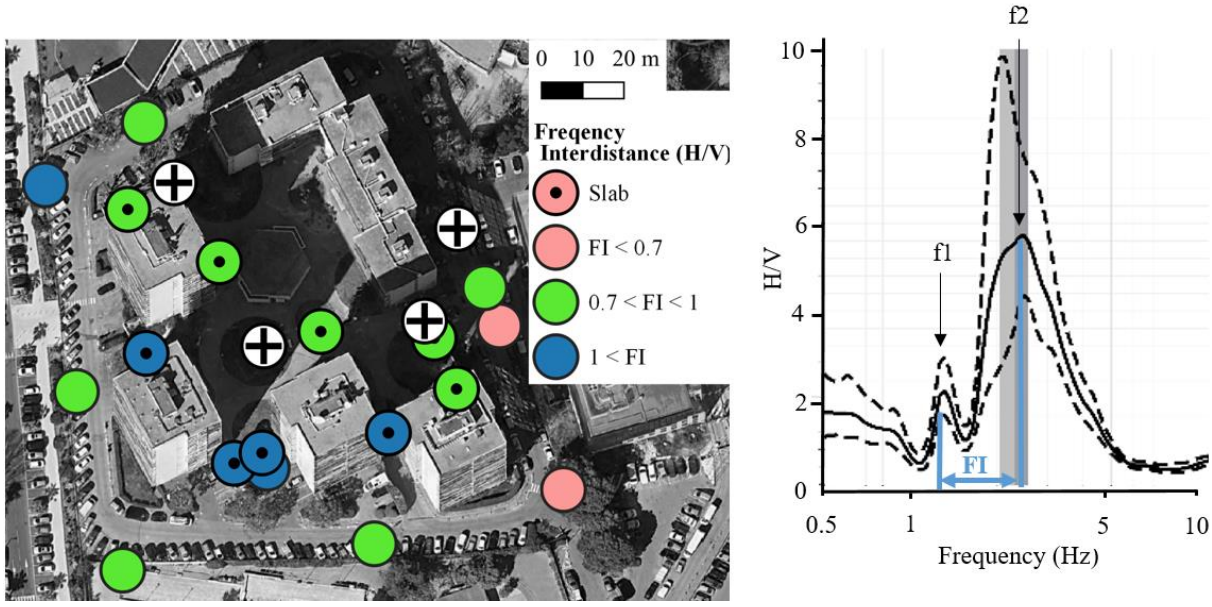

Figure 61: Spatial variability of the frequency peak gap between f_1 and f_2 of HVSR in the residential compound. The frequency peak gap is estimated between the maximum of both peaks and expressed in Hertz. The circles with cross inside indicate unreadable data.

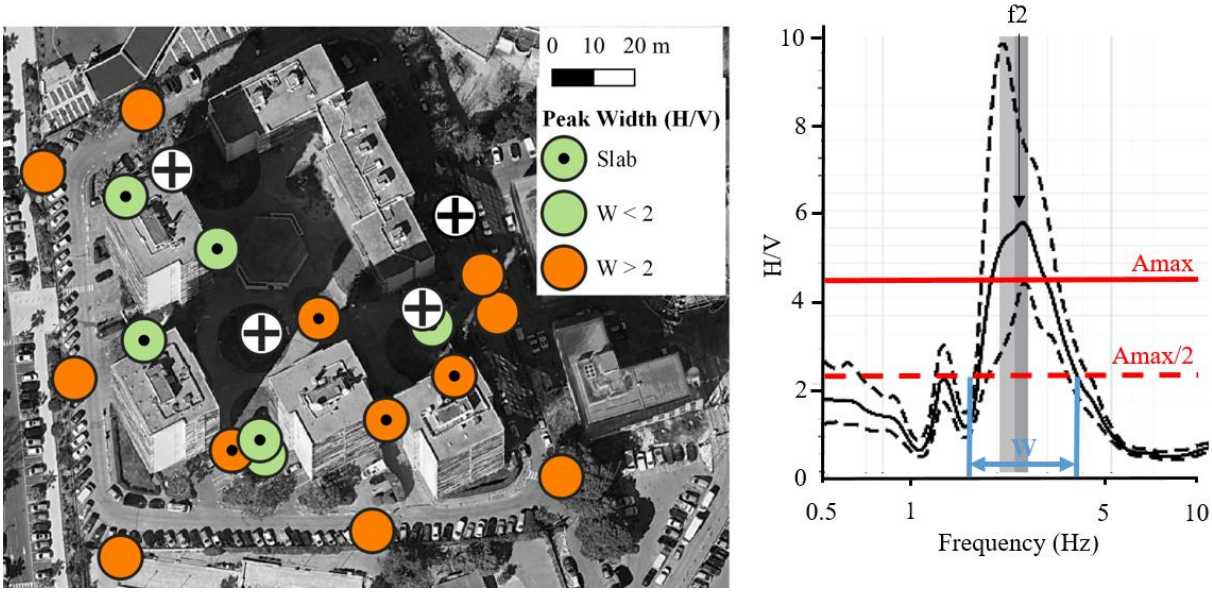

Figure 62: Spatial variability of the frequency peak width (W) of HVSR in the residential compound. The circles with cross inside indicate unreadable data. The frequency peak width is evaluated as function of the half of the maximum amplitude of the f_2 peak of HVSR curves.

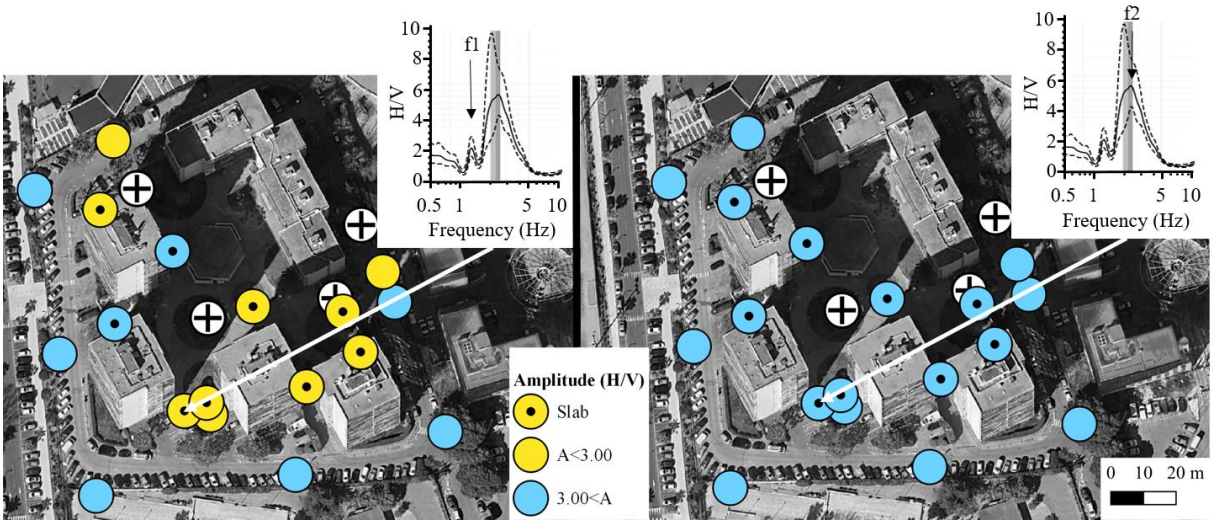

Figure 63: Spatial variability of the maximum amplitude of the HVSR frequency peak in the residential compound. The circles with cross inside indicate unreadable data.

According to the Figure 59, we note that most of the HVSR present double peaks. Based on the Figure 60, we can see that f_1 is around 1 Hz (close to the natural frequency of towers) and f_2 is around 2 Hz (close to f_{s0}). For the analysis of each selected HVSR parameters, both frequency peaks are used as reference. The variability of the frequency value depending on the sensor position is quite low for f_1 which varies from 1 to 1.4 Hz. On the contrary, f_2 shows large variations since it varies from 1.4 to 2.5 Hz. We note that there is not only variability of f_{s0} at large scale within the valley but also at small scale within the residential compound. For sensors located close to the slab edge (Figure 42), the frequency value peaked on the HVSR tends to be higher than for the others.

The Figure 61 presents the frequency gap between two peaks of HVSR. We retrieve a similar tendency to observe variations in the frequency gap between f_1 and f_2 for sensors localized at the slab edge. In fact, the frequency gap tends to be higher at these positions with value above 1 Hz.

A variability in the peak width at 2 Hz is observed on Figure 62. Most of the HVSR present a large peak having more than 2 Hz wide but it seems difficult to extract a particular tendency for this parameter.

The Figure 63 shows the variability in amplitude of the different peaks of HVSR. The maximum peak amplitude around 1 Hz is lower for the sensors located on the slab compared to the one around it. On the contrary, the maximum peak amplitude at 2 Hz is almost similar for both peaks. This can be due to the possible double resonance condition between the soil and the low-

rise buildings having natural frequency of 2.3 Hz. This condition may then amplify the motion at this frequency resulting in higher peak amplitude on HVSR compared to the peak around 1 Hz.

Two profiles across the residential compound are defined to study the variability of the chosen parameters describing the HVSR (Figure 64). One profile goes from north to south of the valley and the other goes from east to west of the valley. They are both 120 m long. Castellaro and Mulargia (2010) concluded, in their study, that the impact of the presence of buildings on the ground motion using microtremor HVSR is not observed after 12 m away from the buildings. In this analysis, we choose to consider points at a maximum distance of 15 m from the profiles.

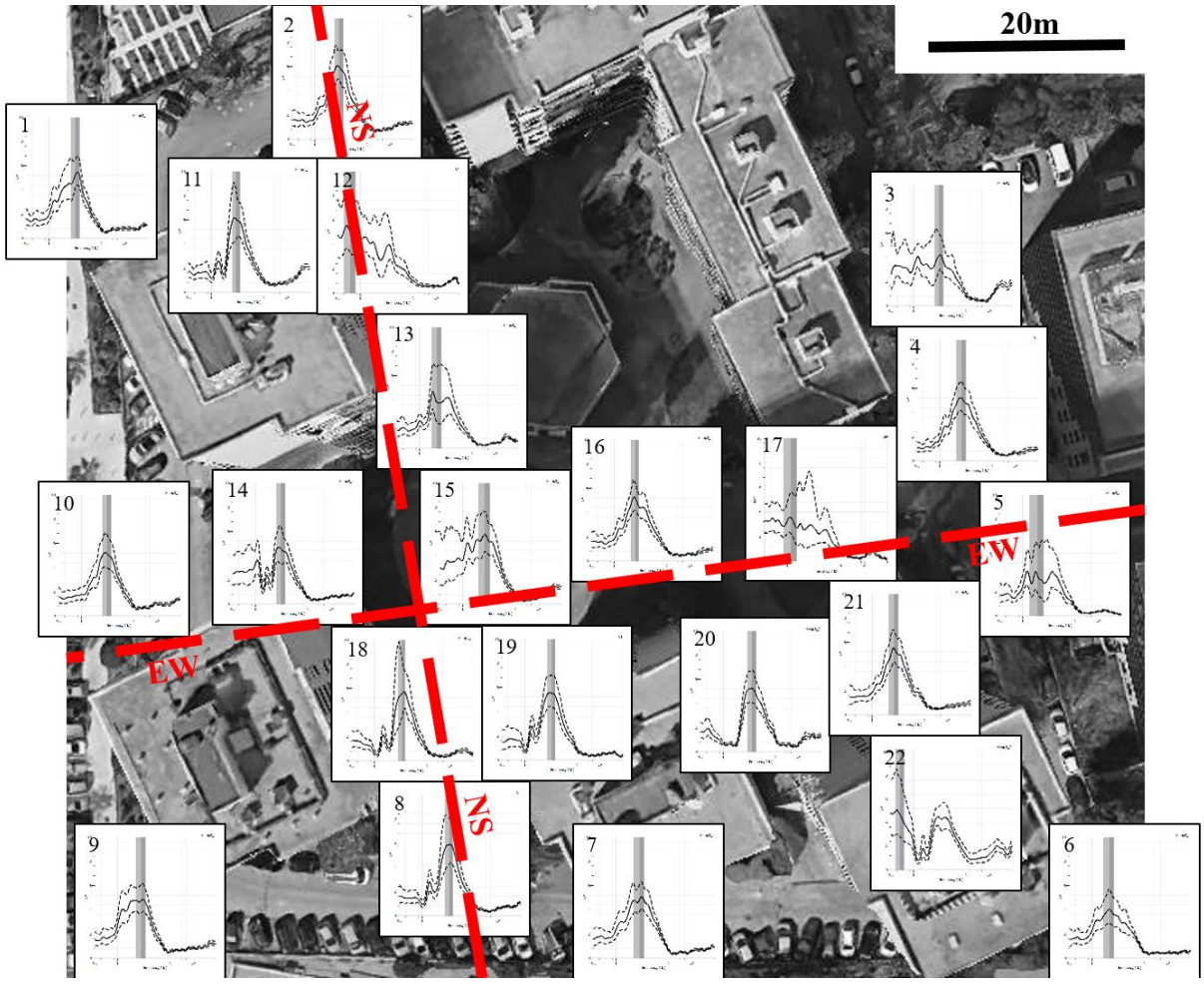

Figure 64: Profiles crossing the residential compound to study the spatial variation of the ground motion.

A tendency in the variation of the HVSR parameters seems difficult to define whatever the parameter (Figure 65). In fact, all of them present no significant variations along both profiles. Their values appear to be well constrained all along the profiles within the residential

compound. For example, even if we observe a decrease of the f_2 value on the East-West profile toward the west, this variation is less than 1 Hz. To refine this analysis, we suggest adding more ambient vibration measurements along the profile in the future.

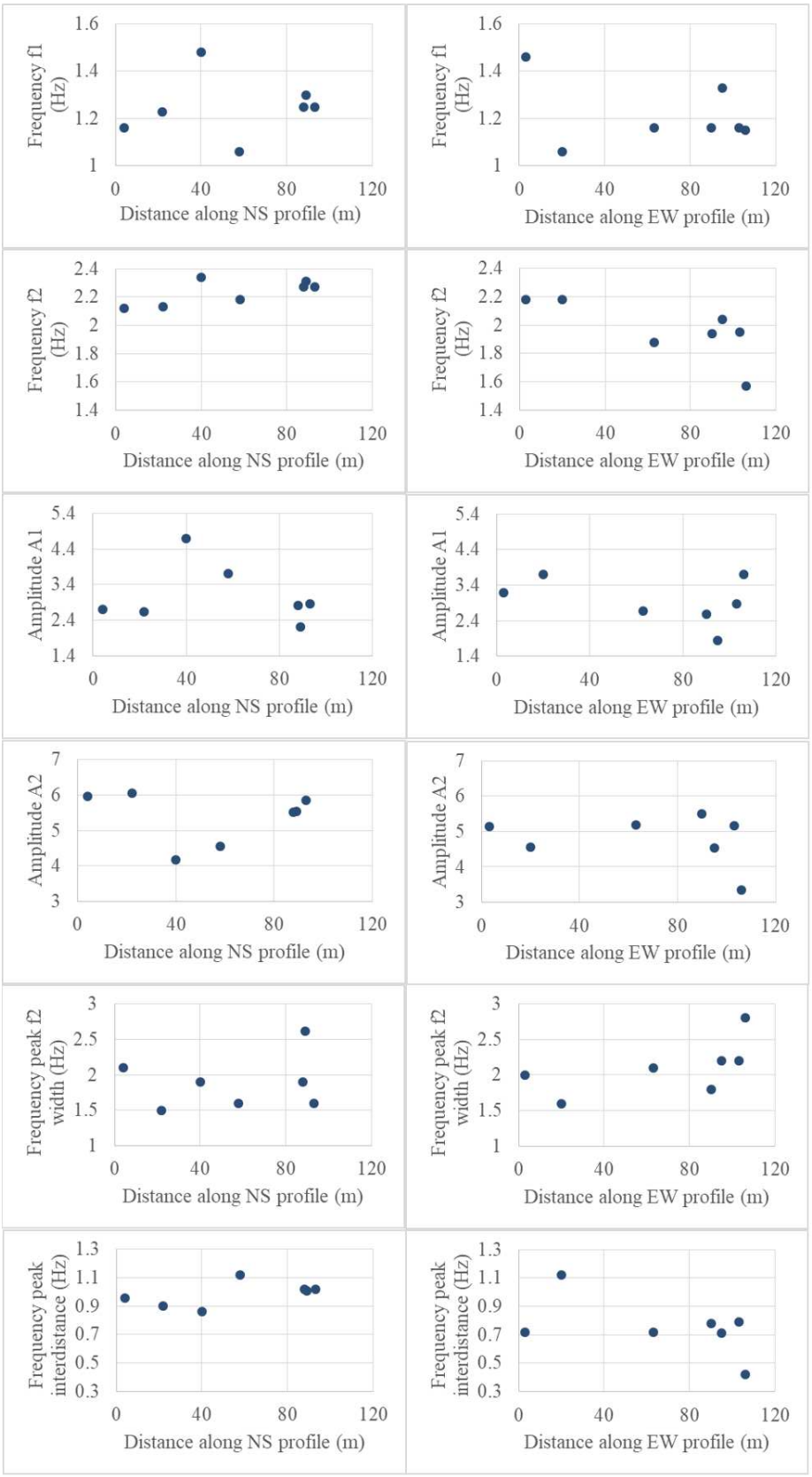

Figure 65: Study of the spatial variability of the HVSR in terms of frequency peak, maximum amplitude of peak, peak width and interdistance frequency peak in the residential compound through North-South and East-West profile crossing the residential compound.

To conclude, in most of the cases, the recordings are sensitive to both the building response and the ground motion. The f_{s0} varies between 1.5 Hz and 2.5 Hz according to the Figure 59 and Figure 60. The peak around 1 Hz is found in all HVSR, it shows that the towers have an influence on the ambient vibration at all recorded locations. For the secondary peak, the conclusion is not so simple since the soil and the E-F buildings have very closed responses, but we may assume that the f_{s0} is not change by the presence of buildings. Besides Kham et al. (2006) observed that the motion in free field tends to keep its resonant frequency despite the presence of buildings.

The analysis of the spatial variability of some parameters describing the HVSR shows that only the frequency value of the peak may give an insight of SSI effects. The peak amplitude, the peak width or the frequency gap between two peaks are not key parameters characterizing the SSI in HVSR. We remark that the study of the peak amplitude around 1 Hz exhibits the fact that the slab tends to attenuate the influence of the seismic response of high-rise structures on the seismic ground motion.

III.6. Structure-soil-structure interaction analysis

Finally, we study SSSI between the towers of the residential compound. To do so, simultaneous records in two distinct towers are used to compute the resonance frequencies and modes of a system composed of towers A and B or C and D linked by the slab (Figure 66). The reference used to normalize the deformation of each structure is taken at the ground floor level in the tower A for the coupled system AB and in the tower C for the coupled system CD. Thus, only one setup is used in this analysis (Figure 42). This imposes a lower discretization of the building mode and therefore a limitation to observe torsion mode. Therefore, we will focus on the flexural bending modes of the towers for the comparison of modes between independent structures and coupled systems. The difference in the mode shape is computed based on the MAC (Table 28).

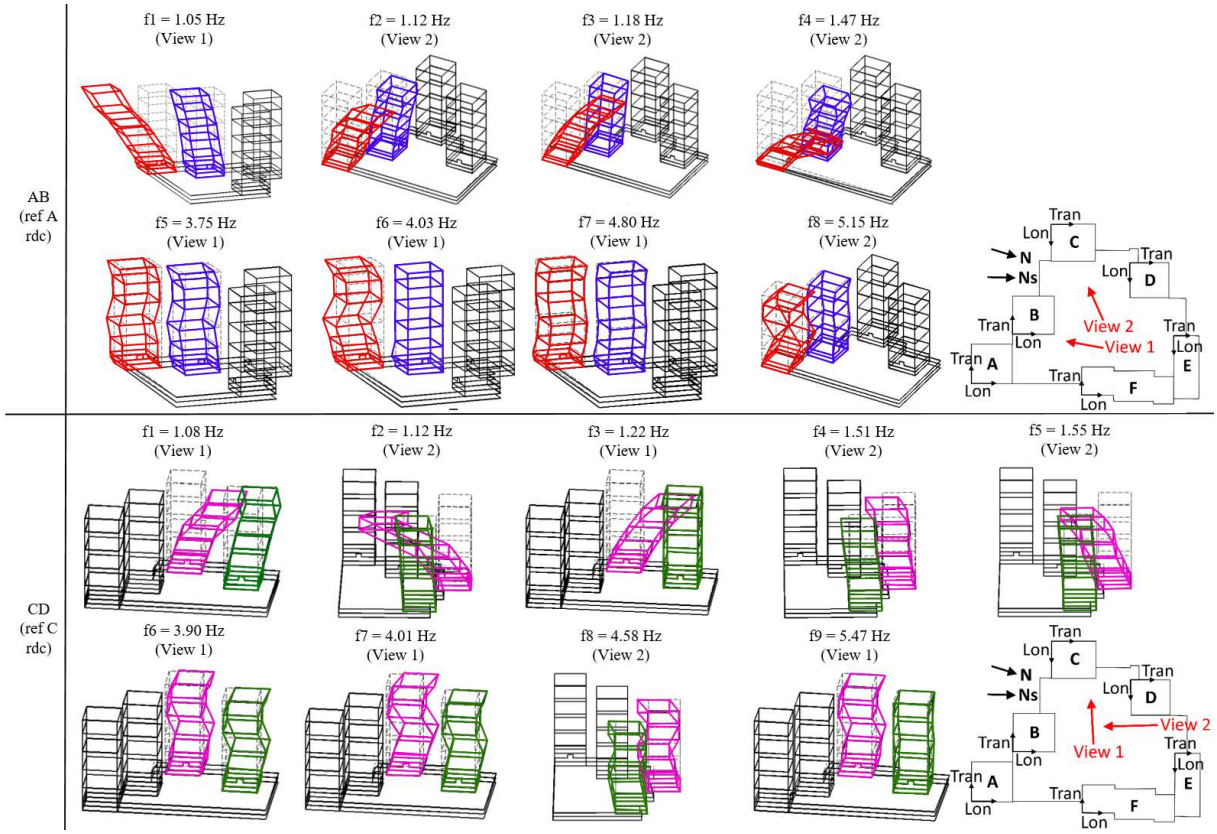

Figure 66: Observed mode shapes from the simultaneous analysis of towers A (red)-B (blue) (top) and C (pink)-D (green) (bottom). The reference data used to compute the mode shapes are recorded at the slab level inside the towers. On the scheme, the arrow "N" indicates the geographic north and the arrow "Ns" indicates the north component of the sensors.

Table 28: Difference in mode shapes between independent towers A, B, C and D and the coupled systems and cross-modal assurance criterion (MAC).

	A		B		Coupled system AB				MAC (%)	
Mode	***f* (Hz)**	**Dir**	***f* (Hz)**	**Dir**	**Mode**	***f* (Hz)**	**Dir (A)**	**Dir (B)**	**A/AB**	**B/AB**
1	/	/	1.03	T	**1**	1.05	/	T	/	99.9
1	1.10	T	/	/	**2**	1.12	T	/	99.3	/
2	1.18	L	1.17	L	**3**	1.18	L	L	99.9	99.4
4	/	/	3.73	T	**5**	3.75	/	L	/	3.6
4	4.10	T	/	/	**6**	4.03	T	/	0.3	/
5	4.82	L	4.80	L	**7**	4.80	L	T	6.4	4.3

	C		D		Coupled system CD				MAC (%)	
Mode	***f* (Hz)**	**Dir**	***f* (Hz)**	**Dir**	**Mode**	***f* (Hz)**	**Dir (C)**	**Dir (D)**	**C/CD**	**D/CD**
1	/	/	1.06	T	**1**	1.08	/	T	/	56.9
1	1.12	T	/	/	**2**	1.12	T	/	99.9	/
2	/	/	1.13	L	**2**	1.12	T	L	99.9	99.4
2	1.23	L	/	/	**3**	1.22	L	/	99.9	/
4	/	/	3.85	T	**6**	3.90	/	T	/	5.4
4	4.04	T	/	/	**7**	4.01	T	/	5.8	/
5	4.70	L	4.56	L	**8**	4.58	T	L	1.0	4.6

For both coupled system AB and CD, we observe that the mode frequencies are the same than the ones of the towers with an alternation of the natural frequency of the tower B first, then of the tower A for the system AB and of the tower D first, then of the tower C for the system CD. The second bending modes of both towers A and B at 1.18 Hz and of the towers C and D respectively at 1.23 Hz and 1.13 Hz are retrieved in the frequency content of the response of the coupled systems.

Looking at the mode shapes, we note that the motions are synchronized with high correlation of the mode shapes (MAC more than 99%). The amplitude of the mode shapes is different due to the location of the reference. For instance, we can see that the mode shapes of the reference building is higher. Indeed, the records of the tower being compared are further from the reference, resulting in a greater loss of signal coherence. The correlation between modes decreases strongly after the second mode reaching only MAC of 4%. This simultaneous analysis of two similar high-rise structures using the *FDDA* technique indicates that there is a clear interaction between close towers of the residential compound.

III.7. Conclusion

The instrumentation of several buildings in Nice using ambient vibration is used not only to characterize the individual building dynamic properties, but also to observe SSI and SSSI effects.

The investigation of the variability of the ground motion at the surface, of the building mode shapes, frequency and damping values, and of the rocking motion is used to highlight the presence of SSI.

Building resonance frequencies are clearly observed at the 2nd underground level of the residential compound on the rocking spectral ratio and at the soil level on the HVSR. This testifies the presence of SSI between the soil and the buildings. The fundamental resonance frequency of the soil in this area has a large variability between 1.5 Hz and 2.5 Hz.

The similarity of the soil and building resonance frequencies suggest the presence of strong SSI effects close to the low-rise buildings. The double resonance condition may be at the origin of the high amplitude of the HVSR peak around 2 Hz.

The comparison of the observed mode shapes of the towers to the theoretical modes exhibits the fact that the observed modes are close to the cantilever beam modes. As it was shown in Chapter II, this model is sensitive to SSI effects, therefore it supports the presence of SSI at the towers level.

Moreover, the damping derived from ambient vibration measurements are generally lower than the one estimated by empirical relationships (except for the Jeary's relationship where the results are similar). Compared to the damping value in high-rise structures that are close, varying between 0.67% and 0.97%, the low-rise structures present higher values reaching 1.98% for the building E and 2.74% for the building F. Jeary (1986) assumed that the damping coefficient computed from the proposed formula is not linked to specific SSI. Compared to the results from the Clough and Penzien's method, the damping values are quite similar between both methods. This may show that the damping is not a significant parameter to study SSI for these buildings.

As observed in the Chapter II using 3D finite element model of buildings, the rocking motion occurs especially at the first resonance frequencies of the bending mode of the structure but also in higher frequencies. Because the dynamic analysis depicts non-zero displacement modes and rocking motion at the base of the buildings, the presence of SSI can be stated in the instrumented buildings.

SSSI effects in the residential compound have been observed through the frequency content of the building responses and the simultaneous analysis of their dynamic behavior. The influence of towers is slightly observed on the frequency content of the response of the low-rise buildings. This suggests that there is some SSSI between close buildings of different heights. However, it is difficult to say if there is SSSI effects between the towers based only on the frequency content of their response. The simultaneous analysis of pair of towers helped to clarify this question by

showing a clear interaction between buildings with high correlated mode shapes. Low-rise buildings present different resonance frequencies according to their different structural configuration and geometry. Despite of the presence of seismic joints between buildings E and F, the simultaneous dynamic analysis shows that a strong interaction linked both of the structures and that the building E controls the deformation of the whole system.

Homogeneous equivalent block models are used to integrate buildings in the realistic 3D site-city model for the simulation of seismic wave propagation. These models consider the structure as an equivalent homogeneous and isotropic large beam. Therefore, the first mode of deformation of this element should be a bending mode. The calibration of the blocks from real data is based on the natural frequency of the instrumented building and can only be done if the selected frequency corresponds to a flexural mode. The torsional motion suggests that the stiffness and mass of the structure are not homogeneously distributed within the building, and so this mode cannot be considered for the model calibration. The dynamic characterization of the single tower and of the high-rise structures in the residential compound shows that, even if the buildings appear identical in terms of geometry and structural configuration, they do not present the same dynamic behavior. The high-rise structures of the residential compound reveal a first bending mode while the single tower has a first mode of torsion potentially induced by its irregular rectangular section and of the decentering staircases. Therefore, in the case of a first mode shape of torsion, the frequency to consider for the calibration of simplified building model is the frequency of the first bending mode. It is then important to investigate at least the first higher modes of a structure if the calibration of the equivalent block models from real data is considered.

It appears that the towers of the residential compound have the same mode shapes (analysis done up to the 8^{th} mode). The torsion behavior is well observed using four sensors at the top of building (as in the single tower) but also with only two sensors placed at close distance at several floors (as in the residential compound).

Here, the dynamic analysis of the structures shows that the first natural frequency of the towers varies between 1.03 Hz and 1.12 Hz in the transverse direction. The one of the building E is equal to 2.35 Hz in the same direction. And the one of building F is 2.36 Hz in the longitudinal direction. The shear wave velocity, computed using the interferometry computation in the high-rise buildings, exhibits a large variability and is find around 300 $m.s^{-1}$ with a standard deviation not exceeding 130 $m.s^{-1}$. This result is lower than the one estimated in the prefecture of Nice

(500 $m.s^{-1}$) (Lorenzo, 2016). Due to the large uncertainties in the evaluation of this parameter, it is not considered for calibration of a simplified building model.

The first natural frequency of the tower A of the residential compound (1.1 Hz) with its geometry properties will be useful parameters to define homogeneous equivalent models in the 3D realistic site-city models for the simulation of seismic wave propagation.

Chapter IV. The 3D model of the Var valley

In seismic hazard studies, site effect assessment is based on an accurate knowledge of mechanical properties and geometry of superficial geological formations. The literature also shows that the characteristics of the soil surface layer can have an impact on the soil-structure interaction (SSI) effects on the building response. For example, Bybordiani and Arici (2019) used numerical 2D finite element model of realistic buildings subjected to vertical incident plane of vertical shear waves (SV) to show through time and frequency domain analysis that the soil class is an important parameter in the study of SSI. Furthermore, according to Kanai, Kiyoshi and Yoshizawa (1961), the more the shear wave velocity ($V_{s)}$ increases in the soil, the more the building vibrates. From these results, they deduced that the damping of structure depends mainly on the kinematic effects.

This Chapter develops a detailed characterization of the lower Var valley (LVV) based on the fusion of all available geophysical and geotechnical data for the integration in the 3D site-city finite element model. The LVV is a natural laboratory for the study of risk because of its similarity with other alpine valleys and also because of the high-stakes present in this area and the increasing urbanization. This valley takes place in one of the most seismic zone in metropolitan France with a peak ground acceleration on reference rock outcrop estimated to 1.6 $m.s^{-2}$. Numerous in-situ instrumentation campaigns of ambient vibration have been performed. At present, only 10% of the data about the sedimentary basin are deep boreholes meaning that they reached the engineering bedrock (Pliocene conglomerates characterized by V_s larger than 800 $m.s^{-1}$). Therefore, they are not sufficient to well constrain the basin at depth in the center of the valley. The integration of geophysical measurements, which constitute 90% of the basin data distributed all along the valley, help to fill this uncertainty. We combined boreholes log-stratigraphy with ambient vibration data to characterize not only a lithostratigraphic profile specific to the LVV, the geometry of sedimentary layers in the basin, but also the spatial variability of the seismic ground motion related to lithological site effect. Furthermore, the fusion of these two types of data allows to define an average velocity zonation all along the valley to constrain the basin-bedrock interface depth and to precise the spatial variability of site effect.

This chapter presents part of the work published in Rohmer et al. (2020) on the construction of the 3D model of the Var valley.

IV.1. Context

The lower Var valley (LVV) is a significant economically developing zone. The building density is indeed constantly increasing since 2008, when the zone got the status of "Operation of National Interest" highlighting the state's commitment to the project (http://www.ecovallee-cotedazur.com/the-eco-vallee/operation-national-interest [last access: 03/10/2018]). Several significant structures are present like the Nice Côte d'Azur airport (with more than 14 million passengers in 2019 (https://societe.nice.aeroport.fr/presse-media/trafic-annuel [last access: 10/01/2022]), the football world cup stadium, the CAP 3000 that is the 5th largest shopping center of France, several institutes from the university, the CADAM (Administrative center of the Alpes Maritimes) including the Prefecture building and many road infrastructures like the A8 highway (with more than 180 000 cars estimated per day in 2019 (https://www.data.gouv.fr/fr/datasets/trafic-moyen-journalier-annuel-sur-le-reseau-routier-national/ [last access: 16/01/2022]) and the Napoleon bridge that cross the Var river.

First, we describe the geological and geomorphological environment of the Var valley. Second, we present a review of the historical seismicity in this region and then, we focus on the site effect estimation in the valley.

IV.1.1. Geological and geomorphological setting

The LVV, in the southeastern part of France, results from multiple marine transgressions and regressions since the early Cenozoic that led into a large delta with continuous sedimentation from the Alps Mountain range (Clauzon, 1978; Dubar, 2003). During the last marine regression in the Messinian age (≈ 6 Ma) (Gargani, 2004), the Mediterranean Sea level decreased by 2 km and induced the creation of the LVV over almost 18 km^2. Because of the reopening of the Strait of Gibraltar from 5.33 Ma, the sea level increased again and flooded the southern part of the valley. Consequently, the valley is filled with recent alluvial deposits overlying a large accumulation of conglomerates from the Pliocene delta characterized by a slope of 15–20 degree toward the south (Clauzon, 1978; Guglielmi, 1993). Because of the complex alpine geodynamic context, the LVV is subjected to the overlaps of the arc of Nice and the presence of horsts and grabens (Pline, 1991; Guglielmi, 1993; Larroque et al., 2001; H2EA and Cabinet Mangan, 2010; Terrier, 2012). In fact, the valley is surrounded by compressive sismo-tectonic systems that are presented in Figure 67.

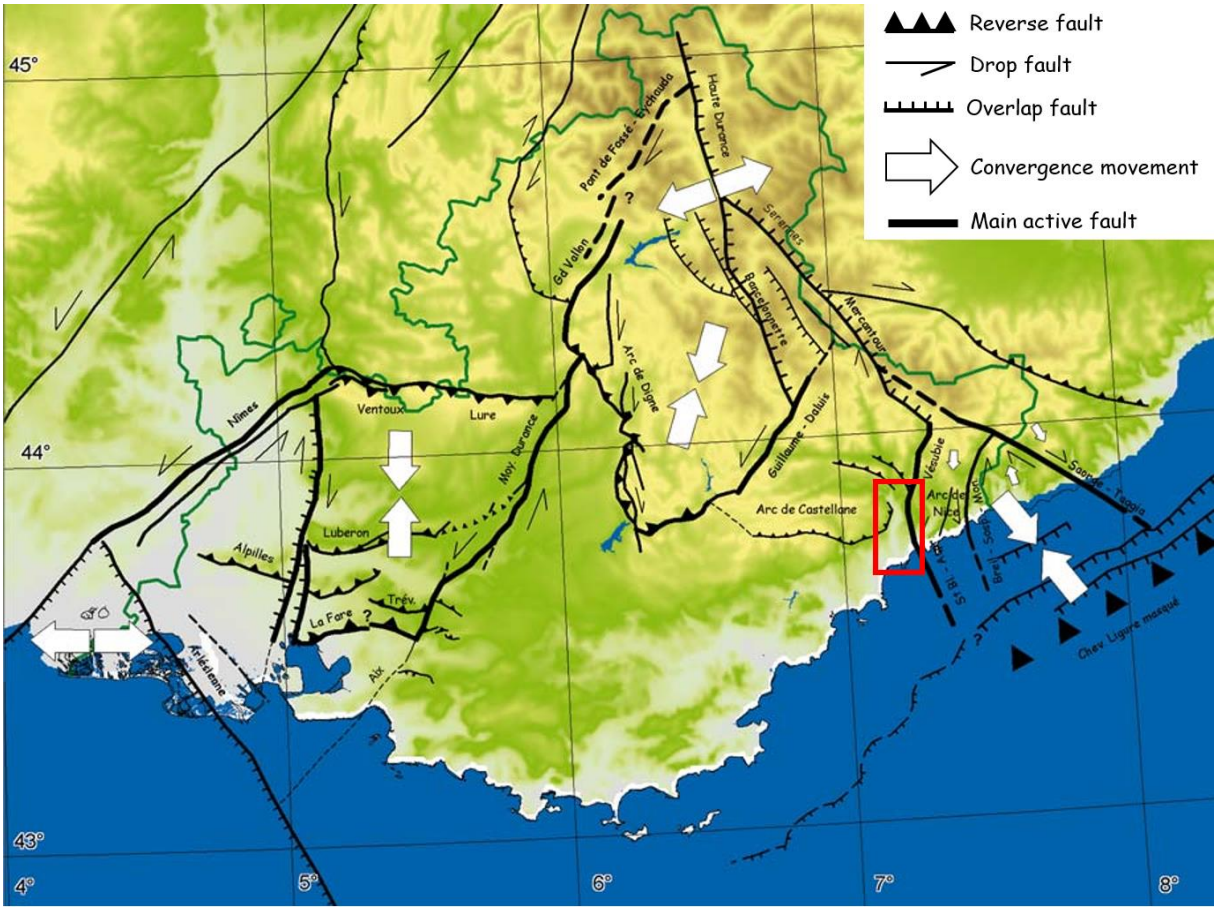

Figure 67 : Sismo-tectonic map of the Provence Alpes Côte d'Azur region. The lower Var valley is located in the red rectangle (modified from http://observatoire-regional-risques-paca.fr/article/convergence-afrique-eurasie [last access: 09/08/2020]).

This configuration induces that the geology of this zone is not only composed of a single rock material but of a mix of Jurassic limestones, Cretaceous sandstones, Pliocene conglomerates and marls. The LVV is marked by a flat relief at the sea level whereas the top of the hills rapidly reach 200 to 500 m of altitude (Figure 68). The Var River bounds the western part of the city of Nice and it is the longer river of the Alpes-Maritimes department with a length of 114 km (Dubar, 2003, 2012; Du, 2016).

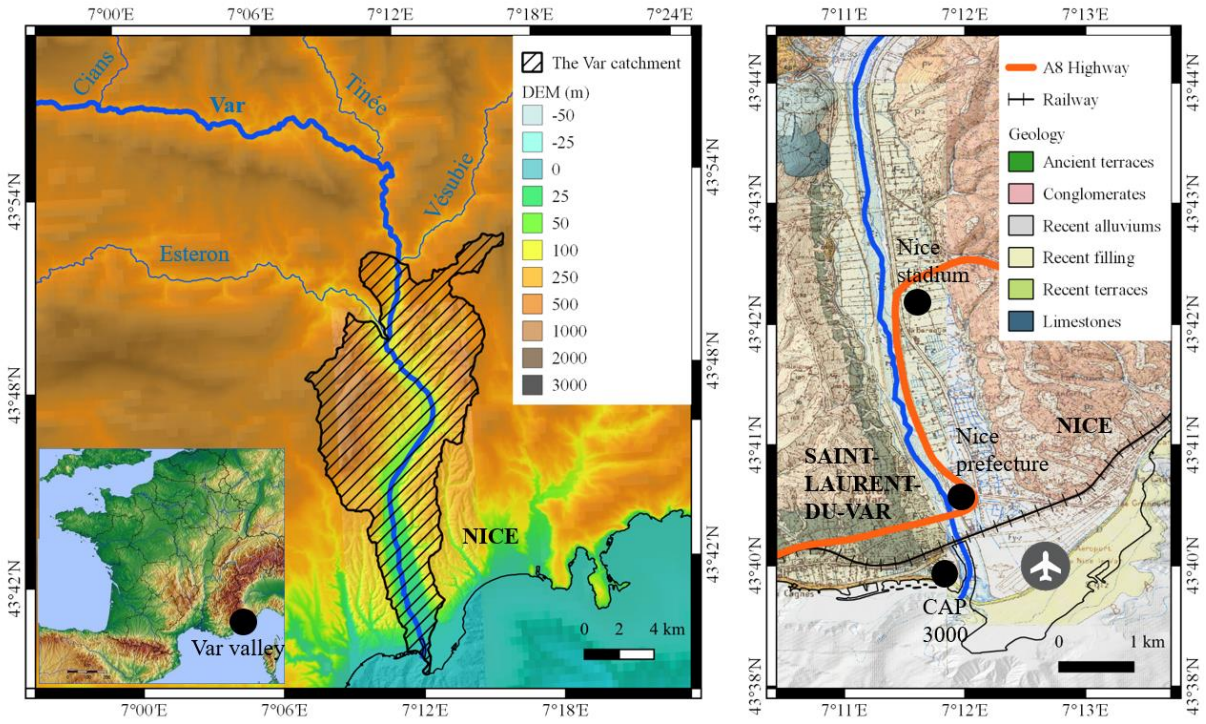

Figure 68.The Var catchment (left) and the 1/50000e geological map from the French Geological Survey (BRGM) focused on the Var valley (right) (source: the 25 m resolution Digital Elevation Model of the entire region (IGN), the 5 m resolution DEM of the Var valley is overlaid on the previous map (GO_06 June 2009, BATHYMETRIE©CANCA, Litto3D, MALISAR and IBCM campaigns)).

The main tributaries from the upstream to the downstream: the Cians, the Tinée, the Vésubie and the Esteron Rivers bring constant sediment contribution all along the Var River. On the right bank of the Var River, the hills are composed of ancient and recent quaternary terraces. On both banks of the river, the valley is surrounded by Pliocene conglomerates (Figure 68). Thanks to its geological and geomorphological structure and notably to the presence of the Pliocene conglomerates, the plain of the Var valley constitutes an important natural reservoir of freshwater for the region where a groundwater table extends to a depth of about 5-10 km (Pline, 1991; Guglielmi, 1993; Du, 2016). Even the geothermal potential of the Var valley alluvial has been highlighted by several studies performed by the French Geological Survey (BRGM) (BRGM, 2015). The evolution of the hydrological network through time, notably of the river meanders, leads the Var riverbed to be reshaped many times and so, induced a complex alluvial sedimentary stratification in the basin. However, since the high urbanization of the LVV from the 1900's and the building of artificial embankments all along the lower part of the Var River, the riverbed became more constrained (Figure 69).

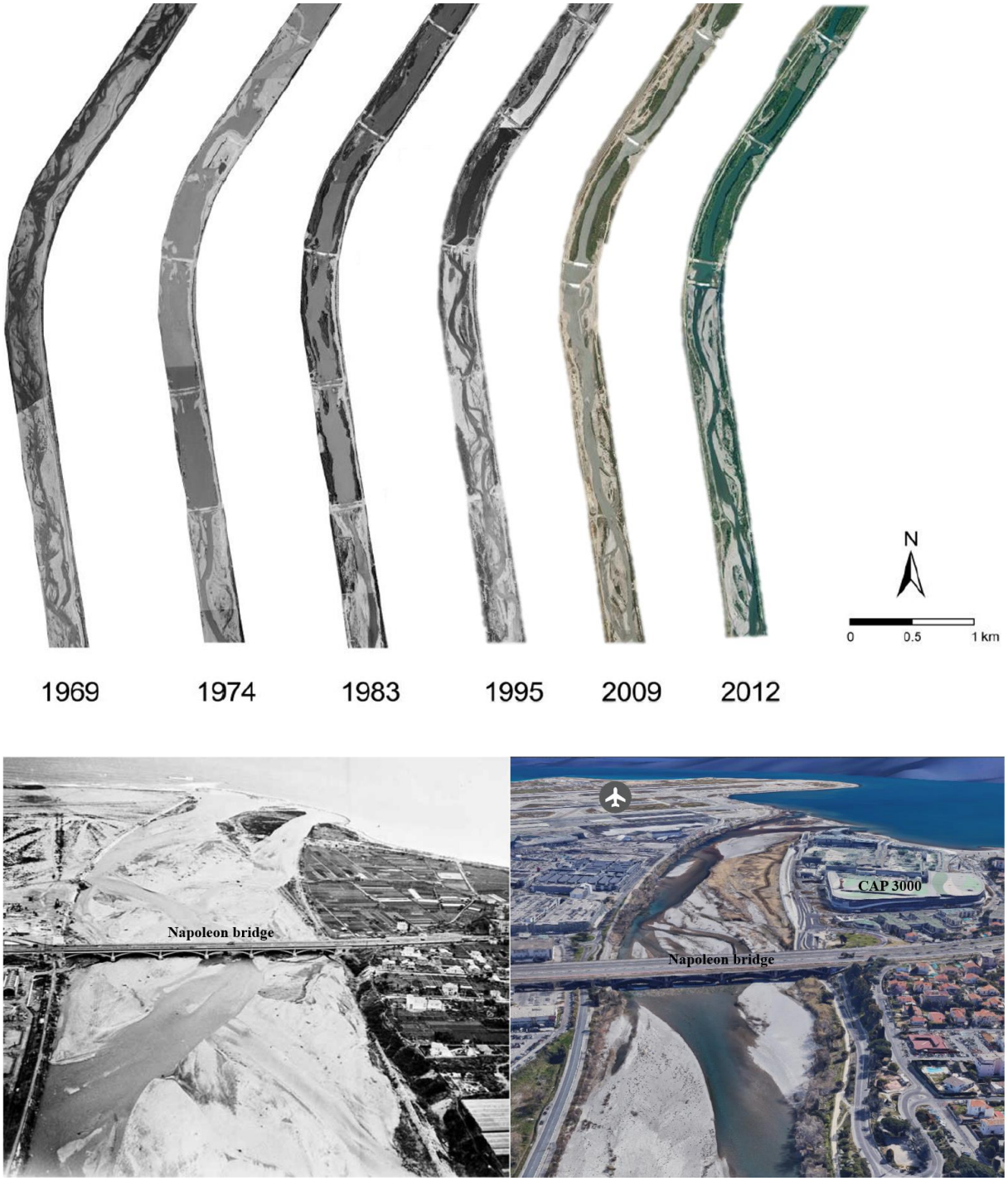

Figure 69: Evolution of the Var riverbed from 1969 to 2012 (top, modified from Du (2016), source: IGN), urbanization and transformation of the Var estuary between 1951 (bottom left, source: DDTM (2011)) and 2021 (bottom right, source: Google maps/CNES 2021). We can note the building of the Nice airport platform in the Mediterranean sea and the shopping center CAP 3000 in Saint-Laurent-du-Var on the right bank of the river.

According to the literature, the quaternary sedimentary thickness reaches 100 m depth at the Var estuary (Dubar, 2012; Migeon et al., 2016; Kopf et al., 2016). Recent studies on the Nice continental slope have also confirmed alluvial deposits with a thickness of more than 100 m

that are responsible for strong offshore seismic wave amplifications (Dan-Unterseh et al., 2007; Courboulex et al., 2020). Dumasdelage et al. (2016) notably showed that the airport platform constitutes a hurdle for the alluvial sediment transport by the alongshore current toward Italy.

IV.1.2. Historical seismicity

The region is one of the most seismically active area of metropolitan France according to the French seismic regulation code (Figure 70). It indicates that the peak ground acceleration on reference rock outcrop is equal to 1.6 $m.s^{-2}$ for a return period of 475 years (corresponding to a 10% of probability to be exceeded in 50 years) for the city of Nice.

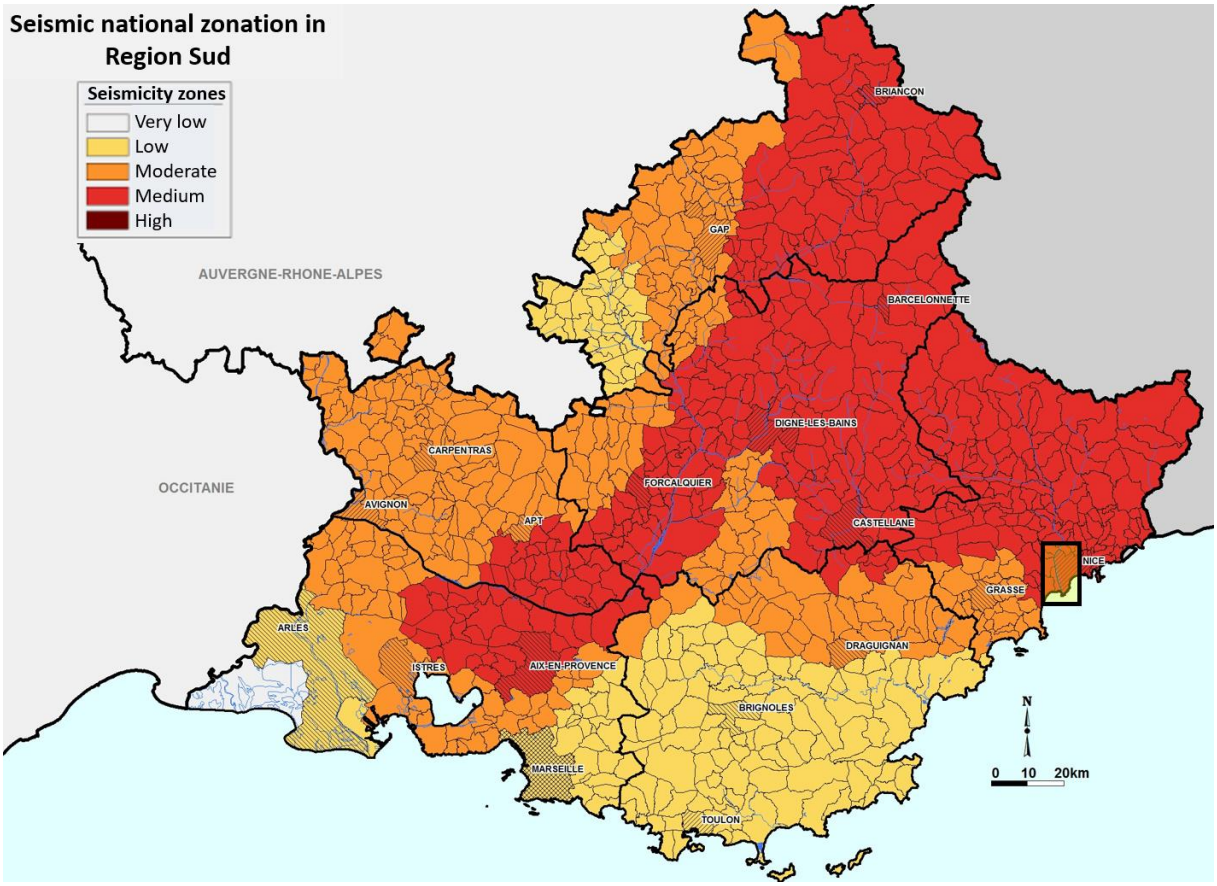

Figure 70: French seismic regulation code of the Region Sud (according to the Décret: 2010-1255 du 22 Octobre 2010). The Var valley is highlighted in the black frame close to the city of Nice.

The high seismic activity of the region is highlighted by the historical and the instrumental seismicity (Figure 71 and Figure 72). As early as the 1500s, the main strong seismic events in the Alpes-Maritimes region have been noted or recorded over time. They are presented in Table

29. To the present time, the 1887 Ligure earthquake is the strongest event (6.8 Mw) perceived in accordance with historical testimony (around 600 dead and 500 injured, building damages, more than 20 000 homeless people) (https://www.azurseisme.com/-Seisme-ligure-de-1887,17-.html [last access: 08/09/2021]). It is important to put in evidence the fact that in major cases, the people loss is not directly due to the seismic event but is due to building destructions. This show the importance to know what the local seismic risk in a region is and how do structures interact with the surface seismic wave field in order to protect people during seismic events.

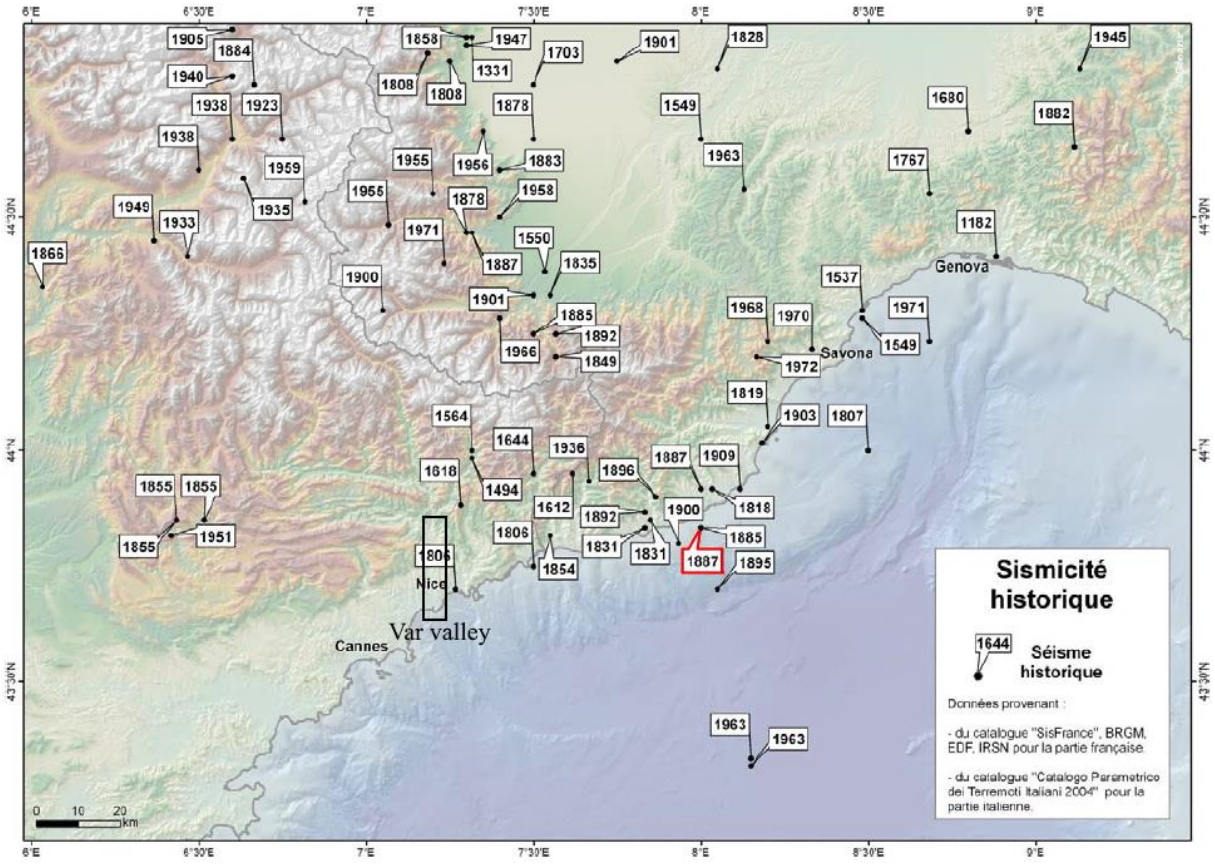

Figure 71: Historical seismicity (1182-1979 A.D.) of the southeastern region of France (modified from Larroque (2009)). Indicated events have seismic intensity higher than VI (according to SISFRANCE and the Cataloguo Parametrico dei Terremoti Italiani 2004). The 1887 Ligure earthquake is indicated in red (6.8 Mw). The Var valley is highlighted by the rectangular black box.

Table 29: Main strong seismic events in the Alpes-Maritimes region since 1494 with an MSK intensity above V or magnitude higher than 4 (modified from https://www.azurseisme.com/Tableau-des-forts-seismes.html [last access 08/09/21]).

Time	Localisation	Mag.	Max. epicentral intensity (MSK scale)	Damages
23/06/1494	Upper valley of the Vésubie	/	VIII	Several deaths due to building damages because of rockfalls
20/07/1564	Upper valley of the Vésubie	/	VIII	Several hundred deaths, destroyed villages, underwater sliding close to the coast of Nice
18/01/1618	Lower valley of the Vésubie	/	VIII	Several deaths due to building damages
15/02/1644	Lower valley of the Vésubie	/	VIII	Several deaths due to building damages
23/02/1887	Ligure sea	6.8 Mw	VIII	More than 600 deaths and 500 injured, destroyed villages and building damages
19/07/1963	80 km off the coast of San Remo	5.9 Ml	VI	Building damages
26/12/1989	25 km to the south of Monaco	4.5 Ml	V	No damages
25/02/2001	27 km to the SSE of Nice and 25 km to the south of Monaco	4.6 Mw	V	No damages
07/07/2011	107 km to the west of Ajaccio	4.9 Mw	V	No damages
26/02/2012	Barcelonnette	4.2 Mw	V	Building damages
04/03/2012	92 km to the west of Ajaccio	4.4 Ml	IV	No damages
07/04/2014	Barcelonnette	4.8 Mw	VI	Building damages

The regional seismicity is characterized by low to moderate seismicity with earthquakes having moment magnitude (Mw) higher than 4 tending to occur every 5 years (Larroque, 2009). The last main event was the 2014 April 7th Barcelonnette earthquake with 4.8 Mw. It was felt in the

whole region up to Milano in Italy (260 km away) and induced light building damages (https://www.azurseisme.com/seisme-de-jausiers-7-avril-2014.html [last access: 08/09/2021]).

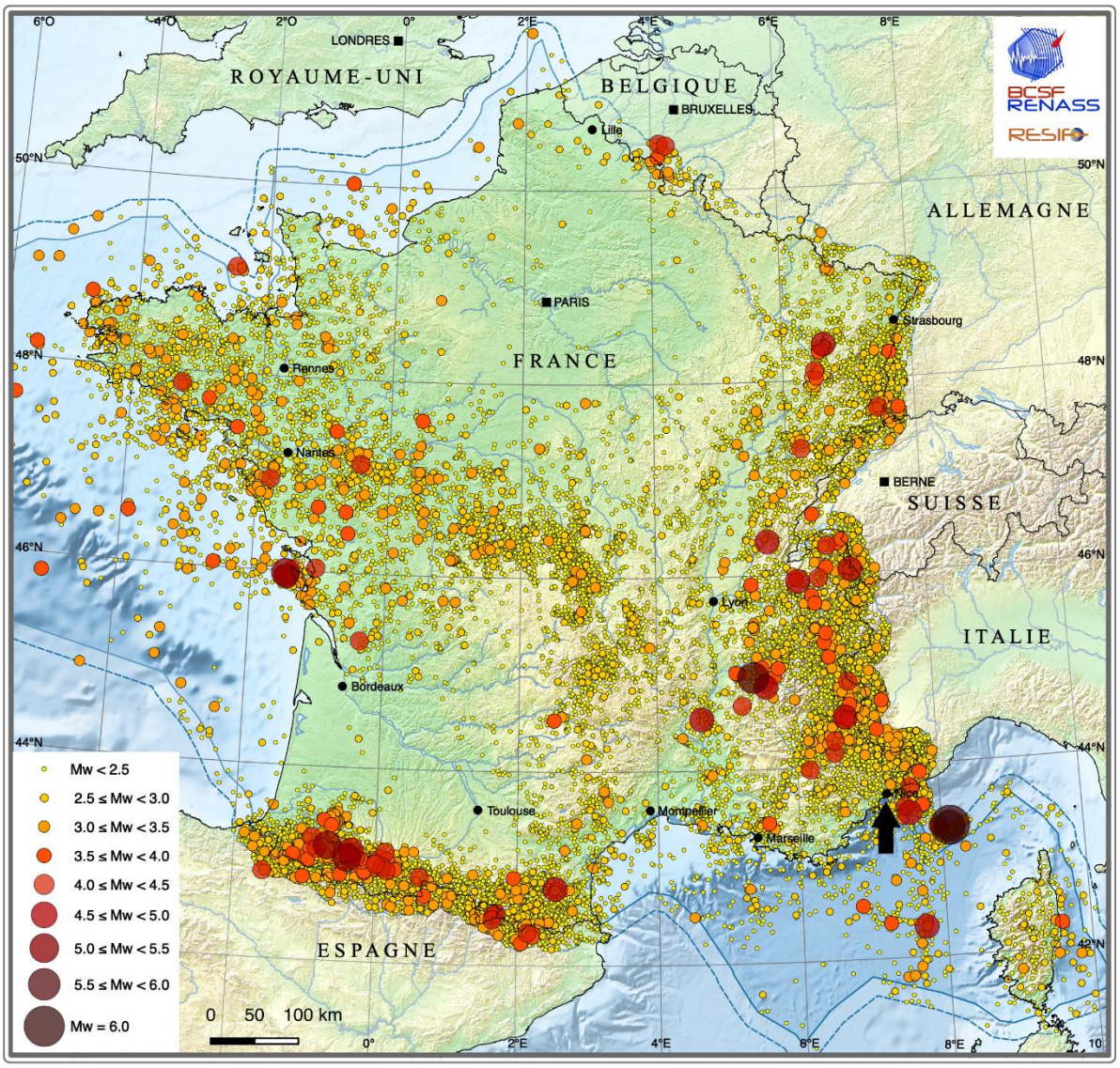

Figure 72: Actual instrumental seismicity of the metropolitan France (modified from BCSF-RéNaSs and RESIF websites). Epicenters of earthquakes from natural origin in the Si-Hex area (Metropolitan France and exclusive economically zone in the sea (ZEE), with 20 km of extension). Seismicity catalog used: on the period 1962-2009 the catalog from the Si-Hex project (Cara et al. 2015, http://www.franceseisme.fr), on the period 2010-2020 the catalog from BCSF-RéNaSs for which the magnitude M_L was converted in M_w. The Var valley is indicated by the black arrow.

Since the 90's, the region is covered by a large seismological network monitored by the Géoazur Laboratory and the seismic risk team of the Cerema (REPSODY). Numerous seismic stations and notably, permanent accelerometric stations from the French permanent accelerometric network (RESIF-RAP) enable to provide a lot of information about strong motions in the region

(localization of epicenters, magnitude, peak ground acceleration, strong motion duration…) (Figure 73) (Pequegnat et al., 2008). Four of the permanent accelerometric stations (NIMR, SLAF, NCAD, NCAU) are located in the LVV, one of which was recently installed in October 2020 (Figure 76).

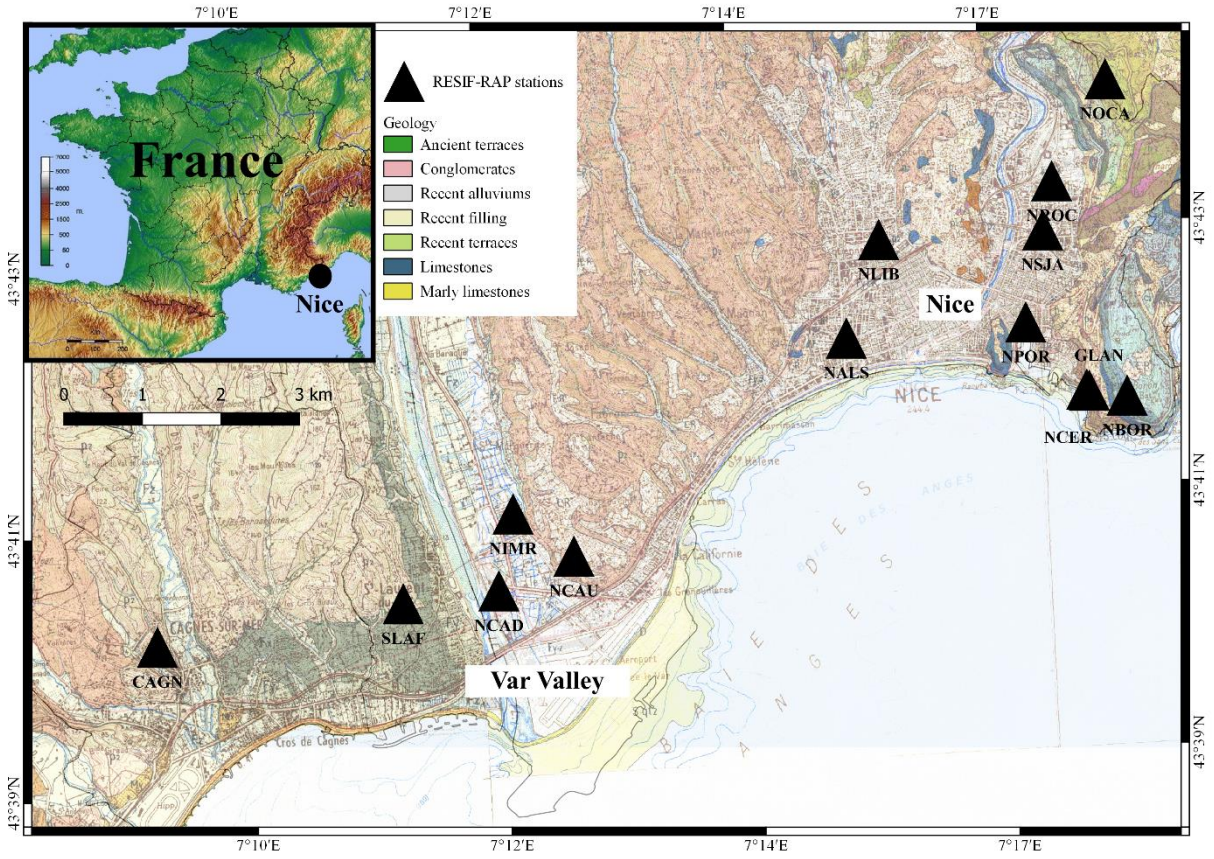

Figure 73: Actual permanent seismologic network (RESIF-RAP network) in the French Riviera. Each station is indicated by a dark triangle. The three stations (SLAF, NCAD, NCAU) are used to highlight site effect in the LVV. The site response at the reference station NCAU is compared to the site response at NCER and NOCA stations and discussed. The NIMR was recently installed on the 20th October 2020.

Because of the recent installation of the NIMR station, the station could not record many earthquakes. Therefore, we focus on recordings at SLAF, NCAD and NCAU stations to investigate site effect in the LVV. These stations are aligned in the transverse direction of the valley and are chosen to evaluate empirically site effect in the studied area. From west to east, SLAF is located at the limit between the ancient alluvial terraces and the Pliocene conglomerates outcrop at the right bank of the river, NCAD is located on recent quaternary sediments and NCAU is lying over the Pliocene conglomerates to the east. NCAU is chosen as the rock reference station for the site effect estimation in the area.

IV.1.3. Site amplification in the Var valley

IV.1.3.1 Previous studies

Several site-specific studies in the city of Nice (Bard, 1983; Bertrand et al., 2007a; Régnier et al., 2020) showed that site effect exists here and particularly in the LVV that corresponds to the western boundary of the city. To prevent and decrease devastating effects of earthquakes, the French national policy sets up “Plans de Prévention des Risques Sismiques” (PPRS) for city presenting high stakes and subjected to important seismic hazard. These PPRS include the definition of seismic microzonations that identify zones where the seismic excitation is homogeneous. The seismic microzonation of the city of Nice was elaborated by the Cerema and is based on the methodology proposed by Régnier et al. (2020) (Figure 74).

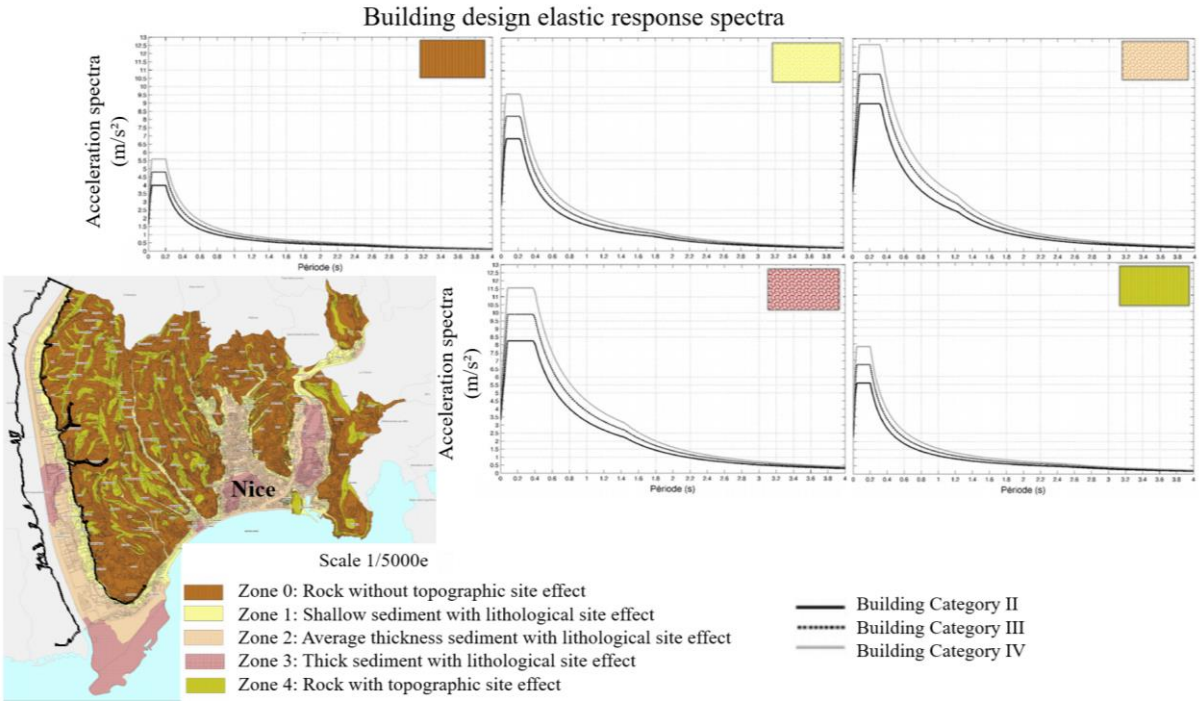

Figure 74. PPRS of Nice (modified from DDTM, 2019). The Var valley is identified by black lines.

Because the city is bounded by the Var River to the west, the microzonation is not applied to the entire Var valley. On the other riverbank, a PPRS is currently under study. As presented before, the LVV belongs to a particular catchment area where the hydrological regime induces a large variety of sediments deposits mixing river and marine deposits (Pline, 1991; Guglielmi, 1993; Du, 2016). Thus, combined with the large thickness of the quaternary sediments, the site

effect in this valley may be slightly different from the other valleys of the region. One of the challenges we are facing in this valley is that traditional geophysical surveys are not feasible due to the dense urbanization. Although, they are useful to retrieve the soil velocity profile. Therefore, one of the goal of our work is to build the best soil model possible without the help of this kind of data.

IV.1.3.2 Earthquake recordings analysis

First and foremost, standard seismic spectral ratio (SSR) (Borcherdt, 1994; Duval and Vidal, 2003; Duval et al., 2013) and earthquake Horizontal-to-Vertical spectral ratio (HVSR) (Lermo and Chavez-Garcia, 1993; Theodulidis and Bard, 1995; Yamazaki and Ansary, 1997) are calculated at the NCAD and SLAF stations (Figure 75) using NCAU as a reference station, and recordings of 67 earthquakes meeting three criteria: an epicentral distance lower than 1500 km, a magnitude larger than 4 and a signal-to-noise ratio above 3 from 0.2 Hz to 30 Hz. These criteria indicate that the considered seismic events are regional earthquakes in order to have enough energy on accelerometric data. In fact, accelerometric sensors are not sensitive to teleseismic events (where the source is more than 3000 km away from the sensor). However, attention must be paid when using the SSR method. Indeed, this method requires to use seismic events where the source is sufficiently away to take into account equivalence between the source-site travel and the source-reference travel. The database from Rohmer et al. (2020) has been recently updated up to August 2021 (see Appendix 4).

The horizontal components are rotated according to the main orientations of the valley (longitudinal and transversal) considering an angle of $\pi/8$ from the geographic north. A Konno and Ohmachi smoothing has been applied before spectral division using a b-parameter equal to 20 (Konno and Ohmachi, 1998).

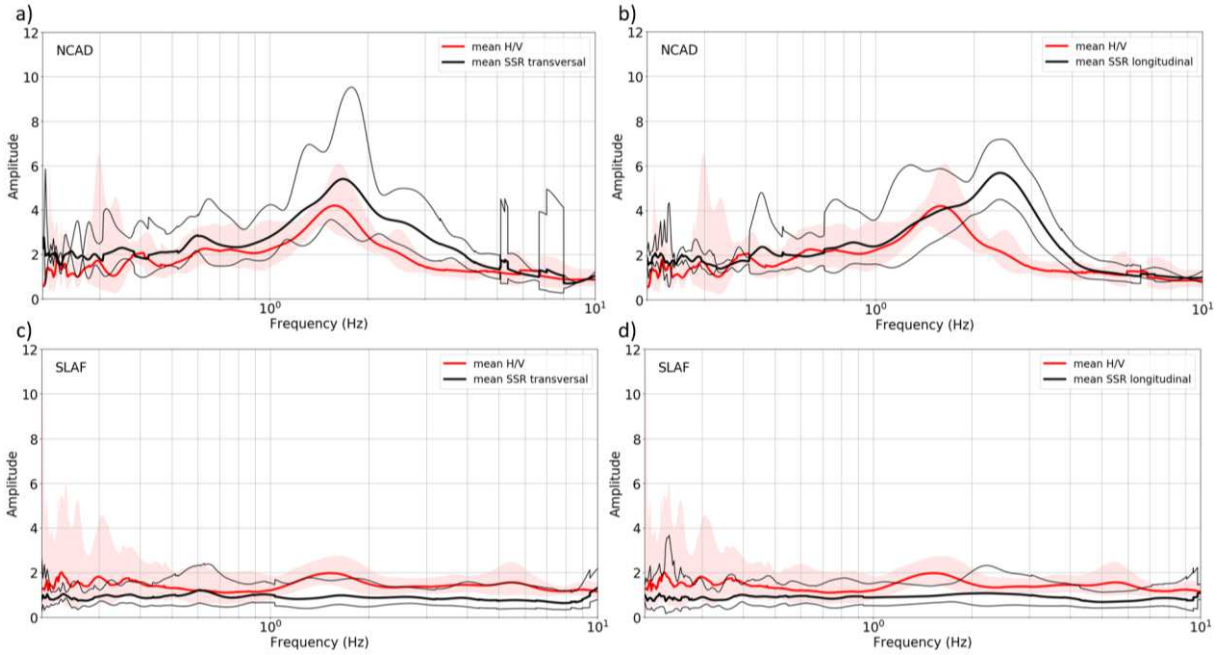

Figure 75: Earthquake HVSR and SSR of the seismic records at the RESIF-RAP stations located in and close to the Var valley computed considering an angle of π/8. (a) Transversal component at NCAD, (b) Longitudinal component at NCAD, (c) Transversal component at SLAF, (d) Longitudinal component at SLAF.

At NCAD station, SSR and HVSR show a mean amplification at 1.68 Hz on the transversal component whereas on the longitudinal component, the results differ. SSR show a maximum amplification at 2.40 Hz while HVSR show it around 1.63 Hz. Compared to HVSR, we can note that SSR show indistinct amplification at this frequency. The difference between the fundamental 1D frequency (from HVSR) and the others (from SSR) may illustrate a 2D resonance in the valley. However, it appears on SSR that the fundamental frequency on the longitudinal component is higher than the one on the transversal component. This is incoherent with a valley 2D resonance for which the fundamental frequency on the longitudinal component is supposed to be lower than the one on the transversal component according to Bard and Bouchon (1985). Sgattoni and Castellaro (2020) presented the case of anisotropic effects in a sedimentary valley. These effects can lead to discrepancies between SSR on horizontal components without having 2D resonance. At SLAF station, the SSR show no particular amplification under 10 Hz. Therefore, the site response of the ancient alluvial terraces (on the left bank of the river) and the Pliocene conglomerates outcrop on the right bank of the river is considered to be the same.

IV.1.3.3 Ambient vibration analysis

Ambient vibration surveys are a powerful tool to investigate the geomorphological structure of a sedimentary basin since they require little money, little time and can be used to cover a large area. They provide good estimation of the fundamental resonance frequency for 1D horizontally layered structures (Bonnefoy-Claudet et al., 2008) and then, parameters like the sediments thickness or the average S-wave velocity (called here V_{sz}) can be deduced by simple relationships. These passive non-invasive measurements are used in many studies for different applications. They helped indeed to map the sub-surface structure in Ohio, USA (Haefner et al., 2010), in the Grenoble basin (Guéguen et al., 2007), in the western lower Rhine embayment (Seht and Wohlenberg, 1999), in Cologne area (Parolai et al., 2002), in Spain (Delgado et al., 2002), and in the Po Plain in Italy (Mascandola et al., 2019). Other studies are investigating V_s profiles and the site response characteristics (amplification factor and fundamental resonance frequency), like in Switzerland in the Rhône valley (Roten et al., 2006), in Italy in the Tagliamento River valley (Barnaba et al., 2010), in Greece in the Mygdonian basin (Raptakis et al., 2005; Manakou et al., 2010) or in USA in the Seattle basin (Stephenson et al., 2019). However, all these studies include an inversion process linked to interpretations and show some uncertainties concerning the estimation of the soil layers geometry and the material geomechanical characteristics.

Complementary to these data, borehole data allow very locally to constrain the basin depth. Geotechnical data are divided in two large categories: the in-situ (as for example standard penetration test, cross penetration test, etc., from which the V_s can be obtained throughout well selected correlation relationships and the laboratory tests (like resonant column, triaxial test, etc., on undisturbed samples), which lead in the quantification of crucial soil properties (such as stiffness and damping) of the soil materials. Nevertheless, each method employed needs specific knowledge and expertise to achieve useful results (in terms of small strain shear modulus (G_0), V_s, shear modulus – shear strain – damping ratio (G-γ-D) curves, etc.) for soil and site characterization.

It is possible to use the corresponding results of the borehole samples, by themselves or in combination with other data (i.e. from seismic or geological prospecting), for the construction of a soil model, that can be adopted for modeling purposes. For example, Bozzano et al., (2000) worked on the definition of the buried Tiber River valley in Rome following this approach. These geotechnical data bring thus strong constraints to the lithology and the geometry of the

basin structure. The combination of borehole data and geophysical surveys is used in many cases for example to build sub-surface model like in Lebanon (Salloum et al., 2012) or in Spain (Delgado et al., 2000), or to investigate site response like in the "Europarco Business Park" in Rome (Bozzano et al., 2016). Indeed, the combination of all available data is a powerful tool to better constrain the study like presented in several papers about the Euroseistest in Greece (http://euroseisdb.civil.auth.gr/ [last access: 23/12/21]). However, in the case of very urban site, the amount of available data can be scarce due to the difficulty to perform geophysical field campaigns. In such environment, the challenge to acquire reliable data is one of the goals of the urban seismology.

In addition, in the absence of in-situ parameters or laboratory tests, the definition of the basin structure at depth is a real challenge. Considering that, on one hand, boreholes are expensive, are time consuming and give information on a very local scale and that, on the other hand, the studied area is a dense urbanized zone, it is very complicated to undertake either an extensive borehole drilling campaign nor a comprehensive geotechnical survey over the whole valley (e.g. Vähäaho, 1998; Kessler et al., 2008; Marache et al., 2009a, 2009b).

In order to better estimate seismic hazard in the LVV, intensive geophysical and geotechnical campaigns were performed (Dufour et al., 2018; Rohmer et al., 2020). We are attempting here to define the 3D model of the LVV combining existing borehole log-stratigraphy and ambient vibration measurements. A new methodology is proposed to investigate the sedimentary basin structure by using a large amount of available data, spatially distributed all along the valley, and by defining an average velocity zonation. The model is first defined, by sedimentary layering constrained by borehole data and second, by the basin-bedrock interface constrained by the combination of borehole data and ambient vibration measurements. The considered geotechnical data consist only in soil log descriptions providing unevenly distributed but strong constraints in the geometry of the subsurface soil layers and the type of sedimentary material. On the contrary, the intensive ambient vibration campaigns provide a dense and regular grid of measurements to improve the spatial resolution of the model.

IV.2. Available borehole log-stratigraphy

331 boreholes collected in the database from the BRGM and recent geotechnical surveys (provided by the city of Nice) are used to build the 3D model of the LVV. The location of the boreholes is illustrated in Figure 76.

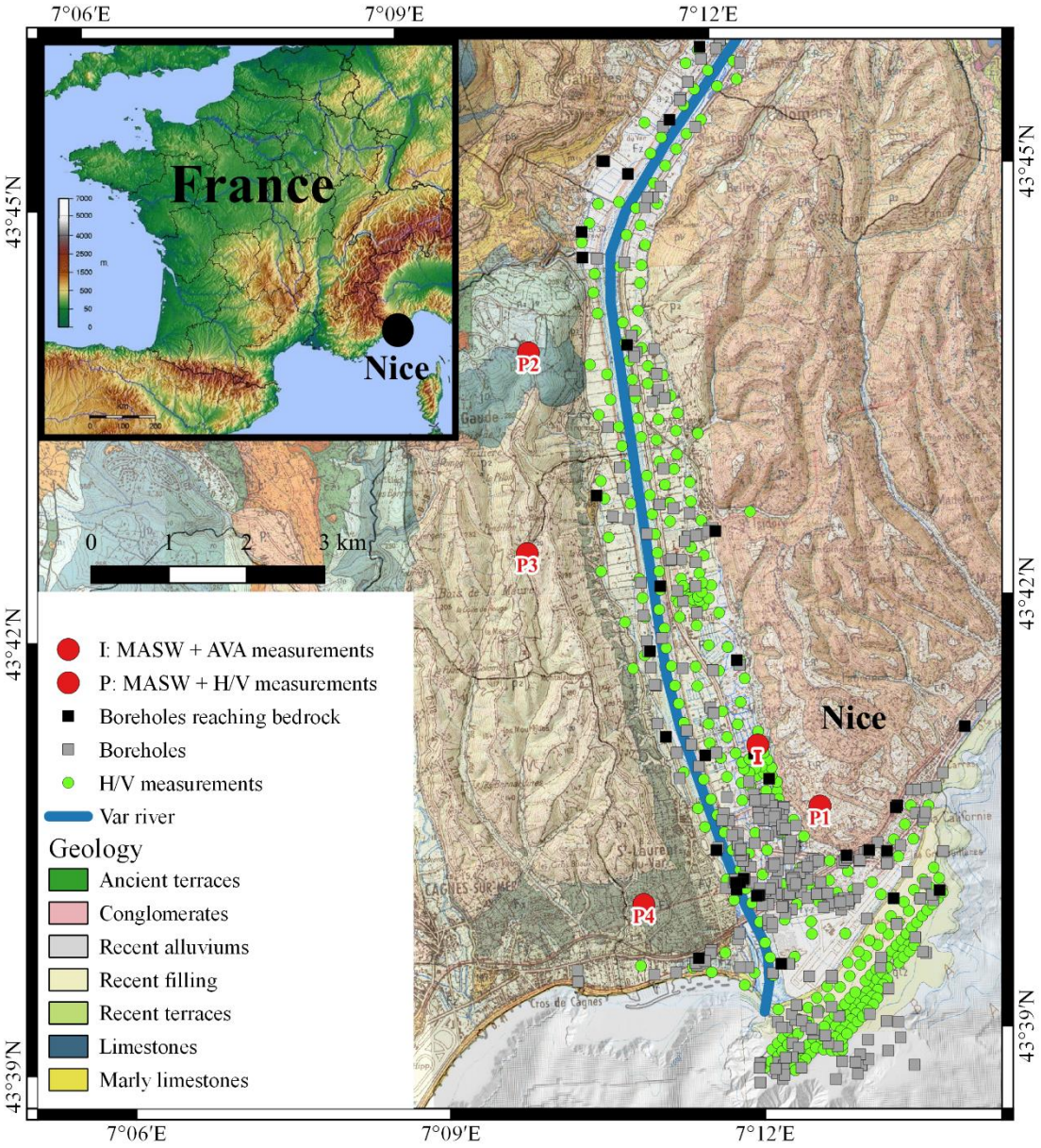

Figure 76: Localization of all geotechnical and seismic data used in the building of the 3D model of the LVV. The background map is the 1/50000e geological map from the French Geological Survey (BRGM) that overlaid the 5 m resolution DEM of the LVV (GO_06 June 2009, BATHYMETRIE©CANCA, Litto3D, MALISAR and IBCM campaigns).

Most of them are located in the southern part of the valley. Only 35 boreholes, located mostly at the edges of the valley, are reaching the engineering bedrock bringing punctual, but strong,

constraints to the basin thickness. However, a large uncertainty exists on the basin geometry in the middle of the valley. Based on a synthesis of available geotechnical and geophysical data at the scale of the city of Nice, a common lithostratigraphic soil profile of the fluvial deposits in the LVV is elaborated (Figure 77).

Layer description	Code	Geology (1/50000e geological map)	Vp (m/s)	Vs (m/s)
Filling, concrete. Topsoil	1	Anthropogenic deposits	600	240
Sand + pebbles + gravels	2	Recent alluvium	1080	435
Fine sand. Silty sand or clay sand.	3	Deltaic deposits	875	350
Silt, clay (sometimes muddy)	4	Muddy deposits and pro-delta	675	270
Sand + pebbles + gravels	5	Recent alluvium. Fluvial deposits	1080	435
Fine sand. Silty sand or clay sand	6	Deltaic deposits	1000	400
Silt, clay (sometimes muddy)	7	Muddy deposits and pro-delta	875	350
Coarse sand	8	Ancient alluvium. Fluvial deposits	1250	500
Sand + pebbles + gravels	9	Ancient alluvium. Fluvial deposits	1750	700
Bedrock	R	Pliocene, Cretaceous, Jurassic, Trias	2234	1290

Figure 77: Lithostratigraphic soil profile applied to the Var valley and estimated seismic wave velocities. The colored scale helps to identify layers in the 3D model of the LVV (Figure 96).

Based on the lithostratigraphic soil profile of the Nice (Régnier et al., 2020) (Figure 78) and on the interpretation of each borehole log-stratigraphy available in the LVV, nine sedimentary layers sorted from the most recent at the top to the oldest at the bottom of the valley are defined to constitute the lithostratigraphic soil profile of the LVV. These layers are mainly composed of sand, gravel, silt and clay. Consequently, geotechnical data provide strong constraints to the quaternary sedimentary thickness and also to the sedimentary layering within the basin. The interpolation of the sedimentary layering for each sedimentary layer is presented in the section IV.6.

	Lithology	Vs[a] (m/s)	ρ[b] (Kg/m^3)	PI[c]	σ'[d] (kN/m^2)
L1	Backfill	180 ± 60	1900	0	10
L2	Sand and gravel	290 ± 80	1900	0	30
L3	Silt and clay	200 ± 100	1700	20	50
L4	Sand and Gravel	330 ± 80	2100	0	90
L5	Fine sand	250 ± 60	1800	0	100
L6	Sand and gravel	300 ± 70	2100	0	120
L7	Silt and clay	220 ± 100	1800	10	140
L8	Sand and gravel	290 ± 90	2000	0	170
L9	Coarse gravel	300	2000	0	280
B	Bedrock	1000	2100		

[a] Is the shear wave velocity
[b] Is the density
[c] PI: Plasticity Index
[d] Is the effective confining pressure

Figure 78: Lithostratigraphic soil profile of the city of Nice (from Régnier et al. (2020))

IV.3. Passive and active seismic measurements

Passive and active seismic measurements have been conducted in the LVV in order to estimate the fundamental resonance frequency (f_{s0}) at each measurement site (Figure 76). Also, one multichannel analysis of surface waves (MASW) experiment and one ambient vibration array (AVA) were jointly performed at a specific location to better constrain the wave propagation velocities in the sedimentary basin. And four active seismic surveys associated with single ambient vibration measurement have been conducted in the surrounding outcrops to estimate the V_s in the engineering bedrock (P points on Figure 76). First, we present the material and the setup configurations employed to obtain seismic data in the valley. Second, the f_{s0} is estimated at each measurement sites in the LVV through the microtremor HVSR (mHVSR) approach (Nakamura, 1989). A focus is made on the mHVSR quality for the interpretation of ambient vibration data.

IV.3.1. Material and setup geometry

For all passive seismic measurements, Lennartz LE-3D-5s seismometers are used. The minimum sampling frequency was 150 Hz. The minimal recording duration was 30min. The digitizer was CityShark II (Chatelain et al., 2000) for the ambient vibration campaign in the LVV that are, with Lennartz LE-3D-5 s seismometers, a performant combination in ambient vibration studies (Guillier et al., 2008). We estimate the f_{s0} in the sedimentary basin of the LVV through each ambient vibration measurement for a total of 439 points presented in Figure 76. The distance between nearby measurement points is smaller than 100 m.

MiniShark station (Chatelain et al., 2000) was used for the four seismic surveys in the surrounding outcrops. For all of these active seismic measurements, 24 vertical 4.5 Hz geophones evenly spaced are used. Two set up were considered. In the first, the geophones were distant from 1.5 m and in the second set up the in-between geophone distance was 3 m. The respective total length of profiles was thus 34 m and 69 m. The frequency sampling was 500 Hz and a mass of 10 kg was used as seismic source. For most of them, the measurements were performed during the working days in spring and summer.

The AVA is composed of 3 circles with a radius varying between 5, 20 and 50 m (Figure 79).

Figure 79: Localization of the MASW and AVA arrays in the LVV.

IV.3.2. f_{s0} in the quaternary sedimentary basin

We analyze the ambient vibration data performed all along the valley in order to estimate the f_{s0} at each measurement point in the sedimentary basin. To do this, we use the mHVSR approach (Nakamura, 1989) through the *Geopsy* open source software (Wathelet et al., 2020) in the frequency range 0.5 – 20 Hz for measurements in the basin and in higher frequency range 0.5 – 60 Hz for recordings on rock site.

The first peak of mHVSR is assumed to indicate the f_{s0} of the soil column at each measurement point. This assumption is applied for curves with well-defined and single sharp peak with amplitude level above than 3 according to the SESAME European project (European Commission, 2004). However, for some recordings, only few stationary windows are found and analyzed leading in some uncertainties in the result at these points. Therefore, for all of the ambient vibration measurements performed in the LVV, the resulting mHVSR are sorted in 5

groups according to their quality. We introduce the method of the mHVSR quality classification in the following section.

IV.3.2.1 Classification of the mHVSR

In order to successfully interpret the mHVSR, we perform a classification of the curves according to the reliability of each measurement based on a visual inspection. The classification table can be found in Table 30.

Table 30: Conditions for the mHVSR quality classification. The reliability of mHVSR decreased from the top to the bottom.

(-) Reliability (+)	**Type A**	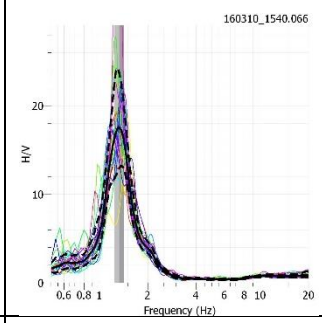	• Only one sharp peak • f_0 well-defined • $A_0 >> 3$ • Very low standard deviation
	Type B	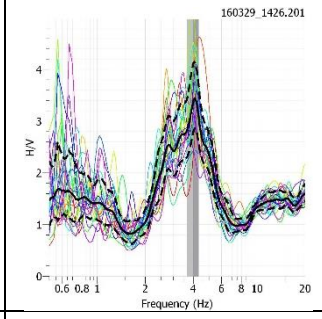	• Other low amplitude peaks are accepted or 2 sharp peaks, or one large peak • f_0 easy to determine • $A_0 > 3$ • Low standard deviation
	Type C	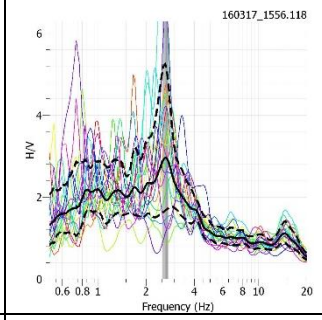	• Only one low amplitude peak or several similar amplitude peaks or one very large peak • f_0 not well-defined • $3 < A_0 > 2$ • Can exhibit a large standard deviation
	Type D	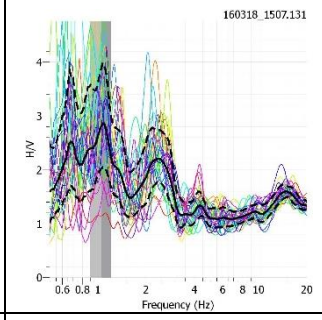	• Several peaks or low frequency plateau (or one very low amplitude peak) • f_0 hard to define • $A_0 > 2$ (or $A_0 \approx 2$ if one peak) • Large standard deviation at low frequency
	Type E	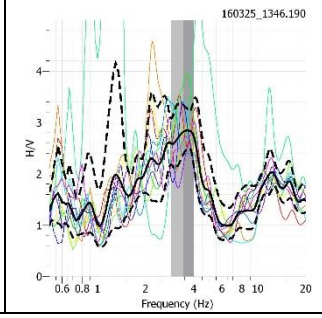	• Curve determined with a few time windows or mostly flat curve but not exactly a flat curve characteristic of a rock site • f_0 hard or impossible to define • $A_0 < 2$ • Large standard deviation (if only a few time windows)

Five groups are defined: A, B, C, D and E where A designates mHVSR containing a well-defined and very sharp peak and E designates curves on which no clear peak is identified according to the SESAME European project criteria (European Commission, 2004). The considered quality criteria are given for each group. In total, 439 sites were investigated but only 357 ambient vibration measurements are used in the model of the LVV. Indeed at 82 sites, recordings show no sufficient windows to be analyzed or the vibration are due to close and sustained anthropogenic sources and so they are not further considered. Among the 357 remaining curves, 115 are classified in group A, 122 in group B, 62 in group C, 38 in group D and 20 in group E.

This classification is a preliminary analysis of the ambient vibration data and allows to have an overview of the data uncertainty in the studied area as seen in Figure 80. The distribution of the different quality classes appears to be heterogeneous all along the valley. It is observed that, at the estuary of the Var River, the quality of mHVSR is mostly in group A. Furthermore, it can be noticed that the mHVSR quality seem better in the lower part of the Var valley and specifically, on the left bank of the river. On the contrary, data on the right bank of the river should be analyzed and interpreted carefully due to the major presence of low-quality mHVSR.

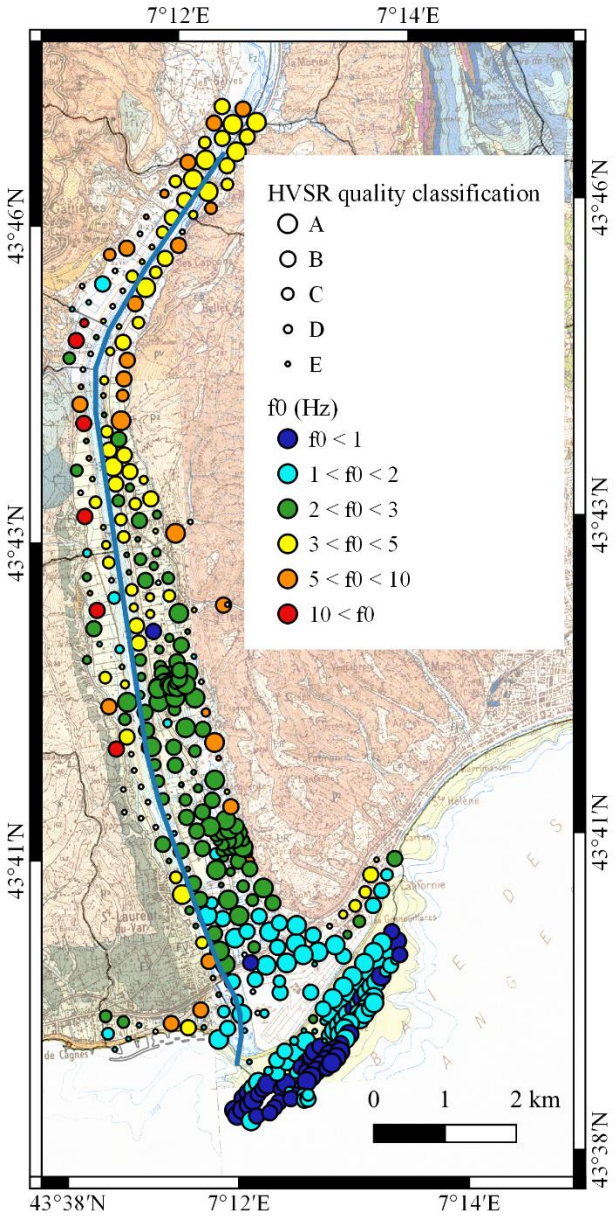

Figure 80: Distribution of the f_{s0} and the quality classification of mHVSR in the LVV.

IV.3.2.2 Distribution of the f_{s0} in the quaternary sedimentary basin

Figure 80 shows the distribution of the f_{s0} considered on mHVSR as related to the Quaternary-Pliocene interface through the valley.

From the south to the middle of the valley, especially on the left bank of the river, the frequencies tend to increase from 1 Hz to 3 Hz, suggesting a slightly decreasing thickness of the sedimentary basin toward the north. From the southern right bank to the northern part of the LVV, the f_{s0} values are very variable between 0.7 Hz and 13 Hz. This zone covers the edge and

the center of the valley where the Var River is, which corresponds to a large difference in the basin thickness at short distances. Also, this zone includes most of the ambient vibration measurements where mHVSR double peaked are observed. As mentioned before, these curves are generally detected in the middle of the valley and in the northern part of the LVV. The estuary of the Var River is characterized essentially with low frequency peaks around 1 Hz. These values are consistent with the large sedimentary thickness assumed at the Var estuary (Guglielmi, 1993; Dubar, 2012; Kopf et al., 2016; Migeon et al., 2016).

IV.4. Seismic wave velocity in the sedimentary basin

The V_s in the LVV basin is estimated using two different approaches. First, the velocity is computed from punctual investigation sites. Second, a seismic velocity zonation in the LVV is developed to take into account all the available data (geotechnical and geophysical) and also, the horizontal spatial variability of the V_{sz}.

IV.4.1. Punctual investigation of V_{sz}

Punctual investigations of V_{sz} have been performed in the LVV in the form of cross holes and AVA and MASW campaigns (Figure 81). Seismic wave velocities are constrained in the basin at depth only from the AVA campaign (site I). This analysis allows to have a first insight of the V_{sz} in the sedimentary basin.

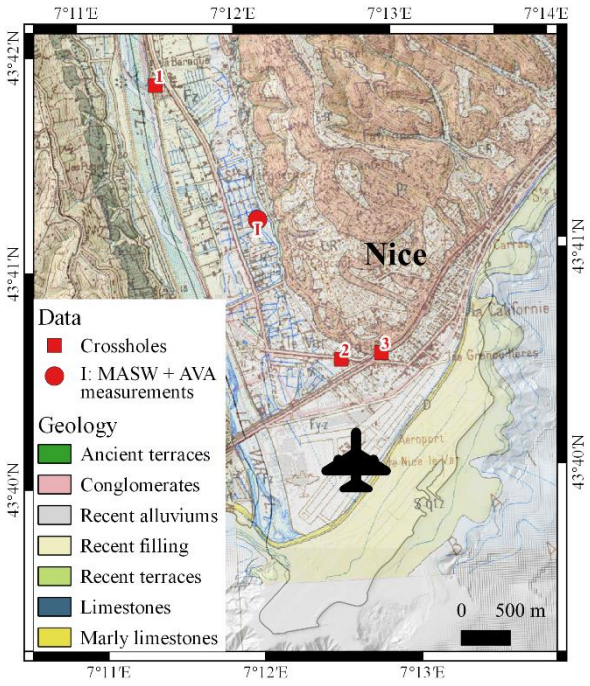

Figure 81: Localization of the sites in the LVV where seismic wave velocity is estimated.

AVA and MASW measurements are jointly analyzed to investigate V_{sz} in the whole quaternary sedimentary basin. The spatial autocorrelation method (Aki, 1957) and the f-k method (Aki, 1957) that provide respectively low frequency (< 5 Hz) and moderate frequency (5 – 15 Hz) information are used to analyze the AVA data. The active seismic data are analyzed using the MASW method (Park et al., 1999; Foti et al., 2017).

We combine the Rayleigh waves dispersion curves obtained from both active and passive seismic surveys in the inversion process to obtain better constraints for the definition of the velocity profiles. When a geotechnical borehole is available in the vicinity of the measurement point, the description log of the borehole is used to define the first model of the inversion.

The combined inversion of the theoretical dispersion curves and mHVSR is performed using a non-linear neighborhood algorithm using the *Dinver* software (Wathelet et al., 2008). The inversion of the mean of the dispersion curves and mHVSR for each investigated site has been performed to constrain both source of data. In fact, the MASW method does not give a unique solution and the mHVSR method has uncertainty on V_s and H parameters according to Eq.(86)

$$f_0 = \frac{V_{sz}}{4H} \tag{86}$$

where f_{s0} is the fundamental resonance frequency at each measurement point [Hz], V_{sz} is the average S-wave velocity above the bedrock [m.s^{-1}] and H is the quaternary sedimentary thickness [m]. Both methods are complementary in the way that they compute V_s in the same frequency domain. The uncertainty of V_s profiles is then reduced by crossing results from each method.

Results from inversion process for each investigated sites are:

- Several V_s profiles ;
- Several theoretical dispersion curves ;
- Several mHVSR ellipticity curves.

The number of runs depends of the minimum standard deviation reached by the inversion process. When the standard deviation becomes stable, the inversion process considers having the best velocity model. Finally, for each studied site, the velocity model having the minimal standard deviation is extracted.

The extracted velocity model is integrated in a *MATLAB*® code that solves a direct problem. The direct problem consists to use present data (here the best velocity model) to define physical data (here the theoretical dispersion curves). Thus, the superposition of the theoretical dispersion curves found using the direct problem on the results from the f-k method enables to valid assumptions made during the inversion process.

According to the results of V_{sz} profiles (Figure 82), a superficial layer with V_s around 250 m.s^{-1} is found followed by a soil layer characterized by a V_s of 380 m.s^{-1} until 30 m depth in the basin above the bedrock. However, as the measurements are located at the edge of the basin, they are not well representative of the overall V_{sz} in the quaternary alluvial deposits of the valley. Considering that the basin is deeper along the Var River, we assumed that V_{sz} should be slightly higher than V_{sz} found here. Thus, we first assumed that the basin is composed of one homogeneous sedimentary layer and estimated constant V_{sz} equals to 400 m.s^{-1} all along the basin.

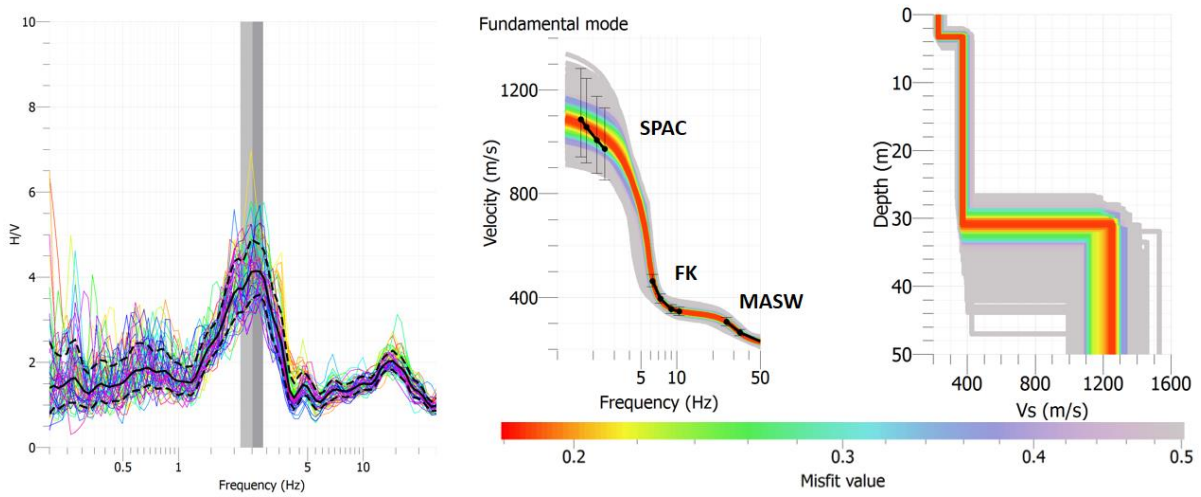

Figure 82: Microtremor HVSR, Rayleigh waves dispersion curve (phase velocity) and inverted V_s profiles at point I in the sedimentary valley. The color scheme for V_s profiles corresponds to the error between the theoretical models generated by the inversion process and the observed data (reddish color correspond to lower misfit).

The V_s value of each sedimentary layer defined for the microzonation of the city of Nice (Régnier et al., 2020) (Figure 78) have been fitted to the sedimentary layers of the lithostratigraphic soil profile of the LVV. In fact, even if the sedimentary layering seems to be similar between the lithostratigraphic soil profiles, the one of the LVV shows slight discrepancies in sediment material. This material is mainly fine in the soil profile of Nice compared to the one of the LVV that contains pebbles due to the stronger energy of the hydrological system of this area. Therefore, we could expect an increase of the V_{sz} values.

The cross holes are interpreted as function of the lithostratigraphic soil profile of the LVV. For each investigated sites, the depth of each sedimentary interfaces from the 3D model is placed in parallel with the obtained velocity profile to assign a mean velocity value to each sedimentary layer (Table 31). For more information, the velocity profiles from cross holes 2 and 3 are presented in Appendix 5.

Table 31: Description and interpretation of the velocity profile from the seismic surveys in site I and from available cross holes in the LVV.

Site I		Lithostratigraphic soil profile of the LVV
Depth (m)	**V_s (m.s^{-1})**	**Interpretation**
0-4	240	layer 1
4-12	435	layer 2
12-17.6	269	layer 4
17.6-44.6	435	layer 5
44.6-50	1080	bedrock
Cross hole 1		
Depth (m)	**V_s (m.s^{-1})**	**Interpretation**
0-10	318.55	layer 1
10-20	454.82	layer 2
Cross hole 2		
Depth (m)	**V_s (m.s^{-1})**	**Interpretation**
0-30	227.75	sediments
Cross hole 3		
Depth (m)	**V_s mean (m.s^{-1})**	**Interpretation**
0-7	337	sediments
7-30	1183.79	bedrock

Table 32: Description of the estimation of the V_s value for each sedimentary layers of the lithostratigraphic soil profile of the LVV. The unity is in meter per second.

Layer	Estimated V_s (m.s^{-1})	*Why this value ?*	Uncertainty (+/-) (m.s^{-1})
1	240	*site I is a good compromised between the results of the different cross holes, taking into account the uncertainty given by the cross holes*	165.95
2	435	*based on site I*	14.015
3	350	*intermediate V_s value, the geology presents softer material than layer 2 but older and harder than layer 4*	no data
4	270	*based on site I*	no data
5	435	*based on site I*	no data
6	400	*same assumed layer than layer 3, but older and harder*	no data
7	350	*same assumed layer than layer 4, but older and harder*	no data
8	500	*same assumed layer than layer 5, but older and harder*	no data
9	700	*same assumed layer than layer 8, but older and harder*	no data
R	1290	*V_s value from seismic field campaign on rock around the LVV basin, close to the V_s value found in cross holes 2 and 3*	no data

The compressional wave velocity (V_p) is deduced using the equation:

$$V_p = V_s * \sqrt{3} \text{ for rock} \quad (87)$$

$$V_p = V_s * 2.5 \text{ for sedimentary layer.} \quad (88)$$

IV.4.2. V_{sz} zonation in the basin

A map showing the horizontal spatial distribution of V_{sz} through the valley is proposed. This map results from the definition of a velocity zonation by combining borehole and ambient vibration data.

First, the horizontal spatial variability of the V_{sz} in the valley is studied analyzing jointly the deep geotechnical boreholes and the mHVSR. The boreholes reaching the bedrock help to constrain the basin depth locally. Combined with nearby f_{s0} from mHVSR, we obtain V_{sz} at each position of deep boreholes according to the well-known Eq.(86). The result shows a large spatial variability of this velocity in the sedimentary soil profile of the valley. A velocity zonation is thus proposed to refine V_{sz} in the quaternary sedimentary basin. The zonation is established from the interpolation of the punctual V_{sz} previously estimated, using the nearest neighborhood algorithm and taking into account the geomorphological structure of the valley. We consider that the valley is deeper along the Var River which implies larger V_{sz}. Indeed, the deeper sediments, as more compacted and thus are characterized by a larger V_{sz} than the superficial ones. The resulting velocity zonation includes 4 zones for which the velocity in the recent sediments varies between 100 m.s^{-1} and 700 m.s^{-1} (Figure 83).

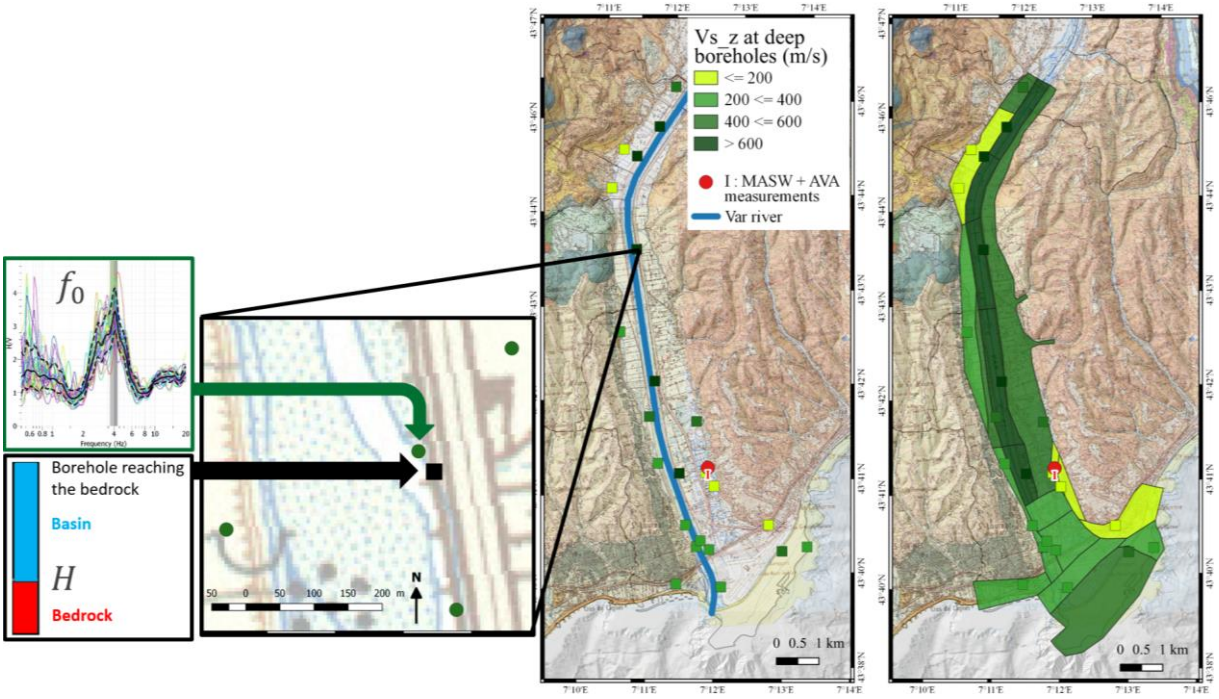

Figure 83: V_{sz} zonation in the LVV. The squares indicate boreholes reaching the bedrock.

Note that the velocity at the airport is found to be higher than 500 m.s^{-1}. This result is in agreement with available geotechnical surveys and laboratory tests showing a high consolidation of the embankments under the landing strips (Serratrice, 2009).

IV.5. Seismic wave velocity in the engineering bedrock

The bedrock geology and its depth have already been the subject of geological, geophysical and hydrogeological studies in the valley (Horn et al., 1965, 1980; Pline, 1991; Guglielmi, 1993; Sultan et al., 2010; Mangan et al., 2012). Guglielmi (1993) suggested that the ante-Pliocene bedrock is structured by faults and tilted blocks. Pliocene conglomerates contain marl lenses heterogeneously distributed and are considered as the impermeable bedrock in studies concerning the water table of the Var valley (BRGM, 2010; Du, 2016). Therefore, it exists lateral variability of the bedrock nature all along the valley. For sake of simplification, in most of the studies, the bedrock is considered as composed by the Pliocene conglomerates. We assumed, in this work, that the engineering bedrock of the LVV is composed of homogeneous Pliocene conglomerates in order to simplify the model. The engineering bedrock represents

rock, or rock-like geological formation characterized by a V_s larger than 800 m.s^{-1} following classification criteria based upon the European building code for seismic design (CEN, 2003).

The geological complexity of the LVV and the uncertainty on the seismic wave velocity in the deep rock of the valley lead to investigate four different sites around the Var valley in addition to the measurements of the dense ambient vibration campaign on the basin. The seismic wave velocity of the engineering bedrock of the valley is investigated through simultaneous MASW survey and single ambient vibration measurements (Figure 76).

IV.5.1. Investigated rock sites

The rock sites are located (Figure 84):

- P1: in the cemetary of Caucade in Nice;
- P2: in the village of La Gaude;
- P3 and P4: around Saint Laurent-du-Var city.

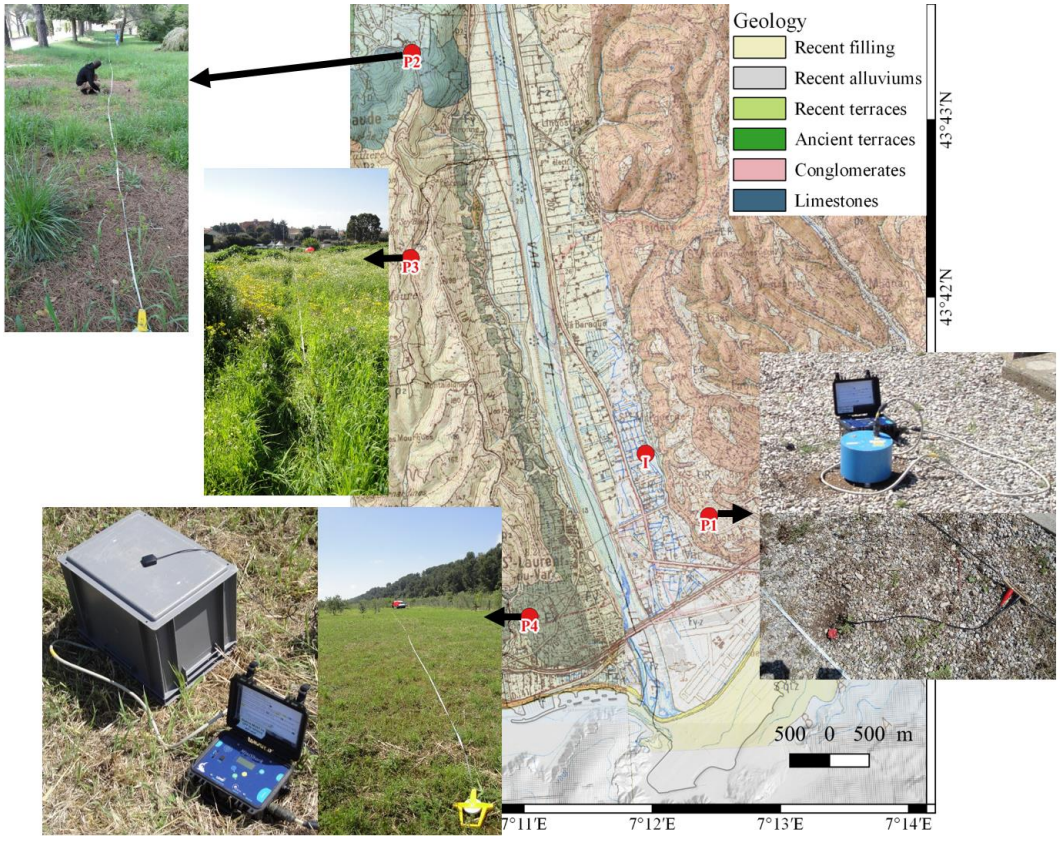

Figure 84: Illustration of the seismic surveys around the LVV to estimate the seismic wave velocity in the engineering bedrock.

For each investigated site, one MASW profile and one single ambient vibration measurement were jointly performed to better constrain the wave propagation velocities in the rock. More description about the material and about the method analysis can be respectively found in section IV.3.1 and in Appendix 6.

Some boreholes are located close to the investigated rock sites P1, P2 and P4 and help to have an idea of the geology of the soil column and of the underlying bedrock altitude. These geotechnical data are useful in the interpretation of the V_s profiles. They are described in Table 33.

Table 33: Description of the boreholes located close to the investigated rock sites.

Rock site	Borehole ID (from BSS*)	Borehole n°	Location (Date)	Lat. (°)	Long. (°)	Depth (m)	Description
P1	BSS002 HHTW	10001X0 345/S	Nice	43.67	7.21	32.7	0-0.6m: filling 0.6-1.4m: silty sand 1.4-…: conglomerate
	BSS002 HHUU	10001X0 411/F3	Nice	43.67	7.21	64.2	0-4.6m: filling 4.6-9.4m: silty sand 9.4-…: conglomerate
P2	BSS002 HEUZ	09994X0 397/S1	La Gaude (1976)	43.73	7.16	25.3	0-6m: scree (limestone, marl, clay) 6-17.3m: fissured limestone
P4	BSS002 HFBC	09994X0 556/F	St Laurent-du-Var (2009)	43.67	7.18	70	Water
	BSS002 HESG	09994X0 178/S	St Laurent-du-Var (1968)	43.66	7.18	18	0-2.5m: red clay 2.5-14.2m: clay sand 14.2-18m: conglomerate
	BSS002 HEUX	09994X0 395/S5	St Laurent-du-Var (1976)	43.66	7.18	13	0-1.2m: brown silty sand 1.2-4.5m: clay 4.5-5.1m: clay gravels 5.1-6m: silty sand 6-6.8m: pebbles, clay gravels 6.8-10m: silty sand
	BSS002 HFDV	09994X0 621/06S C10	St Laurent-du-Var (2015)	43.66	7.18	40	0-1m: topsoil 1-3.9m: clay sand 3.9-7.7m: pebbels and gravels 7.7-32m: silty sand 32-33m: pebbles and gravels 33-40m: sand and pebbels

*Banque de données du Sous-Sol (BRGM)

IV.5.2. mHVSR curves

The mHVSR of each investigated site are different. Globally, the standard deviation of the curves tends to increase in the low frequencies. The ones at site P1 show no peculiar peak and varies around 1.8 slightly exceeding 2 at 4, 15 and 20 Hz. The mHVSR at site P2 present a clear peak at 20 Hz. The curves at site P3 show very low frequency amplification (at 0.6 Hz) with large standard deviation. A large peak, maybe composed of two peaks, is observed around 3.5 Hz. And a sharp peak is noted at 25 Hz. Finally at site P4, a large peak reaches 2.4 at 1.8 Hz, another are observed at 7 Hz and 25 Hz.

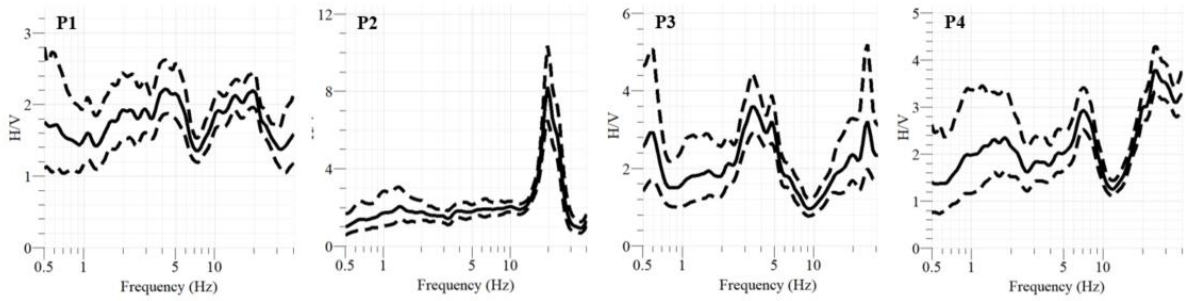

Figure 85: mHVSR at each investigated rock sites around the LVV from the single ambient vibration measurement with recording duration of 30min.

IV.5.3. Seismic velocity profiles

As in the section IV.4.1, we combine the Rayleigh waves dispersion curves obtained from both active and passive seismic surveys in the inversion process to obtain better constraints for the definition of the velocity profiles. The parameters used in the inversion process are presented in Appendix 7. Layers are linked by the V_s. Because we analyzed the seismic wave velocity in rock, we assumed for simplification that the parameters values of bottom layers are always higher than the layers above. In fact, the probability to have velocity inversion in rock medium is considered low.

Several tests were performed in order to obtain the velocity profile considered to be the best for each investigated rock site. For site P1, the definition of the velocity profile was made with no consideration of the mean mHVSR curve. For site P2, the Fourier spectrum was only computed from the data of the seismic network with the in-between sensors distance of 3 m. To obtain the velocity profile, V_s was supposed to range between 100 and 1000 m.s^{-1} up to 100 m depth

knowing the geology at this site. For site P3, the mean velocity dispersion was interpreted as related to the first higher mode of the soil.

The seismic velocity profiles from the inversion of combined MASW and mHVSR results are presented in Figure 86 and detailed in the Table 34. When borehole log-stratigraphy were available nearby investigated sites, the depth at which the velocity changes had been compared to the depth of the different lithology observed on borehole data. It is the case for the sites P1, P2 and P4 (Table 33).

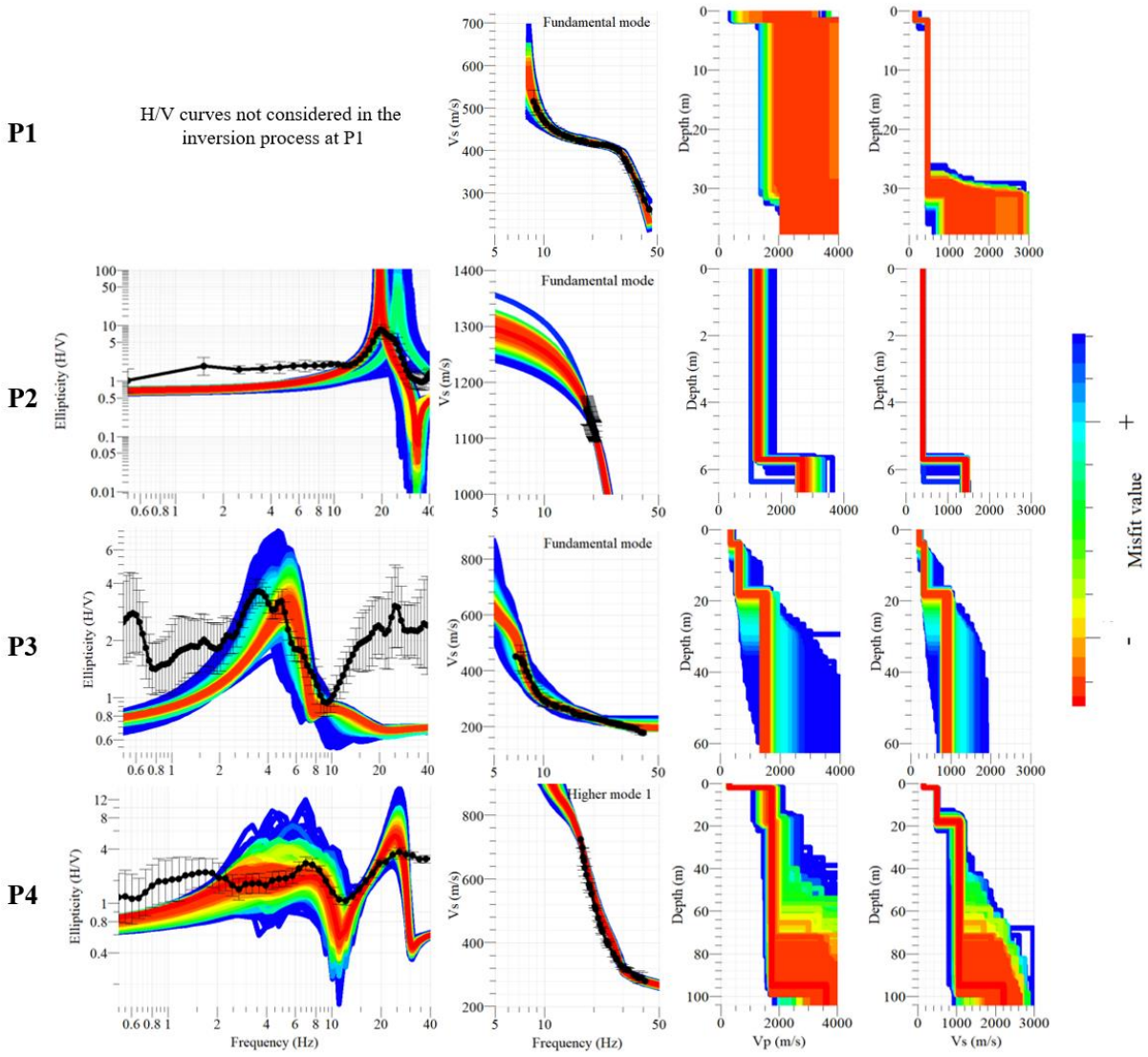

Figure 86: Microtremor HVSR, theoretical dispersion curves and V_s profiles from inversion process at each P site for the estimation of the seismic wave velocity in the bedrock.

Table 34: Velocity profiles for the estimation of the seismic wave velocity in the bedrock at each P site.

Rock site	Layers	Deep (m)	V_p (m.s^{-1})	V_s (m.s^{-1})	Geological interpretation
P1	1	1.6	2721	150	Superficial soil
	2	27.7	2724	466	Sandy silts
	3	Inf	2729	1040	Conglomerates
P2	1	6	1263	406	Superficial soil
	2	Inf	2679	1435	Limestones (fractured)
P3	1	4	346	212	Anthropogenic deposits
	2	18	635	327	Sand gravels
	3	Inf	1451	889	Conglomerates
P4	1	2	245	150	Superficial soil
	2	16	709	434	Ancient alluvium
	3	89	3062	1294	Conglomerates
	4	Inf	4225	2586	Limestones

The results show that the inversion of combined MASW and mHVSR data gives a soil profile close enough to the one observed on borehole log-stratigraphy nearby. An example is presented in the Figure 87. The V_s considered in the conglomerates is around 1300 m.s^{-1} and appears on the model at 15 – 16 m depth. By studying the borehole in the vicinity of the measurement, conglomerates are identified from 14.2 m depth. Layers interfaces are then in the same order of magnitude and indicate that the inversion results are rather coherent with borehole data for these sites.

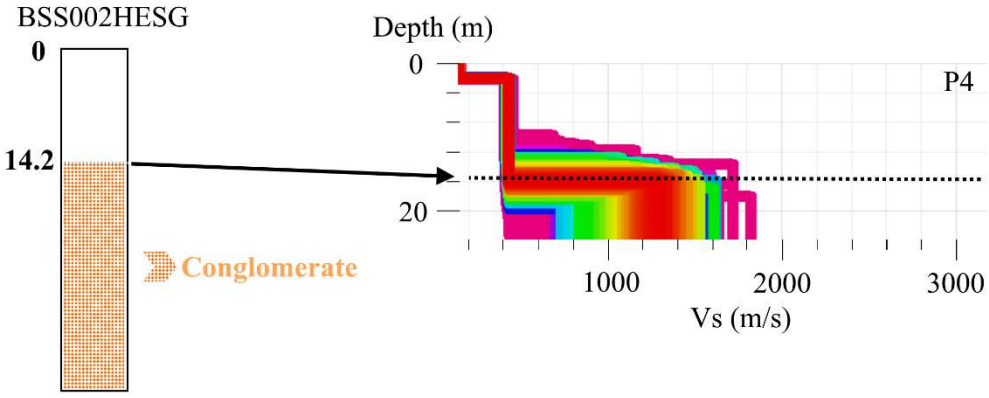

Figure 87: Example of a borehole log-stratigraphy close to the P4 site (BSS002HESG from the BSS database) (left) and velocity profile at P4 site (right).

P1 is on a Pliocene conglomerate outcrop. On the V_s profiles at this site, one layer of 2 m thick with V_s equals to 150 m.s^{-1} is observed. The layer lies on a thicker one that reaches 30 m depth with well constrained V_s equal to 450 m.s^{-1}. From 30 m depth, the standard deviation increases and reaches around 1 000 m.s^{-1}. We note that V_p is not well constrained at this studied site with values between 2000 and 5000 m.s^{-1} (Table 34 and Figure 86).

The velocity profile at site P2 is associated to a bilayer model considering the geological structure at this site (Table 33). This site is characterized by limestones in the village of La Gaude. One interface is well observed on the V_s profile. It delineates a first layer up to 6 m depth with V_s equals to 400 m.s^{-1}. The second layer has V_s equals to 1400 m.s^{-1} that is well constrained by the inversion process. V_p is well constrained too. For the first layer, V_p reaches 1300 m.s^{-1} and for the second layer it reaches 2700 m.s^{-1} (Table 34 and Figure 86).

For P3 site, the velocity profile is associated to a 3 layers model considering the geological structure at this site (a landfill in a small valley). The penetration depth at this site does not allow to observe the impedance contrast between conglomerates and limestones. Considering the dispersion curve, the velocity is well defined between 6 and 40 Hz with a standard deviation of 100 m.s^{-1}, where the plotted dispersion curve is. Below 6 Hz, the standard deviation reaches 1000 m.s^{-1} and the velocity varies between 600 and 1700 m.s^{-1} for a same frequency value. Note that the best results tend to show a V_s around 800 m.s^{-1} in low frequencies and 200 m.s^{-1} in high frequencies. The mHVSR ellipticity curve shows a maximum of energy between 5 and 6 Hz. However, according to the mHVSR theoretical curve, the ellipticity peak is shifted toward high frequencies. This results from the combined inversion of MASW and mHVSR results. In fact, the process tries to fit theoretical results from both methods. Considering the velocity profiles of the site P3, two interfaces are identified. The first one delimits a superficial layer up to 4 m depth with V_s equals to 200 m.s^{-1}. The layer below the superficial one has V_s equals to 300 m.s^{-1} and reaches 18 m depth. The last one, bounded by the second interface indicates a V_s equals to 900 m.s^{-1}. The V_p is as well constrained as the V_s and reaches 1400 m.s^{-1} at 18 m depth (Table 34 and Figure 86).

At site P4, the velocity profile is associated to a 4 layers model considering the geological structure at this site. The first layer barely reaches 2 m thick with V_s equals to 150 m.s^{-1}. The second layer sinks down to 16 m depth and shows V_s equals to 400 m.s^{-1}. The below layer reaches 90 m depth with V_s equals to 1300 m.s^{-1}. The last layer has a high V_s value equivalent

to 2600 m.s^{-1}. For this measurement site, the V_p is well constrained up to 16 m depth (Table 34 and Figure 86).

From three of the obtained velocity models that were carried out on both sides of valley, the Pliocene conglomerates show V_s ranging from 900 m.s^{-1} to 1300 m.s^{-1}. A V_s gradient depending of the depth is observed. At the surface, V_s is around 900 m.s^{-1} and reaches 1300 m.s^{-1} from 18 m depth. This gradient is retrieved at both sides of the sedimentary basin of the LVV. The V_s in ancient alluvial terraces is equal to 400 m.s^{-1}. However this value does not necessarily characterize this kind of geology because the same value is retrieved at the site P2 in alluvial soil. The velocity in the limestones varies between 1400 m.s^{-1} and 3000 m.s^{-1} depending on its alteration state and the depth of the lithology (Table 34 and Figure 86).

IV.6. 3D model geometry

IV.6.1. Methodology

The *GDM* (Geological Data Modeling) software released by the BRGM (Bourgine, 2018) is used to build the 3D model of the LVV. This software allows to create geological models in three dimensions from different data, such as boreholes, geological limits, punctual measurements, among others. The software is used to interpolate the Quaternary-Pliocene interface and all the sedimentary layers within the basin. Several interpolation methods can be used in the software. The interpolation method considered in this study is a krigeage approach (Matheron, 1969; Gratton, 2002) which interpolates by honoring each measurement point and taking into account the spatial density of measurements. In the calculation, the method uses a linear model of variogram of slope equal to 1. In mathematical words, the half variance of the difference between two points separated by a certain distance is computed. More details can be found in Appendix 8. To accurately perform the interpolation, it is necessary to define the interpolation limits. Here, the limits of the recent quaternary deposits from a 1/5000e geological map (Bertrand et al., 2007a; Régnier et al., 2020) are considered as the interpolation limits. To model these limits, fictive boreholes have been created all around the valley where the bedrock altitude is set at the same altitude than the digital elevation model (DEM).

In the case of the model of a valley, the basin thickness is identified by *GDM* as “fin de passes de sondage” at each local constraint. It means that *GDM* assigns the value of the basin thickness

at one investigated site to the depth of the bedrock interface at this same investigated site (Figure 88). When the basin-bedrock interface is not "seen" by the local constraint or sedimentary layer is not bounded in the borehole data, *GDM* assumes the floor of the last sedimentary layer as the last layer in the model even if there is deeper sedimentary material. After loading the DEM and the database of the basin thickness, the interpolation of the basin-bedrock interface is performed. More details about the building process of the 3D model can be found in Appendix 8.

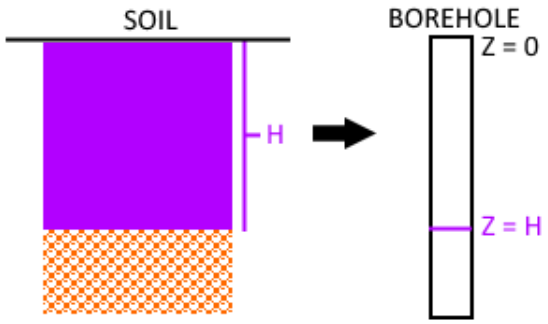

Figure 88: Attribution of the basin depth to the basin-bedrock interface altitude.

Sometime, the interpolation value of the basin-bedrock interface is higher than the DEM value. The *GDM* software allows to correct this error by bringing the value back to the one of the DEM using Eq.(89)

$$z_{bedrock} = \min(z_{bedrock}; z_{DEM}). \quad (89)$$

The estimation of the uncertainty linked to the fusion of different types of data can be difficult to realize. In fact, the simple addition of the uncertainty of each type of data to compute the mean uncertainty can lead to wrong interpretations because of the equal weight assigned to each data. Some probabilistic studies focus on the subject of the combination rules also called "belief functions" (Smets, 1990; Wang, 2019; Dezert et al., 2019). These functions are based on the evidence theory (Dempster, 1967; Shafer, 1976). This means that they estimate the occurrence probability of an event from the merge of data from different sources and assign a specific weight for each data. These methods are powerful when the studied object is roughly known. Indeed, it is necessary to have sufficiently strong clues even if it is a few one, in order to define what they called the "Frame of Discernment" that are the base of the method application. In this thesis, the strong clues are the boreholes reaching the engineering bedrock. Unfortunately, they are not sufficient and well spatially distributed to apply the combination rules (Figure 76).

It is only well known that the basin reaches more than 100 m at the estuary of the Var River. Therefore, we consider separately the uncertainty of each type of data.

IV.6.2. mHVSR double peaks

During the analysis of the ambient vibration data, mHVSR double peaks are observed at some measurement points. Those measurements show a first peak around 1 Hz and another one at higher frequency, generally around 2.5 Hz. Both exhibit generally an amplitude higher than 2 (Figure 89).

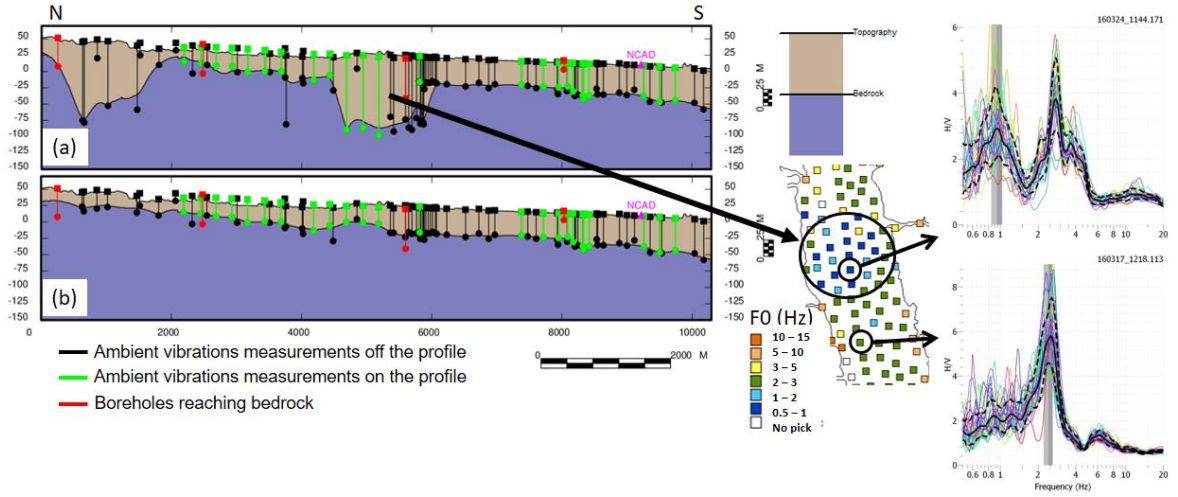

Figure 89: (a) Profile North-South of the geophysical model (based only on ambient vibration data) assuming V_{sz} constant and taking into account the first peak of mHVSR double peaks. (b) Profile North-South of the geophysical model assuming V_{sz} constant taking into account the second peak of mHVSR double peaks. Green lines on profiles indicate data located in the middle of the LVV. Black lines on profiles indicate data from a band of 200 m width on both sides of the middle of the valley. Indicated boreholes are located all along the valley.

In order to know which peak is associated with the f_{s0} of the site, a first model of the LVV is elaborated considering a single homogeneous sedimentary layer in the basin to have a first overview of the geometry of the basin-bedrock interface depending of the frequency peak. The basin-bedrock interface is only constrained by ambient vibration data (Figure 90).

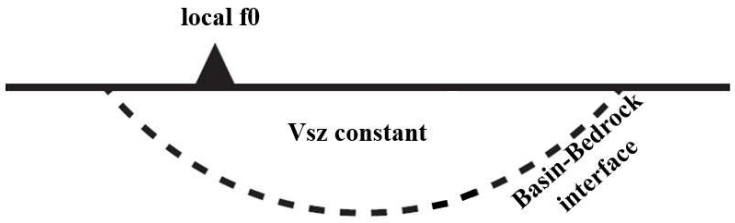

Figure 90: Scheme of the single sedimentary layer model assuming V_{sz} constant.

From the Eq.(86), considering locally a 1D tabular model (defined by the sedimentary basin and the bedrock) and taking into account V_{sz} = 400 m.s^{-1} in the basin, the sedimentary basin thickness is computed for each single ambient vibration point in the valley according to the considered frequency peak. For the first model (Figure 89(a)), we identified the first peak of mHVSR double peaks around 1 Hz as the basin resonance frequency. For the second model (Figure 89b), we identified the second peak of mHVSR double peaks in higher frequencies as the basin resonance frequency. Note that the profiles presented in the Figure 89 are longitudinal profiles (North-South) of the LVV taking into account data from a band of 200 m width on both sides of the middle of the valley.

Discrepancies between the models appear at measurement points where the mHVSR showed double peaks. The use of the first peak of the mHVSR as the f_{s0} at all measurement points leads locally in a deeper bedrock interface. Therefore, in the first model (Figure 89(a)), we observe the presence of two specific areas, in the north and in the middle of the valley, where the basin thickness reaches more than 100 m. Yet, there is no geotechnical or geological evidences for the existence of these deep bedrock zones at the time of the study. Those areas are not observed in the second model (Figure 89(b)). In this later model, the sedimentary basin depth is characterized by greater spatial coherency.

In the majority of studies, the first peak of mHVSR is considered as the f_{s0} of the sedimentary layer overlying the bedrock. Generally when double peaks are observed, the second peak is due to another strong impedance contrast within the sedimentary layers, mechanical discontinuities at depth (i.e. Mascandola et al., 2019) or to anthropogenic sustained sources. In this study, the second peak of mHVSR is interpreted as the indicator of the impedance contrast between the quaternary sedimentary basin and the Pliocene conglomerate bedrock. This statement is first supported by borehole log-stratigraphy data. Indeed, the boreholes seem to indicate that the basin thickness should not reach more than 50 to 60 m around the longitudinal profile. Moreover, Figure 89 shows very well the consequences on the basin structure of interpreting

the first or the second peak of mHVSR. It should be kept in mind that these profiles are computed assuming a constant V_s in the whole basin. Secondly, the presence of a very low frequency peak on some mHVSR could be the indicator of a strong impedance contrast at depth below the Pliocene conglomerate. It is known indeed that the bedrock is vertically not homogeneous and that under the Pliocene conglomerates, limestones and marls can be found (Larroque et al., 2001).

Therefore, we consider the second peak of the mHVSR double peaks as the f_{s0} of the basin linked to the Quaternary-Pliocene interface of the LVV. In the following, we present three different LVV models that will help to understand the procedure of creating the final multilayer 3D sedimentary basin model.

IV.6.3. Single sedimentary layer model

IV.6.3.1 Homogeneous V_{sz} in the basin

The 3D single sedimentary layer model of the LVV is based only on ambient vibration data assuming V_{sz} constant. The model is presented in Figure 91. The basin thickness appears to be larger at the Var estuary that is consistent with the literature. It reaches more than 100 m deep under the airport platform. Then, the sedimentary thickness rapidly decreases toward the north, reaching in the center of the basin 50 m deep at Y = 43°42N and only 30 m deep at the very north part. According to this model, the bedrock seems to be uplift between Y = 43°42N and Y = 43°43N. This is also showed in Figure 89(b) around 5000 m along the longitudinal axis of the valley where the basin thickness reaches around 25 m deep.

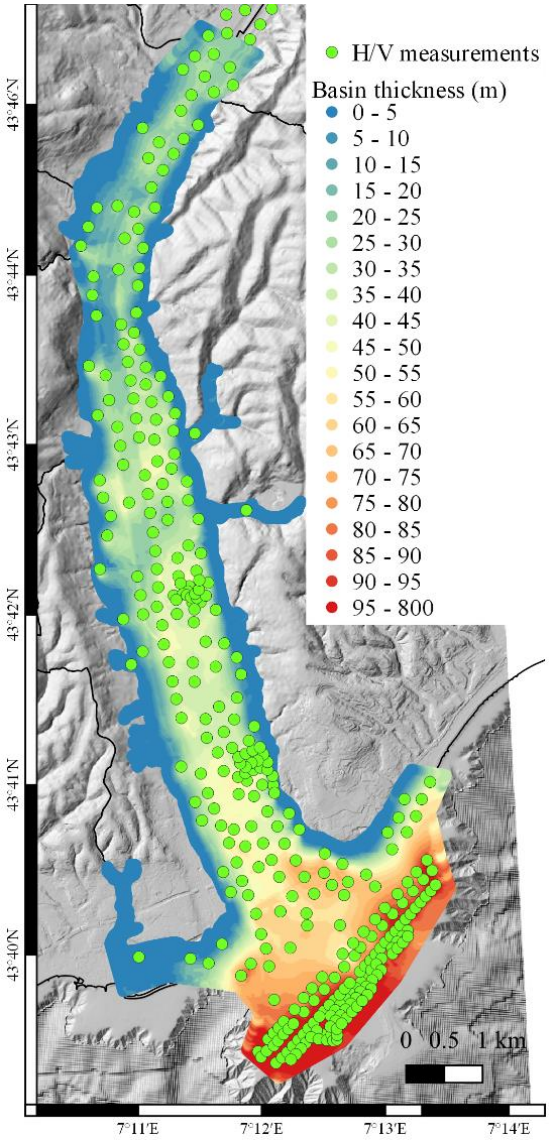

Figure 91: Basin thickness of the LVV from the 3D single sedimentary layer model assuming V_{sz} constant. Green circles are ambient vibration measurements.

The single sedimentary model of the LVV computing from only ambient vibration data presents a symmetric valley with, in the middle of the structure, a smooth slope of the bedrock from the north to the estuary (increasing of the basin thickness of 30 m in 10 km) along with a steep slope at the estuary level (increasing of the basin thickness of 50 m in only 2 km).

IV.6.3.2 V_{sz} zonation in the basin

A 3D single layer model of the LVV is developed taking into account the horizontal spatial variability of V_{sz} all along the valley (Figure 92). This model integrates locally constant V_{sz} profiles in the basin for the estimation of the bedrock depth.

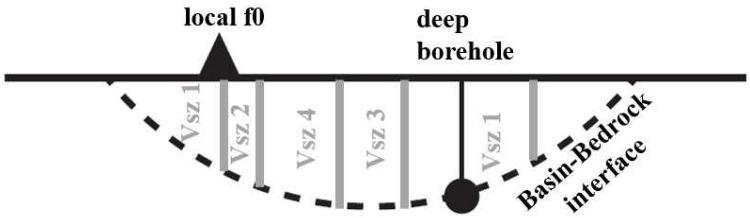

Figure 92: Scheme of the single sedimentary layer model using the seismic velocity zonation.

The basin thickness is computed using the Eq.(86) at each single ambient vibration point in the valley.

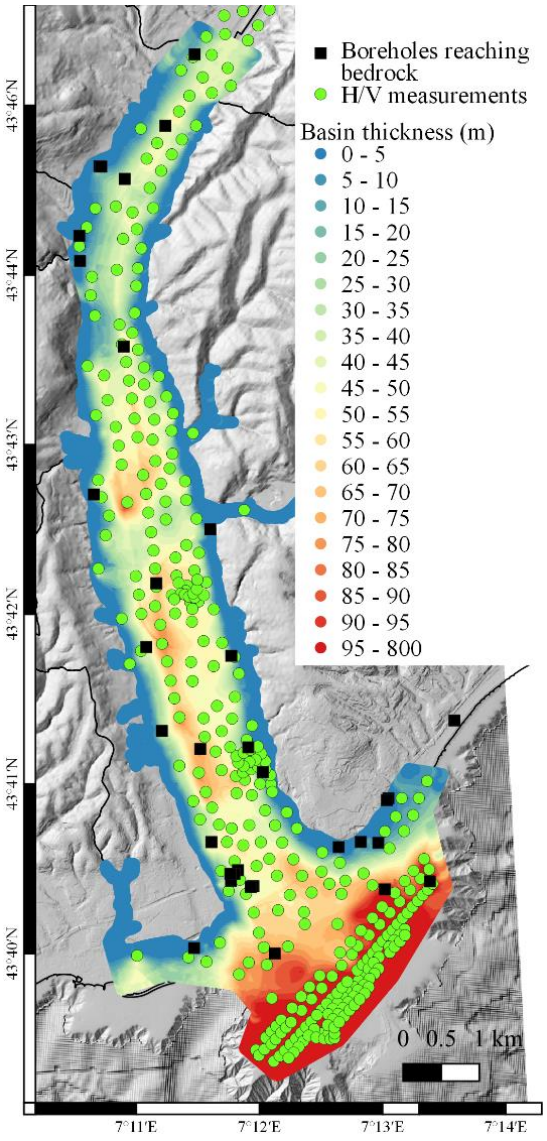

Figure 93: Basin thickness of the LVV from the 3D single sedimentary layer model using the seismic velocity zonation. Dark squares are deep borehole data. Green circles are ambient vibration measurements.

In this model, the bedrock depth is found at 50 m in the north of the LVV and at more than 100 m in the south at the airport in accordance with previous studies (Guglielmi, 1993; Dubar, 2012; Kopf et al., 2016; Migeon et al., 2016) and with the 3D single sedimentary layer model presented before assuming V_{sz} constant (Figure 93). Compared to the first presented single sedimentary layer model, a deep interface is found locally around 80 m depth along the Var River. It is notably constrained by very few deep boreholes (61 m depth and 78 m depth). The basin depth is mainly constrained by the ambient vibration measurements that are numerous compared to the quantity of deep boreholes available.

IV.6.4. Multi-layered model

The multi-layered model of the LVV is developed based on the last presented single layer model. It takes into account no only the horizontal spatial variability of V_{sz} but also, the geometry of the sedimentary layering inside the basin constrained by the borehole log-stratigraphy data (Figure 94).

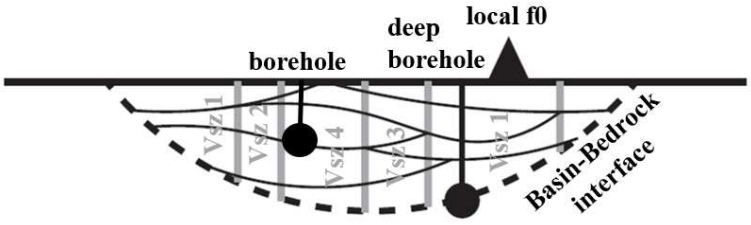

Figure 94: Scheme of the multi sedimentary layer model using the seismic velocity zonation.

Geotechnical data are useful to obtain local values of the bedrock depth as seen in the Figure 93, and they are also useful to detail the sedimentary layers geometry in the valley as shown in Figure 96 that presents a well constrained profile in the model. The improvement of the 3D single layer model does not change the basin-bedrock interface depth through the valley but refined the geometry of the sedimentary layering within the basin.

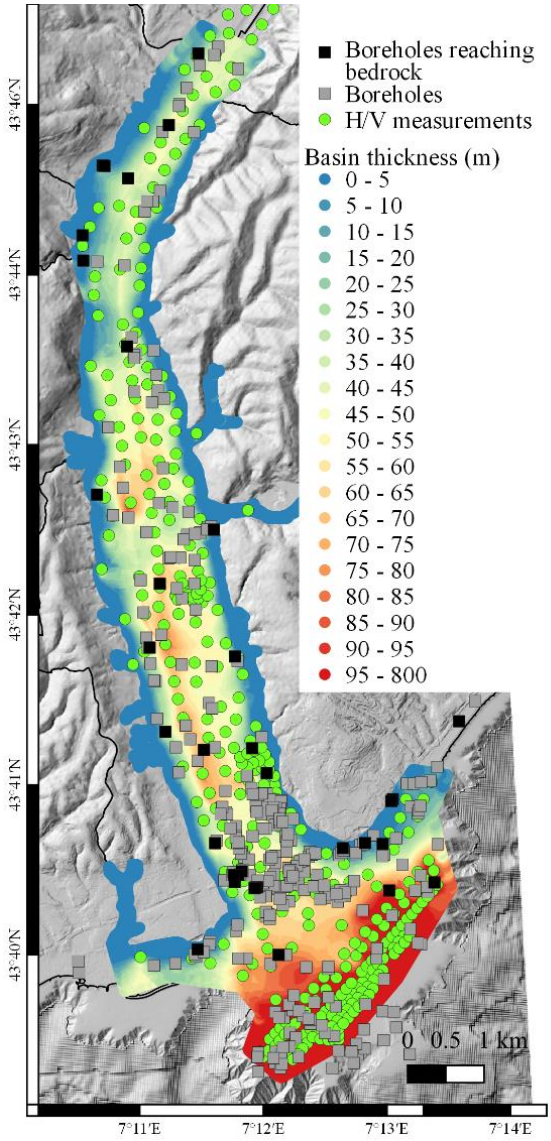

Figure 95: Basin thickness of the LVV from the 3D multi-layered model using the seismic velocity zonation. Squares are borehole log-stratigraphy data. Green circles are ambient vibration measurements.

The Figure 96 illustrates a SW-NE profile crossing the RESIF-RAP stations through the 3D multi-layered model of the LVV. In this part of the valley, the basin thickness reaches 60 m at most. A slight asymmetry of the basin thickness is observed with respect to the middle of the valley. This is different compared to the structure obtained with the single sedimentary model (Figure 91). Moreover, the spatial variability of the sedimentary layering is put in evidence. Actually, the thickness of each layer can be different. For example, on this profile, layer 2 is thicker than layer 3. Some layers are almost nonexistent such as layer 7 and 8. In most cases, the bedrock depth is constrained by ambient vibration measurements (green lines) and not by the geotechnical data (black lines) that do not reach the substratum. The unconstrained layer between the end of the boreholes that are not reaching the bedrock and the bedrock depth

deduced from ambient vibration data and is also indicated in Figure 96 by the maroon color, between ZR and ZR1 interface.

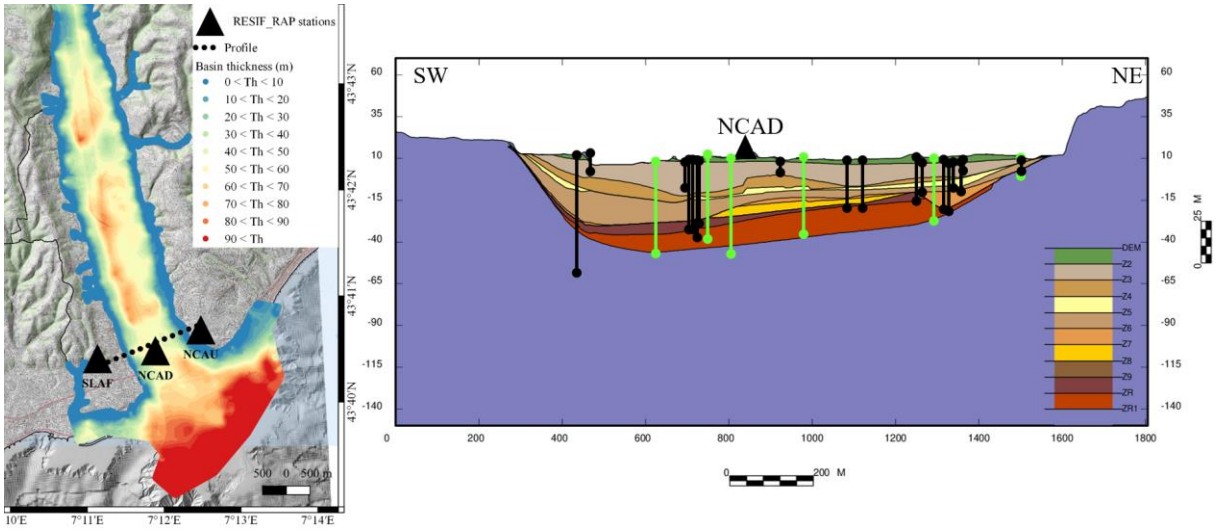

Figure 96: Profile SW-NE in the 3D multi-layered model of the LVV. Different colors represents different layers from the lithostratigraphic profile applied in the LVV (Figure 77). Note that there is one more layer than those defined in the lithostratigraphic profile. It represents the unconstrained layer between the end of the borehole that are not reaching the bedrock and the bedrock depth deduced from ambient vibration data and boreholes reaching the bedrock. The dark lines are boreholes. The green lines are ambient vibration measurements.

Finally, we obtain the 3D multi-layered model of the LVV from the combination of geophysical and geotechnical datasets using a seismic velocity zonation. This model has the advantage to consider not only the spatial variability of site effect in the valley but also the complexity of the sedimentary layering in the basin.

IV.7. Discussion

We made several assumptions in order to build the 3D geotechnical model of the LVV. The first one is the consideration of the LVV as a 1D medium for the interpretation of the mHVSR. The second one is the homogeneity of the engineering bedrock. The last one is the consideration of a velocity zonation where a constant V_{sz} in the sedimentary basin is applied for each defined zone over the valley.

IV.7.1. Hypothesis of 1D medium

The 1D geometry assumption is a strong hypothesis made to use f_{s0} to obtain the basin depth (Lachet and Bard, 1994; Seht and Wohlenberg, 1999; Scherbaum et al., 2003). While this 1D assumption must be true at the center of valley it is likely to be wrong at the edges of the valley. Moczo et al. (2018) numerically showed through several valley structures that there is always an area where the 1D assumption is not sufficient. Tucker and King (1984) also found that 1D resonance is inexistent close to the edge of the valley. The first attempt to parameterize the 2D response can be found in Bard and Bouchon (1985) through time and frequency analysis and latter numerically in Moczo and Bard (1993). Bard and Bouchon (1985) proposed to calculate an aspect ratio that depend on the depth and width of the valley with respect to the velocity contrast between sediment and bedrock. For valleys which have an aspect ratio and an impedance contrast that induces 2D resonance or other complex geometry, the approach of relating the frequency of HVSR first peak directly to 1D frequency of resonance can lead to a wrong interpretation of the valley structure (Roten, 2007). Guillier et al. (2006) showed that HVSR can overestimate by around 15% the resonance frequency at the valley edge for 2D structures, while for 3D structures, HVSR peak frequencies strongly underestimate the 1D resonance frequency at sites with the steepest underground slopes. This happens especially at valley edges or for deep and steep basins, where the horizontally propagating surface waves interfere with vertically propagating waves (e.g. the case of the Grenoble area in Isère valley (Guéguen et al., 2007) or the Rhône valley (Roten et al., 2006) leading to waves conversion and increasing of the ground motion at the surface (Semblat et al., 2005; Moczo et al., 2018). In the case of the LVV, the « critical shape ratio » (Figure 97) calculated at the NCAD profile (Figure 96) indicates that the LVV is composed of a very shallow basin (60 m deep by 2000 m wide) leading to a very low shape ratio of 0.05 for a sediment to bedrock velocity contrast around 2.

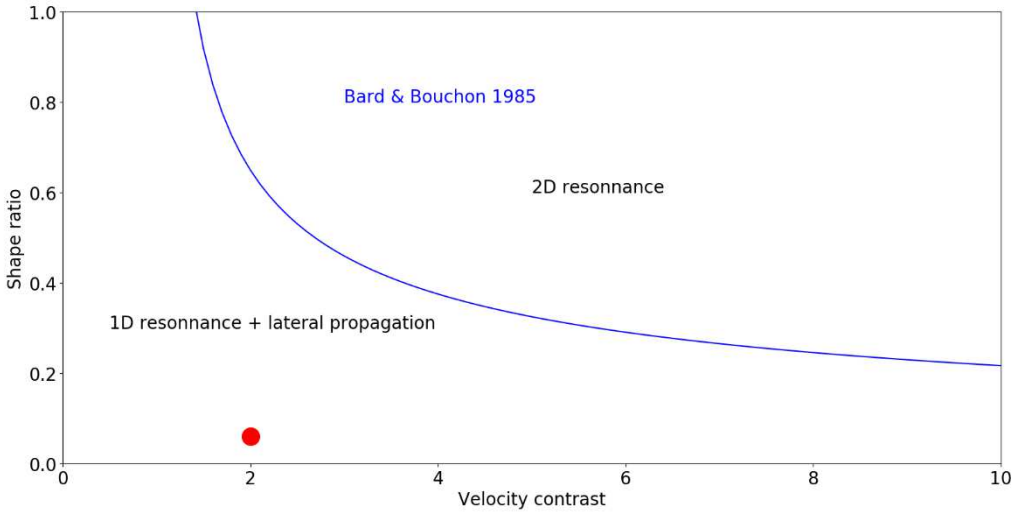

Figure 97: 1D to 2D critical shape ratio as proposed by Bard and Bouchon (1985). The red dot indicates the "critical shape ratio" of the LVV calculated at the NCAD profile.

As indicated in Figure 97, it suggests that the resonance inside the basin is probably dominated by 1D resonance and lateral propagation rather than 2D resonance. The rotational mHVSR at NCAD station support this argument since it does not exhibit an azimuth dependence of the main peak frequency (Figure 98).

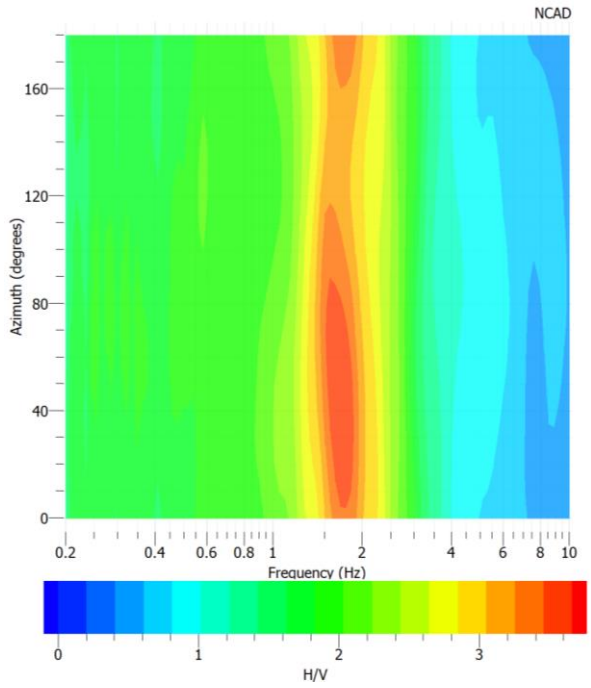

Figure 98: Rotational mHVSR at NCAD station.

However, the difference between the fundamental resonance frequencies observed on the SSR of NCAD/NCAU on horizontal components leads to reinterpret the resonance phenomenon in

the LVV (Figure 75a and Figure 75b). In fact, the fundamental frequency on the longitudinal component is higher than the one on the transversal component. This is incoherent with a valley having 2D resonance for which the fundamental frequency on the longitudinal component is supposed to be lower than the one on the transversal component according to Bard and Bouchon (1985). Sgattoni and Castellaro (2020) presented the case of anisotropic effects in a sedimentary valley. The authors showed that these effects can lead to discrepancies between SSR on horizontal components in a valley where there is a priori no 2D resonance.

Moreover, attention must be paid on the selection of the reference station for the computation of SSR in the LVV. In fact, the lack of assumed good reference station situated close to the Var valley limited the choice to NCAU station. The SSR on both horizontal components at NCAU station were computed using two different reference stations. The first one is NCER located on the eastern part of Nice on limestones. The second one is NOCA located at the Cote d'Azur Observatory on the top of the marly limestones hills surrounding the north eastern part of Nice (Figure 73). The same seismic events as presented in Appendix 4 and the same method are used to compute SSR.

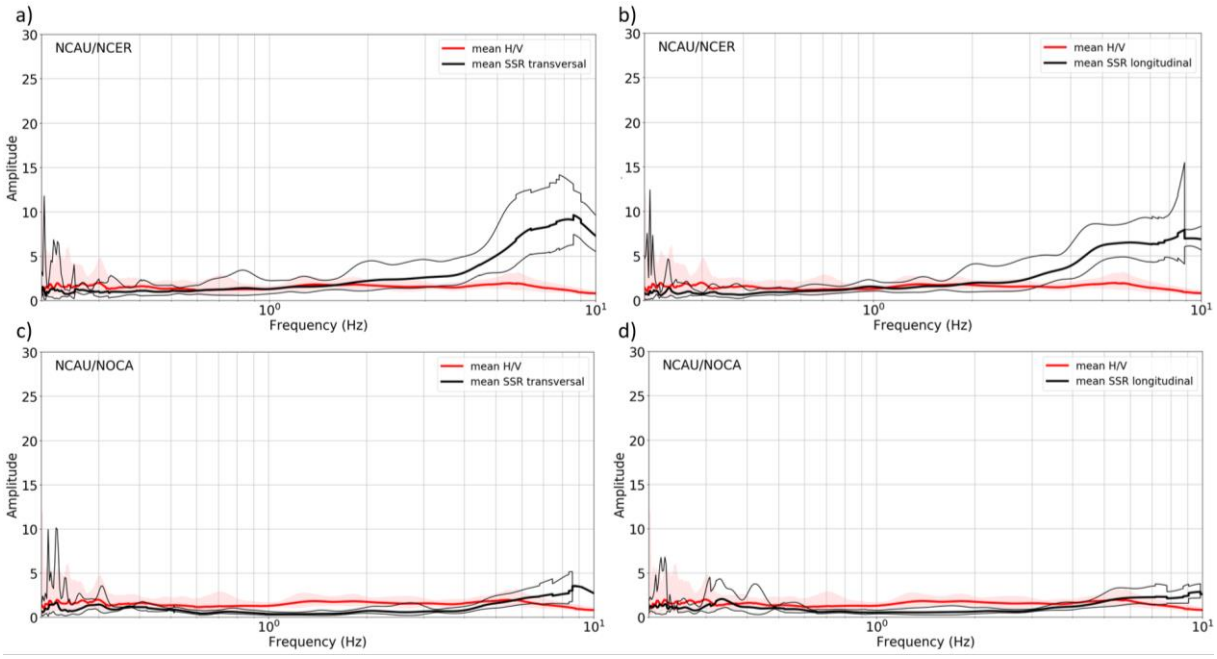

Figure 99: Earthquake HVSR and SSR of the seismic records at the NCAU station located on conglomerates on the hills surrounding the Var valley computed using a Konno-Ohmachi smoothing with b-parameter equal to 20 and considering an angle of π/8. SSR on (a) longitudinal and (b) transversal component computed using NCER as reference station. SSR on (c) longitudinal and (d) transversal component computed using NOCA as reference station.

As the engineering bedrock of the valley is composed of conglomerates and also the site of NCAU, this station seems ideal to use as reference station in SSR. First, the localization is on rock and second it can highlight the amplification of the quaternary sedimentary basin of the LVV. However when analyzing the site response at the NCAU site, it appears that, even if the NCAU site response shows no particular amplification between 0.2 and 3 Hz, it differs from 3 Hz depending on the reference station. An amplification in high frequency range is observed. Considering NCER as the reference station, SSR show a mean amplification on both horizontal components from 3 Hz. This phenomenon is not highlighted when NOCA is considered as the reference station. This result suggest in high frequency range either a deamplification phenomenon on the NCER site response and/or a particular resonance at NCAU site.

IV.7.2. Homogeneous bedrock material

The engineering bedrock is assumed to be composed of homogeneous Pliocene conglomerates. However, studies about the geology in the LVV indicate that Pliocene conglomerates are not the only rock formation underneath the sedimentary basin (Horn et al., 1965, 1980; Guglielmi, 1993; Larroque et al., 2001; BRGM, 2010; Mangan et al., 2012; Du, 2016). Geotechnical borehole log-stratigraphy show locally the presence of marls or limestones directly below the basin. In such a way, a local uncertainty remains regarding the continuity of the Quaternary-Pliocene limit in the LVV. This could lead in a variability of the sedimentary-bedrock impedance contrast from one site to another, influencing the seismic amplification at these sites and complicating the resonance frequency interpretation. Moreover, the acquisition limits of seismological data, whether spatial or temporal, have an impact on the velocity inversion results. The observation of the dispersion curve on some recordings, like for the P2 site, is complicated because seismic waves are propagating very fast in limestones. A larger seismic network could enable to improve the visibility of the dispersion curve. In addition, it could be necessary to perform a campaign of ambient vibration network in the LVV in order to precise the velocity model at depth and maybe, identify the conglomerate-limestone or conglomerate-marl interfaces.

IV.7.3. Spatial variability of V_{sz} in the basin

Large variability of the V_{sz} attributed to the quaternary soils can induce local errors in the basin thickness, especially with the hypothesis of having a 1D tabular environment. Raptakis et al. (2005) observed that V_{sz} is not constant throughout the Mygdonian basin. This is also observed through the V_{sz} profiles in the LVV. As mentioned before, the basin geology of the LVV shows locally the presence of clay lenses potentially increasing or decreasing V_{sz}. Furthermore, the V_{sz} used in the 3D model are the result of a velocity zonation process where the limits of each zone are based on the geographical position of deep boreholes and the geomorphological structure of the valley. These limits remain approximate, especially in the case where the deep boreholes are heterogeneously distributed. One way to validate the velocity zonation could be to test empirical relationships between the fundamental resonance frequency and the soil thickness defined in other studies (Seht and Wohlenberg, 1999; Delgado et al., 2000, 2002; Parolai et al., 2002; Mascandola et al., 2019).

Considering the estimated V_s of each sedimentary layer in the lithostratigraphic soil profile of the LVV and the sedimentary layering inside the basin from the multi sedimentary layer model of the LVV, the V_s profile at each borehole used as strong constrain in the velocity zonation is

interpreted and presented in the Figure 100. Each V_s profile is compared to the V_{sz} estimated in the velocity zonation at the same location.

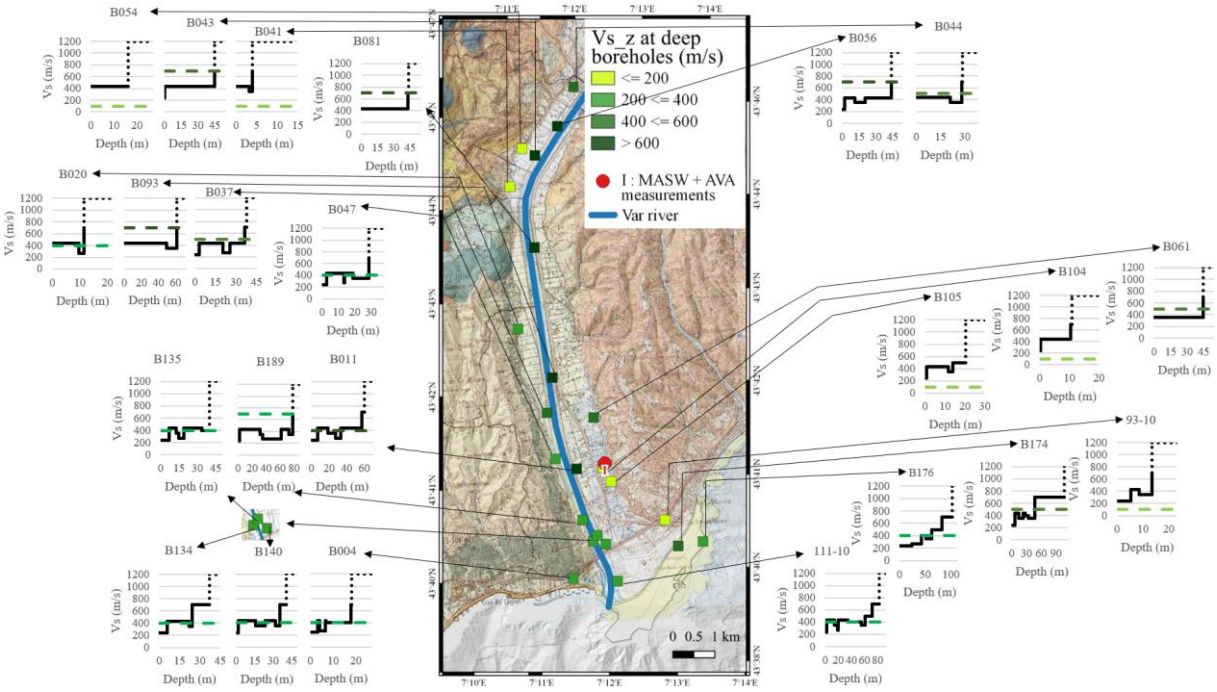

Figure 100: V_s profiles at each borehole reaching the bedrock according to the seismic wave velocity of the lithostratigraphic soil profile of the LVV. The black dashed line represents the basin-bedrock interface. The green one indicates the V_{sz} computed from the closest f_{s0} and the bedrock depth.

The results show that the velocity zonation tends to fit the majority of the V_s profile of the layered model, particularly in the southern part of the valley. Discrepancies are mainly observed in the north. There, the velocity zonation overestimates the V_{sz} in the center of the sedimentary basin whereas it underestimates V_{sz} at the edge of the basin. This underestimation is also observed at the south-east boundary of the valley. This is explained by the strong assumption induced in the interpolation process of the sedimentary layering in the basin. In fact, when boreholes do not reach the bedrock, *GDM* assumed the last sedimentary material of the borehole as the deeper sedimentary layer in the basin at the location of the borehole. This induces large uncertainty in area where few boreholes are located even if ambient vibration data cover the zone. In fact, ambient vibration data only inform about the basin-bedrock interface and not on the sedimentary layering. That is why a supplementary layer is showed in Figure 101 and indicates the uncertainty in the sedimentary layering. The complex hydrogeodynamical context of the LVV can also explained the variation of V_{sz} all along the valley (mixture of marine and fluvial deposits).

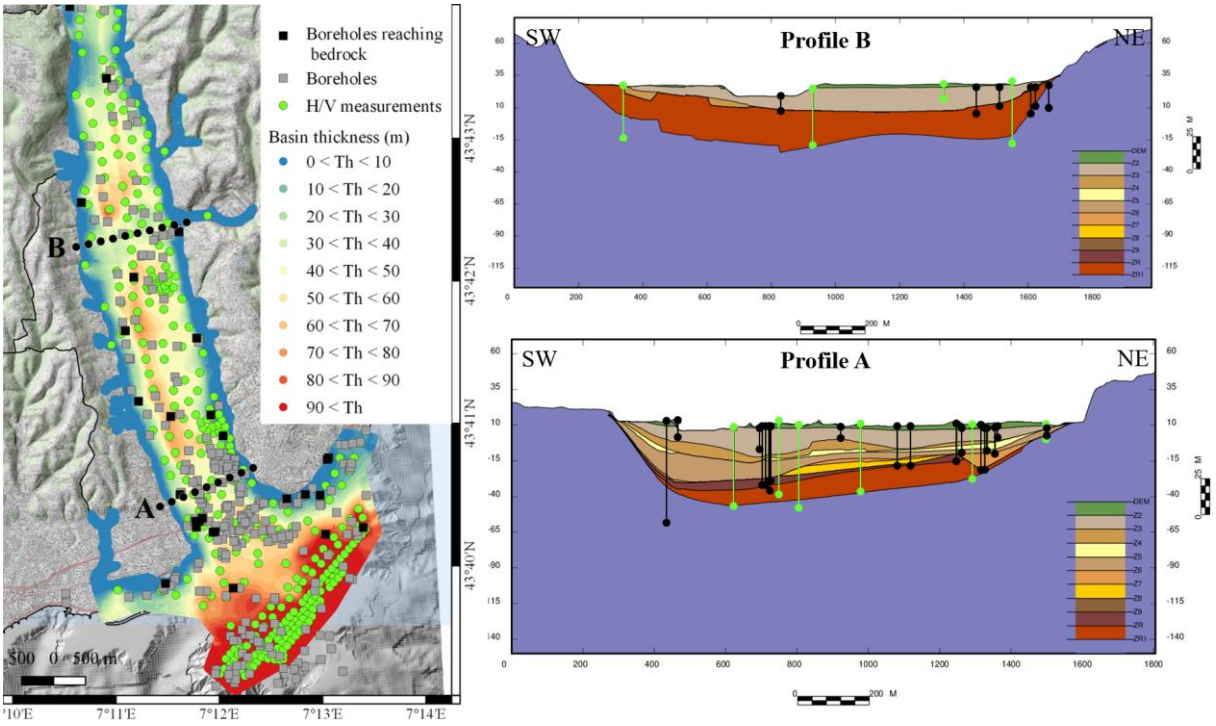

Figure 101: Profiles SW-NE in the 3D multi-layered model of the LVV. Different colors represent different layers from the lithostratigraphic profile applied in the LVV. Note that there is one more layer than those defined in the lithostratigraphic profile. It represents the unconstrained layer between the end of the borehole that are not reaching the bedrock and the bedrock depth deduced from ambient vibration data. The dark lines are boreholes. The green lines are ambient vibration measurements.

We computed a mean V_{sz} profile in the LVV basin from each V_s profiles presented in Figure 100. From this mean profile, a smooth curve is derived using a polynomial equation to model the velocity gradient in the sediments of the basin (Figure 102).

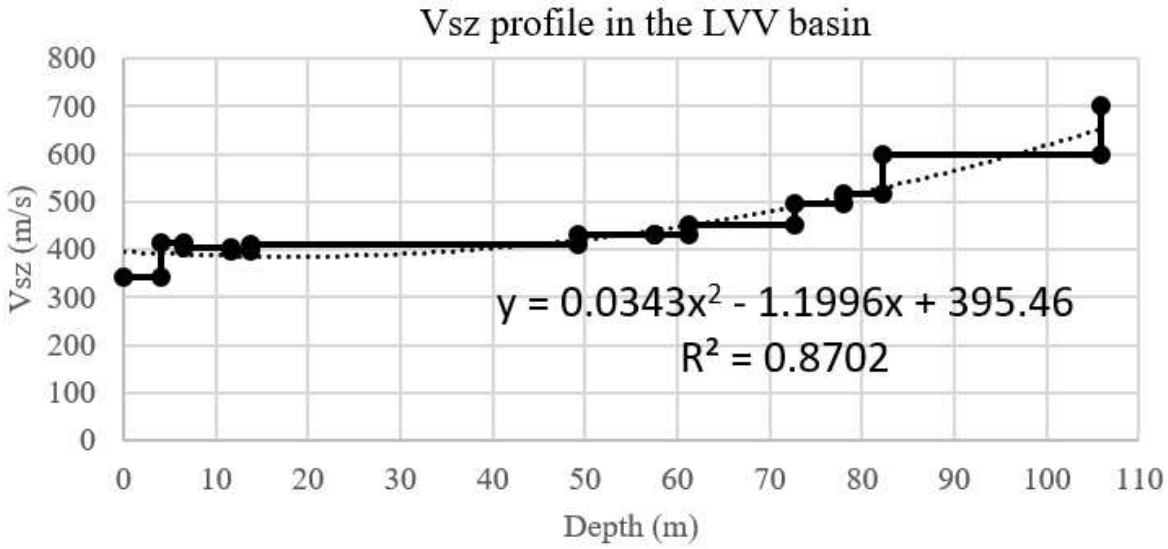

Figure 102: V_{sz} profile in the LVV basin computed from the V_{sz} profiles at each deep boreholes used to define the velocity zonation.

In average, the V_{sz} increases from 341 to 700 m.s^{-1} over 100 m deep according to the V_{sz} profile. This is coherent with the definition of higher V_s value in deeper sedimentary layer of the lithostratigraphic soil profile. Indeed, these layers are assumed older and more compact than superficial one. However, it is important to note that the velocity is not well constrained from 80 m depth because of the low number of boreholes reaching this depth (Figure 103). The estimation of the V_{sz} profile as function of the depth shows that the velocity is bounded between 390 and 450 m.s^{-1} up to 60 m depth and undergoes a very slowly increase deeper. This result support the definition of a constant V_{sz} equals to 400 m.s^{-1} all along the basin in the single homogeneous sedimentary layer model. Furthermore, as expected, the V_{sz} is higher in the LVV than in the other valleys of Nice (Figure 78).

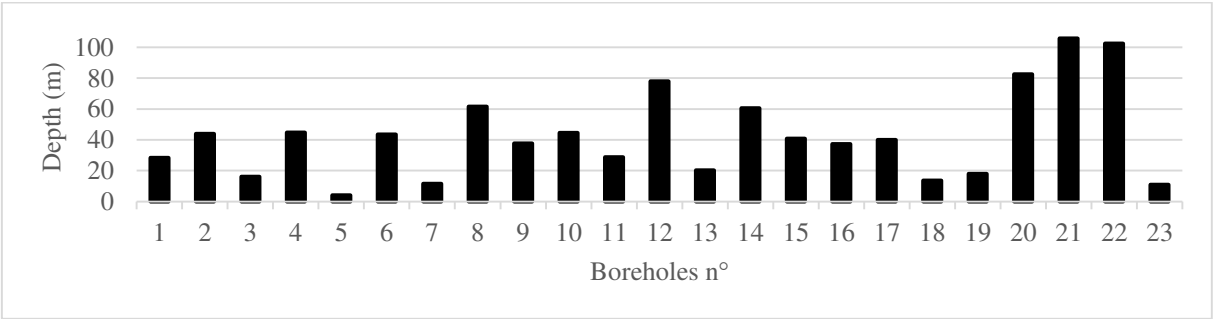

Figure 103: Maximal depth of boreholes used in the velocity zonation.

The f_{s0} at each point of the multi sedimentary layer model is then computed using the basin thickness from the model and the V_{sz} computed from the V_s in the lithostratigraphic soil profile

of the LVV in order to validate the V_s value estimated for each sedimentary layer. The results are compared with the measured f_{s0} all along the valley (Figure 104).

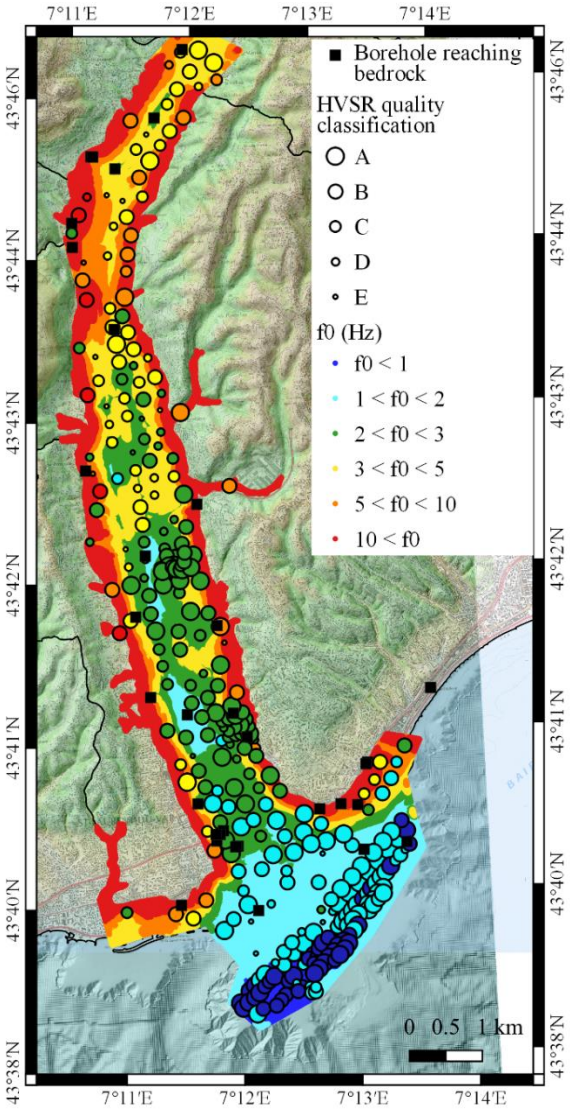

Figure 104: Distribution of the measured f_{s0} (black circles) and the f_{s0} deduced from the V_{sz} profile computed from the lithostratigraphic soil profile of the LVV.

The distribution of the deduced f_{s0} appears to correspond to the measured values in a global way and supports the V_s estimation in the lithostratigraphic soil profile of the LVV.

IV.8. Conclusion

This study determines the basin geometry of the lower Var valley (LVV) (southeastern France) through the combination of borehole log-stratigraphy data and ambient vibration

measurements. The model is defined by the sedimentary layering that is constrained by borehole data. Then, the basin-bedrock interface is constrained using the combination of borehole data and ambient vibration measurements. The large amount of data used in the model definition enabled to improve the precision and the resolution of the quaternary sedimentary basin of the LVV. However, the building process of the model remains complex to perform and the related uncertainties are still not well identified. Therefore, in order to reduce the amount of uncertainties, the interpretation of the microtremor HVSR should be realized with care. These data are not sufficient to well constrain the model, thus borehole lithostratigraphy data are still essential.

An average shear wave velocity (V_{sz}) zonation in the valley has been used to specify the V_{sz} and to take into account the horizontal spatial variability of this important parameter. We found that the sedimentary basin thickness increases from north to south in the LVV, reaching more than 100 m under Nice Côte d'Azur airport and locally reaching 80 m along the Var River.

Some microtremor HVSR are characterized by double peaks locally in the north and the center of the LVV. The second peak has been identified as the fundamental soil frequency of the basin related to the Quaternary-Pliocene interface. In fact, this interpretation led to a geologically consistent shape of a basin. The first peak could imply the existence of a deeper interface inside the bedrock at some sites of the valley. Although this first peak is not used to define the bedrock depth of the valley, it should be taken into account in the site response estimation.

The geometry and the characteristics of the 3D multi-layered model of the LVV is integrated in the realistic 3D site-city finite element model through the well constrained profile presented in Figure 96 assuming a single sedimentary layer and a constant V_{sz} in the valley. The considered part of the valley where the 3D modeling of wave propagation is done is far away from these double-peaked sites.

Chapter V. 3D Simulation of site-city interaction using simplified building in the Var valley

In recent 2D finite element numerical studies, it has been found that the building response at the first resonant mode always decrease due to the structure-soil-structure interaction (SSSI) (Kumar and Narayan, 2018). Bybordiani and Arici (2019) found that this decrease gets stronger when the distance between structures is reduced and put in evidence several parameters that control SSSI effects like sub-soil properties, dynamic features of adjacent structures, geometrical configurations of adjacent structures and natural uncertainties of the ground motion. According to the authors, the comparison of the structure responses in the frequency domain is the most convenient way to study SSSI effects. Kham et al. (2006) and Semblat et al. (2008) proposed the modeling of site-city interaction (SCI) in a 1D case of the sedimentary basin of Nice (southeastern France) subject to incident shear horizontal wave (SH) and shear vertical wave (SV). They show that SCI reduces the ground motion in periodic city and this reduction increases with urban density with maximal effects when double resonance occurs ($f_{0building} = f_{s0}$). In 3D modeling, Isbiliroglu et al. (2015) defined 3D finite element model using the same parameters than Kham et al. (2006) for the definition of simplified 3D homogeneous building model. The authors compared velocity and acceleration time series as well as Fourier spectra to study SCI effects. As in the work of Kham et al. (2006), they found that the building density influence the SCI effects by increasing the ground motion spatial variability.

In this Chapter, all the elements described in the previous chapters are taken into account in the 3D numerical simulations of seismic wave propagation in several site-city finite element models to investigate SCI effects. Here, the Var valley is chosen because of the numerous available geotechnical and geophysical data that provide good quality and precision for the definition of the site-city model. A step-by-step process is used from a « free field » model to a site-city case by adding more and more buildings on the sedimentary basin with different spatial organization together with a parametric study to quantify the SCI effects. This process has already been used to study SCI as for example, in the work of Kham et al. (2006), Semblat et al. (2008), Isbiliroglu et al. (2015), Vicencio and Alexander (2018) or Bybordiani and Arici (2019).

First the 3D Discontinuous Galerkin method is introduced. The conditions and limits of the numerical model are explained. Then, the different mesh elements composing the site-city

models are presented and different studied cases are illustrated. Finally, the results of the parametric study in terms of natural frequency of building, motion intensity parameters, frequency content of the site response and time series comparison are shown and discussed.

V.1. 3D Discontinuous Galerkin method

The Discontinuous Galerkin (DG) finite element (FE) method is used to simulate the seismic wave propagation in the 3D model of the Var valley. This method was first introduced by Reed and Hill (1973) and derived from the FE approach. It is applicable to unstructured meshes to take into account complex geometry of the model using discontinuous element (Hesthaven and Warburton, 2007). This method has already been used in several studies considering the first-order velocity-stress formulation (Käser and Dumbser, 2006; Dumbser and Käser, 2006; Mercerat and Glinsky, 2015; Delcourte and Glinsky, 2015).

Unlike standard FE methods, the discontinuity is expressed by the use of basis functions local to each mesh element. In order to interpolate the numerical solution between elements, centered fluxes are used at the interface between adjacent mesh elements (Delcourte et al., 2009). In 3D DG method, we used FE conforming unstructured mesh composed of tetrahedra, meaning that one face of an element has no more than two neighbors. Solutions in each tetrahedra W_{T_i} are considered as a linear combination of Lagrange polynomial functions (Eq.(90))

$$W_{T_i}(X,t) = \sum_{j=1}^{N_p} W_j^{T_i}(t)\varphi_j^{T_i}(X) \tag{90}$$

where T_i is the considered mesh element, N_p is the number of degrees of freedom per element and $\varphi_j^{T_i}(X)$ is the associated Lagrange nodal interpolant.

Based on fourth-degree Lagrange polynomial functions, this method allows a high spatial accuracy. For p the polynomial degree equal to 4, the value of N_p reaches 35 per element. The time interpolation method is an explicit leap-frog scheme of order 2. The stability condition of the simulation is directly linked to the seismic wave velocity. In fact, the minimum time step of the numerical computation dt_{min} is related to the compressional wave velocity (V_p) using Eq.(91)

$$\mathrm{dt} = \min dt_j = \frac{1}{2p+1}\frac{h_j}{V_{p_j}} \tag{91}$$

where dt_j is the local time step in the mesh element j, p is the degree of the spatial approximation, here equal to 4 and h is a concept of element size (for example the diameter of the inscribed sphere).

The DG method was first established for the velocity-stress formulation (Delcourte and Glinsky, 2015) and then, extended to the velocity-strain system (Chabot, 2018) to take into account non-linear elastoplastic media. This last version, applicable to parallel calculation platforms via message passing interface (MPI), is used in this thesis whereas the method is supposed to be linear elastic.

A free surface condition $\sigma_{\vec{n}} = \vec{0}$ is applied at the surface topography. σ is the stress tensor, $\vec{n}$ is the outward normal. An impedance contrast describes the limit between buildings, soil and bedrock. Absorbing conditions are applied at the four lateral sides of the model.

V.2. Input data

The FE method allows to study complex geometry and to take into account nonhomogeneous properties of soil. The DG method supposes that the medium is constant in each mesh element. Then, the mesh must honor the discontinuities in the model. For this thesis, we use the *GMSH* open source software (version 4.6.0) (Geuzaine and Remacle, 2020) and the *OpenCASCADE* geometry kernel to create a 3D unstructured conforming tetrahedral mesh. This software allows to develop 1D, 2D and 3D, unstructured or structured meshes and proposes various generation and optimization techniques to obtain the best optimized mesh to reduce computational costs. It has the advantage of being very intuitive for the user and shows instantly the modifications applied to the mesh.

V.2.1. Structural properties of the domain

The site-city model is composed of three various media: the bedrock, the sedimentary basin and the buildings. Each of these media have specific mechanical and structural properties which are presented in the following.

V.2.1.1 Building equivalent model

Because, it is technically not possible yet to consider detailed buildings in numerical models including a large soil domain, simplified equivalent models for building are generally defined

by simple relationships. These simplified models of building are developed either in the form of lumped mass model, or in the form of equivalent block.

Although the lumped mass model is interesting to estimate the structure response, it is difficult to integrate in numerical model when the number of degrees-of-freedom increases. On the other side, the equivalent block model can be related to a parallelepiped medium defined by an equivalent Young modulus to that of a real building. The use of a homogeneous continuous elastic block model to represent buildings in the simulation enables to keep the real building volume and notably the real foundation surface that is important for the study of SSI. In this case, we deal with a 3D element that is easier to integrate in 3D soil model than the lumped mass model. It has been already used in previous studies to investigate not only SSI effects but also free field motion in the presence of SSI (for 2D soil-block model: Pitilakis and Karatzetzou, 2014; Karapetrou et al., 2015; Mitropoulou et al., 2016 and for 2D and 3D soil-block model: Conti et al., 2016; Cavalieri et al., 2021). It is this type of model that we use in the FE mesh.

In this way, the building is considered as a large shear beam having the same dimensions of the building and equivalent dynamical features. Other authors already used this method to integrate building in numerical modeling (Taborda and Bielak, 2011; Mazzieri et al., 2013). The limitation of this kind of 3D model is the calibration of orthotropic material that implies the definition of different equivalent Young modulus in the block. For sake of simplicity, we only focus on isotropic blocks.

To calibrate the block model, the seismic wave velocity should be defined. This parameter can be directly measured with ambient vibration recordings along the building height using the deconvolution technique, it can also be deduced from the fundamental resonance frequency of the building. Some authors refer to the relationship $V_s = f_0 * 4H$ (Bard et al., 2005; Sahar et al., 2015; Sahar and Narayan, 2016; Kumar and Narayan, 2018, 2019a, 2019b).

If we apply this formulation using the first natural frequency of the tower A of the residence Bois de Boulogne (1.10 Hz) and its height (57 m) (see Chapter III), we find $V_s = 250.80\ m.s^{-1}$. This result is slightly lower than the shear wave velocity (V_s) value found by deconvolution interferometry method from ambient vibration data (300 m.s^{-1}) and even lower compared to the velocity value found with the expression proposed by Michel and Guéguen (2018) (around 500 m.s^{-1}). The same result is observed for the CADAM highest reinforced concrete tower where

V_s computed from the formulation equals to 316.8 m.s^{-1} whereas the measured velocity is between 490 and 540 m.s^{-1} (Lorenzo, 2016).

Other authors used another parametric relationship to determine the velocity in buildings that is $V_s = 28H_s$ with H_s corresponding to the inter-storey height whatever the kind of building material (Taborda and Bielak, 2011; Mazzieri et al., 2013) and define $V_p = 2.5V_s$ (Mazzieri et al., 2013). The application of this relation to the tower A of the residence Bois de Boulogne and the CADAM respectively leads to $V_{s_{Tower\,A}} = 70$ m.s^{-1} and $V_{s_{CADAM}} = 84$ m.s^{-1}. These values are extremely low compared to the usual velocity values found in real buildings.

Considering the high variability in the V_s measured or inferred, we decided to strictly respect the measured fundamental resonance frequency of tower A in the Bois de Boulogne residency that is f_1 = 1.10 Hz corresponding to the first bending mode of the tower and to adjust the V_s in order to retrieve the same resonant frequency of the equivalent building model using the spectral ratio between the signal at the top and at the base of the building.

An iterative approach has been performed to find the appropriate V_s. Several test simulations have been made to estimate V_s in the block model and for each test, the transfer function between the top of the block model and the bottom has been computed (Table 35). To fit f_1, the estimated velocity value is equal to 900 m.s^{-1}. The relation linking V_s to the height of building is found as $f_1 = V_s/14H$ (Figure 105). This result is much higher than the velocity found using the deconvolution interferometry approach (300 m.s^{-1}) and the equation from Michel and Guéguen (2018) (around 500 m.s^{-1}). V_p is estimated from V_s value considering a constant Poisson coefficient constant equal to 0.48. We found V_p equals to 5400 m.s^{-1}.

Table 35: Estimation of the shear wave velocity in the simplified building model.

Test	V_s	Estimated V_p	f_0 from transfer function
1	1000	6000	1.213
2	900	5400	**1.12**
3	750	4500	0.93
4	500	3000	0.65

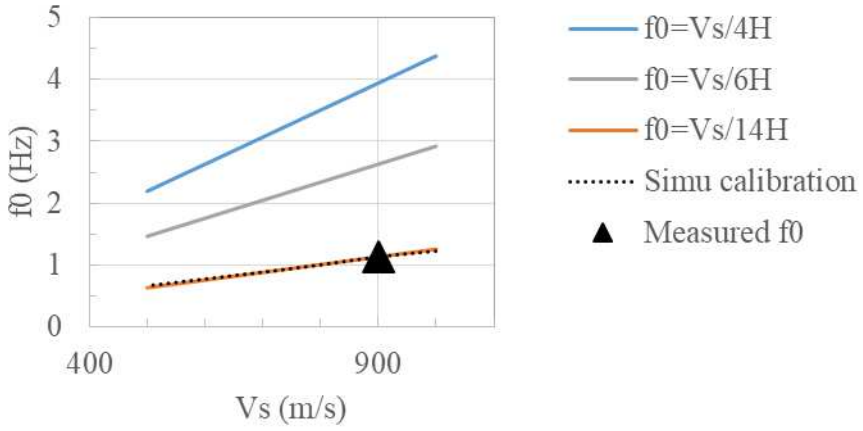

Figure 105: Estimation of the relationship between V_s defined in the block model and the height of the structure.

The determination of V_s in the equivalent building model enables to retrieve the shear modulus of the equivalent block G by the Eq.(92). The density ρ is fixed to 350 kg.m^{-3} as suggested in the studies of Kumar and Narayan (2019b, 2018).

$$G = \rho V_s^2 \tag{92}$$

The Lamé parameters are then found by the Eq.(93)

$$\lambda = G * \left(V_p^2 - V_s^2\right). \tag{93}$$

V.2.1.2 Basin and bedrock mechanical properties

The mechanical properties of the basin and bedrock medium are based on the 3D multi-layered model of the lower Var valley (see Chapter IV). For the sake of simplicity, a homogeneous single layer with a constant average V_s equals to 400 m.s^{-1} in the basin is considered in the 3D numerical site-city model. The mean value of V_s is estimated at 1300 m.s^{-1} in the bedrock. The density of the bedrock is set to 2100 kg.m^{-3} and the one of the basin is equal to 1900 kg.m^{-3}.

The quality factor Q corresponds to the inverse of the attenuation parameter and defines the damping properties of the materials. In the bedrock, it can be set at ten percent of V_s (Peyrusse et al., 2014). In order to take into account the stronger attenuation behavior in the sedimentary basin, the quality factor is chosen to be slightly more than ten percent of V_s and so $Q = 50$. The

quality factor of building is set to 10 according to other studies (Tsogka and Wirgin, 2003; Kham et al., 2006; Mazzieri et al., 2013; Kumar and Narayan, 2019a, 2019b), corresponding to a critical damping ratio of 5%.

In order to propagate accurately the seismic waves, ten interpolation points per wavelength are at least recommended. The characteristic length of the mesh elements is then estimated by Eq.(94) (Chabot, 2018)

$$lc = \frac{\lambda}{2.5}, \quad \lambda = \frac{V_s}{f_{max}}. \tag{94}$$

Here V_s is the shear wave velocity and f_{max} is the maximum frequency of analysis equal to 15 Hz. This value is in the range of frequency 10 Hz < f_{max}< 15 Hz that is appropriate to study civil engineering object.

The medium properties are supposed to be constant in each tetrahedron of the model. All mechanical features are summarized in Table 36.

Table 36: Mechanical properties of the different medium composing the numerical models of the lower Var valley.

Domain	ρ (kg.m^{-3})	G (N.m^{-2})	λ (N.m^{-2})	V_p (m.s^{-1})	V_s (m.s^{-1})	Q	lc (m)
Basin	1900	$3.04.10^8$	$6.084731.10^8$	693	400	50	10
Bedrock	2100	$3.549.10^9$	$7.1011584.10^9$	2252	1300	130	34
Building	350	$9.639.10^9$	$2.835.10^8$	5400	900	10	24

V.2.2. Meshing of the lower Var valley basin

The topographic boundary and the basin-bedrock interface are defined from the 2D profile perpendicular to the Var valley and going through the NCAD accelerometric station (Figure 106). At the NCAD position, the measured fundamental frequency of the soil is close to 2 Hz. Considering that the natural frequency of building is 1.1 Hz, we do not consider the double resonance condition between the site and buildings in our models.

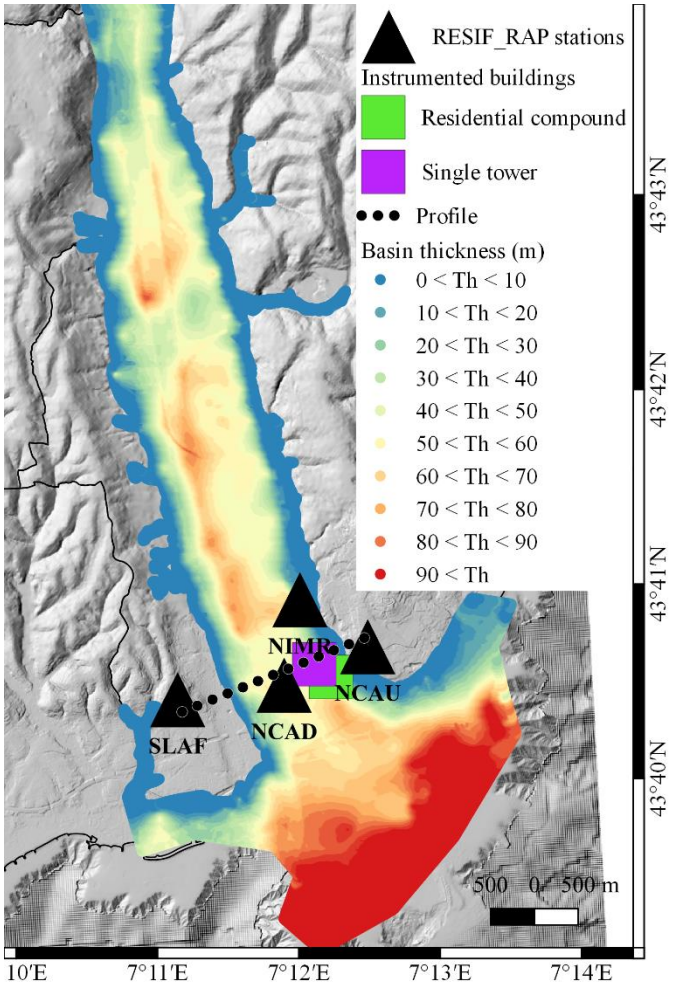

Figure 106: Localization of the 2D profile in the Var valley used in the numerical simulation. The basin thickness is extracted from the 3D multi-layered model of the lower Var valley.

For the sake of simplification, the 2D profile is extruded in the longitudinal direction of the valley to obtain a simplified 3D model of the LVV. This is performed in order to avoid the complex structure of the valley aperture at the south and to improve the observations of SSI, SSSI and SCI effects. We choose to extrude the profile on 1 km to have a 3D model for two reasons. The first one is to take into account the finite volume of the equivalent building model in the transverse direction (we can expect diffraction of seismic waves at the edge of the building that participate to SSI effects). And the second one is to avoid lateral boundary effects on the numerical results. The last reason also explained the choice to extend the profile on both sides. Finally, we obtain a 3000x1000x500 m^3 domain (Figure 107).

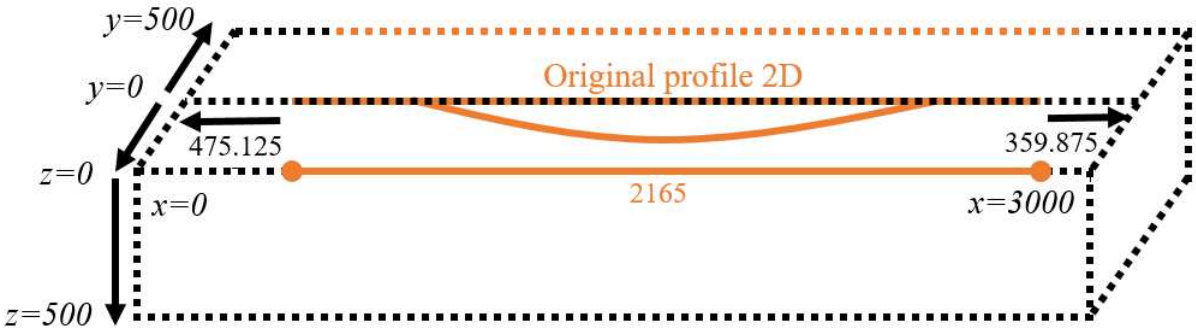

Figure 107: Scheme and dimensions in meters of the 3D numerical model of the lower Var valley (free field case (FF)).

Anquez et al. (2021) showed, considering simulations in a 2D profile of the LVV, that modifying slightly the aperture angle of a sedimentary basin does not lead to change drastically the numerical results. In order to reduce the computation time, we slightly increased the aperture angle of the basin in order to increase the minimal height of mesh elements in this area. This modification directly impacts the minimum time step of the simulations and then helps to reduce the computation time. The topographic surface has also been slightly modified by decimating points in order to smooth out some very localized heterogeneities. The sampling rate went from 1 point every 5 m to 1 point every 10 m.

In order to ensure the continuity between the basin surface and equivalent building models in the 3D domain, we flatten some parts of the topographic surface in the basin to make them horizontal (Figure 108c). The flattening process enables to remove local surface heterogeneities in the concerned area to correctly connect the building block models to the basin domain and avoid any gap between the surface basin interface and the bottom of the building. To be sure that the connection is well performed, the block models are slightly embedded in the basin domain before intersecting the two domains during the mesh construction process. In that way, the block model is only laid on the sedimentary basin. Then, we may expect weak kinematic interaction because of the absence of building foundation in the model.

The original profile extracted from the 3D multi-layered model of the LVV and the modified profile are compared in Figure 108. We can see that, at the scale of the basin, these changes are negligible. Moreover, the presence of a borehole (10001X0458 in the BSS catalog) (Appendix 9) located 70 m away from the eastern border of the basin on the sediments indicates that the bedrock is not reached at 7.5 m depth and supports the consistency to perform little modifications.

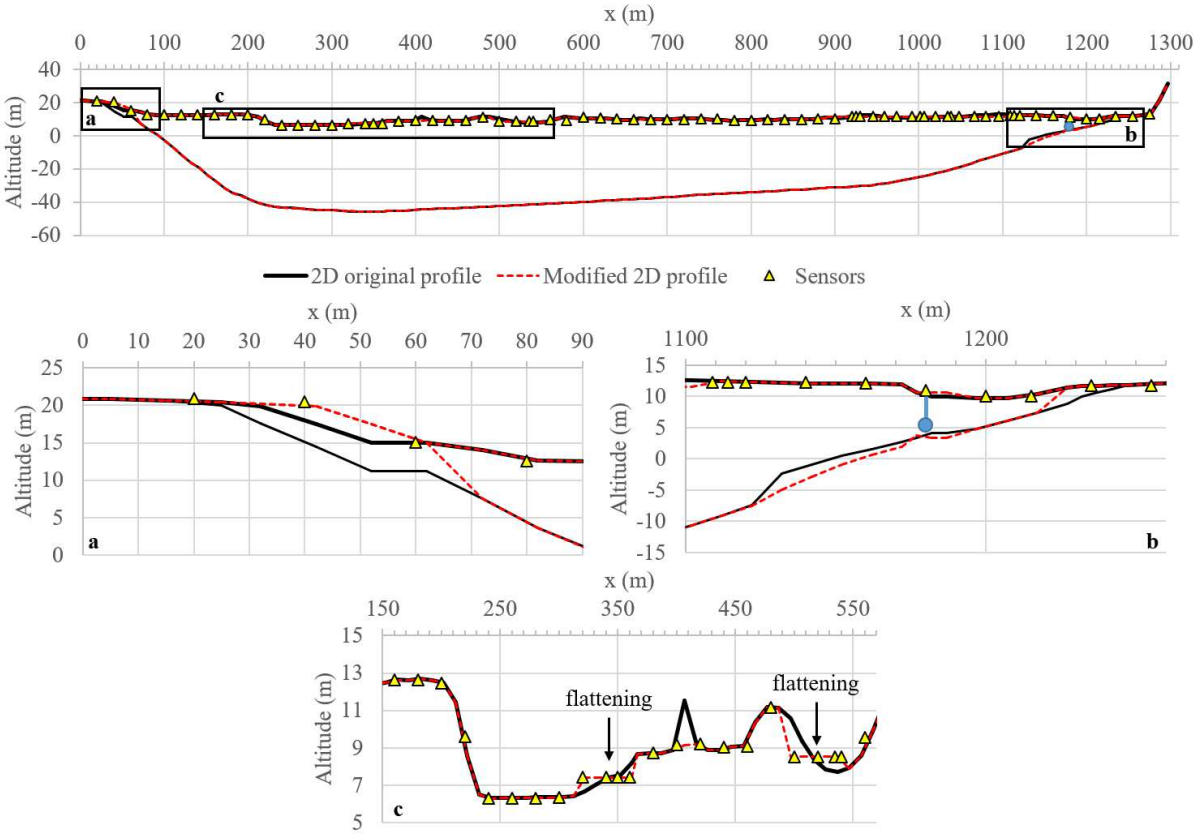

Figure 108: Modification of the 2D profile of the lower Var valley before extrusion. Considered sensors for the analysis are represented by yellow triangles. The position of the borehole 10001X0458 from the BSS catalog is indicated by the blue mark.

The *GMSH* software proposes several generation techniques to create FE meshes in the 3D domain (Geuzaine and Remacle, 2020). We chose the better compromise between mesh element quality and total number of elements in order to reduce the computation time. The selected methods are described below:

- For 1D interpolation, linear interpolation method is used to construct lines from points.
- For 2D interpolation, we choose the *MeshAdapt* algorithm to interpolate triangles on each surface of the domain. As it is named, this method applies the most appropriate interpolation method for each surface based on the surface geometry (flat or curved) in order to have the minimum mesh elements with high quality. The quality of an element reaches the value 1 if the triangle is equilateral. The mesh takes into account heterogeneities by describing the basin-bedrock interface by a set of triangular faces.
- For 3D interpolation, we employed the *Frontal-Delaunay* interpolation method to interpolate tetrahedra in the different volumes of the domain.

The obtained 3D FE model of the LVV presents a soil fundamental frequency of 2 Hz equal to the one measured at the NCAD station (Figure 109). Frequency at 4.5 Hz and 5.8 Hz are also highlighted by the transfer functions.

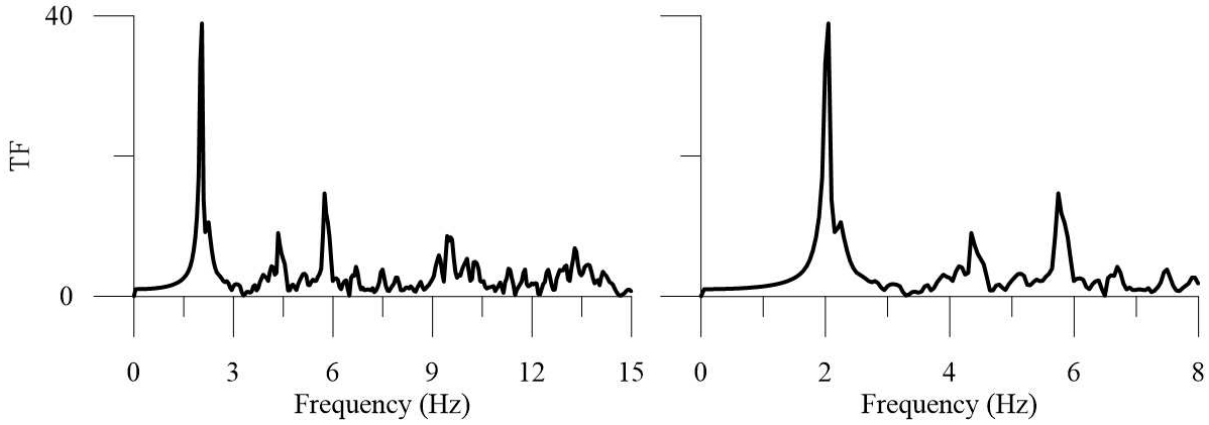

Figure 109: Transfer functions of the 3D finite element model of the LVV basin computed at x=332 m for the transverse component (V_x), zoom on the transfer function (right).

V.2.3. Site-city models

In the 2D SCI study of Bybordiani and Arici (2019), the authors tested three different distances between buildings in a cluster. They defined the building inter-distance (dx) as a function of the height of the building (H): $dx_1 = H$, $dx_2 = H/2$ and $dx_3 = H/3$. Moreover, they find that SSSI effects are stronger when the cluster is composed of more than five structures. In 3D case, Kumar and Narayan (2019a) used an inter-distance between buildings equal to the height of them (low-rise building of 12 m height). They advised to take into account at least nine structures in a cluster for 3D SCI studies and only three in the case of 2D models to better observe SCI effects. The authors focused on a square shape cluster of buildings that they enriched with more and more buildings to study variations of SCI. Based on this literature, five models are meshed to study the influence of lithological site effect and buildings on the seismic ground motion in this thesis (Figure 110):

1. FF: The Var valley without buildings.
2. IB: The Var valley with three isolated buildings located on the sedimentary basin.
3. SC: The Var valley with two isolated buildings and a square cluster of buildings composed of nine structures located on the sedimentary basin and distant from 28.5 m (corresponding to the half-height of the buildings).

4. LSC: The Var valley with two isolated buildings and a large square cluster of buildings made of nine structures located on the sedimentary basin and distant from 57 m (corresponding to the height of the buildings).
5. CC: The Var valley with two isolated buildings and a circle cluster of buildings containing seven structures located on the sedimentary basin and distant from 28.5 m.

Isolated buildings represent structures sufficiently far away one from another so as not to influence the response of each of them. Vicencio and Alexander (2018) observed that, for stiff soil, SSSI effects are negligible when the building inter-distance is equal to twice the structure height. Here, the minimum distance between buildings in the IB case is 157 m that is more than double the height of structure (114 m) (Figure 110).

We choose to reproduce the square shape of cluster as in Kumar and Narayan (2019a) and to test the influence of the inter-distance between buildings using the LSC case. An additional model is developed considering a circle shape cluster of buildings to identify variations in SCI effects due to the different organization in a cluster. The localization of the cluster is set close to the eastern basin edge that is an appropriate position to observe the generation of surface waves and trapping in the basin, and to study the interactions between site and city responses.

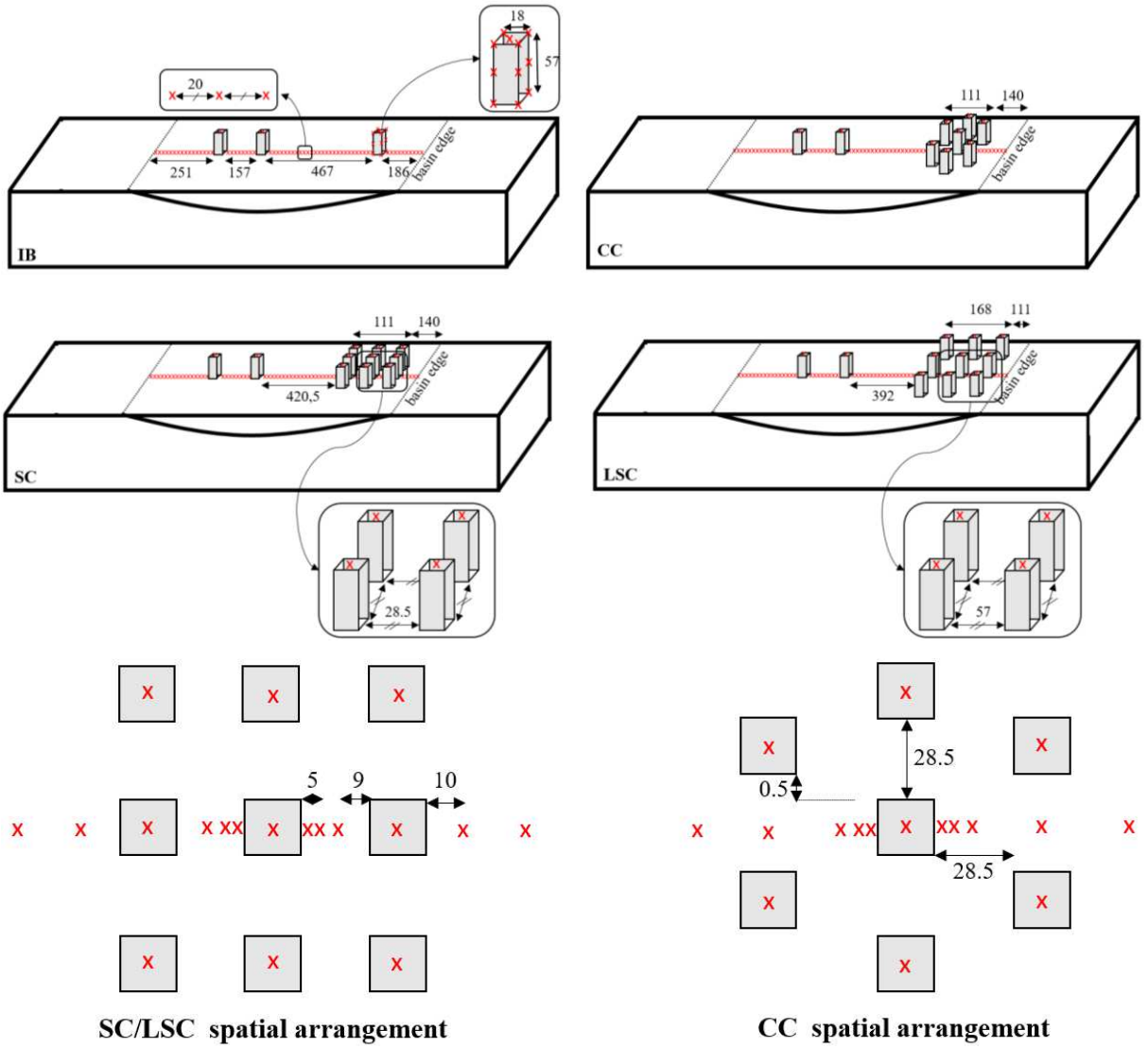

Figure 110: Illustrations of the four 3D site-city models considered. IB: the isolated buildings case, SC: the square cluster case, LSC: the large square cluster case, CC: the circle cluster case. The spatial organization of the cluster in the cases SC, LSC and CC are presented. Sensors are indicated by red crosses. The dimensions are in meters.

In total, 136 sensors have been placed on the basin surface to study the spatial variability of the ground motion (Figure 110). A maximum of 20 sensors are placed in the buildings mainly at the top depending on the site-city model to compare the response of each building. The valley is cut by a transverse profile of sensors where the minimum distance interval is 5 m and generally close to the buildings. The maximum sensor interval is 20 m. Within a building cluster, there is at least one sensor to observe the influence of the distance between buildings on the ground motion. The number of mesh elements composing each model is presented in Table 37. For one iteration and for each studied case, the computational time step and the minimum length of a mesh element are reported in Table 37.

Table 37: Geometrical characteristics of the different 3D mesh models before partitionning. X is the transverse direction in the valley, Y is the longitudinal direction in the valley, Z is the depth of the 3D model, N_s is the total number of points, N_t is the number of tetrahedra and N_{fr} is the number of boundary faces of the mesh, $dt_{1\text{-iter}}$ is the computation time step for one iteration and H_{min} is the minimum length of all mesh elements.

Model	X (m)	Y (m)	Z (m)	N_s	N_t	N_{fr}	$dt_{1\text{-iter}}$ (10^{-5}s)	Total CPU	H_{min} (m)
FF	3000	1000	500	93286	478954	49358	8.03	18h	1.79
IB	3000	1000	500	93745	480903	49820	2.96	>24h	1.76
SC	3000	1000	500	94482	483528	50748	3.07	>24h	1.76
LSC	3000	1000	500	94534	483791	50802	3.18	>24h	1.76
CC	3000	1000	500	94299	482963	50494	3.20	>24h	1.76

The Table 37 shows that adding one or several block models in the domain slightly increases the number of mesh elements but strongly decreases the computational time step leading to an increase in computation time. For example, the maximum number of elements added with the LSC case does not exceed 1% of the number of elements of the FF case whereas the time step decreases by more than 60% compared to the FF case. Furthermore, we note that the obtained minimum length of the mesh elements is very small compared to the characteristic lengths defined in the previous section. This means that the resulting meshes are more refined than initially defined and therefore can explain the decrease of the time step.

V.2.4. Simulation parameters

Each mesh model is partitioned in 256 sub-domains using the *Metis* package to decrease the computation time. For the output results, the time step is set to 0.02s and the minimum signal duration is equal to 15s. The whole system is considered in linear elastic regime. Rayleigh damping with a central frequency of 2 Hz is also considered (Chabot, 2018). Parallel computing was used to run the numerical simulation.

V.2.5. Input seismic signal

As introduced in the Chapter II, one of the challenges in the numerical computation of seismic wave propagation is to select a relevant seismic input to get reliable and significant results. The use of real earthquake recordings is always interesting to compare numerical results to real observations. However, this needs to meet certain requirements. First, a good knowledge of the recording site is needed. The recording must be performed in a similar environment than the

studied area and preferably on rock site to avoid site effect in the data. It needs to have enough duration to analyze intensity parameters of the ground motion (peak ground acceleration (PGA), peak ground velocity (PGV), peak ground displacement (PGD), Arias intensity (AI), integral energy (EI), and cross-correlation) and a large frequency content. Moreover, if the earthquake produces strong motion, nonlinearity should be taken into account in the numerical analysis. Because of the complexity of earthquake recordings, scientific community often use synthetic input signals. These data present the advantage to allow a user's specific design to put in evidence parameters in the results analysis. They are also easier to manipulate due to the absence of random noise and represents the ideal recording of a specified seismic event on perfect rock site (meaning that the rock is not watered or fractured and there is no topographic site effect).

In this thesis, we used the stochastic algorithm developed by Sabetta and Pugliese (1996) and recently improved by Sabetta et al. (2021) to generate synthetic recording. This code allows to produce synthetic signals considering specific parameters as the magnitude, the epicenter depth, etc.… A vertical propagation of a horizontal plane shear wave is introduced at the base of the domain through an upwind boundary flux according to Glinsky et al. (2019). This means that incident and outgoing waves are well-balanced. The input is a synthetic seismic signal of duration 8s having a PGV of 2.9 $cm.s^{-1}$ on the transverse velocity component (Figure 111). It simulates an earthquake of magnitude 5 recorded at an epicentral distance of 5 km on rock site. The Fourier spectrum amplitude exhibits a large frequency content having energy between 0.5 to 15 Hz and maximum energy around the basin fundamental frequency (2 Hz according to Rohmer et al. (2020)). Finally, the synthetic input is divided by two and only the transverse component of the valley V_x is excited (Figure 107).

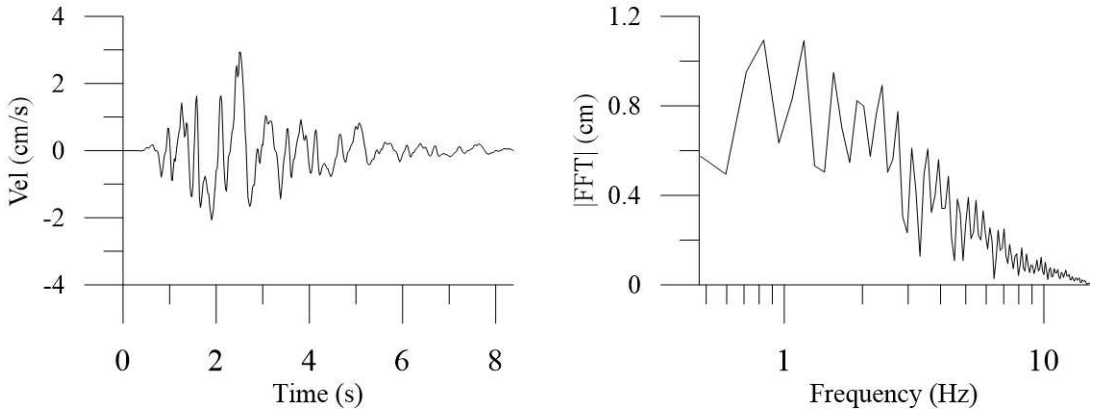

Figure 111: Synthetic seismic input time serie (left) and Fourier spectra amplitude (|FFT|) (right).

V.3. Pre-processing of the outputs

The outputs of the numerical simulation consist in velocity time series at each sensor situated on the 3D domain (Figure 110). Before analyzing the results, signals are filtered by a low pass Butterworth filter of order 4 using a maximum frequency of 15 Hz.

For each model, the acceleration and displacement time series are retrieved respectively from the derivation and the integration of the outputs. The Fast Fourier Transform (FFT) is computed for each signal using the total output duration in the frequency range 0 – 15 Hz. The ratio between the FFT of signal in each model is computed to observe variability in the frequency content of the building response as function of the site-city models. The building transfer function is estimated using the ratio between the signal at the top and at the bottom of the building to look at least for the first natural frequency of the structures. The high discretization of one of the building model (Figure 110) allows to study the mode shape of the structure and investigate the dynamic behavior of this element. Several parameters of the motion intensity are also evaluated in terms of cross-correlation, PGA, PGV, peak acceleration (PA), peak velocity (PV), AI and EI.

V.4. Seismic response of the isolated buildings

At first, we observe in Figure 112 that the velocity time series and transfer functions differ slightly from one building to another. The maximum signal amplitude is larger for building 2 (B2) localized in the center of the basin profile. Compared to the building 3 (B3), the maximum signal amplitude increases of 15% for building 1 (B1) and of 69% for B2. The first natural frequency at 1.1 Hz is retrieved with the same peak amplitude for all the structures, while the second mode frequency varies between 5.5 and 5.7 Hz with varying peak amplitude. This second frequency peak amplitude is 62% higher for B1 and reaches more than 145% for B2 compared to B3.

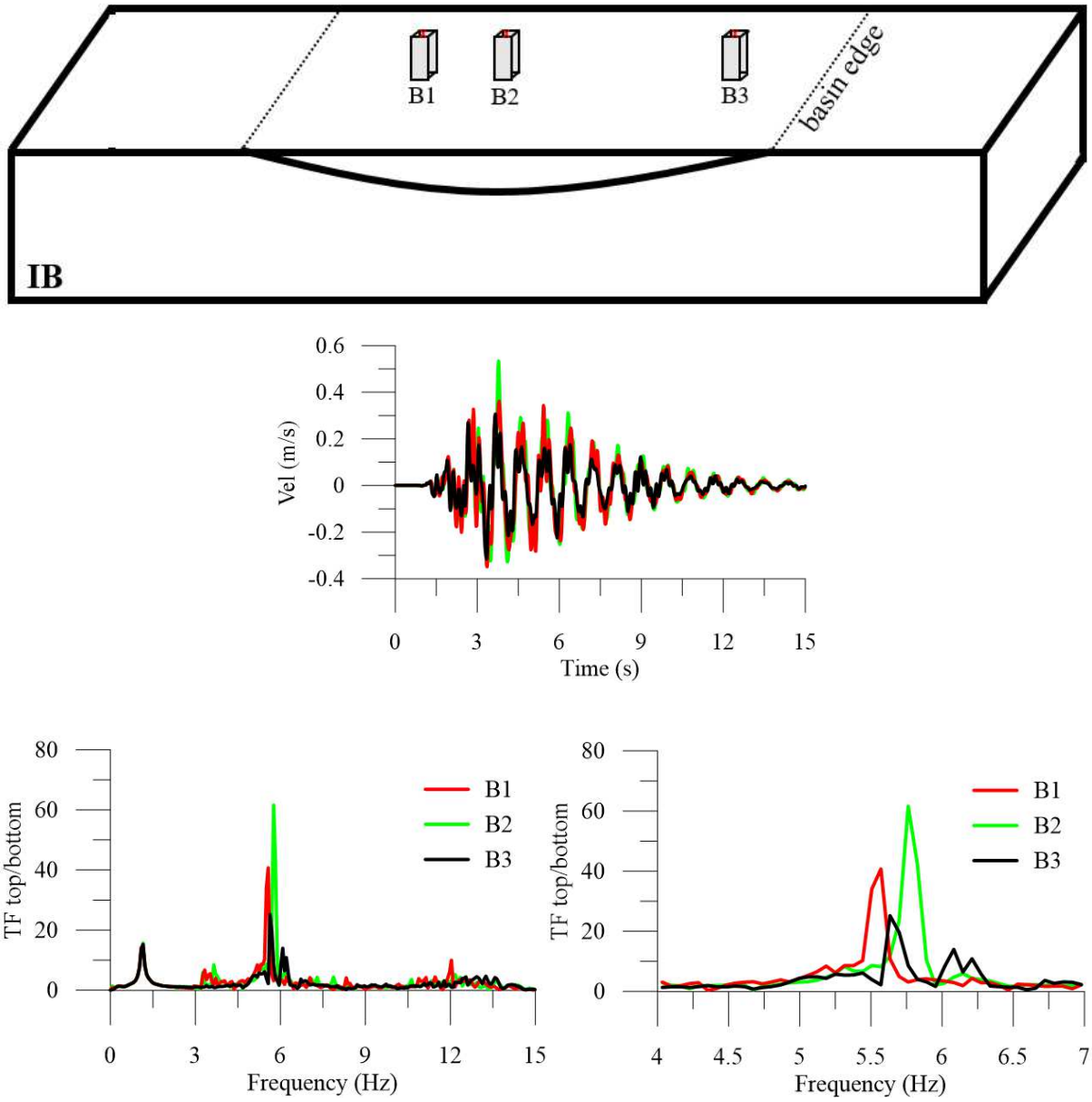

Figure 112: Velocity time series and transfer functions at the top of the three isolated buildings for the transverse component. The source vibration is in the transverse direction only.

According to the natural frequency ratio f_1/f_2, we can estimate the Timoshenko parameter of the building (Michel, 2007). We found that the equivalent block model may be characterized by a Timoshenko behavior close to the bending type (Figure 113). Because the dynamic behavior is not a pure bending type, the SSI may be weak.

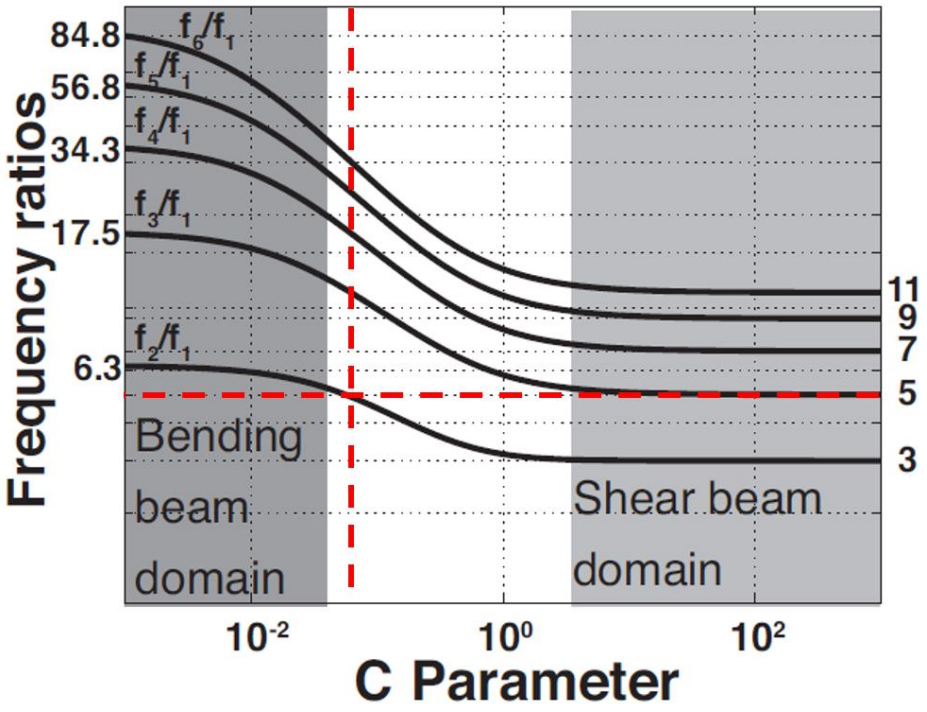

Figure 113: Estimation of the Timoshenko parameter using natural frequency ratio of the equivalent block model of building from Michel (2007).

The first mode shapes of B3 are investigated through filtered displacement time series at several corners of the block model. Displacement time series at three corners respectively at the top, the middle and the bottom of the building filtered around the first natural frequency of the building (1.1 Hz) and around the second one (5.5 Hz) are used to compute the mode shapes. This analysis shows that the simplified building model has a first order flexural mode at 1.1 Hz and a second order flexural mode at 5.5 Hz (Figure 114).

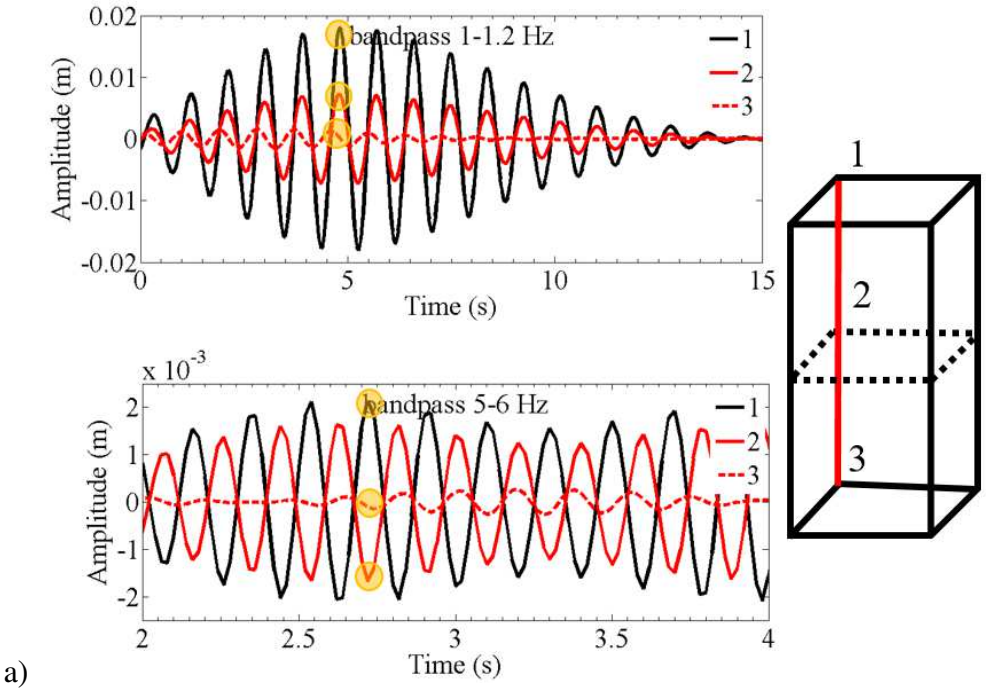

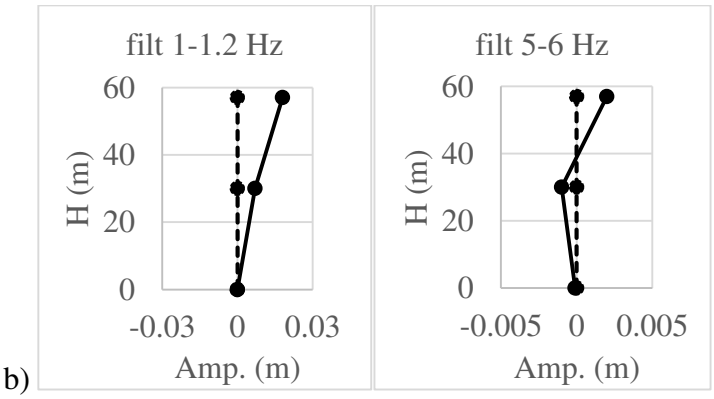

Figure 114: a) Displacement time series at corners 1, 2 and 3 filtered around the first and second natural frequencies of the building. Yellow circle indicate the amplitude of the mode shape at each corner reported in Figure 114 b). b) Mode shape of the simplified model of building B3. In the graphs, the dashed line indicates the initial position of the building. The solid line represents the interpreted mode shape.

At the four top corners of the building, the superposition of displacement time series shows similar motions at all point. Therefore, the first and second mode shapes of the building are not governed by torsion behavior (Figure 115).

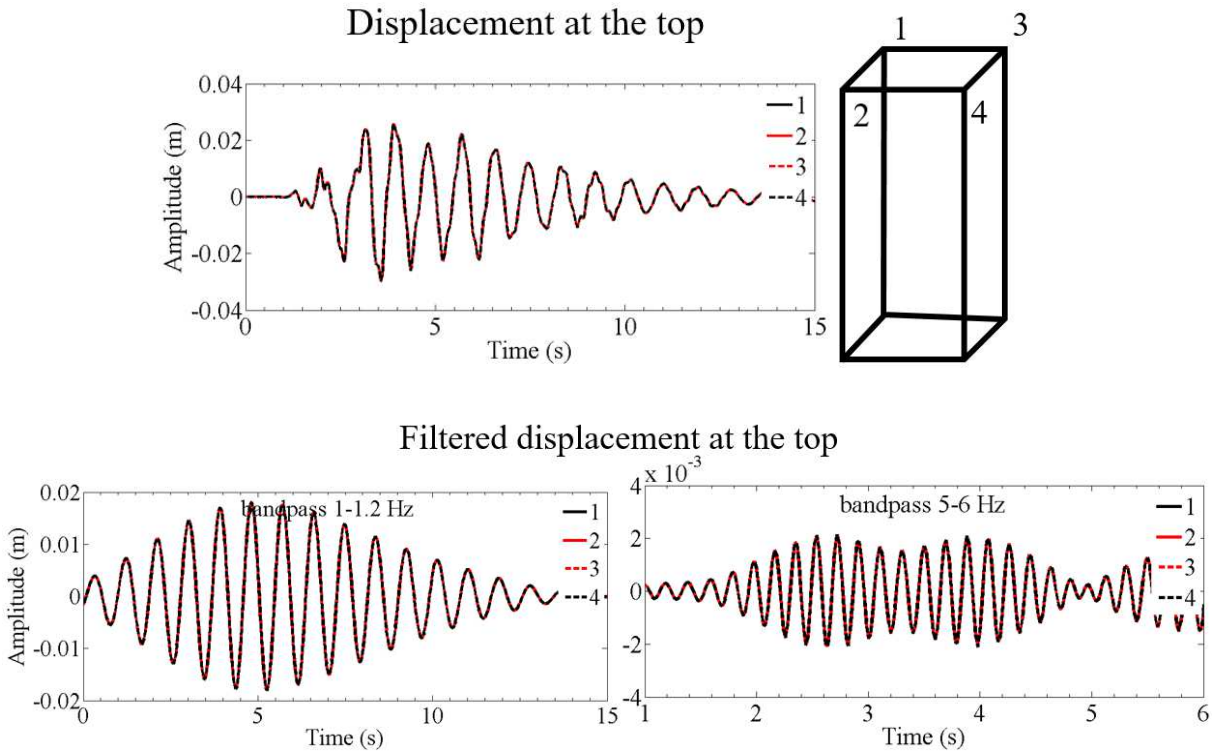

Figure 115: Identification of torsion motion at the top of building B3.

V.5. Seismic response of the building cluster

When we compute the different models (IB, SC, CC and LSC), two main observations can be done: (1) the SSSI tends to decrease the signal amplitude and (2) the first natural frequency of buildings is not affected and the main modification occurs in higher frequencies.

The comparison of signals at the top of B3 between all site-city models shows that the SC and CC cases tend to reduce the signal amplitude whereas the LSC model tends to increase it (Figure 116). The cross-correlation results exhibit differences of 20% between signals from 1.5s in the SC and CC models and of 10% from 3s in the LSC case where we can observe the change in amplitude. However, if we consider only the building response filtered around the first natural frequency, we observe no variations between the studied cases. This observation is in agreement with the existing literature. Indeed, Kham et al. (2006) and Kumar and Narayan (2018) observed a decrease in amplitude and duration in the signal at the top of an isolated building situated at the center of the city as compared to that at the top of a single building situated in the basin. It appears that the signal amplitude depends on the structure position, the spacing between

buildings and the number of structures in the cluster (Guéguen, 2000; Guéguen et al., 2002; Kham et al., 2006; Semblat et al., 2008; Bybordiani and Arici, 2019).

The analysis of the Fourier spectra ratio considering the IB case as reference shows that there are negligible variations in the frequency content of the building response between 0.5 Hz and 3 Hz that is a frequency band that includes the first natural frequency of the block model (1.1 Hz). After 3 Hz, the Fourier spectra ratio exhibits large amplification or deamplification depending on the frequency and of the type of cluster. It is shown that the Fourier spectra ratio of IB-SC and IB-CC are quite similar on the considered frequency range. The reason may be that these site-city cases share the same spacing between buildings (28.5 m). However, slight discrepancies are observed which can be due to the different number of buildings located around the central structure (B3). The maximum amplification is found at 4.7 Hz for the IB-SC and IB-CC ratio and at 5.9 Hz for the IB-LSC ratio. The IB-LSC ratio differs from the others in amplification level and in the affected frequency band. This analysis highlights the fact that a building cluster influences the frequency content of the central building response particularly in high frequencies. Contrary to the conclusions of other studies where splitting or shifting of the fundamental mode frequency with SSSI has been observed (Kitada et al., 1999; Kham et al., 2006; Guéguen, 2008; Laurenzano et al., 2010; Guéguen and Colombi, 2016), here the first natural frequency appears not to be changed. Bybordiani and Arici (2019) showed that for a cluster composed of identical structures, the number of buildings has no impact on the natural frequency. Here, the absence of foundation in the model and the non-respect of the double resonance condition are probably a limitation to the observation of SSSI effects at the low frequency range.

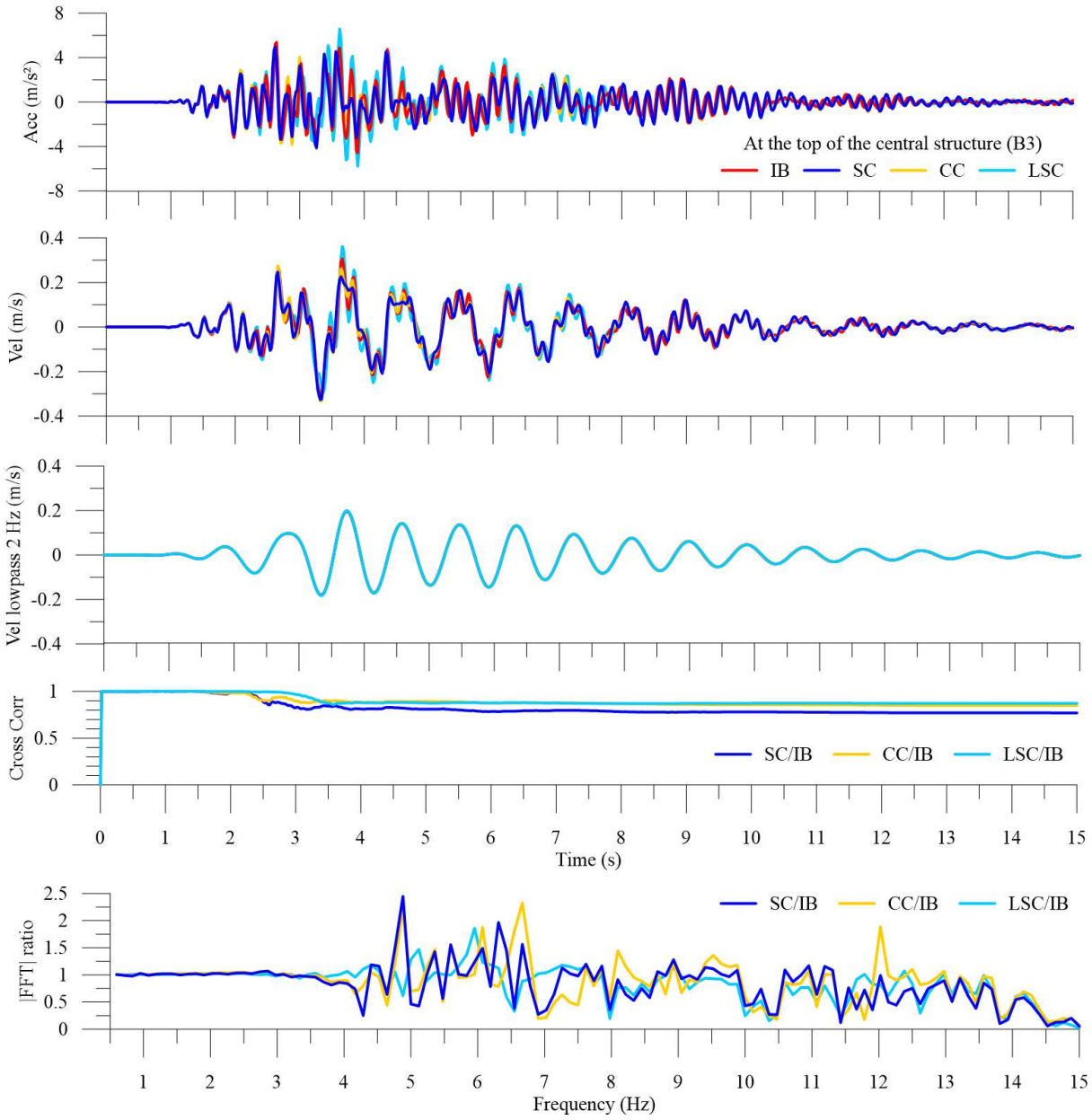

Figure 116: Acceleration and velocity time series, cross-correlations and Fourier spectra amplitude (|FFT|) ratio computed for building B3 top transverse component for all the site-city models.

The analysis of the PA, PV, AI and EI on the longitudinal component (*y*-component in Figure 107) shows that the modifications of the building response due to the presence of a building group in this direction is negligible (Figure 117 and Table 38). This may be explained by the fact that most of the seismic vibration occurs in the transverse and vertical directions in the basin (Figure 118). Differences in the values of the motion intensity parameters are therefore observed in the transverse and vertical directions (respectively *x*- and *z*-component in Figure 107) at the top of the central building. We note that, with respect to the IB case, the PA is increased by 22% in the LSC case and decreased by 2% in the CC case on the transverse

component. The comparison on the vertical component exhibits a general decrease of 4% in each site-city case. AI increases more in the SC case (29%) than in the LSC model (11%) on the vertical component. The increase of AI and the decrease of the PA on the vertical component means that the signal duration is influenced by the presence of a building group. In fact, these results may be explained by the increasing signal duration that is represented by an increase of AI. The comparison of the PV on the transverse component shows an increase of the value up to 16% in the LSC case and 6% in the SC and CC cases whereas it decreases by 6% on the vertical component for all the site-city models. Finally, the EI shows a slight increase of 12% in the LSC and CC models on the transverse component and negligible variations in the SC case. But we notice an increase of this value of more than 100% on the vertical component in the SC and CC cases.

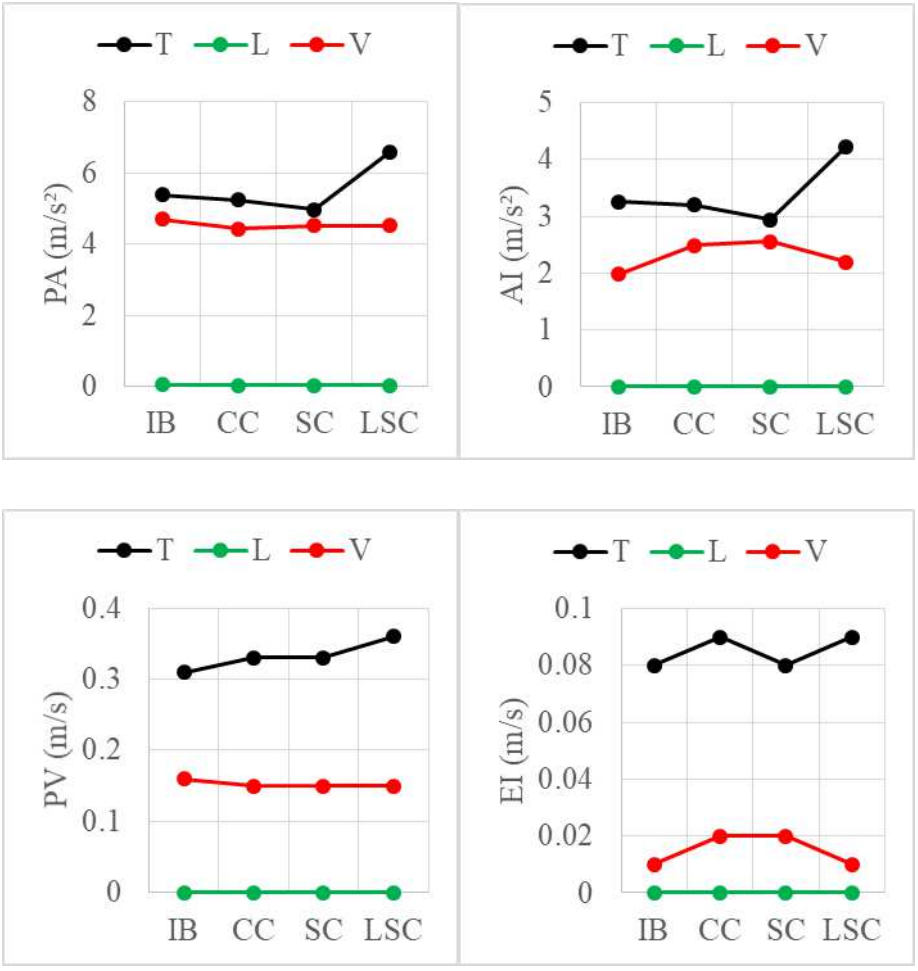

Figure 117: Peak acceleration (PA), peak velocity (PV), Arias intensity (AI) and energy integral (EI) for the longitudinal (L), transverse (T) and vertical (V) components at the top of the building either isolated (IB) or located in the center of the circle cluster (CC), the square cluster (SC) and the large square cluster (LSC). The transverse component is in the direction of the source vibration.

Table 38: Difference in peak acceleration (PA), peak velocity (PV), Arias intensity (AI) and energy integral (EI) parameters between the isolated buildings (IB) case and other site-city models for the transverse (T), longitudinal (L) and vertical (V) components.

	IB-CC (%)			IB-SC (%)			IB-LSC (%)		
	T[+]	L[*]	V[°]	T	L	V	T	L	V
PA (m/s²)	-2	-25	-5	-7	-25	-4	+22	-25	-4
AI (m/s²)	-1	/	+26	-9	/	+29	+30	/	+11
PV (m/s)	+6	/	-6	+6	/	-6	+16	/	-6
EI (m/s)	+12	/	+100	0	/	+100	+12	/	0

[+]Transverse component; [*]Longitudinal component; [°]Vertical component

V.6. Site response analysis

Bard et al. (1996) showed that the coupling effect between SSI and the trapping of the surface waves in the superficial soil layers may induce kind of wave packages in the shape of spindle up to about a hundred meters away from the structures. These phenomena were also observed by Schwan et al. (2016) based on 2D boundary element model and acceleration spectra, transfer functions and time series analysis.

In this thesis, for each sensor localized along the transverse profile of the sedimentary basin, the velocity time series is presented using an amplitude coefficient equivalent on the three components to better visualize the results. The Fourier spectra, AI, PGA, EI and PGV values are shown. We consider the FF case and the IB case as baselines for comparison with the results of the different site-city models to observe spatial variation of the ground motion. On one hand, the comparison by respect to the FF case aims to remove the site response in order to only visualize the influence of buildings on the ground motion. On the other hand, the comparison by respect to the IB model aims to highlight SSSI and SCI effects.

V.6.1. Comparison with the free field

The numerical simulation of the seismic wave propagation in the FF case shows that the fundamental resonance frequency of the basin is around 2 Hz (Figure 118d) that is close to the measured fundamental resonance frequency at NCAD station (2 Hz). Energy in high frequency

ranging up to 6 Hz is noticed at the eastern edge of the basin. In the velocity time series (Figure 118a-c), an increase in signal amplitude and duration is observed toward the center of the sedimentary basin on the transverse and vertical components. No energy is observed on the longitudinal one. The increase in the signal amplitude and duration are due to reflection and diffraction phenomena that lead to the generation of surface waves at the basin edge and to waves trapping in the sedimentary layers. Waves reflections are well represented on the vertical component by several wave front that intersect approximately in the center of the basin. We notice that, for the transverse component, most of the signal energy arrives between 1s and 10s from the western border of the basin to the eastern one. This is illustrated by the increase of PGV with the basin depth, ranging from 0.06 $m.s^{-1}$ at the western edge, to 0.16 $m.s^{-1}$ at x=400 m, then 0.22 $m.s^{-1}$ at x=800 m, to finish at 0.05 $m.s^{-1}$ at the eastern edge (Figure 122). Before x=200 m and after x=900 m, the variation of PGV reflects the break in slope of the basin edges. The maximum value of PGV in the transverse component reaches 22.4 $cm.s^{-1}$ that is greater than five times the PGV of the input signal. It is only equal to 0.3 $cm.s^{-1}$ on the longitudinal one and can be considered as negligible motion. On the vertical component, seismic energy arrived from x=120 m to x=1160 m between 1.5s and 10s (Figure 118c). The PGV variations show the same tendency as the one on the transverse component meaning that the value increases with depth (Figure 124). However, values are lower than on the transverse component. In fact, the maximum PGV value is only 10.6 $cm.s^{-1}$ that is the half of the PGV on the transverse component.

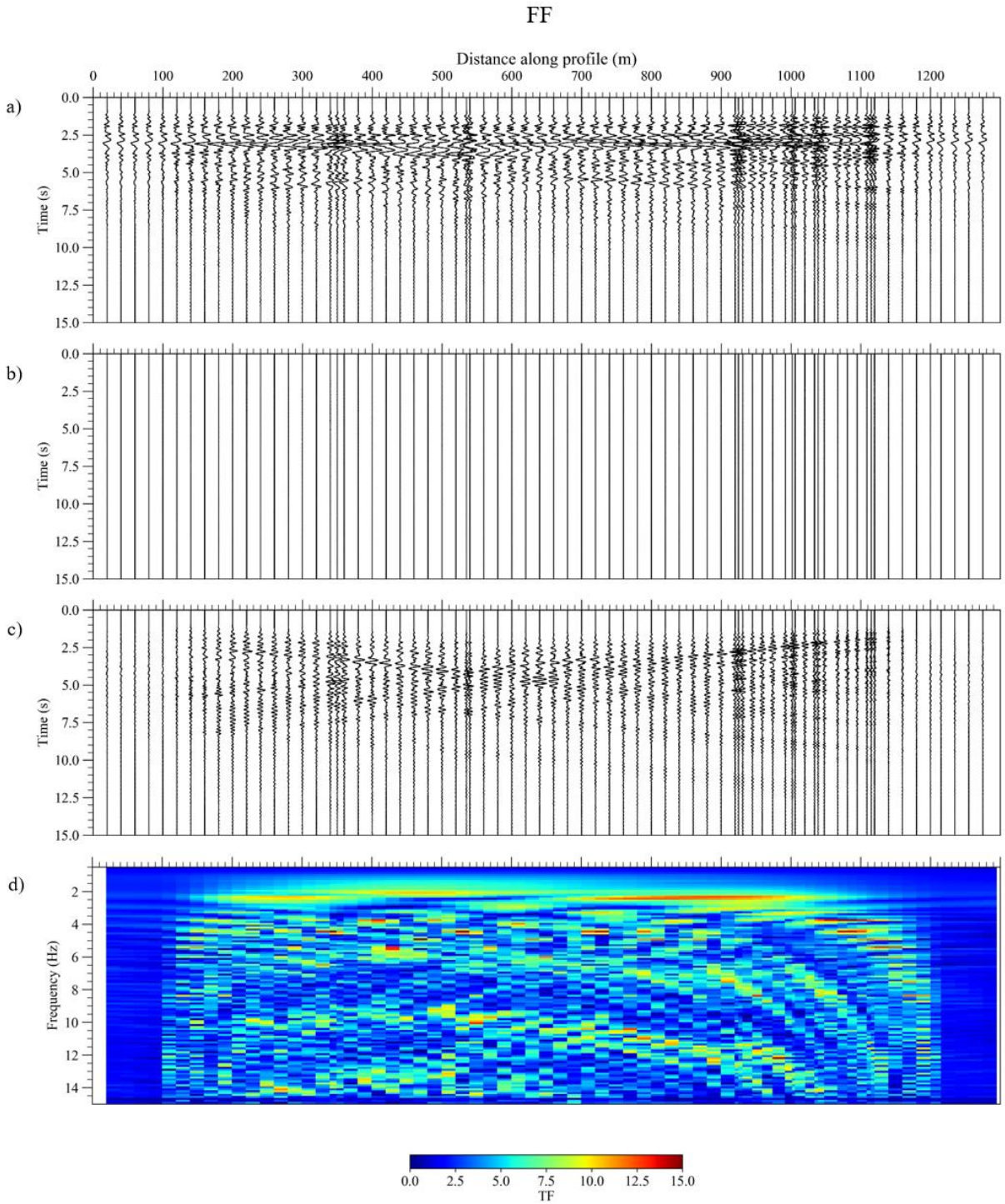

Figure 118: Velocity time series for the transverse (a), longitudinal (b) and vertical (c) components and transfer functions on the transverse component (d) along the SW-NE transverse profile of the basin for the free field (FF) case.

The analysis of the velocity time series and transfer functions of the IB case (Figure 119) shows that they are quite similar to the FF case for all components. No significant effects induced by the presence of isolated buildings are observed. Small changes are noticed on the PGV at the building position. On the transverse component (Figure 122), the value is increased by 7% at x=360 m compared to the FF case (B1), by 14% at x=540 m (B2) and decreased by 7% around

x=1000 m (B3). On the vertical component (Figure 124), the PGV increases of 16% at x=540 m and of 34% at x=1020 m compared to the FF case. The maximal PGV on the transverse component is equal to 22.4 $cm.s^{-1}$, it is 0.4 $cm.s^{-1}$ on the longitudinal one and on the vertical component it is 10.9 $cm.s^{-1}$. These values are quite identical to the maximum PGV values of the FF case on the same components.

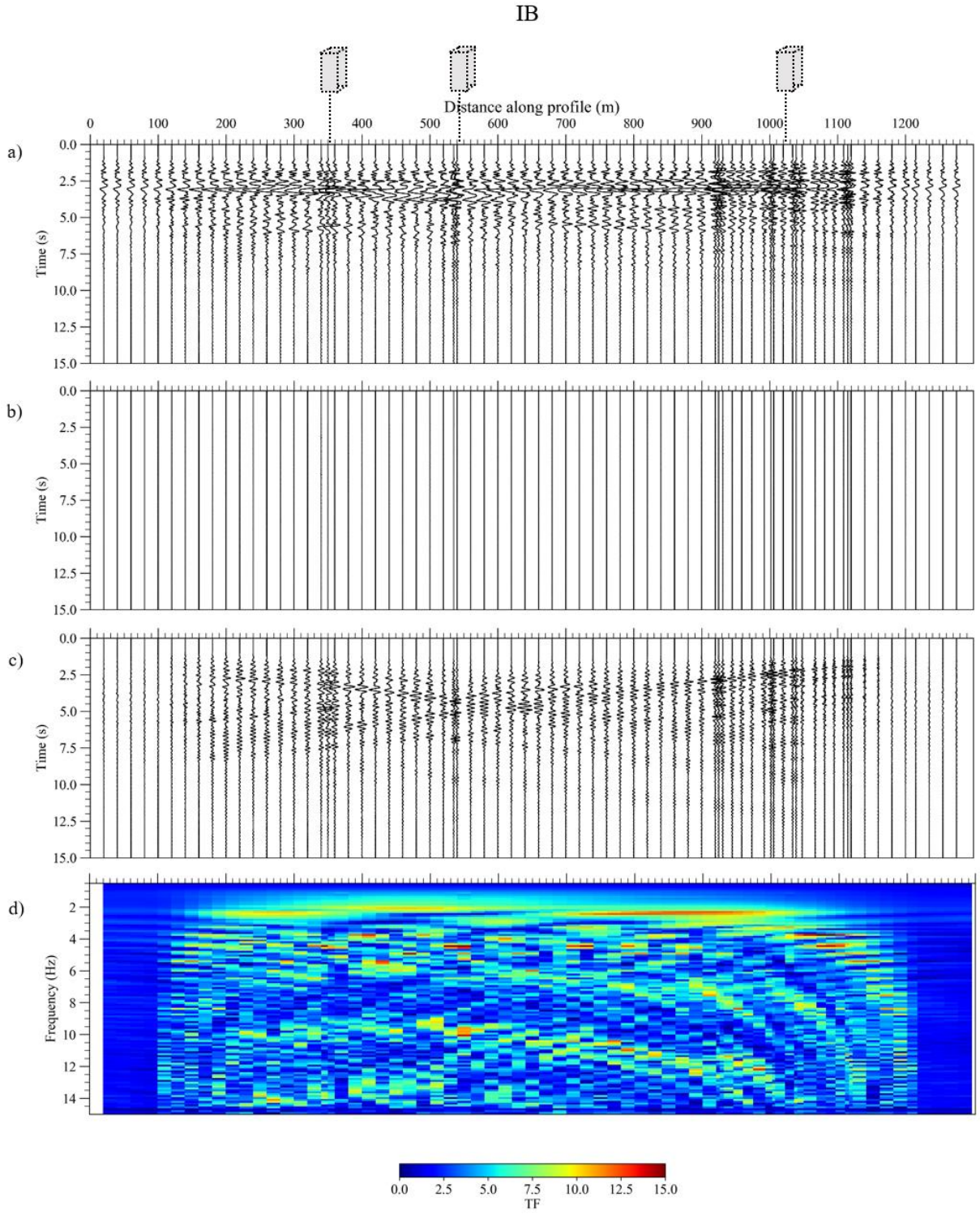

Figure 119: Velocity time series for the transverse (a), longitudinal (b) and vertical (c) components and transfer functions on the transverse component (d) along the SW-NE transverse profile of the basin for the isolated buildings case (IB). Building positions are schematically indicated at the top of the figure.

The comparison of PGV between the IB case and the FF one (Figure 120) shows that the maximal differences is equal to 14% on the transverse component and 34% on the vertical one (Table 39).

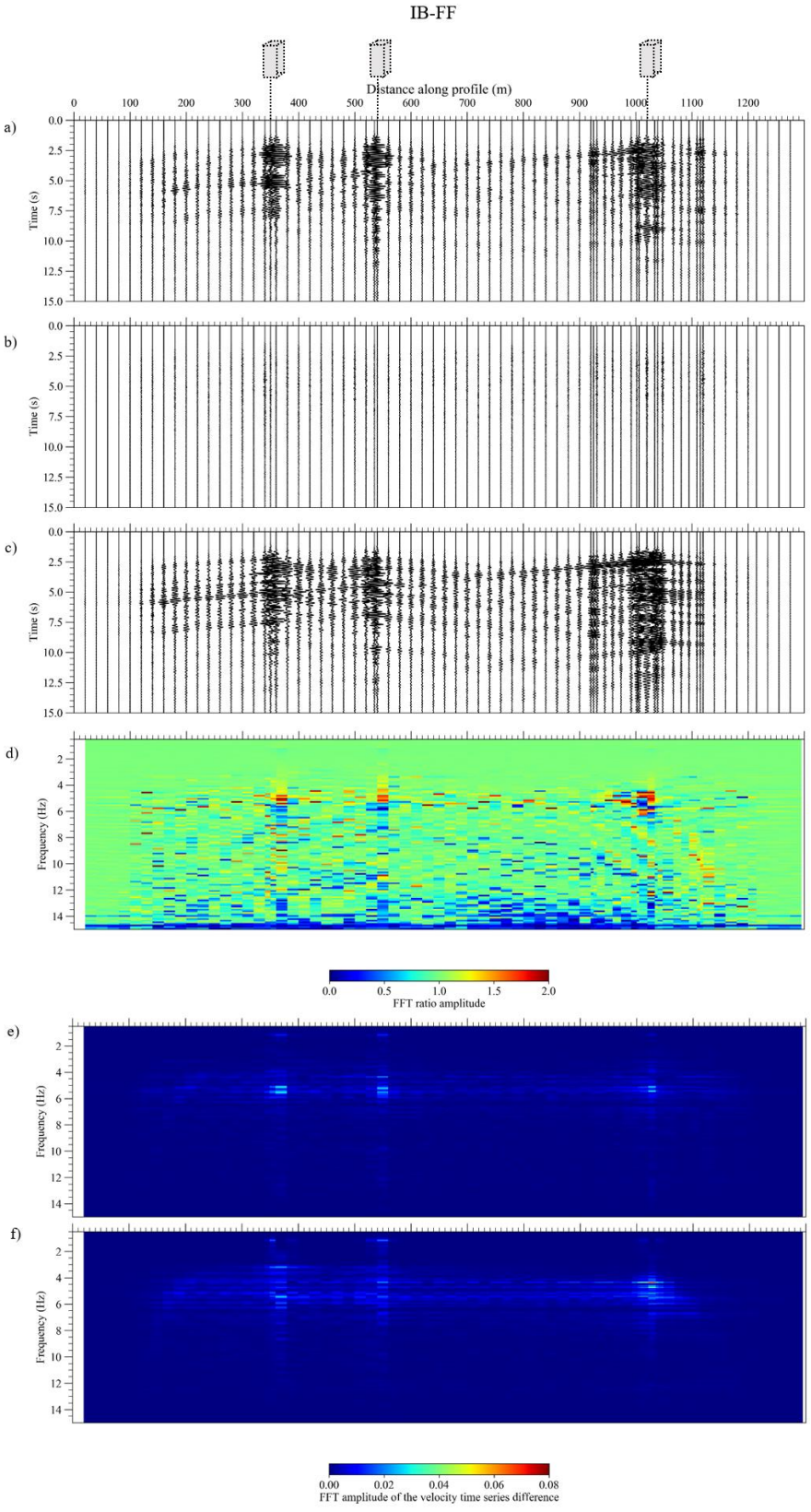

Figure 120: Difference in velocity time series for the transverse (a), longitudinal (b) and vertical (c) components and Fourier spectra amplitude on the transverse component (d) along the SW-NE transverse profile of the basin for the isolated buildings case (IB) compared to the free field (FF) case. (e) and (f) are the Fourier spectra of the difference respectively for the transverse and vertical components. Building positions are schematically indicated at the top of the figure.

Table 39: Maximum difference in peak ground velocity between the free field (FF) and the site-city cases: isolated buildings (IB), circle cluster (CC), square cluster (SC) and large square cluster (LSC).

FF REF		IB	CC	SC	LSC
Max diff (%)	Transverse	+14	+15	+16	+16
	Vertical	+34	+56	+62	-34

The discrepancies are highlighted from x=120 m up to x=1180 m. They are notably marked at the building positions where all the considered intensity parameters exceed at least 5% of deviation compared to the FF case on the transverse component (Figure 121 and Figure 122). On the vertical component, the effects are more noticeable with differences observed up to 15s on the time series and stronger at the building positions and between them (Figure 120c). AI notably increases by 91% at x=1020 m on the vertical component. Differences in the motion intensity parameters are also observed at these positions for the comparison between the FF-CC, FF-SC and FF-LSC models (Figure 125 and Figure 128).

The Fourier spectra amplitude comparison exhibits some amplification higher or equal to 2 at the building positions between 5 and 5.5 Hz (Figure 120d) which corresponds to the second natural frequency of the block models. These amplifications are directly followed by an amplitude reduction at 6 Hz. This is also observed on the Fourier spectra amplitude ratio of FF-CC (Figure 125d). We note that the first natural frequency of building (1.1 Hz) has not enough energy to express significant variations compared to the second resonant frequency (Figure 112). The energy on the vertical component seems to be higher than the one on the transversal component (Figure 125e-f)

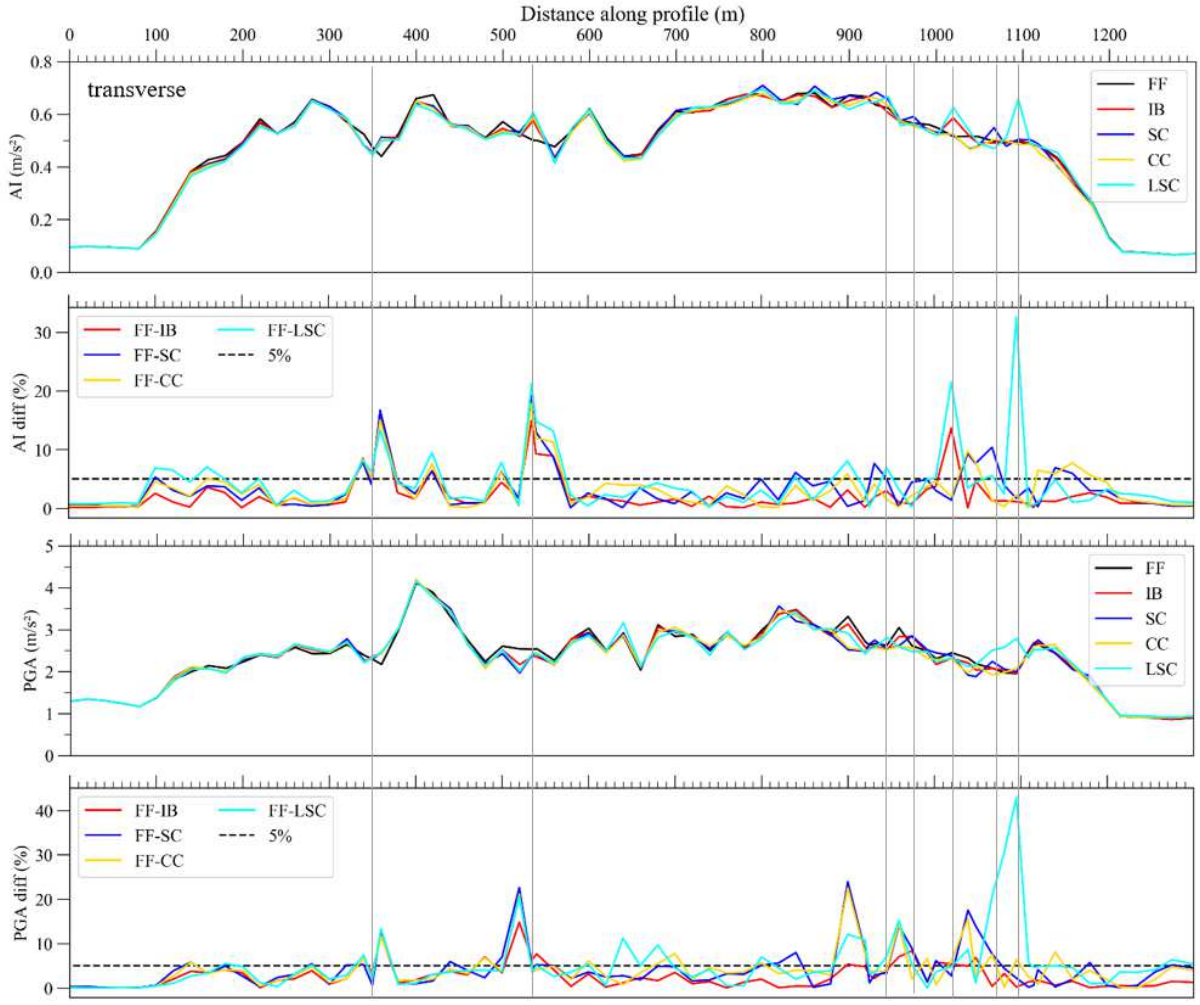

Figure 121: Arias intensity (AI) and peak ground acceleration (PGA) for the transverse component for each site-city model and related differences by respect to the free field (FF) case. Gray lines indicate the positions of buildings depending on the site-city model.

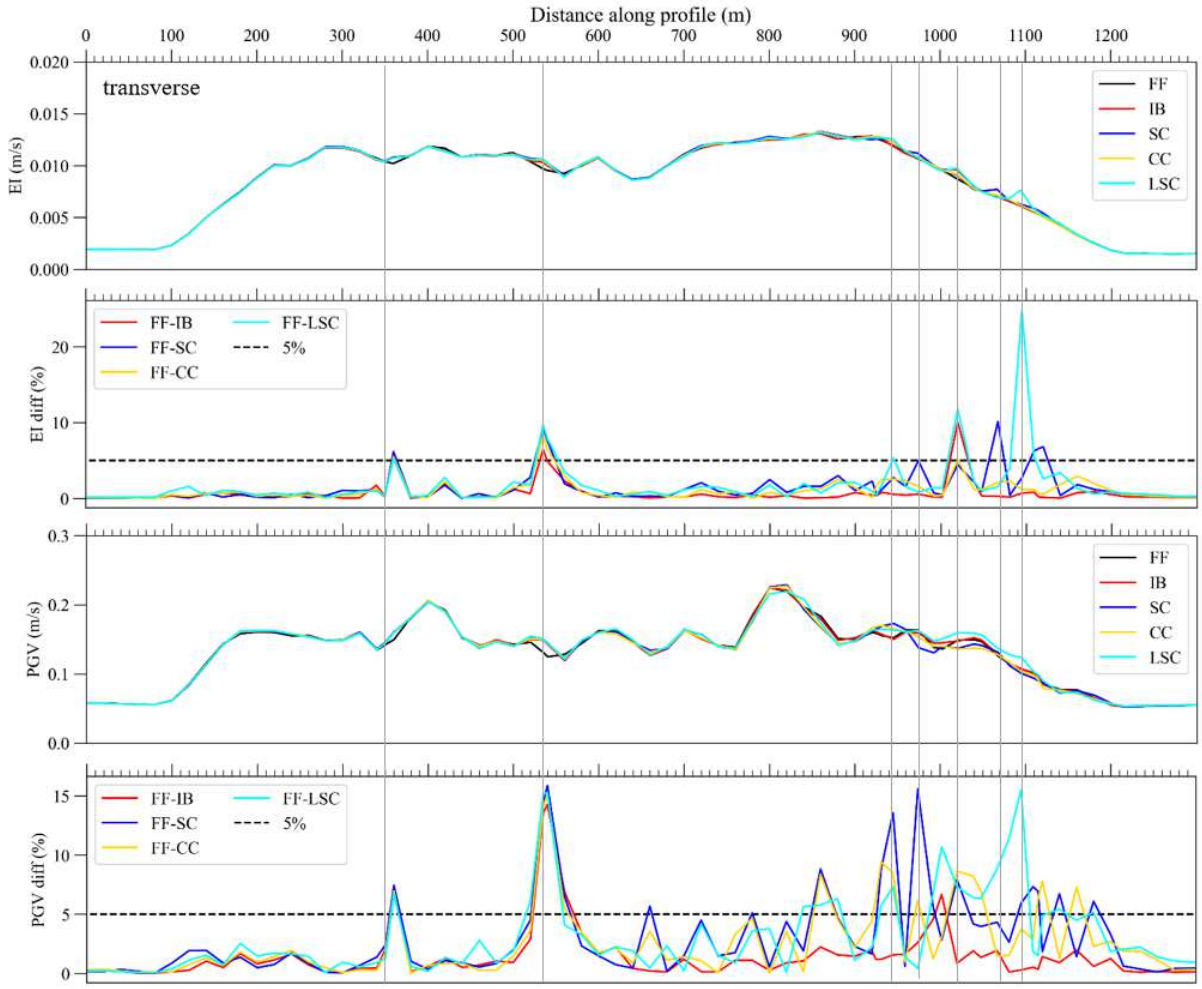

Figure 122: Energy integral (EI) and peak ground velocity (PGV) for the transverse component for each site-city model and related difference by respect to the free field (FF) case. Gray lines indicate the positions of buildings depending on the site-city model.

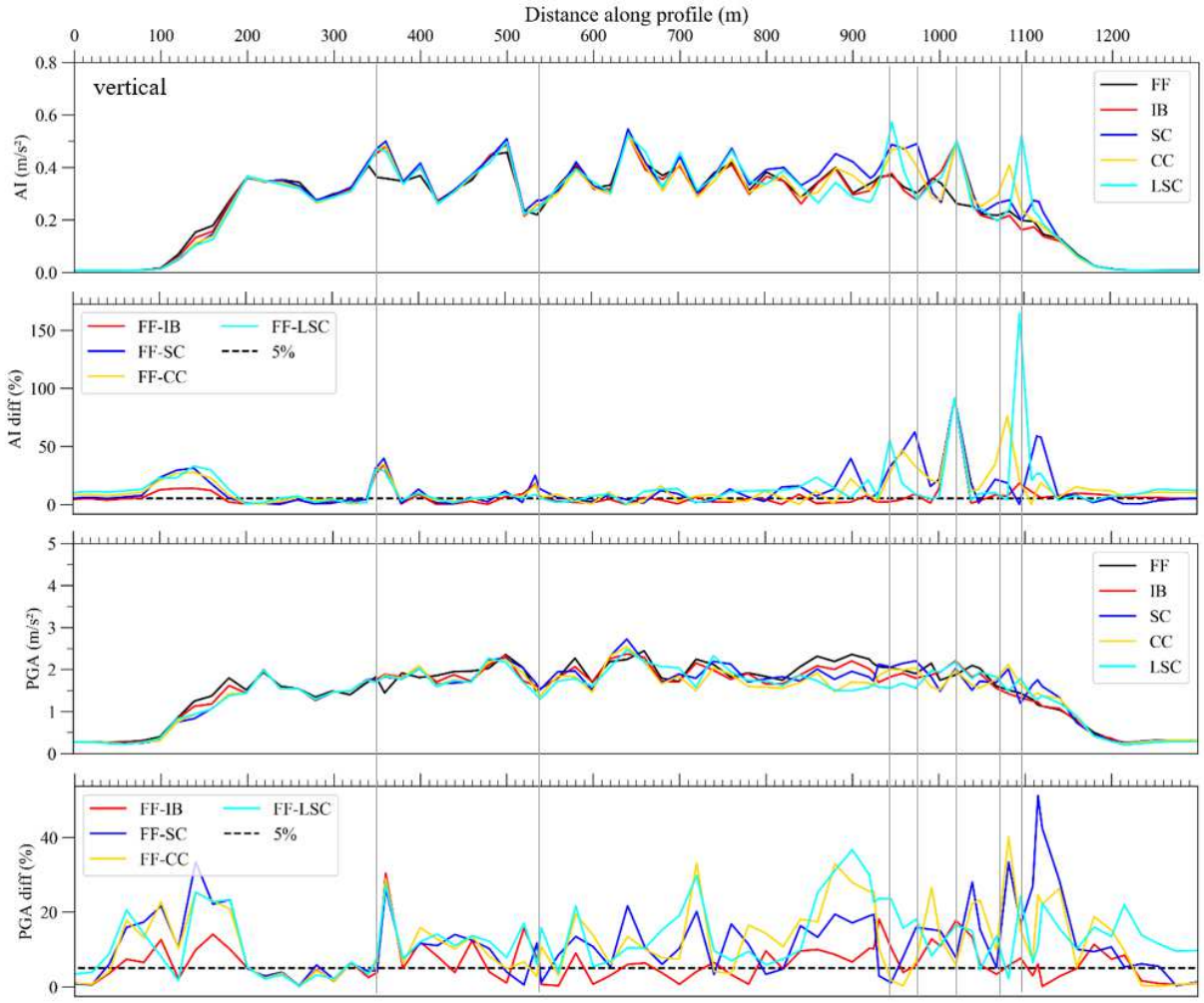

Figure 123: Arias intensity (AI) and peak ground acceleration (PGA) for the vertical component for each site-city model and related difference by respect to the free field (FF) case. Gray lines indicate the positions of buildings depending on the site-city model.

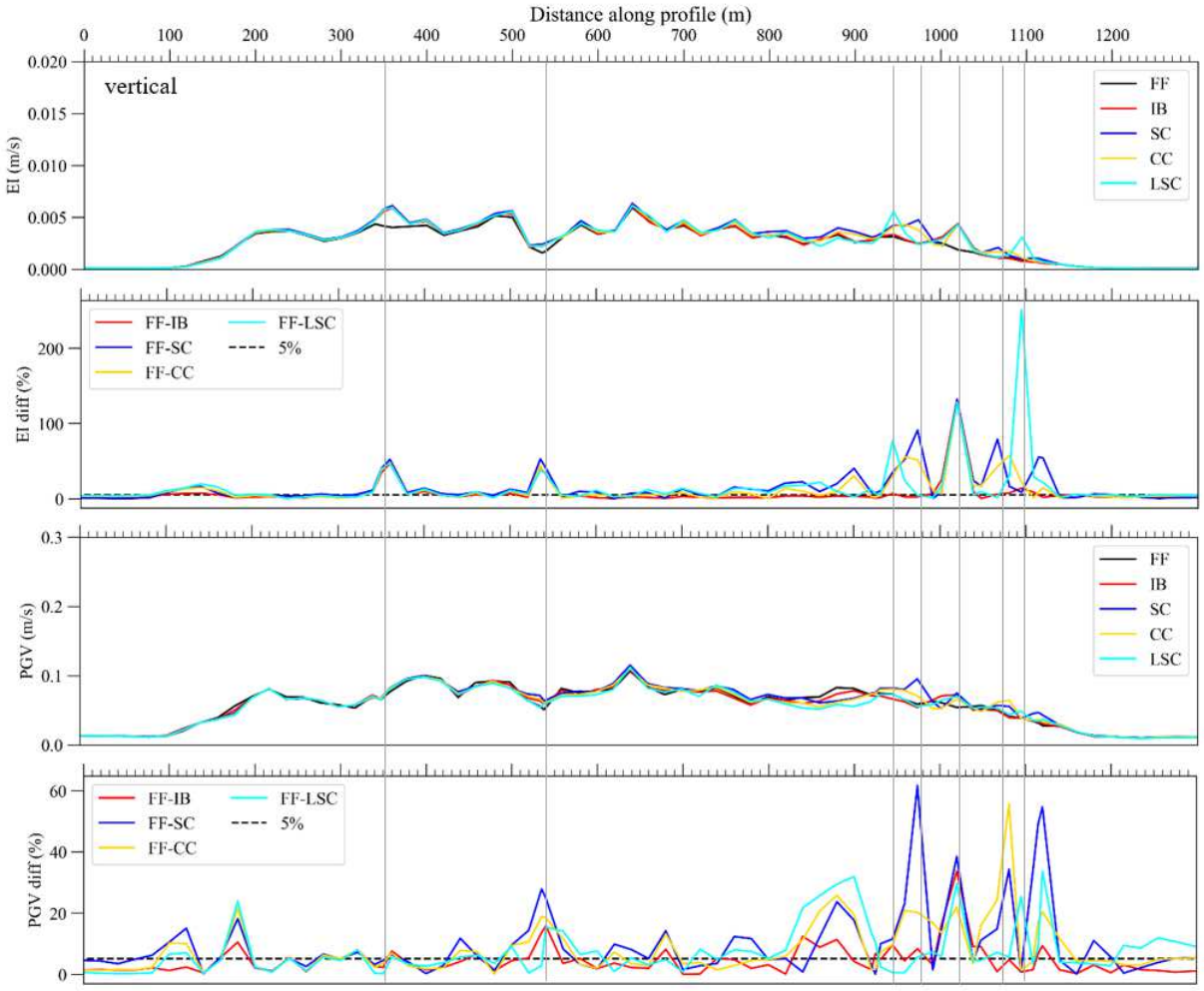

Figure 124: Energy integral (EI) and peak ground velocity (PGV) for the vertical component for each site-city model and related difference by respect to the free field (FF) case. Gray lines indicate the positions of buildings depending on the site-city model.

We observe on the transverse and vertical components that the differences in the velocity time series between the CC and the FF cases (Figure 125) behave like a wave plane characterized by a strong difference starting from x=1050 m at 1s and propagating to x=200 m at 6s. This phenomenon is also observed with SC-FF (Figure 128), LSC-FF (Figure 129) and CC-IB (Figure 130). The maximum value of PGV is reached at x=540 m at the B2 level with an increase of 15% on the transverse component and of 56% on the vertical one compared to FF (Table 39). From x=880 m corresponding to the slope break of the basin-bedrock interface at the east, the PGV, AI and EI slightly increase while the PGA decreases compared to the FF model (Figure 121 and Figure 122). The velocity time series differences are more emphasized on the vertical component where we can possibly observe a second plane wave starting from x=1060 m at 4s and going up to x=180 m at 7.5s (Figure 125c). At the building positions, the differences are observed on the whole duration of the signal. The comparison between the SC

and FF cases shows the same results. Moreover, the main effects of the presence of buildings in the cluster seem to be concentrated around the central building B3 from x=960 m to x=1070 m. This is well depicted on Figure 126 for the transverse component and on Figure 127 for the vertical component. These figures show a spatial zoom of the velocity time series filtered below 2 Hz at the cluster level in order to better follow the building response influence. In comparison, the time series differences for the analysis of the SC model are highlighted in the whole cluster from x=920 m to x=1120 m. Stronger differences are also noted after B3 at x=1080 m where the PGV on the vertical component reaches 56% of difference compared to the FF case (Figure 122). This position corresponds to a sensor placed at 37.5 m from the B3 between two buildings in the longitudinal direction of the valley (see CC spatial arrangement in Figure 110). These observations may be linked to the reflection of seismic waves by the buildings that create constructive interferences with other building responses and surface waves.

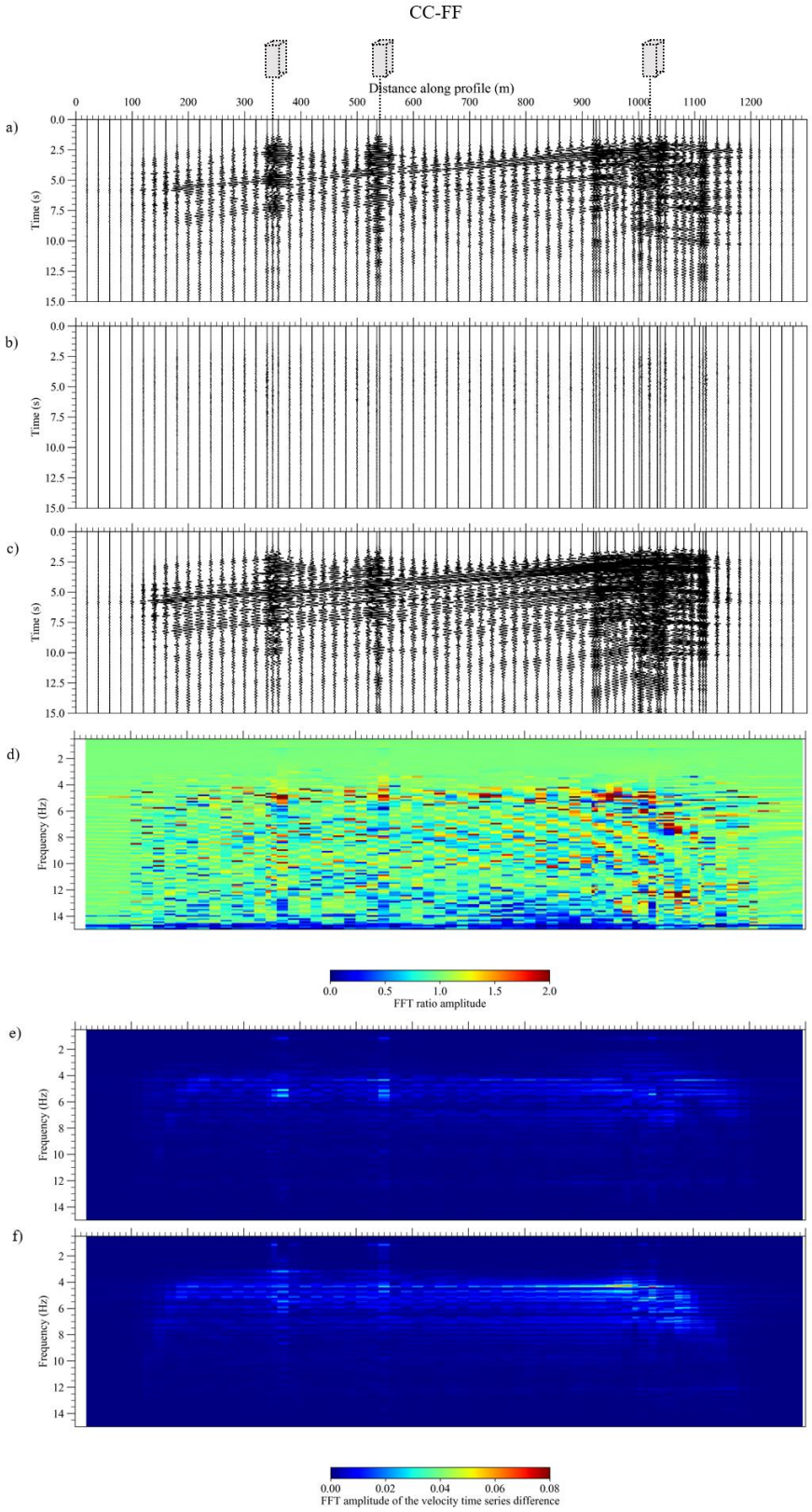

Figure 125: Difference in velocity time series for the transverse (a), longitudinal (b) and vertical (c) components and Fourier spectra amplitude on the transverse component (d) along the SW-NE transverse profile of the basin for the circle cluster (CC) case compared to the free field (FF) case. (e) and (f) are the Fourier spectra of the difference respectively for the transverse and vertical components. Building positions are schematically indicated at the top of the figure.

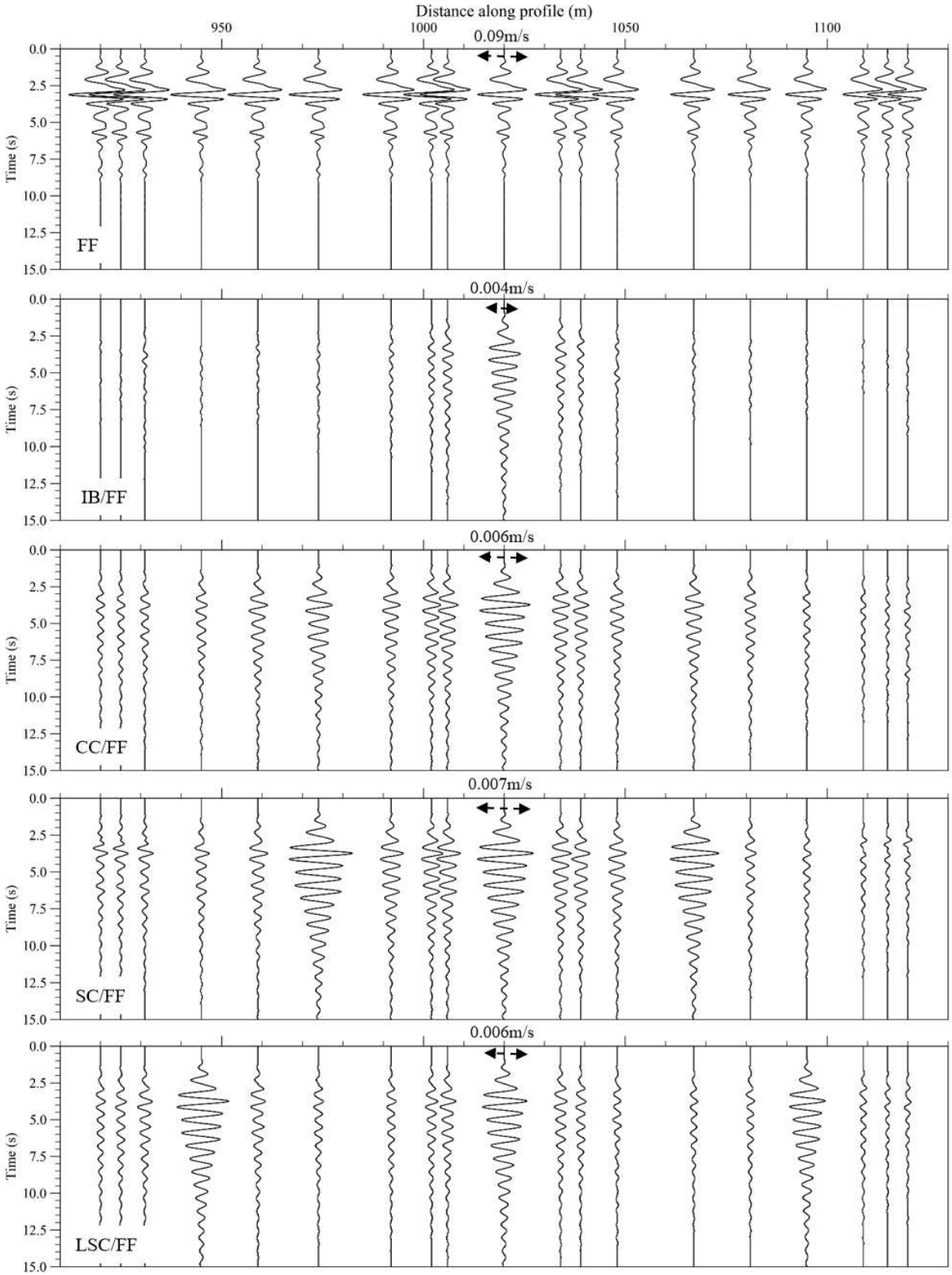

Figure 126: Zoom on the velocity time series filtered below 2 Hz on the transverse component for the free field case (FF). Zoom on the difference in velocity time series filtered below 2 Hz on the same component for the isolated buildings (IB), the circle cluster (CC), the square cluster (SC) and the large square cluster (LSC) cases compared to the FF case.

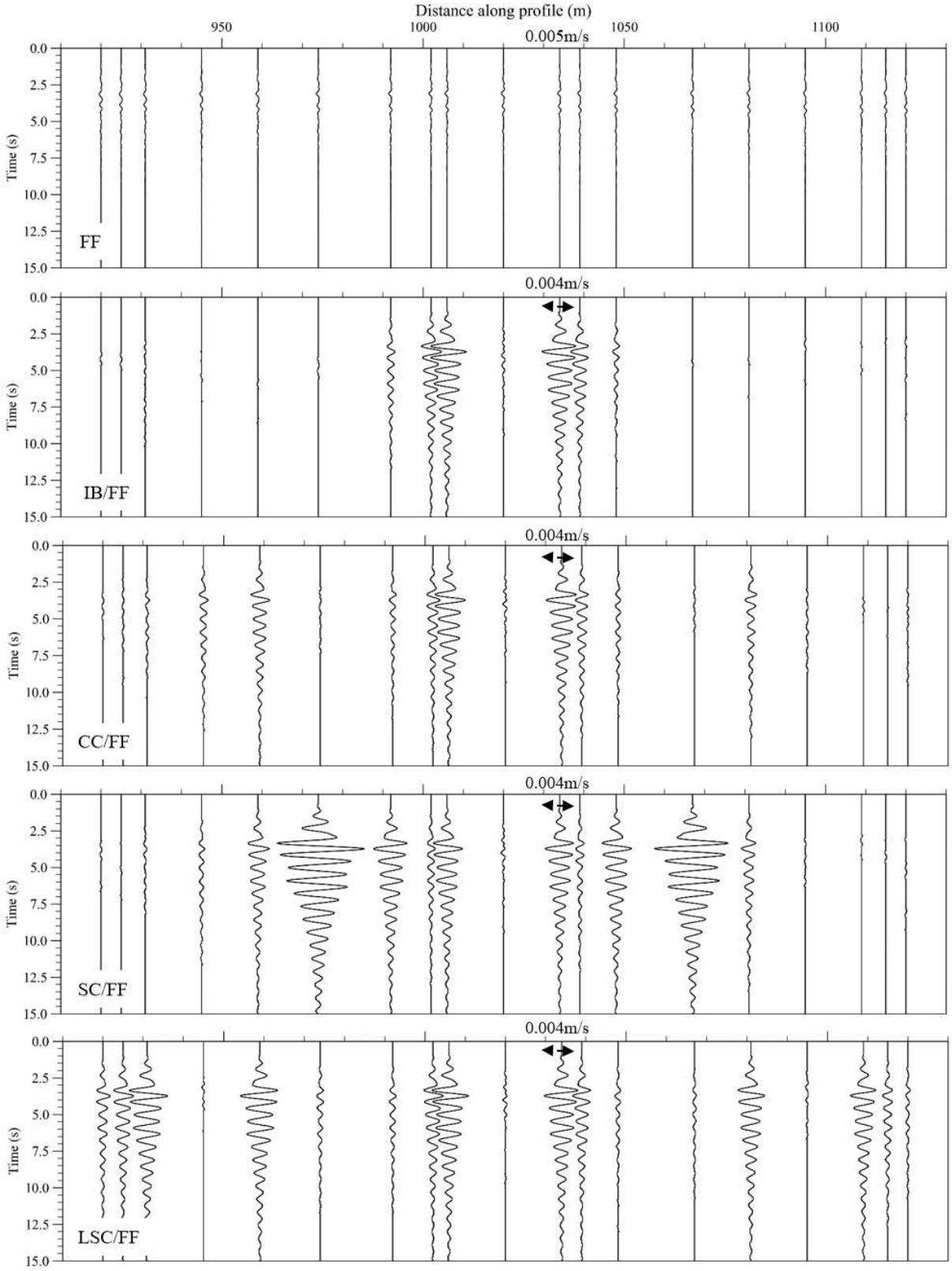

Figure 127: Zoom on the velocity time series filtered below 2 Hz on the vertical component for the free field case (FF). Zoom on the difference in velocity time series filtered below 2 Hz for the same component for the isolated buildings (IB), the circle cluster (CC), the square cluster (SC) and the large square cluster (LSC) cases compared to the FF case.

The Fourier spectra amplitude ratio between the CC and FF cases exhibits complex frequency content compared to the ratio of FF-IB (Figure 125d). Amplifications are marked on a large frequency range from 4 Hz to 13.5 Hz. We observe strong energy at 4.5 Hz on the vertical component up to 200 m from the cluster toward the west (Figure 120e-f). These results are retrieved for the comparison FF-SC (Figure 128e-f), FF-LSC (Figure 129e-f) and all the comparison with respect to IB case (CC-IB in Figure 130, SC-IB in Figure 133 and LSC-IB in Figure 134). In the building cluster, the maximum of amplification is spread from 5.5 Hz at x=920 m to the high frequency range up to 8 Hz at x=1210 m. It follows the eastern slope break of the basin. This was also observed in the FF model (Figure 118d). The same observation can be made with the spectral ratio of FF-SC (Figure 128d), IB-CC (Figure 130d), IB-SC (Figure 133d) and IB-LSC (Figure 134d).

The comparison between the SC and FF cases provides quite similar results than the FF-CC comparison. The maximum difference in PGV on the transverse component reaches 16% and the one on the vertical one is 62% (Table 39). The analysis of the motion intensity parameters shows that the maximum difference on the transverse component occurs at x=540 m close to B2 (Figure 121 and Figure 122). These results are retrieved in the comparison of the LSC and the FF cases. The SC model presents, among the other models, the higher level of deviations on the PGA and PGV values on the vertical component with an increase of more than 50% at x=1120 m compared to FF. The results are similar in the comparison of the SC model to the IB model.

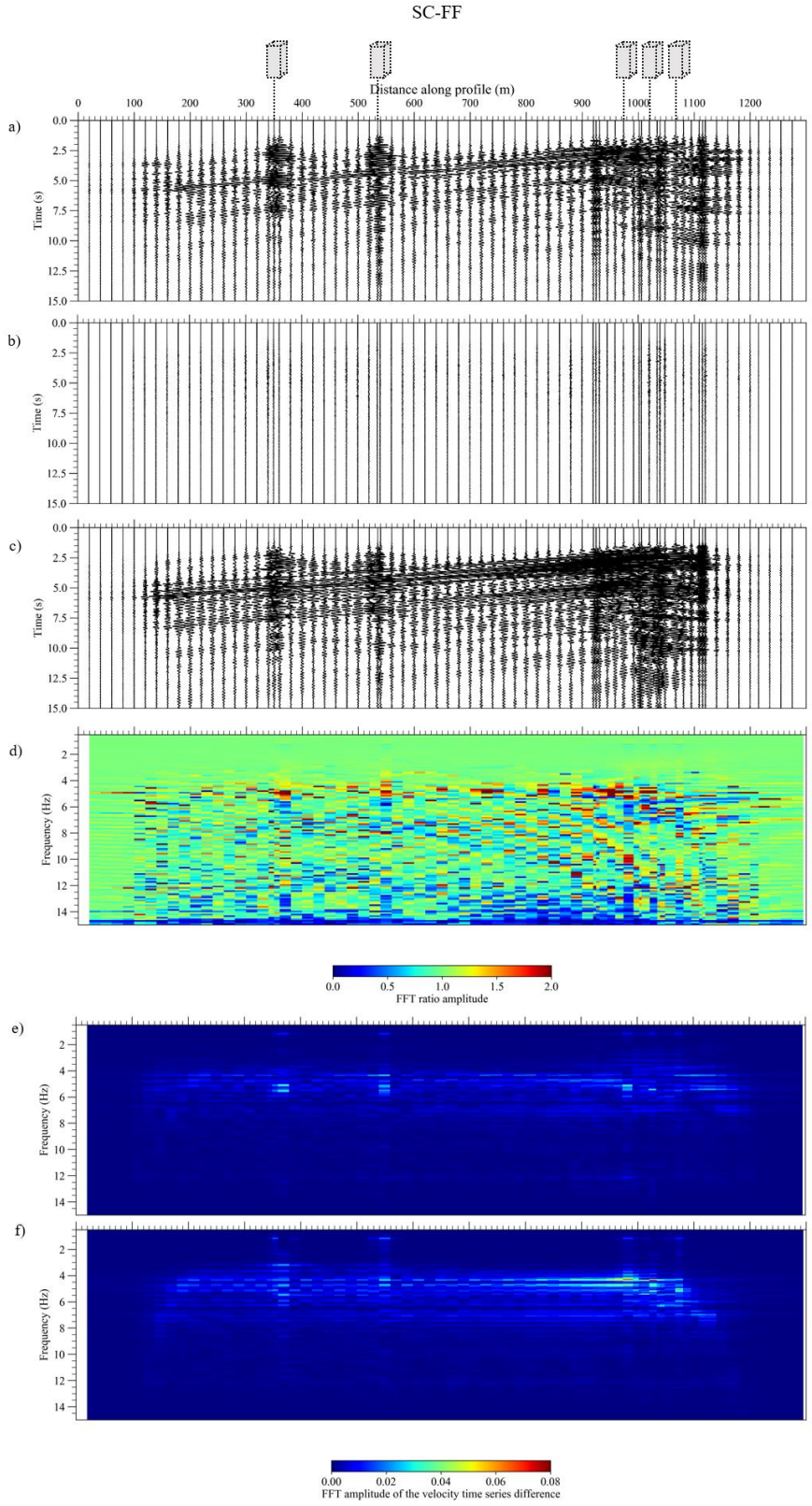

Figure 128: Difference in velocity time series for the transverse (a), longitudinal (b) and vertical (c) components and Fourier spectra amplitude on the transverse component (d) along the SW-NE transverse profile of the basin for the square cluster (SC) case compared to the free field (FF) case. (e) and (f) are the Fourier spectra of the difference respectively for the transverse and vertical components. Building positions are schematically indicated at the top of the figure.

The comparison of the LSC model to the FF case presents stronger differences in the velocity time series of the transverse component at x=540 m (B2) than the other model comparisons (Figure 129a). These differences are notably observed on the whole signal duration up to 15s and for most of the seismic traces whether it is on the transverse or vertical components (Figure 129c). In the building cluster, the time series discrepancies seem to be concentrated in three areas around the three buildings aligned in the transverse direction: 1) between x=920 m and x=960 m, 2) between x=990 m and x=1050 m and 3) between x=1080 m and x=1120 m. This is particularly well observed on Figure 126 and Figure 127 where the amplitude of the differences is higher close to building positions. The maximum difference in the motion intensity parameter is shown at x=1090 m at the eastern part of the building cluster with an increase of more than 15% for all the parameters (Figure 121 and Figure 122) while the maximal difference in PGV is equal to 16% on the transverse component and to 34% on the vertical one (Table 39).

On the vertical component, the time series differences are lower at B1 (x=350 m) and B2 (x=540 m) positions than the other site-city models. This is also observed in the analysis of the motion intensity parameters with a lower difference compared to FF (Figure 123 and Figure 124). We also note a decrease up to 35% of the AI and PGA values at the western border of the basin compared to the FF case. The results are similar in the comparison of the LSC model to the IB one.

The FF-LSC Fourier spectra amplitude ratio (Figure 129d) is comparable to that of FF-CC rather than FF-SC. The major difference occurs from x=1040 m where the amplification equal or higher than 2 occurs around 5.5 Hz contrary to the FF-CC ratio (visible at high frequency). Strong amplification is also observed between 11 and 12 Hz at this position. This phenomenon may be explained by the impact of the distance between the buildings on the modification of the frequency content of the surface ground motion. In fact, the building distance for the LSC model is two times larger than the one of the SC and CC cases (Figure 110). Also, the presence of buildings closer to the eastern basin edge (x=1090 m) compared to the SC model (x=1070 m) may induce a shift or a concentration of the energy amplification from the high frequency to the second natural frequency of building (Figure 129e-f).

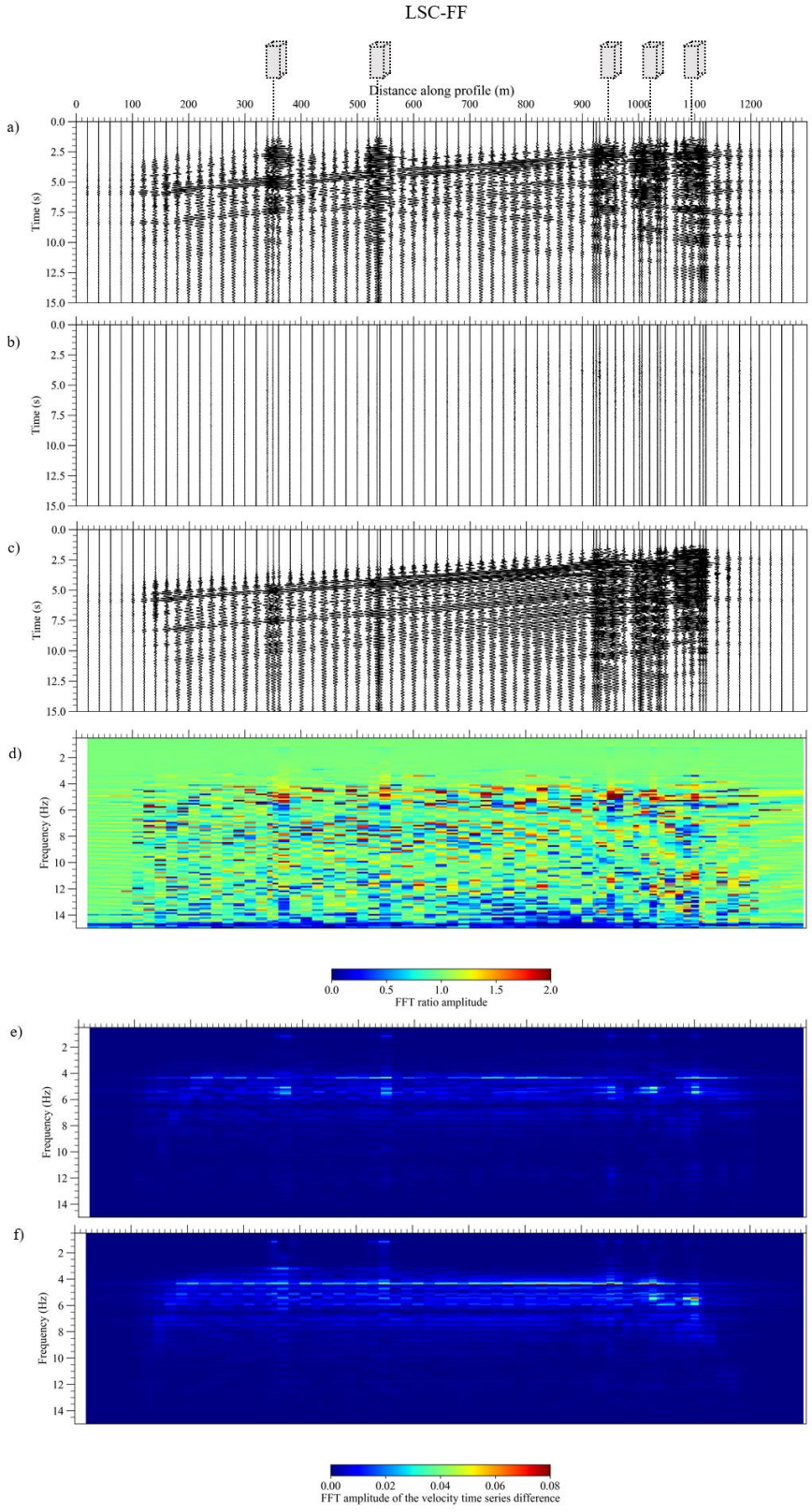

Figure 129: Difference in velocity time series for the transverse (a), longitudinal (b) and vertical (c) components and Fourier spectra amplitude on the transverse component (d) along the SW-NE transverse profile of the basin for the large square cluster case (LSC) compared to the free field (FF) case. (e) and (f) are the Fourier spectra of the difference respectively for the transverse and vertical components. Building positions are schematically indicated at the top of the figure.

V.6.2. Comparison with the isolated buildings case

Considering the similarities of the FF and IB time series (Figure 118 and Figure 119), we expect comparable results between the comparison of the CC, SC and LSC models to IB model than the comparison to FF. The only expected discrepancies should appear at the position of the city.

In the comparison between the CC and IB cases, we notice slight time series differences at the position of B1 (x=350 m) and B2 (x=540 m) on the transverse component (Figure 130a). This is also observed in the comparison between SC and IB models (Figure 133a). On the vertical component, the results are quite similar to the FF-CC comparison (Figure 125c). The maximum difference in PGV is equivalent to 10% on the transverse component and more than 60% on the vertical one (Table 40).

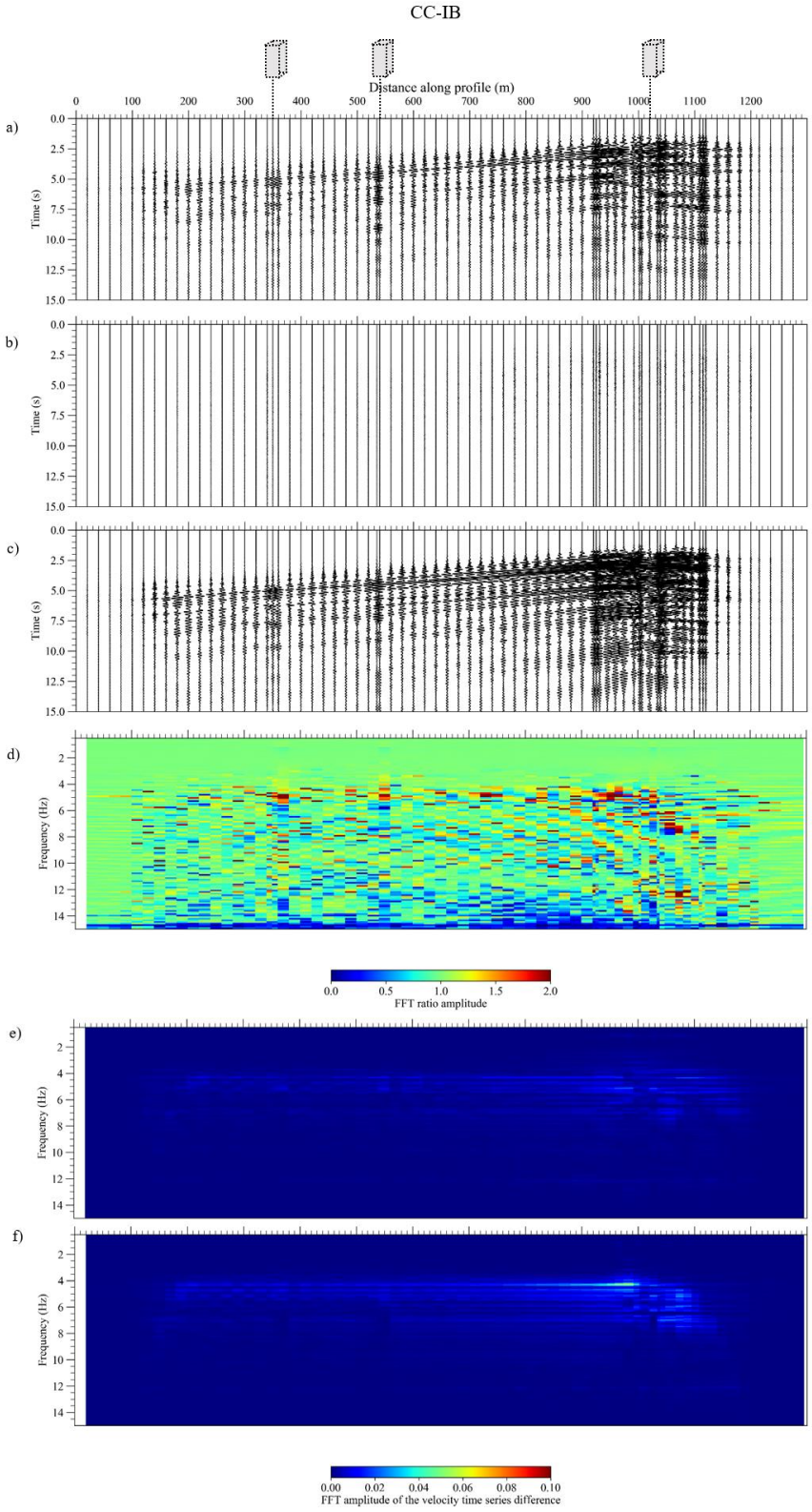

Figure 130: Difference in velocity time series for the transverse (a), longitudinal (b) and vertical (c) components and Fourier spectra amplitude on the transverse component (d) along the SW-NE transverse profile of the basin for the circle cluster (CC) case compared to the isolated buildings (IB) case. (e) and (f) are the Fourier spectra of the difference respectively for the transverse and vertical components. Building positions are schematically indicated at the top of the figure.

Table 40: Maximum difference in peak ground velocity between the isolated buildings (IB) and the other site-city cases: circle cluster (CC), square cluster (SC) and large square cluster (LSC).

IB REF		CC	SC	LSC
Max diff (%)	Transverse	+10	+15	-16
	Vertical	+63	+76	-29

The only differences are a decrease of 20% of the motion intensity parameters at the western border of the basin between x=40 m and x=190 m compared to IB model (Figure 131 and Figure 132).

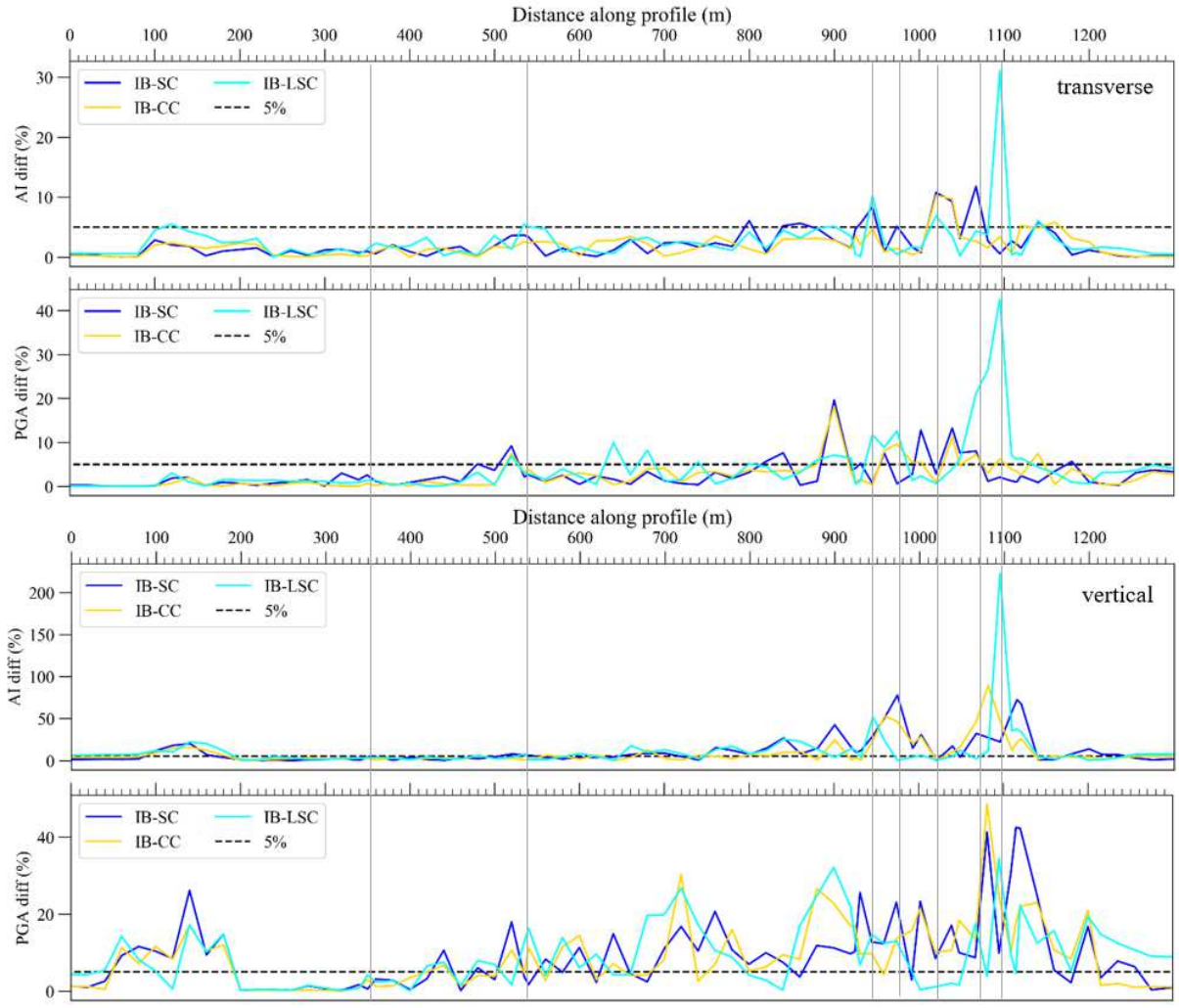

Figure 131: Arias intensity (AI) and peak ground acceleration (PGA) difference for the transverse and vertical components for each case compared to the isolated buildings (IB) case. Gray lines indicate the positions of buildings depending on the site-city model.

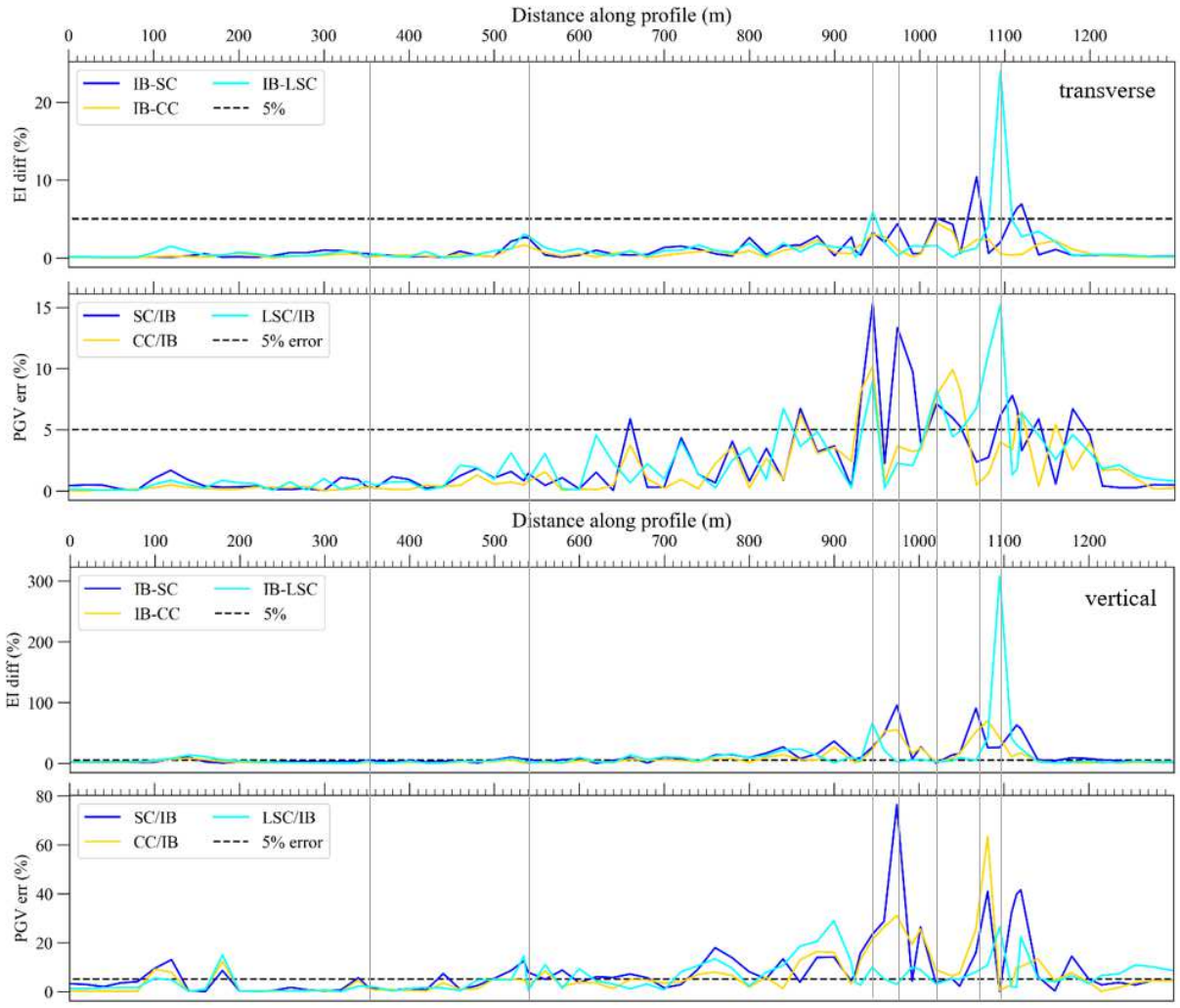

Figure 132: Energy integral (EI) and peak ground velocity (PGV) difference for the transverse and vertical components for each case compared to the isolated buildings (IB) case. Black lines indicate the positions of buildings depending on the site-city model.

For the transverse and vertical components, strong discrepancies between the motion intensity parameters are noticed from x=540 m (B2) with a deviation increase compared to the IB case, exceeding 5% at x=900 m that corresponds to the slope break of the basin and reaching a maximum value of 18% with a decrease of the PGA at this same location (Figure 131 and Figure 132).

As in the comparison of CC with IB cases, the differences between the motion intensity parameters tend to increase after x=540 m (B2) between the SC and IB models (Figure 131 and Figure 132). This is also observed in the comparison of IB-LSC. On the transverse component, the maximum deviation occurs at x=940 m at the position of the first building at the west of the city with an increase of 15% of the PGV. On the vertical component, the maximum difference

is found between B2 and the cluster location at x=970 m with a strong increase of EI (95%) and PGV (76%).

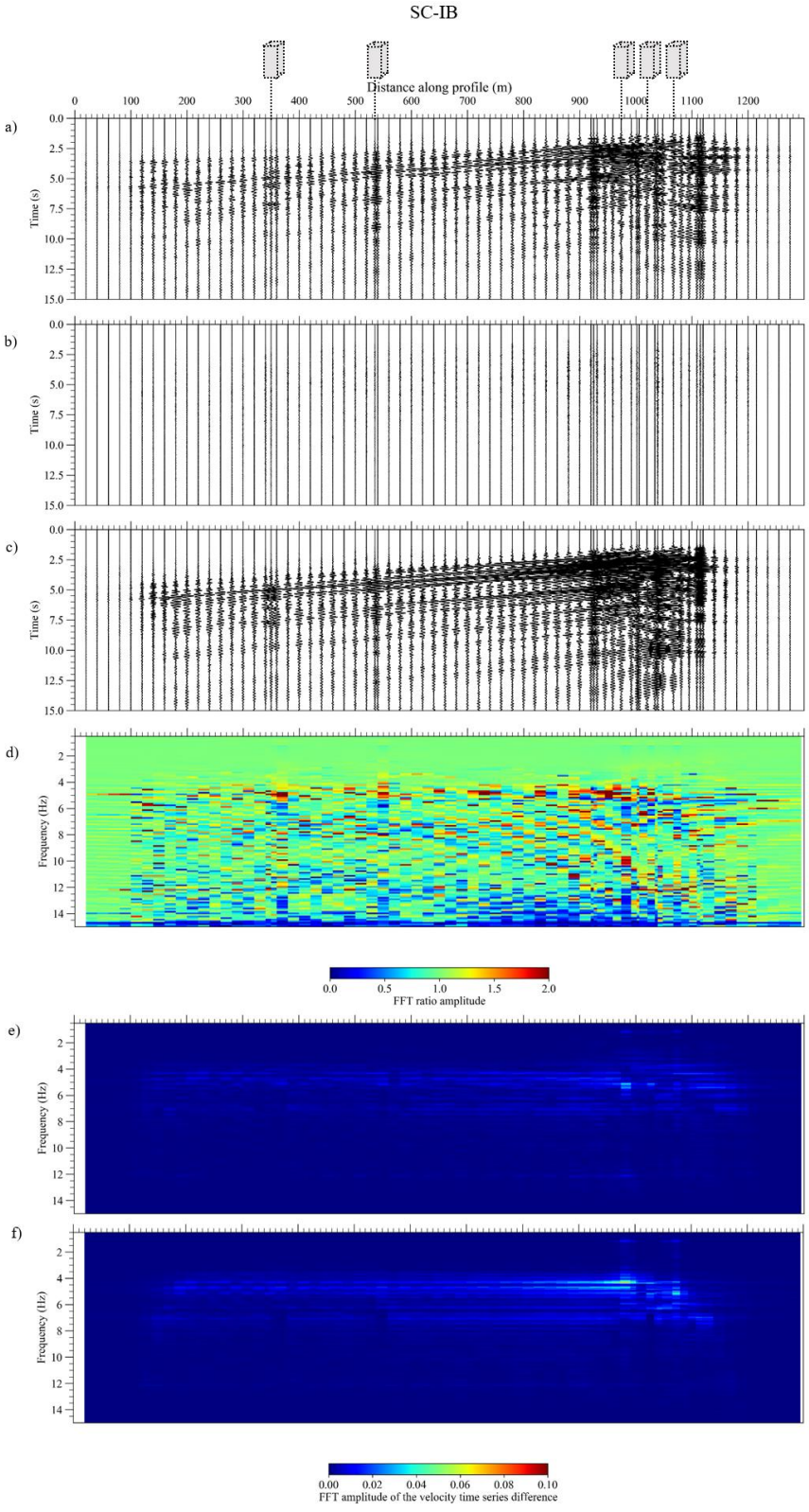

Figure 133: Difference in velocity time series for the transverse (a), longitudinal (b) and vertical (c) components and Fourier spectra amplitude on the transverse component (d) along the SW-NE transverse profile of the basin for the square cluster (SC) case compared to the isolated buildings (IB) case. (e) and (f) are the Fourier spectra of the difference respectively for the transverse and vertical components. Building positions are schematically indicated at the top of the figure.

The comparison between LSC and IB cases shows that the maximum difference in the motion intensity parameters is observed at x=1090 m with an increase of all the considered parameters (at least 15%) on the transverse component (Figure 131 and Figure 132). At this same position, a major increase of AI (223%) and EI (308%) is highlighted with an increase of PGA and PGV around 20% compared to the IB model on the vertical component. At the western border of the basin, the PGA decreases by 17% on the vertical component compared to the IB model.

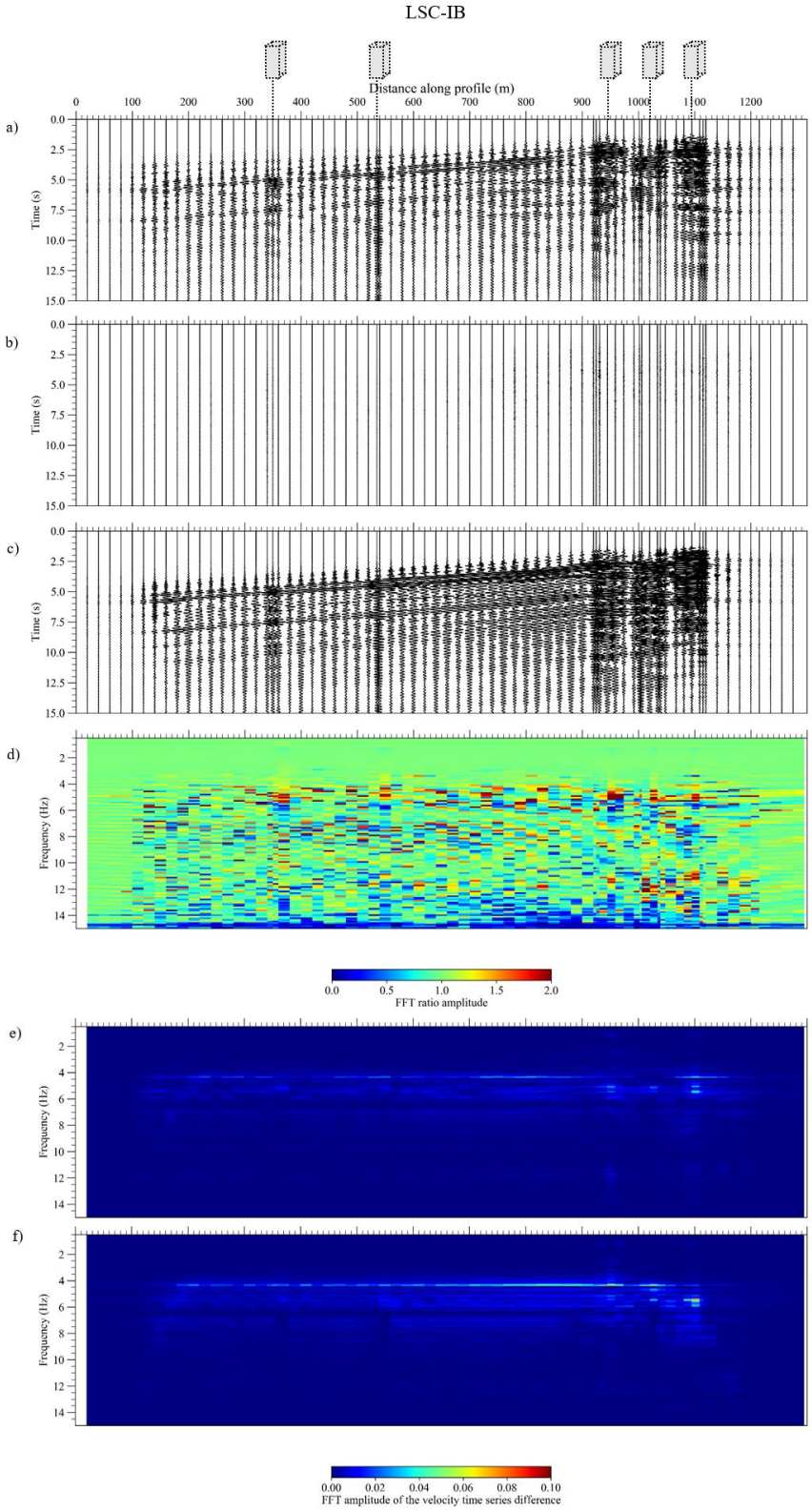

Figure 134: Difference in velocity time series for the transverse (a), longitudinal (b) and vertical (c) components and Fourier spectra amplitude on the transverse component (d) along the SW-NE transverse profile of the basin for the large square cluster (LSC) case compared to the isolated buildings (IB) case. (e) and (f) are the Fourier spectra of the difference respectively for the transverse and vertical components. Building positions are schematically indicated at the top of the figure.

V.7. Discussion

Even if the energy radiated by the building in the basin is well observed on the velocity time series, its amplitude is small compared to the total signal amplitude of the FF model. This shows that the impact of the presence of structures on the considered motion intensity parameters remains weak.

Because of the high calculation time required, we decided not to introduce 3D foundation elements under the buildings in the model. In fact, these elements lead to complex mesh process and therefore, increase computation time. As a slab foundation generally does not exceed 1 to 2 m thick, numerically, it leads to very fine meshes in the foundation and its vicinity and a strong decrease in the global time step. Contrary to a very thin slab foundation, the large embedding height makes the numerical simulation more feasible in terms of computational cost. Mesh elements created at the interface soil foundation could be larger than in presence of slab foundation.

Moreover, this model can be improved by adding complex features as:

- Building cluster composed of buildings with different height. Bybordiani and Arici (2019) notably observed variations in the frequency content of the building response by testing this parameter. And Guéguen (2000) noted that SSSI effects increase in this configuration.
- Plane wave of non-vertical incidence.
- Nonlinearity of the soil occurring during strong earthquake. Vicencio and Alexander (2018) based their study on several different 2D non-linear systems under strong motion excitation. Through time domain analysis (acceleration and displacement time series comparison), they conclude that SSI effects are stronger in the case of non-linear soil. They note that SSSI effects increase when buildings are very close and located on soft soil.

V.8. Conclusion

V.8.1. Site-city influence on the ground motion

V.8.1.1 Impact of site effect

We notice that the motion intensity parameters (PGA, PGV, AI and EI) and the frequency content of the ground motion show strong spatial variability at the basin surface whatever the model (free field or site-city).

The numerical simulation of seismic wave propagation in a realistic 3D model of the lower Var valley has been calibrated to obtain the measured fundamental resonance frequency of the basin around 2 Hz obtained close to the NCAD station position (Rohmer et al. (2020). This value is distributed along the basin surface and increasing at the basin edge.

Since the seismic solicitation is only in the transverse direction of the basin, only the transverse and vertical components of the output signal have significant energy to be analyzed. The analysis of the motion intensity parameters shows that the ground motion increases in terms of amplitude and duration with the basin depth. Particularly, the maximum value of the PGV in the transverse direction is greater than five times the PGV of the input signal and the spatial variability of this parameter reflects the break in slope of the basin edges. This increase results from reflection and diffraction phenomena that lead to the generation of surface waves at the border of the valley and to waves trapping inside the sedimentary layers.

V.8.1.2 Impact of the city

The presence of buildings tends to increase the PGV value close to the buildings. Specifically, at the building positions, slight variations in the motion intensity parameters happen depending on the site-city model. The transverse component of the PGV increases by more than 10% close to building located in the center of the basin for all the site-city models. Moreover, the vertical component of the PGV increase by more than 30% at building located in the city center.

We note that the ground motion is higher in the square city when the building spacing is small. The motion is 60% higher than in free field on the vertical component and 16% on the transversal component of the valley. This is also observed on the comparison with the isolated building case and suggest that this increase is related to the radiated waves from the building

group. In 2D analysis, Kham et al. (2006) identified this phenomenon as group effect and observed an increase of the ground motion by 30% inside an irregular city. Isbiliroglu et al. (2015) used the same parameters to calibrate buildings than in Kham et al. (2006) and studied 3D finite element SCI model. They observed that the ground motion is subjected to more variations if the density of buildings increases. These variations can reach more than 10% in the case of soft soil sites. As those authors, we observed that the smaller the building spacing the stronger the group effect.

The analysis of the difference in time series and in frequency content of the site response at the basin surface shows that the presence of buildings tend to influence the high frequency content of the site response in the vicinity of them. Indeed, strong energy at 4.5 Hz that corresponds to the second resonance frequency of the basin is observed for each site-city model. For small building spacing, the energy at this frequency is stronger at the building positions and up to 200 m away from the city.

V.8.2. Site-city influence on the building response

In the case of isolated buildings, the motion at the top of the building differs as function of the building localization. Indeed, the amplitude of the motion of the building located at the center of the valley appears to increase by 69% comparatively to the one obtained for the building at the eastern edge of the basin. Moreover, the second natural frequency peak amplitude, observed on the transfer function, is 145% larger than the one of the building at the edge of the basin.

We show that the seismic response of a building localized in the center of a cluster can be modified depending on the cluster spatial distribution and density.

Firstly, it appears that, for large distance between buildings (H/2), the signal amplitude at the top of the central building tends to increase. Several studies indicate that the building top motion decreased in the city and this decrease is more pronounced under double resonance condition (e.g. Guéguen, 2000; Bard et al., 2005; Kham et al., 2006; Semblat et al., 2008; Kumar and Narayan, 2019b). Here, this phenomenon is observed only for the dense building configuration with a decrease of the acceleration amplitude limited to 9%. Also, we note that the central building response coherency between the different models tends to decrease for small building

spacing. Furthermore, the EI is increased notably by 100% of the isolated building response on the vertical component.

Secondly, the presence of city influences the central building impulse response especially at high frequencies. No variation is observed at the first natural frequency of the structure contrary to other investigations (Kitada et al., 1999; Bybordiani and Arici, 2019). This may be explained because the model does not respect the double resonance condition that may amplify SCI effects. Furthermore, the absence of foundation may lead to underestimate kinematic interaction and therefore, the SCI effects can be lower than expected. To compare, Makrypidi et al. (2017) used hybrid FEM-BEM to model SCI and analyze the motion intensity parameters and displacement time series of a building located at the center of a city. The authors found that this structure undergoes lower SSI effects than the one located at the group limit. This conclusion is retrieved in the work of Knappett et al. (2019) where low-rise FE structure models are used and analyzed through frequency ratio and peak acceleration comparison.

We may expect from the seismic response analysis of the isolated buildings that all these buildings share the same impulse response. However, we note that it is the case at the first mode frequency but not at the second one. It appears that the building impulse response differs according to the position of the building in the basin. This may be due either to numerical variability in high frequencies or to the generation of surface waves at the edge of the basin. This last assumption is possible since the numerical model considers three dimensions and may include non-vertical incident waves at the base of buildings. Consequently, the impulse building response becomes more complex compared to a 1D model.

Finally, this work allows to put in evidence the contribution of lithological site effect and buildings on seismic ground motion. It appears that the major impact on the ground motion at the basin scale is induced by lithological site effect. Indeed, they lead to increase the motion at the basin surface by more than five times the motion amplitude at rock site while building effects constitute local increase of seismic ground motion that are pronounced particularly close to buildings and inside the city with small building spacing. Locally, these variations remain significant by representing a maximal increase of 62% on the vertical component and of 16% on the transverse component compared to the free field motion.

General conclusion

To study the influence of lithological site effect and buildings on the surface ground motion, seismic wave propagation has been numerically simulated in five different 3D finite element site-city models characterized using ambient vibration recordings and including various city configurations. Beforehand, the soil-structure interaction (SSI) effects have been investigated numerically and empirically in the time and frequency domain at the scale of the building and of the basin. To do so, we used the lower Var Valley close to Nice as a natural laboratory. This valley presents indeed high stakes, high-rise buildings and an increasing urbanization which has already been the subject of previous risk studies. Notably strong lithological site effect has already been documented.

Several building typologies and their dynamic parameters have been numerically investigated to find which of them are the most sensitive to SSI effects. Five different 3D finite element types of building, high and low-rise, reinforced concrete or masonry, have been solicited at their base with white noise and simulated earthquake recordings. The responses of identical fixed and flexible base buildings were compared in order to identify the building types and dynamic parameters that are the most sensitive to SSI effects. Our main conclusions are as follow:

- Bending type buildings are the most sensitive to SSI, especially high-rise structures.
- Shear type and masonry buildings are less sensitive to SSI effects. We note that even if the first natural frequency of the shear type building is closed to the soil fundamental frequency and induced a double resonance condition, the influence of SSI effects on the building response remains lower than the one of the bending type buildings.
- For all types of building, the aspect ratio (height-width ratio) and the non-uniform distribution of rigidity in the structure are strong structural features that control the building response with SSI.
- The dynamic analysis shows significant modifications in several parameters that are the first natural frequency, the mode shapes and order of apparition of modes, the signal amplitude and phase at the top of building, the signal duration, the motion intensity in high and medium frequency content and the presence of rocking motion at the base of building. Particularly, we note that with SSI:
    - The first natural frequency decreases for all the reinforced concrete buildings.

  - The mode shapes and the order of apparition of the modes differ in the case of low-rise reinforced concrete buildings.
  - The amplitude and the phase of the signal are modified for all the reinforced concrete buildings. For shear type, irregular bending type and high rise models, the amplitude decreases at the top of the building whereas it increases for the regular bending type model.
  - The signal duration decreases in the case of low-rise reinforced concrete buildings but increases for high-rise building.
  - The motion intensity in high and medium frequency content tends to decrease for shear type and high-rise buildings whereas it increases for the regular bending type model.
- A rocking motion is highlighted at the base of the reinforced concrete bending type buildings at their first natural frequency but also at higher frequency.
- One effect of the SSI is a rocking motion at the base of the structure. Therefore, the proposed rocking spectral ratio combined with filtered seismic signal or RD functions from ambient vibration recordings are useful to investigate SSI effects in buildings. The rocking motion occurs especially at the first resonance frequencies of the bending mode of the structure but also at higher frequencies. One of the main advantages of this SSI characterization is that it is self-sufficient and does not need a comparison with a fixed base model. Thus, this method appears relevant to study SSI using vibration recordings on real structures.

Then, SSI and SSSI effects have been empirically investigated using dense in-situ ambient vibration instrumentations performed in the tallest buildings of the Var Valley. We tested several methods to highlight these interaction effects in our recordings such as the microtremor Horizontal-to-Vertical ratio (mHVSR), the operational modal analysis and the rocking spectral ratio and made the following observations:

- Synchronous ambient vibration recordings could be used to characterize SSI. To do that, it is necessary to have at least sensors at all extremities of the base of the instrumented structures.
- The analysis of the mode shape compared to theoretical mode confirms the type behavior of the building (shear, bending, Timoshenko beam).

- Non-zero displacement mode and rocking motion at the base of the buildings highlight the presence of SSI.
- The analysis of the building influence on the ground motion spatial variability using mHVSR shows that only the frequency value of the peak gives an insight of SSI effects. The peak amplitude, the peak width or the frequency gap between two mHVSR high amplitude peaks are not significant for the SSI characterization.
- The coincidence of the soil and building resonance frequencies on mHVSR suggest the presence of strong SSI. This is also observed in the singular value decomposition plot where similarities of resonance frequencies of close buildings suggest the presence of strong SSSI effects. The SSSI observation was confirmed using a simultaneous modal analysis of the buildings by the high correlation between the mode shapes of each structure.

The operational modal analysis has shown its high potentiality to characterize the dynamic behavior of the structures, the main limitations we reach in our investigations are as follow:

- Lack of precision in the modal computation may be induced by the difficulty to perform frequency peaking due to the coupling resonance modes in singular value decomposition plot.
- When synchronous ambient vibration recordings are used for the simultaneous modal analysis of structures, the increasing distance of the recordings to the reference station may cause a decrease of the coherency in the signals. Consequently, the mode shape amplitude, calculated using an average of time windows signals with a triggering performed on the reference station, could be different between the buildings where the reference sensor is located and the adjacent building. To reduce this uncertainty, the number of references in the setup can be increased.
- It appears that longer ambient vibration recordings (>30min) are more suitable to refined the rocking spectral ratio in order to make easier the analysis of the rocking motion and to precise the velocity estimation in the building through deconvolution interferometry technique.

The next stage to the site-city model is the calibration of homogeneous equivalent block model to represent building. In order to stay accurate, they need to be calibrated using real data. We showed that:

- Large uncertainties exist in the estimation of the shear wave velocity. Therefore, this parameter is not a suitable criterion to calibrate simplified model of building.
- It is better to calibrate simplified model of building from real data based on the natural frequency of the real building.
- Because the block model has not torsion mode, the considered natural frequency should corresponds to the first mode of flexion of the targeted building. It is then important to investigate at least the first higher modes of a structure.

The last stage is the development of the sedimentary model of the Var valley based on the combination of geotechnical borehole and ambient vibration data already available. Additional active and passive non-invasive in-situ instrumentation campaigns completed this database by enabling us to characterize the valley bedrock, and determine an average velocity zonation in the basin. Most has been made to interpret wisely the mHVSR and to work on the complementarity of the geophysical and geotechnical data. In the final model, the organization of the different lithological layers is constrained by the borehole data. The basin-bedrock interface geometry is defined by using both the borehole data and the ambient vibration measurements. We assumed a 1D soil domain in the whole sedimentary basin to interpret mHVSR. This induce potential overestimation of the sedimentary thickness especially at the basin edge where it is known that the soil domain is more 2D/3D than 1D.

The model construction remains complex to perform and the related uncertainties are still not well identified. The interpretation of mHVSR may be challenging, especially when the curve is characterized by low quality or/and two high amplitude peaks. In this thesis, when mHVSR double peaks were observed, the second peak has been identified as the fundamental soil frequency related to the Quaternary-Pliocene interface. This interpretation led to a geologically consistent shape of a basin. The first peak could be due to a deeper interface inside the bedrock, seen at some sites of the valley. Although this first peak is not used to define the bedrock depth of the valley, we should keep in mind that it should be taken into account for a proper seismic hazard assessment, at least where it has been seen. However, the considered part of the valley where the 3D modeling of wave propagation is done is far away from these double-peaked sites.

Finally, five different 3D finite element site-city models have been calibrated using ambient vibration recordings and including various city configurations are used to study SSI and SCI. The seismic wave propagation was simulated using the Discontinuous Galerkin finite element method. A parametric study was performed in the time and frequency domain to quantify the

influence of lithological site effects and buildings on the ground motion in the valley. We conclude in particular that:

- The motion intensity parameters (PGA, PGV, AI and EI) as well as the frequency content of the ground motion show strong spatial variability at the basin surface in all cases (free field or city).
- The amplitude and duration of the surface ground motion is greater at the center of the basin whatever the model (free field or site-city cases). It results from reflection and diffraction phenomena that lead to the generation of surface waves at the basin edge and to waves trapping inside the sedimentary layers.
- The ground motion amplitude increases also locally close to buildings and in city with small building spacing.
- The frequency content of the ground motion at the basin surface is subjected to variations especially in high frequencies, close to the buildings and inside the city with small building spacing. For such a city, the energy at the second resonance frequency of the basin is stronger up to 200 m away from the city.
- Comparing the contribution of site effect and buildings, it appears that the major impact on the ground motion at the basin scale is induced by lithological site effect which lead to increase the motion at the basin surface more than five times the motion amplitude at rock site while building effects constitute only local increase of seismic ground motion. Close to buildings and inside the city with small building spacing, these variations remain significant by representing a maximal increase of 62% on the vertical component and of 16% on the transverse component compared to the free field motion.

The 3D site-city modeling not only allows to study the ground motion throughout the valley but also the impact of the city and the valley on the building response. We show here that:

- The cluster spatial distribution and density are strong factors of SSSI effects. In fact, it appears that, for large distance between buildings (height/2), the signal amplitude at the top of the city central building tends to increase. A decrease of the motion at the top of the building is observed only for small building spacing, with a decrease limited to 9%. Also, we note that the coherency of the central building response between the different models tends to decrease.
- It appears that the building response differs according to the localization of the building in the basin. The motion at the top of the building located at the center of the valley is

69% larger than the one of the building at the edge of the basin. On the transfer function, the first mode frequency stays identical for all isolated buildings contrary to other investigations (Bybordiani and Arici, 2019; Kitada et al., 1999). This may be explained because the model does not respect the double resonance condition ($f_{0building} = f_{0soil}$) that may amplify SCI effects. However, the second natural frequency peak amplitude is 145% larger than the one of the building at the edge of the basin and a little frequency shift of 0.5 Hz at around 5.5 Hz. The variability of the building impulse response at high frequencies could be of two origins. First, the numerical uncertainties at high frequencies and second, the generation of surface waves at the basin edge in the 3D model producing non-vertical incident seismic solicitation at the base of the building.

Perspectives

This thesis has notably shown that the 3D Discontinuous Galerkin simulation is a powerful tool for the study of the soil-structure interaction (SSI), the structure-soil-structure interaction (SSSI) and the site-city interaction (SCI). To perform these simulations, it has been necessary to associate engineering and seismologist point of views and to work beforehand on numerical and empirical explorations of SSI from in-situ vibration recordings. Besides the results we presented in this thesis, this work raises multiple further investigations:

- *In-situ SSI characterization*

The temporary field experiment that we conduct on the selected buildings gave interesting results for the SSI characterization. To estimate the influence of distance on the building group effect on the ground motion, ambient vibration arrays may be deployed along a several hundred meters profile from the instrumented building group. Furthermore, to solve the last uncertainties, it would be worth to consider a permanent seismic network to record future earthquakes using different kind of sensor as rotational sensor or distributed acoustic sensing (DAS).

- *Geotechnical 3D model*

To refine the soil subsurface model, we propose to:

- Investigate the capability of artificial intelligence (AI) to interpret borehole core sample and mHVSR.
- Use DAS and existing fiber optic line to increase the spatial coverage of geophysical data in the basin.
- Further investigate the double peaked mHVSR and better understand the origin of the first frequency peak.
- Compare the average velocity profiles to other empirical relationships between the fundamental resonance frequency and the soil thickness proposed in other studies (Seht and Wohlenberg, 1999; Delgado et al., 2000, 2002; Parolai et al., 2002; Mascandola et al., 2019).

- *Numerical SSI investigation at the building level*

The numerical study of SSI using 3D finite element model of building can be refined by considering the nonlinearity of structures or/and various types of foundations (deep and shallow). To limit the underestimation of SSI effects, the soil non-linearity can be integrated in the soil domain. In addition, 2D/3D resonances and surface waves may be considered. The SSSI effects at the building scale can be investigated through close multiple 3D finite element model of buildings having different height and shape. And then, the numerical results can be compared to ambient vibration recordings from the instrumentation campaign.

Moreover, finding a method to incorporate the non-uniform stiffness distribution in a simple manner into an equivalent building block model may be an additional line of study. For example, by directly modifying the geometry of the block such as tubular model or asymmetric model or by varying the velocity in the element.

- *Numerical SSI investigation at the city level*

The comparison of all the building responses in the city would give an insight of the impact of the building position on its seismic response. The investigation of the rocking motion at the base of buildings is also a potential line of study. Increasing the number of virtual sensors at the basin surface would be useful to precise the variability of the ground motion.

Finally, the SSI, SSSI and SCI effects could be studied by considering a foundation slab under the building models or deeper foundations in order to enhance kinematic interaction. Indeed, a more complex city geometry (different building heights, variable building orientation, number of buildings, etc...) could lead to a different SCI. Other perspectives as the consideration of non-vertical incident plane wave and soil nonlinearity occurring during strong earthquake could be integrated in the numerical model to refine the study of SCI. Finally, the SSI, SSSI and SCI effects should be studied using a more realistic 3D model of the valley to consider not only the surface heterogeneities in the transverse direction of the valley but also in the longitudinal direction. In this case, a three-component seismic source could be applied as input to the modeling. The modeling of the actual real city in the Var valley would allow the comparison with the seismological data continuously recorded by the RAP-RESIF stations inside the valley.

Data and resources

The study was conducted in the framework of the Ritmica project. This work has been supported by the French government, through the UCA-JEDI Investments for the future project managed by the National Research Agency (ANR) with the reference number ANR-15-IDEX-01.

The numerical simulations of the 3D realistic site-city models have been made possible thanks to the SIGAMM computing resources hosted by the Observatoire de la Côte d'Azur (https://crimson.oca.eu/fr/mesocentre-sigamm [last access:13/12/2021]).

The numerical investigation of SSI at building scale was performed using high performance computing (HPC) resources from GENCI-[CINES] (Grant 2018-[A0050410071]). The seismogram used in the numerical analysis of finite element buildings is provided by the Instituto Nazionale di Geofisica e Vulcanologia (INGV) in Italy and can be obtained from Itaca database (Italian Accelerometric Archive) at https://doi.org/10.13127/SD/X0FXnH7QfY [last access: 10/05/2020].

The contextualization map backgrounds are extracted from the IGN geoservices database at https://geoservices.ign.fr/documentation/donnees.

Also, the authors acknowledge the use of data obtained by the RESIFRAP French Accelerometric Network. RESIF is a national Research Infrastructure, recognized as such by the French Ministry of Higher Education and Research. RESIF is managed by the RESIF Consortium, composed of 18 Research Institutions and Universities in France. RESIF additionally supported by a public grant overseen by the French National Research Agency (ANR) as part of the Investments for the future program (reference: ANR-11-EQPX-0040) and the French Ministry of Ecology, Sustainable Development and Energy.

Firstly, we would like to thank the H2EA company for the geological and geotechnical knowledge sharing on the lower Var valley. Secondly, we thank the ADAM's association premises and the syndicate council of the Bois de Boulogne residency for having given us the authorization and access to instrument the buildings. Thirdly, we thank IRSN for lending us a Cityshark recorder for the instrumentation of the buildings. Finally, we thank Geoazur for providing us with the 5m resolution DEM and the bathymetry of the Var valley obtained by the GO_06 June 2009, BATHYMETRIE©CANCA, Litto3D, MALISAR and IBCM campaigns.

Bibliography

Aden, M.A., Al-Attar, A.A., Hejazi, F., Dalili, M., Ostovar, N., 2019. Effects of soil-structure interaction on base-isolated structures. IOP Conf. Ser.: Earth Environ. Sci. 357, 012031. https://doi.org/10.1088/1755-1315/357/1/012031

Aki, K., 1993. Local site effets on weak and strong ground motion. Tectonophysics 218, 93–111.

Aki, K., 1957. Space and time spectra of stationary stochastic waves, with special reference to microtremors. Bulletin of the Earthquake Research Institute.

Aki, K., Richards, P.G., 1980. Quantitative Seismology: Theory and Methods. W. H. Freeman.

Allemang, R.J., Brown, D.L., 1982. A correlation coefficient for modal vector analysis, in: Proceedings of the 1st International Modal Analysis Conference. SEM Orlando, pp. 110–116.

Alvandi, A., 2003. Contribution à l'utilisation pratique de l'évaluation dynamique pour la détection d'endommagement dans les ponts. Marne-la-vallée, ENPC.

Anderson, J.G., 2004. Quantitative measure of the goodness-of-fit of synthetic seismograms. 13th World Conference on Earthquake Engineering Conference Proceedings, Vancouver, Canada, Paper 243.

Anquez, P., Glinsky, N., Cupillard, P., Caumon, G., 2021. Impacts of geometric model simplifications on wave propagation - Application to ground motion simulation in the lower Var valley basin (France). GJI.

Apsel, R.J., Luco, J.E., 1987. Impedance functions for foundations embedded in a layered medium: An integral equation approach. Earthquake Engineering & Structural Dynamics 15, 213–231. https://doi.org/10.1002/eqe.4290150205

Apsel, R.J., Luco, J.E., 1976. Torsional response of rigid embedded foundation. Journal of the Engineering Mechanics Division 102, 957–970.

Asmussen, J.C., Brincker, R., Ibrahim, S.R., 1999. Statistical theory of the vector random decrement technique. Journal of Sound and Vibration 329–344.

Asten, M., Henstridge, J., 1984. Array estimators and the use of microseisms for reconnaissance of sedimentary basins. Geophysics 49, 1828–1837. https://doi.org/10.1190/1.1441596

Athanasiou, A., Oliveto, N.D., Ponzo, F.C., 2020. Identification of first and second order models for the superstructure of base-isolated buildings using free vibration tests: A case study. Soil Dynamics and Earthquake Engineering 135, 106178. https://doi.org/10.1016/j.soildyn.2020.106178

Barbero, E.J., 2013. Finite Element Analysis of Composite Materials Using Abaqus, CRC Press. ed.

Barbieri, N., Novak, P.R., Barbieri, R., 2004. Empirical identification of damping. International Journal of Solids and Structures 41, 3585–3594.

Bárcena, A., Esteva, L., 2007. Influence of dynamic soil–structure interaction on the nonlinear response and seismic reliability of multistorey systems. Earthquake Engineering & Structural Dynamics 36, 327–346. https://doi.org/10.1002/eqe.633

Bard, P.-Y., 1988. The importance of rocking in building motion: an experimental evidence. Presented at the Proc. of the Ninth World Conference on Earthquake Engineering, pp. 333–338.

Bard, P.-Y., 1983. Les effets de site d'origine structurale en sismologie: modélisation et interprétation, application au risque sismique (Thèse). Université Scientifique et Médicale de Grenoble, Grenoble.

Bard, P.-Y., Bouchon, M., 1985. The two-dimensional resonance of sediment-filled valleys. B. Seismol. Soc. Am 75, 519–541.

Bard, P.Y., Bouchon, M., 1980a. The seismic response of sediment-filled valleys - Part 1 - The case of incident SH waves. B. Seismol. Soc. Am 70, 1263–1288.

Bard, P.Y., Bouchon, M., 1980b. The seismic response of sediment-filled valleys - Part 2 - The case of incident P and SV waves. B. Seismol. Soc. Am 70, 1921–1941.

Bard, P.-Y., Chazelas, J.-L., Kham, M., Semblat, J.F., 2005. Site-city interaction, in: Assessing and Managing Earthquake Risk (Geo-Scientific and Engineering Knowledge for Earthquake Risk Mitigation: Developments, Tools and Techniques).

Bard, P.Y., Gueguen, P., Wirgin, A., 1996. A note on the seismic wavefield radiated from large building structures into soft soils. Presented at the Eleventh World Conference on Earthquake Engineering, Acapulco, Mexico.

Barnaba, C., Marello, L., Vuan, A., Palmieri, F., Romanelli, M., Priolo, E., Braitenberg, C., 2010. The buried shape of an alpine valley from gravity surveys, seismic and ambient noise analysis. Geophys. J. Int. 180, 715–733. https://doi.org/10.1111/j.1365-246X.2009.04428.x

Bataillon, C., 1988. Le tremblement de terre de Mexico: bilan du moyen terme. Géocarrefour 63, 5–8. https://doi.org/10.3406/geoca.1988.3352

Benjemaa, M., Glinsky-Olivier, N., Cruz-Atienza, V.M., Virieux, J., 2009. 3-D dynamic rupture simulations by a finite volume method. Geophysical Journal International 178, 541–560. https://doi.org/10.1111/j.1365-246X.2009.04088.x

Benjemaa, M., Glinsky-Olivier, N., Cruz-Atienza, V.M., Virieux, J., Piperno, S., 2007. Dynamic non-planar crack rupture by a finite volume method. GJI 171, 271–285.

Beresnev, I.A., Wen, K.-L., Yeh, Y.T., 1995. Nonlinear Soil Amplification: Its Corroboration in Taiwan. Bulletin of the Seismological Society of America 85, 456–515.

Bertrand, E., Duval, A., Castan, M., Vidal, S., 2007a. 3D Geotechnical Soil Model of Nice, France, Inferred from Seismic Noise Measurements, for Seismic Hazard Assessment, in: AGU Fall Meeting 2007. San Francisco, United States.

Bertrand, E., Duval, A.M., Saad, A., 2007b. Scénario de risque sismique dans une vallée alpine : La haute Tinée, Alpes Maritimes, France, in: 7ème Colloque National de Génie Parasismique AFPS'07. Paris, France.

Beskos, D.E., 1997. Boundary element methods in dynamic analysis: Part II (1986-1996). Appl. Mech. Rev. 50, 149–197. https://doi.org/10.1115/1.3101695

Betbeder-Matibet, J., 2008. Seismic Engineering, John Wiley and Sons. ed. New Jersey.

Bielak, J., Ghattas, O., Kim, E.J., 2005. Parallel octree-based finite element method for large-scale earthquake ground motion simulation. Computer Modeling in Engineering and Sciences 10, 99.

Bielak, J., Loukakis, K., Hisada, Y., Yoshimura, C., 2003. Domain Reduction Method for Three-Dimensional Earthquake Modeling in Localized Regions, Part I: Theory. B. Seismol. Soc. Am 93, 817–824. https://doi.org/10.1785/0120010251

Bonkowski, P.A., Zembaty, Z., Yan Minch, M., 2019. Engineering analysis of strong ground rocking and its effect on tall structures. Soil Dynamics and Earthquake Engineering 116, 358–370. https://doi.org/10.1016/j.soildyn.2018.10.026

Bonnefoy-Claudet, S., Kohler, A., Cornou, C., Wathelet, M., Bard, P.-Y., 2008. Effects of Love Waves on Microtremor H/V Ratio. B. Seismol. Soc. Am 98, 288–300. https://doi.org/10.1785/0120070063

Bonnet, M., 1999. Boundary integral equation methods for solids and fluids, Wiley. ed.

Boore, D.M., 2015. Notes on relating density to velocity for use in site amplification calculations.

Boore, D.M., 2001. Effect of Baseline Corrections on Displacements and Response Spectra for Several Recordings of the 1999 Chi-Chi, Taiwan, Earthquake. Bulletin of the Seismological Society of America 91, 1199–1211. https://doi.org/10.1785/0120000703

Boore, D.M., 1972. A note on the effect of simple topography on seismic SH waves. Bull. Seismol. Soc. Am. 62, 275–284.

Boore, D.M., Bommer, J.J., 2005. Processing of strong-motion accelerograms: needs, options and consequences. Soil Dynamics and Earthquake Engineering 25, 93–115.

Borcherdt, R., 1994. Estimates of site-dependent response spectra for design (methodology and justification). Eathq. Spectra 10, 617–653.

Borghei, A., Ghayoomi, M., 2019. The role of kinematic interaction on measured seismic response of soil-foundation-structure systems. Soil Dynamics and Earthquake Engineering 125, 105674. https://doi.org/10.1016/j.soildyn.2019.05.013

Bourgine, B., 2018. GDM Outils Géostatistiques, Manuel de référence, in: GDM. BRGM.

Boutin, C., Hans, S., 2009. How Far Ambient Noise Measurement May Help to Assess Building Vulnerability?, in: Mucciarelli, M., Herak, M., Cassidy, J. (Eds.), Increasing Seismic Safety by Combining Engineering Technologies and Seismological Data, NATO Science for Peace and Security Series C: Environmental Security. Springer Netherlands, Dordrecht, pp. 151–180. https://doi.org/10.1007/978-1-4020-9196-4_13

Boutin, C., Hans, S., Ibraim, E., Roussillon, P., 2005. In situ experiments and seismic analysis of existing buildings. Part II: Seismic integrity threshold. Earthquake engineering & structural dynamics 34, 1531–1546.

Bozzano, F., Andreucci, A., Gaeta, M., Salucci, R., 2000. A geological model of the buried Tiber River valley beneath the historical centre of Rome. B. Eng. Geol. Environ. 59, 1–21. https://doi.org/10.1007/s100640000051

Bozzano, F., Marra, F., Lenti, L., Martino, S., Paciello, A., Scarascia Mugnozza, G., Varone, C., 2016. Seismic response of the geologically complex alluvial valley at the "Europarco Business Park" (Rome - Italy) through instrumental records and numerical modelling. IJEGE 1. https://doi.org/10.4408/IJEGE.2016-01.O-04

Bradford, S.C., Clinton, J.F., Favela, J., Heaton, T.H., 2004. Results of Millikan Library forced vibration testing (No. EERL 2004-03). California Institut of Technology, Pasadena, California.

Brandt, A., 2011. Noise and Vibration Analysis: Signal Analysis and Experimental Procedures. Wiley.

BRGM, 2015. Eléments de développement de la géothermie dans le secteur du Grand Arénas (Rapport final No. 64401). BRGM.

BRGM, 2010. La carte géologique harmonisée de la zone d'emprise du programme LGV-PACA, Méthodologie et aperçu géologique. BRGM.

Brincker, R., Ventura, C., 2015. Introduction to operational modal analysis. John Wiley & Sons.

Brincker, R., Zhang, L., Andersen, P., 2001. Modal identification of output-only systems using frequency domain decomposition. Smart Mater. Struct. 10, 441. https://doi.org/10.1088/0964-1726/10/3/303

Brunel, D., Bertrand, E., 2010. Instrumentation de la Préfecture de Nice (Lettre d'information du RAP No. 12).

Bybordiani, M., Arici, Y., 2019. Structure-soil-structure interaction of adjacent buildings subjected to seismic loading. Earthq. Eng. Struct. Dyn. 48, 731–748. https://doi.org/10.1002/eqe.3162

Campillo, M., Gariel, J., Aki, K., Sanchez-Sesma, F., 1989. Destructive strong ground motion in Mexico city : source, path, and site effects during great 1985 Michoacan earthquake. B. Seismol. Soc. Am 79, 1718–1735.

Carder, D.S., 1936. Observed vibrations of buildings, in: The Seismological Society of America. Pasadena, pp. 245–277.

Castellaro, S., Mulargia, F., 2010. How Far from a Building Does the Ground-Motion Free-Field Start ? The Cases of Three Famous Towers and a Modern Building. Bull. Seismol. Soc. Am. 100, 2080–2094.

Castellaro, S., Padrón, L.A., Mulargia, F., 2014. The different response of apparently identical structures: a far-field lesson from the Mirandola 20th May 2012 earthquake. Bull Earthquake Eng 12, 2481–2493. https://doi.org/10.1007/s10518-013-9505-9

Caughey, T.K., Stumpf, H.J., 1961. Transient Response of a Dynamic System Under Random Excitation. J. Appl. Mech. 28, 563–566.

Cavalieri, F., Correia, A.A., Pinho, R., 2021. Variations between foundation-level recordings and free-field earthquake ground motions: numerical study at soft-soil sites. Soil Dynamics and Earthquake Engineering 141, 106511. https://doi.org/10.1016/j.soildyn.2020.106511

Çelebi, M., 1996. Comparison of damping in buildings under low-amplitude and strong motions. Journal of Wind Engineering and Industrial Aerodynamics, Meeting on Structural Damping International Wind Engineering Forum and Additional Papers 59, 309–323. https://doi.org/10.1016/0167-6105(96)00014-1

CEN, 2003. Eurocode 8: Design of Structures for earthquake resistance - Part 1 : General rules, seismic actions and rules for buildings.

CETE, 2010a. Instrumentation du bâtiment de la préfecture des Alpes Maritimes, Nice (06), France.

CETE, 2010b. Méthodes et outils pour microzonage sismique : Application au microzonage de Nice. CETE Méditerranée.

Cetin, K.O., Altun, S., Askan, A., Akgün, M., Sezer, A., Kincal, C., Ozdag, O.C., Ipek, Y., Unutmaz, B., Gülerce, Z., Ozacar, A.A., Ilgaç, M., Can, G., Cakir, E., Söylemez, B., El-Sayeed, A., Zarzour, M., Bozyigit, I., Tuna, C., Köksal, D., Karimzadeh, S., Uzel, B., Karaali, E., 2022. The site effects in Izmir Bay of October 30 2020, M7.0 Samos Earthquake. Soil Dyn. Earthq. Eng. 152. https://doi.org/10.1016/j.soildyn.2021.107051.

Chabot, S., 2018. Modélisation numérique de la propagation des ondes par une méthodeéléments finis Galerkin discontinue: prise en compte des rhéologies nonlinéaires des sols (Thesis). Université Paris-Est, Paris, France.

Chaillat, S., Bonnet, M., Semblat, J.-F., 2009. A new fast multi-domain BEM to model seismic wave propagation and amplification in 3-D geological structures. Geophys. J. Int. 177, 509–531.

Chaillat, S., Bonnet, M., Semblat, J.-F., 2008. A multi-level fast multipole BEM for 3-D elastodynamics in the frequency domain 197, 4233–4249.

Chaljub, E., Moczo, P., Tsuno, S., Bard, P.-Y., Kristek, J., Käser, M., Stupazzini, M., Kristekova, M., 2010. Quantitative comparison of four numerical predictions of 3D ground motion in the Grenoble Valley, France. B. Seismol. Soc. Am 100, 1427–1455.

Chatelain, J.-L., Gueguen, P., Guillier, B., Frechet, J., Bondoux, F., Sarrault, J., Sulpice, P., Neuville, J.-M., 2000. CityShark: A user-friendly instrument dedicated to ambient noise (microtremor) recording for site and building response studies. Seismol. Res. Lett. 71, 698–703.

Cheng, M.H., Heaton, T.H., 2015. Simulating Building Motions Using Ratios of the Building's Natural Frequencies and a Timoshenko Beam Model. Earthquake Spectra 31, 403–420. https://doi.org/10.1193/011613EQS003M

Chin-Joe-Kong, M.J.S., Mulder, W.A., Van Veldhuizen, M., 1999. Higher-order triangular and tetrahedral finite elements with mass lumping for solving the wave equation. Journal of Engineering Mathematics 35, 405–426.

Chopra, A.K., 2007. Dynamics of structures, Pearson Education India. ed.

Clauzon, G., 1978. The Messinian Var canyon (Provence, Southern France)—paleogeographic implications. Marine Geology 27, 231–246.

Clough, R.W., Penzien, J., 1993. Dynamics of Structures, McGraw-Hill. ed.

Cole, H.A., 1973. On-line failure detection and damping measurement of aerospace structures by random decrement signatures. National Aeronautics and Space Administration.

Constantino, C.J., Miller, C.A., 1979. Soil-Structure Interaction Methods: SLAVE Code (Vol 2 No. NUREG/CR-1717).

Conti, R., Morigi, M., Viggiani, G.M.B., 2016. Filtering effect induced by rigid massless embedded foundations. B. Earthq. En. 15, 1019–1035.

Cornou, C., Gueguen, P., Bard, P.-Y., Haghshenas, E., 2004. Ambient noise energy bursts observation and modeling: Trapping of harmonic structure-soil induced–waves in a topmost sedimentary layer. J. Seismol. 8, 507–524. https://doi.org/10.1007/s10950-004-1980-7

Courboulex, F., Mercerat, E.D., Deschamps, A., Migeon, S., Baques, M., Larroque, C., Rivet, D., Hello, Y., 2020. Strong Site Effect Revealed by a New Broadband Seismometer on the Continental Shelf Offshore Nice Airport Slope (Southeastern France). Pure Appl. Geophys. https://doi.org/10.1007/s00024-019-02408-9

Crémona, C., Barbosa, F., Alvandi, A., 2001. Identification modale sous excitation ambiante: application aux ponts, in: Colloque Méthodes Modales Expérimentales, EIVL Blois (Loir et Cher), CDRom (20p.). pp. 29–30.

Cundall, P.A., Strack, O.D.L., 1979. A discrete numerical model for granular assemblies. Geotechnique 29, 47–65.

Dan-Unterseh, G., Sultan, N., Savoye, B., 2007. The 1979 Nice harbour catastrophe revisited: Trigger mechanism inferred from geotechnical measurements and numerical modelling. Mar. Geol. 245, 40–64. https://doi.org/10.1016/j.margeo.2007.06.011

Day, S.M., 1977. Finite-element analysis of seismic scattering problems, Iniversity of California. ed. San Diego.

DDTM, 2019. Le projet de Plan de Prévention des Risques naturels prévisibles de séisme (P.P.R.S.).

DDTM, 2011. Evolution générale de la basse vallée du Var (Plan de prévention des risques d'inondation de la basse vallée du Var). Direction départementale des territoires et de la mer des Alpes-Maritimes.

Delcourte, S., Fezoui, L., Glinsky-Olivier, N., 2009. A high-order discontinuous Galerkin method for the seismic wave propagation. ESAIM: Proceedings, EDP Sciences 70–89.

Delcourte, S., Glinsky, N., 2015. Analysis of a high-order space and time discontinuous Galerkin method for elastodynamic equations. Application to 3D wave propagation. ESAIM: Mathematical Modelling and Numerical Analysis 49, 1085–1126.

Delgado, J., Alfaro, P., Galindo-Zaldivar, J., Jabaloy, A., López Garrido, A.C., Sanz de Galdeano, C., 2002. Structure of the Padul-Nigüelas Basin (Spain) from H/V Ratios of Ambient Noise: Application of the Method to Study Peat and Coarse Sediments. Pure Appl. Geophys. 159, 2733–2749. https://doi.org/10.1007/s00024-002-8756-1

Delgado, J., López Casado, C., Giner, J., Estévez, A., Cuenca, A., Molina, S., 2000. Microtremors as a Geophysical Exploration Tool: Applications and Limitations: Pure Appl. Geophys. 157, 1445–1462. https://doi.org/10.1007/PL00001128

Demirdzic, I., Muzaferija, S., 1994. Finite volume method for stress analysis in complex domains. International Journal for Numerical Methods in Engineering 37, 3751–3766.

Dempster, A.P., 1967. Upper and Lower Probabilities Induced by a Multivalued Mapping. The annals of mathematical statistics 38, 325–339.

Dezert, T., Lopes, S.P., Fargier, Y., 2019. Fusion d'informations géophysiques et géotechniques acquises sur banc d'essai pour application au diagnostic de digues. Digues Maritimes et Fluviales de Protection contre les Inondations.

Dobry, R., Vucetic, M., 1987. Dynamic properties and seismic response of soft clay deposits.

Du, M., 2016. Modélisation intégrée des écoulements souterrains et des échanges nappe-rivière dans la basse vallée du Var (Thesis). Université Côte d'Azur.

Dubar, M., 2012. Les dépôts pliocènes et pléistocènes de la basse vallée du Var (Nice, Alpes-Maritimes): variations du niveau marin et néotectonique depuis 5 millions d'années. Ann. Mus. Hist. nat. Nice XXVI, 35–54.

Dubar, M., 2003. The Holocene deltas of Eastern Provence and the French Riviera: geomorphological inheritance, genesis and vulnerability. Geomorphologie 9, 263–270. https://doi.org/10.3406/morfo.2003.1189

Dufour, N., Payeur, J.-B., Bertrand, E., Mercerat, D., Régnier, J., Vancraenenbroeck, V., Alliaume, M., 2018. Installation d'un forage vertical instrumenté dans la basse vallée du Var (Nice, France), in: Journées Nationales de Géotechnique et de Géologie de l'Ingénieur. Champs-sur-Marne.

Dumasdelage, R., Delestre, O., Clamond, D., Philippe, G., 2016. Storm Events of Nice Bay: A Numerical Modeling of the Interactions Between Wave, Current, and Solid Transport. Advances in Hydroinformatics 17–27.

Dumbser, M., Käser, M., 2006. An arbitrary high-order discontinuous Galerkin method for elastic waves on unstructured meshes—II. The three-dimensional isotropic case. Geophysical Journal International 167, 319–336.

Dunand, F., 2005. Pertinence du bruit de fond sismique pour la caractérisation dynamique et l'aide au diagnostique sismique des structures de génie civil (Thèse). Université Joseph Fourier, Grenoble.

Dunand, F., Bard, P.Y., Chatelain, J.L., Guéguen, P., Vassail, T., Farsi, M.N., 2002. Damping and frequency from RandomDec method applied to in situ measurements of ambient vibrations. Evidence for effective soil structure interaction., in: Elsevier Science Ltd. Presented at the 12th European Conference on Earthquake Engineering, p. 9.

Duval, A.M., Bertrand, E., Régnier, J., Grasso, E., Gance, J., Glinsky, N., Semblat, J.F., 2009. Experimental and numerical approaches of topographic site effects claimed to be responsible for 1909 Provence earthquake damage distribution, in: Fall Meeting 2009. Presented at the American Geophysical Union.

Duval, A.M., Bertrand, E., Vidal, S., Delgado, J., 2013. Détection des effets de site sismiques: Mise au point de méthodes expérimentales et application à Nice. BLPC 3–20.

Duval, A.M., Vidal, S., 2003. Contribution à l'étude de l'aléa local à Nice : Complément d'analyse du bruit de fond sismique. (No. 987400136/04). CETE Méditerranée.

Ellis, B.R., 1980. An assessment of the accuracy of predicting the fundamental natural frequencies of buildings and the implications concerning the dynamic analysis of structures. Proceedings of the ICE 69, 763–776. https://doi.org/10.1680/iicep.1980.2376

Erlingsson, S., 1999. Three-dimensional dynamic soil analysis of a live load in Ullevi Stadium. Soil Dynamics and Earthquake Engineering 14.

Erlingsson, S., Bodare, A., 1996. Live load induced vibrations in Ul!evi Stadium dynamic soil analysis. Soil Dynamics and Earthquake Engineering 15, 171–188.

European Commission, 2004. SESAME-HV-User-Guidelines.

Eymard, R., Gallouët, T., Herbin, R., 2000. Finite volume methods, Handbook of numerical analysis. ed.

Fares, R., 2018. Modeling techniques for building design considering soil-structure interaction (Thesis). Université Côte d'Azur, Nice.

Fares, R., Santisi d′Avila, M.P., Deschamps, A., 2019. Soil-structure interaction analysis using a 1DT-3C wave propagation model. Soil Dynamics and Earthquake Engineering 120, 200–213. https://doi.org/10.1016/j.soildyn.2019.02.011

Farghaly, A.A., 2017. Seismic analysis of adjacent buildings subjected to double pounding considering soil–structure interaction. Int J Adv Struct Eng 9, 51–62. https://doi.org/10.1007/s40091-017-0148-y

Field, E., Johnson, P.A., Beresnev, I.A., Zeng, Y., 1997. Nonlinear ground-motion amplification by sediments during the 1994 Northridge earthquake. Letters to Nature 599–602.

Finkelstein, A., 2019. Understanding Mass Participation Factor Results in Frequency Studies.

Fleissner, F., Gaugele, T., Eberhard, P., 2007. Applications of the discrete element method in mechanical engineering. Multibody system dynamics 18, 81–94.

Foti, S., Hollender, F., Garofalo, F., Albarello, D., Asten, M., Bard, P.-Y., Comina, C., Cornou, C., Cox, B., Di Giulio, G., Forbriger, T., Hayashi, K., Lunedei, E., Martin, A., Mercerat, D., Ohrnberger, M., Poggi, V., Renalier, F., Sicilia, D., Socco, V., 2017. Guidelines for the good practice of surface wave analysis: a product of the InterPACIFIC project. B. Earthq. En. 16, 2367–2420. https://doi.org/10.1007/s10518-017-0206-7

Gaffet, S., Bouchon, M., 1989. Effects of two-dimensional topographies using the discrete wavenumber-boundary integral equation method in P–SV cases. J. Acoust. Soc. Am. 85, 2277–2283.

Gallipoli, M., Mucciarelli, M., Vona, M., 2009. Empirical estimate of fundamental frequencies and damping for Italian buildings. Earthquake Engineering & Structural Dynamics 38, 973–988. https://doi.org/10.1002/eqe.878

Gallipoli, M.R., Mucciarelli, M., Castro, R.R., Monachesi, G., Contri, P., 2004. Structure, soil-structure response and effects of damage based on observations of horizontal-to-vertical spectral ratios of microtremors. Soil Dynamics and Earthquake Engineering 24, 487–495.

Ganev, T., Nagata, S., Katayama, T., 1993. Creation of Database of Earthquake Records for a Reinforced Concrete Tower and Observation of Soil-Structure Interaction Effects. Bulletin of Earthquake Resistant Structure Research Center 57–73.

Gargani, J., 2004. Modelling of the erosion in the Rhone valley during the Messinian crisis (France). Quaternary International 121, 13–22.

Genikomsou, A.S., Polak, M.A., 2015. Finite element analysis of punching shear of concrete slabs using damaged plasticity model in ABAQUS. Eng. Struct. 98, 38–48. https://doi.org/10.1016/j.engstruct.2015.04.016

Geuzaine, C., Remacle, J.-F., 2020. Gmsh Reference Manual, The documentation for Gmsh 4.6.0 A finite element mesh generator with built-in pre- and post-processing facilities.

Ghaboussi, J., Barbosa, R., 1990. Three-dimensional discrete element method for granular materials. International Journal for Numerical and Analytical Methodsin Geomechanics 14, 451–472.

Ghandil, M., Aldaikh, H., 2017. Damage-based seismic planar pounding analysis of adjacent symmetric buildings considering inelastic structure–soil–structure interaction.

Earthquake Engineering & Structural Dynamics 46, 1141–1159. https://doi.org/10.1002/eqe.2848

Ghannad, M.A., Jahankhah, H., 2007. Site-dependent strength reduction factors for soil-structure systems. Soil Dynamics and Earthquake Engineering 27, 99–110. https://doi.org/10.1016/j.soildyn.2006.06.002

Giner, E., Sukumar, N., Tarancón, J.E., Fuenmayor, F.J., 2009. An Abaqus implementation of the extended finite element method. Engineering Fracture Mechanics 76, 347–368. https://doi.org/10.1016/j.engfracmech.2008.10.015

Glinsky, N., Bertrand, E., Régnier, J., 2019. Numerical simulation of topographical and geological site effects. Applications to canonical topographies and Rognes hill, South East France. Soil Dynamics and Earthquake Engineering 116, 620–636. https://doi.org/10.1016/j.soildyn.2018.10.020

Gratton, Y., 2002. Le krigeage: la méthode optimale d'interpolation spatiale. Les articles de l'Institut d'Analyse Géographique.

Guéguen, P., 2008. Urban seismic ground motion: a coupled effect of site and urban environment, in: The 14th World Conference on Earthquake Engineering. Beijing, China.

Guéguen, P., 2000. Interaction sismique entre le sol et le bâti: de l'Interaction Sol-Structure à l'Interaction Site-Ville (Thesis). Université Joseph Fourier.

Guéguen, P., Bard, P.-Y., Chávez-García, F.J., 2002. Site-City Seismic Interaction in Mexico City–Like Environments: An Analytical Study. B. Seismol. Soc. Am 92, 794–811.

Guéguen, P., Colombi, A., 2016. Experimental and Numerical Evidence of the Clustering Effect of Structures on Their Response during an Earthquake: A Case Study of Three Identical Towers in the City of Grenoble, France. Bull. Seismol. Soc. Am. 106, 2855–2864. https://doi.org/10.1785/0120160057

Guéguen, P., Cornou, C., Garambois, S., Banton, J., 2007. On the Limitation of the H/V Spectral Ratio Using Seismic Noise as an Exploration Tool: Application to the Grenoble Valley (France), a Small Apex Ratio Basin. Pure Appl. Geophys. 164, 115–134. https://doi.org/10.1007/s00024-006-0151-x

Guglielmi, Y., 1993. Hydrogéologie des aquifères plio-quaternaires de la basse vallée du Var (Alpes-Maritimes, France): contrôle néotectonique des écoulements souterrains: l'outil, chimique et isotopique, pour l'étude du fonctionnement et de la vulnérabilité des aquifères (Thesis). Université d'Avignon et des pays de Vaucluse.

Guillier, B., Atakan, K., Chatelain, J.-L., Havskov, J., Ohrnberger, M., Cara, F., Duval, A.-M., Zacharopoulos, S., Teves-Costa, P., The SESAME Team, 2008. Influence of instruments on the H/V spectral ratios of ambient vibrations. B. Earthq. En. 6, 3–31. https://doi.org/10.1007/s10518-007-9039-0

Guillier, B., Cornou, C., Kristek, J., Moczo, P., Bonnefoy-Claudet, S., Fäh, D., 2006. Simulation of seismic ambient vibrations : does the H/V provide quantitative

information in 2D-3D structures ? Presented at the Third International Symposium on the Effects of Surface Geology on Seismic Motion, Grenoble, France, p. 185.

H2EA, Cabinet Mangan, 2010. Etude hydrogéologique des nappes profondes de la basse vallée du Var (Alpes-Maritimes). Conseil Général des Alpes-Maritimes.

Haefner, R.J., Sheets, R.A., Andrews, R.E., 2010. Evaluation of the Horizontal-to-Vertical Spectral Ratio (HVSR) Seismic Method to Deter- mine Sediment Thickness in the Vicinity of the South Well Field, Franklin County, OH. OJS 110, 77–85.

Hans, S., 2002. Auscultation dynamique de bâtiments et modélisation par homogénéisation: contribution à l'analyse de la vulnérabilité sismique (Thesis). INSA, Lyon.

Hardin, B.O., Drnevich, V.P., 1972. Shear Modulus and Damping in Soils. Journal of the Soil Mechanics and Foundations Division, 98, 667–692.

Helwany, S., 2007. Applied Soil Mechanics with ABAQUS Applications, John Wiley&Sons. ed.

Hesthaven, J.S., Warburton, T., 2007. Nodal discontinuous Galerkin methods: algorithms, analysis, and applications, Science&Business Media. ed. Springer.

Horn, R., Menard, F., Munck, F., 1965. Etude géophysique de la basse vallée du Var (No. DS.65.A 37). BRGM.

Horn, R., Mercier, F., Moal, A., Valentin, J., 1980. Reconnaissance des fonds marins dans la zone du delta du Var par sismique réflexion continue (No. 80SGN360GPH). BRGM.

Housner, G.W., 1957. Interaction of building and ground during an earthquake. Bulletin of the Seismological Society of America 179–186.

Huang, C.-S., Yeh, C.H., 1999. Some properties of randomdec signatures. MSSP 13, 491–507.

Huerta, C.I., Roesset, J.M., Stokoe, K.H., 1998. Evaluation of the random decrement method for in-situ soil properties estimation. The effects of surface geology on seismic motion 749–756.

Hughes, T.J.R., 1987. The finite element method - linear static and dynamic finite element analysis. Prentice Hall Englewood Cliff 490–567.

Ibrahim, S.R., Asmussen, J.C., Brincker, R., 1998. Vector Triggering Random Decrement for High Identification Accuracy. J. Vib. Acoust. 120, 970–975.

Iguchi, M., 1982. An approximate analysis of input motions for rigid embedded foundations. Architectural Institut of Japan 61–75.

Isbiliroglu, Y., Taborda, R., Bielak, J., 2015. Coupled soil-structure interaction effects of building clusters during earthquakes. Earthquake Spectra 31, 463–500.

Javelaud, E., 2016. Déplacements et rotations du sol lors de forts séismes à proximité de failles actives : apports des capteurs accélérométriques. Rev. Fr. Geotech. 3. https://doi.org/10.1051/geotech/2016003

Jeary, A.P., 1997. Damping in structures. J. Wind. Eng. 72, 345–355.

Jeary, A.P., 1986. Damping in tall buildings—a mechanism and a predictor. Earthquake engineering & structural dynamics 14, 733–750.

Jennings, P.C., 1970. Distant motion from a building vibration test. Bull. Seismol. Soc. Am. 60, 2037–2043.

Joyner, W.B., Chen, A.T.F., 1975. Calculation of nonlinear ground response in earthquakes. Bull. Seismol. Soc. Am. 65, 1315–1336. https://doi.org/10.1785/BSSA0650051315

Kanai, K., 1983. Engineering Seismology. University of Tokyo Press.

Kanai, K., 1950. A Method of Determining the Stiffness of Each Storey of a n-storied Building. Bull Earthq Res Inst 28, 161–163.

Kanai, Kiyoshi, Yoshizawa, S., 1961. On the period and the damping of vibration in actual buildings. Bull Earthq Res Inst 39, 477–489.

Kanamori, H., Mori, J., Anderson, D.L., Heaton, T.H., 1991. Seismic excitation by the space shuttle Columbia. Nature 349, 781–782. https://doi.org/10.1038/349781a0

Kaneko, T., 1975. On Timoshenko's correction for shear in vibrating beams. J. Phys. D: Appl. Phys. 8, 1927–1936. https://doi.org/10.1088/0022-3727/8/16/003

Karapetrou, S., Fotopoulou, S., Pitilakis, K., 2015. Seismic vulnerability assessment of high-rise non-ductile RC buildings considering soil–structure interaction effects. Soil Dynamics and Earthquake Engineering 73, 42–57. https://doi.org/10.1016/j.soildyn.2015.02.016

Käser, M., Dumbser, M., 2006. An arbitrary high-order discontinuous Galerkin method for elastic waves on unstructured meshes—I. The two-dimensional isotropic case with external source terms. Geophys. J. Int. 166, 855–877.

Kashima, T., Kitagawa, Y., 1988. Observation and Analysis of Earthquake Motions in and Around the SRC Building as Local Earthquake Instrument Array System. Presented at the 9th World Conference on Earthquake Engineering, pp. 721–726.

Kausel, E., 2010. Early history of soil–structure interaction. Soil Dynamics and Earthquake Engineering 30, 822–832. https://doi.org/10.1016/j.soildyn.2009.11.001

Kessler, H., Turner, A.K., Culshaw, M.G., Royse, K.R., 2008. Unlocking the potential of digital 3D geological subsurface models for geotechnical engineers, in: European Econference of the International Association for Engineering Geology. Asociacion Espanola de Geologia Aplicada a la Ingenieria, Madrid, Spain.

Kham, M., Semblat, J.-F., Bard, P.Y., Dangla, P., 2006. Seismic Site-City Interaction: Main Governing Phenomena through Simplified Numerical Models. Bull. Seismol. Soc. Am. 96, 1934–1951. https://doi.org/10.1785/0120050143

Khennane, A., 2013. ntroduction to Finite Element Analysis Using MATLAB® and Abaqus, CRC Press. ed.

Kim, S., Stewart, J.P., 2003. Kinematic Soil-Structure Interaction from Strong Motion Recordings. J. Geotech. Geoenviron. Eng. 129, 323–335. https://doi.org/10.1061/(ASCE)1090-0241(2003)129:4(323)

Kitada, Y., Hirotani, T., Iguchi, M., 1999. Models test on dynamic structure–structure interaction of nuclear power plant buildings. Nucl. Eng. 192, 205–216. https://doi.org/10.1016/S0029-5493(99)00109-0

Komatitsch, D., Liu, Q., Tromp, J., Suss, P., Stidham, C., Shaw, J.H., 2004. Simulations of ground motion in the Los Angeles basin based upon the spectral-element method. Bull. Seismol. Soc. Am. 94, 187–206.

Komatitsch, D., Vilotte, J.-P., 1998. The spectral element method: an efficient tool to simulate the seismic response of 2D and 3D geological structures. Bull. Seismol. Soc. Am. 88, 368–392.

Konno, K., Ohmachi, T., 1998. Ground-Motion Characteristics Estimated from Spectral Ratio between Horizontal and Vertical Components of Microtremor. B. Seismol. Soc. Am 88, 228–241.

Kontoni, D.-P., Farghaly, A., 2018. Seismic Response of Adjacent Unequal Buildings Subjected to Double Pounding Considering Soil-Structure Interaction. Computation 6. https://doi.org/10.3390/computation6010010

Kopf, J.A., Stegmann, S., Garziglia, S., Sultan, N., Henry, P., Dennielou, B., Haas, S., Weber, K.-C., 2016. Soft sediment deformation in the shallow submarine slope off Nice (France) as a result of a variably charged Pliocene aquifer and mass wasting processes. Sediment. Geol. 344. https://doi.org/10.1016/j.sedgeo.2016.05.014

Kotronis, P., Davenne, L., Mazars, J., 2003. Poutre 3D multifibre Timoshenko pour la modélisation des structures en béton armé soumises à des chargements sévères, in: VIème Colloque National Génie Parasismique, Aspects dynamiques et vibratoire en génie civil. Presented at the AFPS, Paris, France, pp. 59–66. https://doi.org/hal-01008667

Kumar, N., Narayan, J.P., 2019a. Effects of site–city interaction and polarization of the incident S-wave on the transfer function and fundamental frequency of structures. Nat. Hazards 97, 747–774. https://doi.org/10.1007/s11069-019-03671-8

Kumar, N., Narayan, J.P., 2019b. Quantification of Fundamental Frequencies of 3D Basins and Structures and Site–City Interaction Effects on Responses of Structures. Pure Appl. Geophys. 176, 4477–4502. https://doi.org/10.1007/s00024-019-02158-8

Kumar, N., Narayan, J.P., 2018. Study of 2D Basins and Site-City Interaction Effects on Ground Motion Characteristics. J-IGU 22, 16–23.

Lachet, C., Bard, P.-Y., 1994. Numerical and Theoretical Investigations on the Possibilities and Limitations of Nakamura's Technique. J. Phys. Earth. 42, 377–397. https://doi.org/10.4294/jpe1952.42.377

Lagomarsino, S., 1993. Forecast models for damping and vibration periods of buildings. Journal of Wind Engineering and Industrial Aerodynamics 48, 221–239. https://doi.org/10.1016/0167-6105(93)90138-E

Larroque, C., 2009. Aléa sismique dans une région intraplaque à sismicité modérée: la jonction Alpes - Bassin Ligure (HDR). Université Nice Sophia Antipolis, Nice Sophia Antipolis.

Larroque, C., Béthoux, N., Calais, E., Courboulex, F., Deschamps, A., Déverchère, J., Stéphan, J.-F., Ritz, J.-F., Gilli, E., 2001. Active and recent deformation at the Southern Alps – Ligurian basin junction. Netherlands Journal of Geosciences 80, 255–272. https://doi.org/10.1017/S0016774600023878

Laurenzano, G., Priolo, E., Gallipoli, M.R., Mucciarelli, M., Ponzo, F.C., 2010. Effect of Vibrating Buildings on Free-Field Motion and on Adjacent Structures: The Bonefro (Italy) Case History. Bulletin of the Seismological Society of America 100, 802–818. https://doi.org/10.1785/0120080312

Lebrun, B., Hatzfeld, D., Bard, P.Y., 2001. Site effect study in urban area: Experimental results in Grenoble (France). Pure Appl. Geophys. 158, 2543–2557.

Lermo, J., Chavez-Garcia, F.J., 1993. Site effect evaluation using spectral ratios with only one station. B. Seismol. Soc. Am 83, 1574–1594.

Levesque, J.R., 1998. The Code Aster: a product for mechanical engineers; Le Code Aster: un produit pour les mecaniciens des structures. Epure 7–20.

Li, P., Liu, S., Lu, Z., 2017. Studies on pounding response considering structure-soil-structure interaction under seismic loads. Sustainability 9, 2219.

Lorenzo, G.W.F., 2016. Des données accélérométriques au comportement dynamique des bâtiments existants. Côte d'Azur.

Lorenzo, G.W.F., d'Avila, M.P.S., Deschamps, A., Bertrand, E., Mercerat, E.D., Foundotos, L., Courboulex, F., 2018. Numerical and Empirical Simulation of Linear Elastic Seismic Response of a Building: The Case of Nice Prefecture. Earthquake Spectra 34, 169–196. https://doi.org/10.1193/042216EQS064M

Lubineau, G., Ladevèze, P., 2008. Construction of a micromechanics-based intralaminar mesomodel, and illustrations in ABAQUS/Standard. Computational Materials Science 43, 137–145. https://doi.org/10.1016/j.commatsci.2007.07.050

Lysmer, J., Ostadan, F., Tabatabaie, M., Vahdani, S., Tajirian, F., 1988. SASSI-A System for Analysis of Soil-Structure Interaction, Theoretical Manual. University of California, Berkeley, Berkeley.

Lysmer, J., Udaka, T., Tsai, C.F., Seed, H.B., 1975. FLUSH A Computer Program for Approximate 3-D Analysis of Soil-Structure Interaction Problems (No. UCB/EERC-75/30). Earthquake Engineering Research Center, University of California, Berkeley.

Madani, B., Behnamfar, F., Tajmir Riahi, H., 2015. Dynamic response of structures subjected to pounding and structure–soil–structure interaction. Soil Dynamics and Earthquake Engineering 78, 46–60. https://doi.org/10.1016/j.soildyn.2015.07.002

Mahmoud, S., Abd-Elhamed, A., Jankowski, R., 2013. Earthquake-induced pounding between equal height multi-storey buildings considering soil-structure interaction. Bull Earthquake Eng 11, 1021–1048. https://doi.org/10.1007/s10518-012-9411-6

Makrypidi, T., Chatzigogos, C., Ferro, A.N., Greffet, N., 2017. Assessment of analysis methods for linear and nonlinear soil-structure interaction in view of increasing seismic intensity and foundation uplift, in: 16th World Conference on Earthquake. Santiago, Chile.

Manakou, M.V., Raptakis, D.G., Chávez-García, F.J., Apostolidis, P.I., Pitilakis, K.D., 2010. 3D soil structure of the Mygdonian basin for site response analysis. Soil Dyn. Earthq. Eng. 30, 1198–1211. https://doi.org/10.1016/j.soildyn.2010.04.027

Mangan, C., Emily, A., Tennevin, G., 2012. Synthèse géologique de la basse vallée du Var (Alpes-Maritimes, France) Données nouvelles sur la structure profonde. Ann. Mus. Hist. nat. Nice XXVII, 21–33.

Marache, A., Denys, B., Piette, C., Thierry, P., 2009a. Geotechnical modeling at the city scale using statistical and geostatistical tools: The Pessac case (France), in: Journées Nationales de Géotechnique et de Géologie de l'Ingénieur : Actes. https://doi.org/10.1016/j.enggeo.2009.04.003

Marache, A., Dubost, J., Denys, B., Denis, A., Dominique, S., 2009b. Understanding subsurface geological and geotechnical complexity at various scales in urban soils using a 3D model. Georisk 3, 192–205. https://doi.org/10.1080/17499510802711994

Mascandola, C., Massa, M., Barani, S., Albarello, D., Lovati, S., Martelli, L., Poggi, V., 2019. Mapping the Seismic Bedrock of the Po Plain (Italy) through Ambient-Vibration Monitoring. B. Seismol. Soc. Am XX. https://doi.org/10.1785/0120180193

Matheron, G., 1969. Le krigeage universel, Ecole Nationale Supérieure des Mines de Paris. ed, Les Cahiers du Centre de Morphologie Mathématique de Fontainebleau.

Mazzieri, I., Stupazzini, M., Guidotti, R., Smerzini, C., 2013. SPEED: SPectral Elements in Elastodynamics with Discontinuous Galerkin: a non-conforming approach for 3D multi-scale problems. International Journal for Numerical Methods in Engineering 95, 991–1010. https://doi.org/10.1002/nme.4532

Meli, R., Faccioli, E., Muria-Vila, D., Quaas, R., Paolucci, R., 1998. A study of site effects and seismic response of an instrumented building in Mexico city. Journal of earthquake engineering.

Mercerat, E.D., Glinsky, N., 2015. A nodal discontinuous Galerkin method for non-linear soil dynamics. 6th International Conference on Earthquake Geotechnical Engineering.

Merritt, R.G., Housner, G.W., 1954. Effect of foundation compliance on earthquake stresses in multistory buildings. Bull. Seismol. Soc. Am. 44, 551–569.

Meza-Fajardo, K.C., Semblat, J.-F., Chaillat, S., Lenti, L., 2016. Seismic-wave amplification in 3D alluvial basins: 3D/1D amplification ratios from fast multipole BEM simulations. Bull. Seismol. Soc. Am. 106, 1267–1281.

Miari, M., Choong, K.K., Jankowski, R., 2019. Seismic pounding between adjacent buildings: Identification of parameters, soil interaction issues and mitigation measures. Soil Dynamics and Earthquake Engineering 121, 135–150. https://doi.org/10.1016/j.soildyn.2019.02.024

Michel, C., 2007. Vulnérabilité Sismique de l'échelle du bâtiment à celle de la ville Apport des techniques expérimentales in situ Application à Grenoble (Thèse). Université Joseph Fourier, Grenoble.

Michel, C., Guéguen, P., 2018. Interpretation of the velocity measured in buildings by seismic interferometry based on Timoshenko beam theory under weak and moderate motion. Soil. Dyn. Earthq. Eng 104, 131–142.

Michel, C., Guéguen, P., Bard, P.-Y., 2008. Dynamic parameters of structures extracted from ambient vibration measurements: An aid for the seismic vulnerability assessment of existing buildings in moderate seismic hazard regions. Soil. Dyn. Earthq. Eng 28, 593–604.

Migeon, S., Kelner, M., Tric, E., Courboulex, F., Dano, A., Lebourg, Th., Taboada, A., 2016. Frequency and triggering of small-scale submarine landslides on decadal timescales: Analysis of 4D bathymetric data from the continental slope offshore Nice (France). Mar. Geol. 379, 281–297. https://doi.org/10.1016/j.margeo.2016.06.009

Mikael, A., 2011. Evaluation des paramètres physiques des bâtiments : amortissement, fréquence et modes de comportement des structures de génie civil : Approche expérimentale. Université de Grenoble, Grenoble, France.

Mikael, A., Gueguen, P., Bard, P.-Y., Roux, P., Langlais, M., 2013. The Analysis of Long-Term Frequency and Damping Wandering in Buildings Using the Random Decrement TechniqueLong-Term Frequency Analysis and Damping Wandering in Buildings Using RDT. Bulletin of the Seismological Society of America 103, 236–246. https://doi.org/10.1785/0120120048

Mita, A., Luco, J.E., 1986. Response of structures to a spatially random ground motion. Earthquake Engineering Research Institut 2, 907–918.

Mitropoulou, C.C., Kostopanagiotis, C., Kopanos, M., Ioakim, D., Lagaros, N.D., 2016. Influence of soil–structure interaction on fragility assessment of building structures. Structures 6, 85–98.

Moczo, P., Bard, P.-Y., 1993. Wave diffraction, amplification and differential motion near strong lateral discontinuities. Bull. Seismol. Soc. Am. 83, 85–106.

Moczo, P., Kristek, J., Bard, P.-Y., Stripajová, S., Hollender, F., Chovanová, Z., Kristeková, M., Sicilia, D., 2018. Key structural parameters affecting earthquake ground motion in 2D and 3D sedimentary structures. B. Earthq. En. 16, 2421–2450. https://doi.org/10.1007/s10518-018-0345-5

Moczo, P., Kristek, J., Gális, M., 2014. The finite-difference modelling of earthquake motions: Waves and ruptures. Cambridge University Press.

Moczo, P., Kristek, J., Halada, L., 2004. The finite-difference method for seismologists. An Introduction, Comenius University Bratislava. ed, Marie Curie Research Training Network SPICE Contract No MRTN-CT-2003-504267.

Mucciarelli, M., Gallipoli, M.R., 2007. Non-parametric analysis of a single seismometric recording to obtain building dynamic parameters. Ann. Geophys. 50, 259–266.

Muria-Vila, D., Alcorta, R.G., 1992. Soil-Structure Interaction Effects in a Building. Presented at the 10th World Conference of Earthquake Engineering, pp. 1905–1910.

Mylonakis, G., Gazetas, G., 2000. Seismic Soil-Structure Interaction: Beneficial or Detrimental? Journal of Earthquake Engineering 4, 277–301. https://doi.org/10.1080/13632460009350372

Nakamura, Y., 1989. A method for dynamic characteristics estimation of subsurface using microtremor on the ground surface. Railway Technical Research Institute, Quarterly Reports 30.

Nakata, N., Snieder, R., Kuroda, S., Ito, S., Aizawa, T., Kunimi, T., 2013. Monitoring a Building Using Deconvolution Interferometry. I: Earthquake-Data Analysis. Bulletin of the Seismological Society of America 103, 1662–1678. https://doi.org/10.1785/0120120291

Nakhaei, M., Ali Ghannad, M., 2008. The effect of soil–structure interaction on damage index of buildings. Eng. Struct. 30, 1491–1499. https://doi.org/10.1016/j.engstruct.2007.04.009

Naserkhaki, S., Aziz, F.N.A.A., Pourmohammad, H., 2012. Earthquake induced pounding between adjacent buildings considering soil-structure interaction. Earthq. Eng. Eng. Vib. 11, 343–358. https://doi.org/10.1007/s11803-012-0126-0

Naserkhaki, S., El-Rich, M., 2013. Separation gap, a critical factor in earthquake induced pounding between adjacent buildings 19.

Naserkhaki, S., El-Rich, M., Aziz, F.N.A.A., Pourmohammad, H., 2014. Pounding between adjacent buildings of varying height coupled through soil. Structural Engineering and Mechanics 52, 573–593. https://doi.org/10.12989/sem.2014.52.3.573

Nordpil, 2021.

Olsen, K.B., 2000. Site Amplification in the Los Angeles Basin from Three-Dimensional Modeling of Ground Motion. B. Seismol. Soc. Am 90, S77–S94. https://doi.org/10.1785/0120000506

Paolucci, R., 2002. Amplification of earthquake ground motion by steep topographic irregularities. Earthquake Engineering & Structural Dynamics 31, 1831–1853. https://doi.org/0.1002/eqe.192

Paolucci, R., 1993. Soil-structure interaction effects of an instrumented building in Mexico City. European Earthquake Engineering 3, 33–44.

Park, C., D. Miller, R., Xia, J., 1999. Multichannel analysis of surface waves (MASW). Geophysics 64. https://doi.org/10.1190/1.1444590

Parolai, S., Bormann, P., Milkereit, C., 2002. New Relationships between Vs, Thickness of Sediments, and Resonance Frequency Calculated by the H/V Ratio of Seismic Noise for the Cologne Area (Germany). B. Seismol. Soc. Am 92, 2521–2527. https://doi.org/10.1785/0120010248

Pastor, M., Binda, M., Harčarik, T., 2012. Modal Assurance Criterion. Procedia Engineering 48, 543–548. https://doi.org/10.1016/j.proeng.2012.09.551

Pequegnat, C., Gueguen, P., Hatzfeld, D., Langlais, M., 2008. The French Accelerometric Network (RAP) and National Data Centre (RAP-NDC). Seismol. Res. Lett. 79, 79–89. https://doi.org/10.1785/gssrl.79.1.79

Peyrusse, F., Glinsky, N., Gélis, C., Lanteri, S., 2014. A nodal discontinuous Galerkin method for site effects assessment in viscoelastic media—verification and validation in the Nice basin. Geophysical Journal International 199, 315–334.

Pitilakis, D., Karatzetzou, A., 2014. Dynamic stiffness of monumental flexible masonry foundations. Bulletin of Earthquake Engineering 13. https://doi.org/10.1007/s10518-014-9611-3

Pline, C., 1991. Contribution à l'étude géologique, hydrogéologique et géotechnique de la basse-plaine alluviale du Paillon (Thesis). Université Nice Sophia Antipolis.

Prevosto, M., Benveniste, A., Bernouin, B., 1982. Modélisation et identification des caractéristiques d'une structure vibratoire:un problème de réalisation stochastique d'un grand système non stationnaire (No. RR-0130). INRIA.

Rahmani, M., Ebrahimian, M., Todorovska, M.I., 2015. Wave dispersion in high-rise buildings due to soil-structure interaction. Earthquake Engng Struct. Dyn. 44, 317–323. https://doi.org/10.1002/eqe.2454

Raptakis, D.G., Manakou, M.V., Chávez-García, F.J., Makra, K.A., Pitilakis, K.D., 2005. 3D configuration of Mygdonian basin and preliminary estimate of its site response. Soil Dyn. Earthq. Eng. 25, 871–887. https://doi.org/10.1016/j.soildyn.2005.05.005

Reed, W.H., Thomas, R.H., 1973. Triangular mesh methods for the neutron transport equation (No. LA-UR-73-479; CONF-730414-2). Los Alamos Scientific Lab., N. Mex.(USA).

Régnier, J., Bertrand, E., Cadet, H., 2020. Repeatable process for seismic microzonation using 1-D site-specific response spectra assessment approaches. Application to the city of Nice, France. Engineering Geology 270, 105569. https://doi.org/10.1016/j.enggeo.2020.105569

Régnier, J., Cadet, H., Bonilla, L., Bertrand, E., Semblat, J.-F., 2013. Assessing Nonlinear Behavior of Soils in Seismic Site Response: Statistical Analysis on KiK-net Strong-Motion Data. B. Seismol. Soc. Am 103, 1750–1770. https://doi.org/10.1785/0120120240

Rix, G.J., Leipski, E.A., 1991. Accuracy and resolution of surfaces wave inversion. Recent advances in instrumentation, data acquisition and testing in soil dynamics, in: Proceedings of Sessions Sponsored by the Geotechnical Engineering Division of the American Society of Civil Engineers in Conjunction with the ASCE Convention. Presented at the American Society of Civil Engineers, Orlando, Florida.

Rohmer, O., Bertrand, E., Mercerat, E.D., Régnier, J., Pernoud, M., Langlaude, P., Alvarez, M., 2020. Combining Geotechnical and Geophysical Data to Build a 3D Model of the Lower Var Valley, Nice (France). Eng. Geol. 270. https://doi.org/10.1016/j.enggeo.2020.105588

Roten, D., 2007. Site effects in the Rhône valley analysed by ambient noise, weak motion records and numerical simulations (Thesis). ETH Zurich. https://doi.org/10.3929/ethz-a-005592923

Roten, D., Fäh, D., Cornou, C., Giardini, D., 2006. Two-dimensional resonances in Alpine valleys identified from ambient vibration wavefields. Geophys. J. Int. 165, 889–905. https://doi.org/10.1111/j.1365-246X.2006.02935.x

Rukos, E.A., 1971. LAYER - Deconvolution of Surface Accelerograms for Horizontally Stratified Soil Layers. NISEE/Computer Applications, University of California, Berkeley.

Sabetta, F., Pugliese, A., 1996. Estimation of Response Spectra and Simulation of Nonstationary Earthquake Ground Motions. Bull. Seismol. Soc. Am. 86, 337–352.

Sabetta, F., Pugliese, A., Fiorentino, G., Lanzano, G., Luzi, L., 2021. Simulation of non-stationary stochastic ground motions based on recent Italian earthquakes. Bull. Earth. Eng. 19, 3287–3315. https://doi.org/10.1007/s10518-021-01077-1

Saez, E., Lopez-Caballero, F., Modaressi-Farahmand-Razavi, A., 2011. Effect of the inelastic dynamic soil-structure interaction on the seismic vulnerability assessment. Struct. Saf 33, 51–63. https://doi.org/10.1016/j.strusafe.2010.05.004

Safak, F., Celebi, M., 1992. Recorded seismic response of Pacific Park Plaza. II. System identification. Journal of Structural Engineering 118, 24. https://doi.org/10.1061/(ASCE)0733-9445(1992)118:6(1566)

Sahar, D., Narayan, J.P., 2016. Quantification of modification of ground motion due to urbanization in a 3D basin using viscoelastic finite-difference modelling. Natural Hazards 81, 779–806.

Sahar, D., Narayan, J.P., Kumar, N., 2015. Study of role of basin shape in the site–city interaction effects on the ground motion characteristics. Nat Hazards 75, 1167–1186. https://doi.org/10.1007/s11069-014-1366-2

Salameh, C., Guillier, B., Harb, J., Cornou, C., Bard, P.-Y., Voisin, C., Mariscal, A., 2016. Seismic response of Beirut (Lebanon) buildings: instrumental results from ambient vibrations. B. Earthq. En. 14, 2705–2730. https://doi.org/10.1007/s10518-016-9920-9

Salloum, N., Jongmans, D., Cornou, C., Voisin, C., Mariscal, A., Massih, D.Y.A., Chehade, F.H., Hammoud, M., 2012. Imaging Heterogeneity Of Soil By Means Of Geophysical

And Geotechnical Investigation: In The Alluvial Plain Of Beirut. Presented at the 15 WCEE, Lisboa.

Sanchez-Sesma, F.J., Luzon, F., 1995. Seismic response of three-dimensional alluvial valleys for incident P, S, and Rayleigh waves. Bull. Seismol. Soc. Am. 85, 269–284.

Sarrazin, M.A., Roesset, J.M., Whitman, R.V., 1972. Dynamic soil-structure interaction. Journal of the Structural Division 98.

Satake, N., Suda, K., Arakawa, T., Sasaki, A., Tamura, Y., 2003. Damping Evaluation Using Full-Scale Data of Buildings in Japan. Journal of Structural Engineering-asce - J STRUCT ENG-ASCE 129. https://doi.org/10.1061/(ASCE)0733-9445(2003)129:4(470)

Sato, T., Graves, R.W., Somerville, P.G., 1999. Three-dimensional finite-difference simulations of long-period strong motions in the Tokyo metropolitan area during the 1990 Odawara earthquake (MJ 5.1) and the great 1923 Kanto earthquake (MS 8.2) in Japan. Bull. Seismol. Soc. Am. 89, 579–607.

Scanlan, R.H., 1976. Seismic wave effects on soil-structure interaction. Int. J. of Earthq. Engng and Struct. Dyn. 4, 379–388.

Scherbaum, F., Hinzen, K.-G., Ohrnberger, M., 2003. Determination of shallow shear wave velocity profiles in the Cologne, Germany area using ambient vibrations. Geophys. J. Int. 152, 597–612. https://doi.org/10.1046/j.1365-246X.2003.01856.x

Schnabel, P.B., Lysmer, J., Seed, H.B., 1972. SHAKE - A Computer Program for Earthquake Response Analysis of Horizontally Layered Sites (No. UCB/EERC-72/12). Earthquake Engineering Research Center, University of California, Berkley.

Schwan, L., Boutin, C., Padrón, L.A., Dietz, M.S., Bard, P.-Y., Taylor, C., 2016. Site-city interaction: theoretical, numerical and experimental crossed-analysis. Geophys. J. Int. 205, 1006–1031. https://doi.org/10.1093/gji/ggw049

Seht, M.I., Wohlenberg, J., 1999. Microtremor Measurements Used to Map Thickness of Soft Sediments. B. Seismol. Soc. Am 89, 250–259.

Semblat, J.F., 2011. Modeling Seismic Wave Propagation and Amplification in 1D/2D/3D Linear and Nonlinear Unbounded Media. Int. J. Geomech. 11, 440–448. https://doi.org/10.1061/(ASCE)GM.1943-5622.0000023

Semblat, J.-F., Dangla, P., 2005. Modélisation de la propagation d'ondes et de l'interaction sol-structure : approches par éléments finis et éléments de frontière 16.

Semblat, J.-F., Duval, A.-M., Dangla, P., 2000. Numerical analysis of seismic wave amplification in Nice (France) and comparisons with experiments. Soil. Dyn. Earthq. Eng 19, 347–362. https://doi.org/10.1016/S0267-7261(00)00016-6

Semblat, J.-F., Kham, M., Bard, P.-Y., 2008. Seismic-wave propagation in alluvial basins and influence of site-city interaction. Bull. Seismol. Soc. Am. 98, 2665–2678.

Semblat, J.F., Kham, M., Parara, E., Bard, P.Y., Pitilakis, K., Makra, K., Raptakis, D., 2005. Seismic Wave Amplification : Basin Geometry Vs Soil Layering. Soil Dyn. Earthq. Eng. 25, 529–538.

Serratrice, J.F., 2009. Aéroport de Nice Sondages carottés 2007-2008 Essais de laboratoire (No. jfs i09-032). CETE Méditerranée.

Sgattoni, G., Castellaro, S., 2020. Detecting 1-D and 2-D ground resonances with a single-station approach. Geophysical Journal International 223, 471–487. https://doi.org/10.1093/gji/ggaa325

Shafer, G., 1976. A mathematical theory of evidence, Princeton university press. ed.

Sinaei, H., Shariati, M., Abna, A.H., Aghaei, M., Shariati, A., 2012. Evaluation of reinforced concrete beam behaviour using finite element analysis by ABAQUS. Scientific Research and Essay 7, 2002–2009. https://doi.org/10.5897/SRE11.1393

Smets, P., 1990. The combination of evidence in the transferable belief model. IEEE transactions on pattern analysis and machine intelligence 12, 447–458.

Snieder, R., Şafak, E., 2006. Extracting the building response using seismic interferometry: Theory and application to the Millikan Library in Pasadena, California. B. Seismol. Soc. Am 96, 586–598.

Sotiriadis, D., Klimis, N., Margaris, B., Sextos, A., 2020. Analytical expressions relating free-field and foundation ground motions in buildings with basement, considering soil-structure interaction. Engineering Structures 216, 110757. https://doi.org/10.1016/j.engstruct.2020.110757

Sotiriadis, D., Klimis, N., Margaris, B., Sextos, A., 2019. Influence of structure–foundation–soil interaction on ground motions recorded within buildings. Bull. Earth. Eng. 17, 5867–5895.

Stephenson, W.J., Asten, M.W., Odum, J.K., Frankel, A.D., 2019. Shear Wave Velocity in the Seattle Basin to 2 km Depth Characterized with the krSPAC Microtremor Array Method: Insights for Urban Basin-Scale Imaging. Seismol. Res. Lett. XX. https://doi.org/10.1785/0220180194

Stewart, J.P., Fenves, G.L., 1998. System identification for evaluating soil-structure interaction effects in buildings from strong motion recordings. Earthq. Eng. Struct. Dyn. 27, 869–885. https://doi.org/10.1002/(SICI)1096-9845(199808)27:8<869::AID-EQE762>3.0.CO;2-9

Stewart, J.P., Fenves, G.L., Seed, R.B., 1999. Seismic Soil-Structure Interaction in Buildings. I: Analytical Methods. J. Geotech. Geoenviron. Eng. 125, 26–37. https://doi.org/10.1061/(ASCE)1090-0241(1999)125:1(26)

Stokoe, K.H., Wright, G.W., James, A.B., Jose, M.R., 1994. Characterization of geotechnical sites by SASW method, Geophysical characterization of sites, ISSMFE technical committee #10. R. D. Woods, Oxford Publishers, New Delhi, India.

Stupazzini, M., Paolucci, R., Igel, H., 2009. Near-fault earthquake ground-motion simulation in the Grenoble valley by a high-performance spectral element code. Bull. Seismol. Soc. Am. 99, 286–301.

Sultan, N., Bruno, S., Gwenael, J., Didier, L., Cochonat, P., Henry, P., Stegmann, S., Kopf, A., 2010. Investigation of a possible submarine landslide at the Var delta front (Nice continental slope, southeast France). Can. Geotech. J. 47, 486–496. https://doi.org/10.1139/T09-105

Taborda, R., Bielak, J., 2011. Large-scale earthquake simulation: computational seismology and complex engineering systems. Computing in Science & Engineering 13, 14–27.

Tamura, Y., Suganuma, S., 1996. Evaluation of amplitude-dependent damping and natural frequency of buildings during strong winds. Journal of Wind Engineering and Industrial Aerodynamics 59, 115–130.

Tang, Y., Zhang, J., 2011. Probabilistic seismic demand analysis of a slender RC shear wall considering soil–structure interaction effects. Engineering Structures 33, 218–229. https://doi.org/10.1016/j.engstruct.2010.10.011

Tang, Y.K., 1989. , in: Proceedings: NSF/EPRI Workshop on Dynamic Soil Properties and Site Characterisation. Paolo Alto, California.

Terrier, M., 2012. Étude et classification des failles potentiellement actives de la région Provence-Alpes- Côte d'Azur (France) implications sur l'évaluation de l'aléa sismique, Actes des IXe Rencontres du Groupe AFPS. Archéosismicité et Tsunamis en Méditerranée IXes Rencontres du Groupe APS, Cagnes-sur-mer.

Theodulidis, N.P., Bard, P.-Y., 1995. Horizontal to vertical spectral ratio and geological conditions: an analysis of strong motion data from Greece and Taiwan (SMART-1). Soil Dyn. Earthq. Eng. 14, 177–197. https://doi.org/10.1016/0267-7261(94)00039-J

Tobita, J., Fukuwa, N., Yagi, S., 2000. Experimental Evaluation of Dynamic Characteristics of low and medium-rise buildings with soil-structure interaction. Presented at the 12th World Conference of Earthquake Engineering.

Todorovska, M.I., 2009a. Soil-Structure System Identification of Millikan Library North-South Response during Four Earthquakes (1970-2002): What Caused the Observed Wandering of the System Frequencies? Bulletin of the Seismological Society of America 99, 626–635. https://doi.org/10.1785/0120080333

Todorovska, M.I., 2009b. Seismic Interferometry of a Soil-Structure Interaction Model with Coupled Horizontal and Rocking Response. Bulletin of the Seismological Society of America 99, 611–625. https://doi.org/10.1785/0120080191

Todorovska, M.I., Trifunac, M.D., 1990. Propagation of Earthquake Waves in Buildings with Soft First Floor. J. Eng. Mech. 116. https://doi.org/10.1061/(ASCE)0733-9399(1990)116:4(892)

Todorovska, M.I., Trifunac, M.D., 1989. Antiplane Earthquake Waves in Long Structures. J. Eng. Mech. 115. https://doi.org/10.1061/(ASCE)0733-9399(1989)115:12(2687)

Trifunac, M. D., Ivanovic, S.S., Todorovska, M.I., 2001. Apparent periods of a building. I : Fourier analysis. journal of structural engineering 517–526.

Trifunac, M.D., Todorovska, M.I., 1999. Recording and interpreting earthquake response of full-scale structures (Proc. nota advanced research). University of southern California.

Trifunac, Mihailo D, Todorovska, M.I., Hao, T.-Y., 2001. Full-scale experimental studies of soil-structure interaction - A review, in: Proc. 2nd U.S. - Japan Workshop on Soil-Structure Interaction. Tsukaba City, Japan, p. 52.

Tsogka, C., Wirgin, A., 2003. Simulation of seismic response in an idealized city. Soil Dynamics and Earthquake Engineering 23, 391–402. https://doi.org/10.1016/S0267-7261(03)00017-4

Tucker, B.E., King, J.L., 1984. Dependence of sediment-filled valley response on input amplitude and valley properties. Bull. Seismol. Soc. Am. 74, 153–165.

Vähäaho, I., 1998. From geotechnical maps to three-dimensional models. Tunn. Undergr. Sp. Tech. 13, 51–56. https://doi.org/10.1016/S0886-7798(98)00020-0

Vandiver, J.K., Dunwoody, A.B., Campbell, R.B., Cook, M.F., 1982. A Mathematical Basis for the Random Decrement Vibration Signature Analysis Technique. J. Mech. Des. 104, 307–313.

Veletsos, A.S., Prasad, A.M., 1989. Seismic Interaction of Structures and Soils: Stochastic Approach. Journal of Structural Engineering 115, 935–956. https://doi.org/10.1061/(ASCE)0733-9445(1989)115:4(935)

Vicencio, F., Alexander, N.A., 2018. Dynamic interaction between adjacent buildings through nonlinear soil during earthquakes. Soil Dynamics and Earthquake Engineering 108, 130–141. https://doi.org/10.1016/j.soildyn.2017.11.031

Vidale, J.E., Helmberger, D.V., 1988. Elastic finite-difference modeling of the 1971 San Fernando, California earthquake. Bull. Seismol. Soc. Am. 78, 122–141.

Wang, F., 2019. Time domain stochastic finite element simulation towards probabilistic seismic soil-structure interaction analysis. Soil Dynamics and Earthquake Engineering 116, 460–475. https://doi.org/10.1016/j.soildyn.2018.10.021

Ward, H.S., Crawford, R., 1966. Wind-induced vibrations and building modes. Bulletin of the Seismological Society of America 56, 793–813.

Wathelet, M., Chatelain, J.-L., Cornou, C., Giulio, G.D., Guillier, B., Ohrnberger, M., Savvaidis, A., 2020. Geopsy: A User-Friendly Open-Source Tool Set for Ambient Vibration Processing. Seismological Research Letters. https://doi.org/10.1785/0220190360

Wathelet, M., Jongmans, D., Ohrnberger, M., Bonnefoy-Claudet, S., 2008. Array performances for ambient vibrations on a shallow structure and consequences over V s inversion. J. Seismol. 12, 1–19. https://doi.org/10.1007/s10950-007-9067-x

Welch, P.D., 1967. The use of Fast Fourier Transform for the estimation of Power Spectra : A method based on time averaging over short, modified periodograms. I.E.E.E 15, 70–73.

Wirgin, A., Bard, P.-Y., 1996. Effects of Buildings on the Duration and Amplitude of Ground Motion in Mexico City. Bull. Seismol. Soc. Am. 86, 914–920.

Wolf, J.P., 1994. Foundation vibration analysis using simple physical models, Pearson Education. ed.

Wolf, J.P., 1985. Dynamic soil-structure interaction. Prentice-Hall.

Wong, H.L., Luco, J.E., 1980. Soil Structure Interaction: A Linear Continuum Mechanics Approach (CLASSI) (No. CE 70-03). Dept. of CE, University of Southern California, Los Angeles, California.

Wong, H.L., Trifunac, M.D., 1975. Two-dimensional, antiplane, building-soil-building interaction for two or more buildings and for incident plane SH waves. Bull. Seismol. Soc. Am. 65, 1863–1885.

Wong, H.L., Trifunac, M.D., Westermo, B., 1977. Effects of surface and subsurface irregularities on the amplitudes of monochromatic waves. Bull. Seismol. Soc. Am. 67, 353–368.

Xu, J., Philippacopoulas, A.J., Miller, C.A., Constantino, C.J., 1990. CARES (Computer Analysis for Rapid Evaluation of Structures) Version 1.0, Seismic Module, Theoretical Manual (Vol.1 No. NUREG/CR-5588, BNL-NUREG-52241). Brookkhaven National Laboratory.

Yamazaki, F., Ansary, M.A., 1997. Horizontal-to-Vertical spectrum ratio of earthquake ground motion for site characterization. Earthq. Eng. Struct. D. 26, 671–689.

Zhang, L., Brincker, R., 2005. An overview of operational modal analysis: major development and issues. In : 1st international operational modal analysis conference. Presented at the 1st International Operational Modal Analysis Conference, Aalborg Universitet, pp. 179–190.

Appendix 1

Chapter I. Numerical methods for the modeling of seismic wave propagation

In 2011, Semblat presented an overview of different numerical methods used in the modeling of the seismic wave propagation for simple and complex geometry (Figure 135).

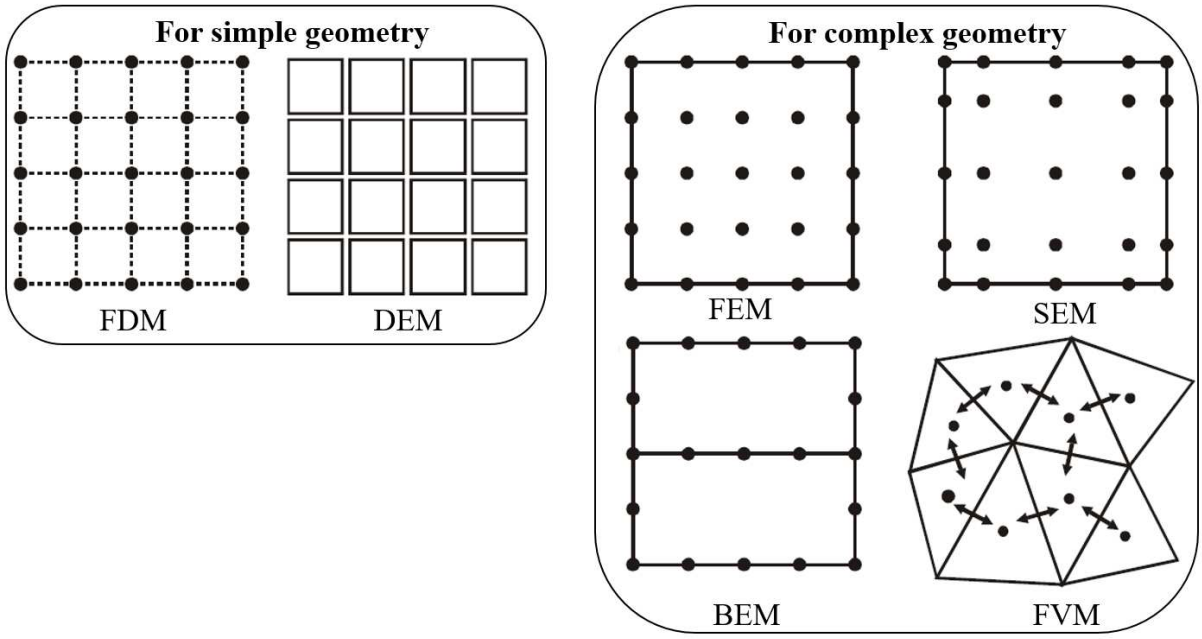

Figure 135: Illustrations of the different numerical methods used to model simple or complex geometry (adapted from Semblat (2011)). Methods convenient for simple geometry are the finite difference method (FDM) and the discrete element method (DEM). Methods powerful for complex geometry are the finite element method (FEM), the spectral element method (SEM), the boundary element method (BEM) and the finite volume method (FVM).

The finite difference method (FDM) (Moczo et al., 2014, 2004) and the discrete element method (DEM) (Cundall and Strack, 1979) constitute discrete mesh approaches powerful in discontinuous medium. The FDM is one of the most used method in the simulation of the ground motion (Olsen, 2000; Sato et al., 1999; Vidale and Helmberger, 1988) because of its facility to be implement and the efficiency to calculate in parallel process. However this approach has limitations to dial with complex geometry in particular due to the difficulty to integrate boundary conditions. The DEM is based on a Lagrangian description of the particle motion. It is generally used for mechanical engineering problems to model large scale material for example to study the complex interactions between granular materials (Ghaboussi and Barbosa, 1990) or damage and failure in complex system (Fleissner et al., 2007). This method enables to consider each element as independent of the system and distributed properties to obtain a model of different components.

The spectral element method (SEM) is commonly used to numerically solve 2D and 3D seismic wave propagation in heterogeneous media (Chaljub et al., 2010; Stupazzini et al., 2009; Komatitsch et al., 2004; Komatitsch and Vilotte, 1998). It consists to divide the unknowns into Lagrangian polynomials, sampled at the Legendre-Gauss-Lobatto quadrature points. SEM provides high precision due to the high polynomial degrees but does not consider adaptive meshing and nonlinearity.

The finite volume method (FVM) (Eymard et al., 2000) is often employed for 2D modeling of rupture (Benjemaa et al., 2009, 2007; Demirdzic and Muzaferija, 1994). This approach calls on low order polynomial functions and therefore is a low precision method.

Appendix 2

Chapter I. Application of the algorithm combining the FDD and the vectorial RD technique to compute the modal frequency, the damping coefficient and the mode shapes of a structure (here for one setup)

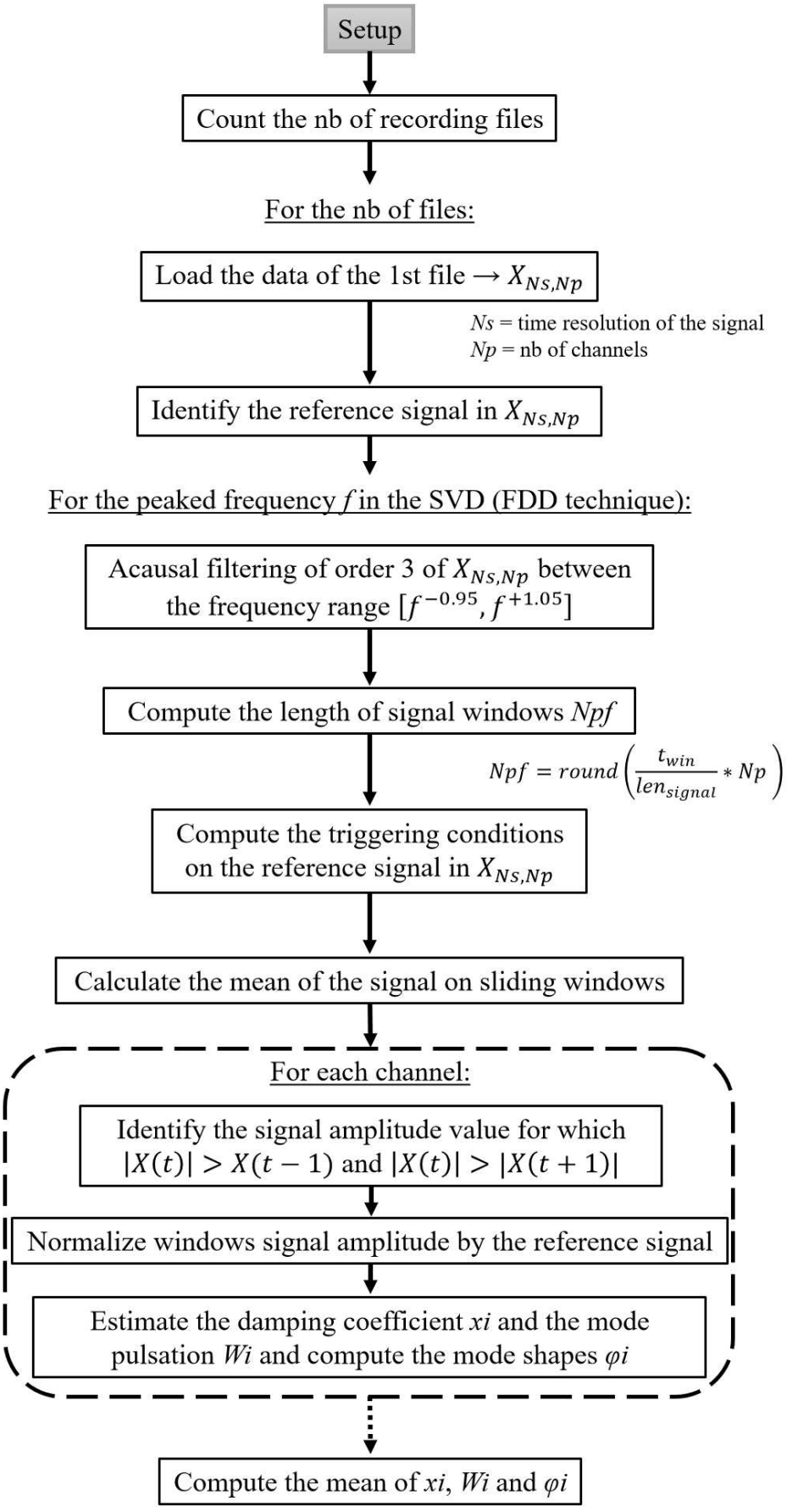
Setup
Count the nb of recording files
For the nb of files:
Load the data of the 1st file → $X_{Ns,Np}$
Ns = time resolution of the signal
Np = nb of channels
Identify the reference signal in $X_{Ns,Np}$
For the peaked frequency f in the SVD (FDD technique):
Acausal filtering of order 3 of $X_{Ns,Np}$ between the frequency range $[f^{-0.95}, f^{+1.05}]$
Compute the length of signal windows Npf
$Npf = round\left(\frac{t_{win}}{len_{signal}} * Np\right)$
Compute the triggering conditions on the reference signal in $X_{Ns,Np}$
Calculate the mean of the signal on sliding windows
For each channel:
Identify the signal amplitude value for which $|X(t)| > X(t-1)$ and $|X(t)| > |X(t+1)|$
Normalize windows signal amplitude by the reference signal
Estimate the damping coefficient xi and the mode pulsation Wi and compute the mode shapes φi
Compute the mean of xi, Wi and φi

Appendix 2

Chapter III. HVSR computed from the recordings in the instrumented residential compound

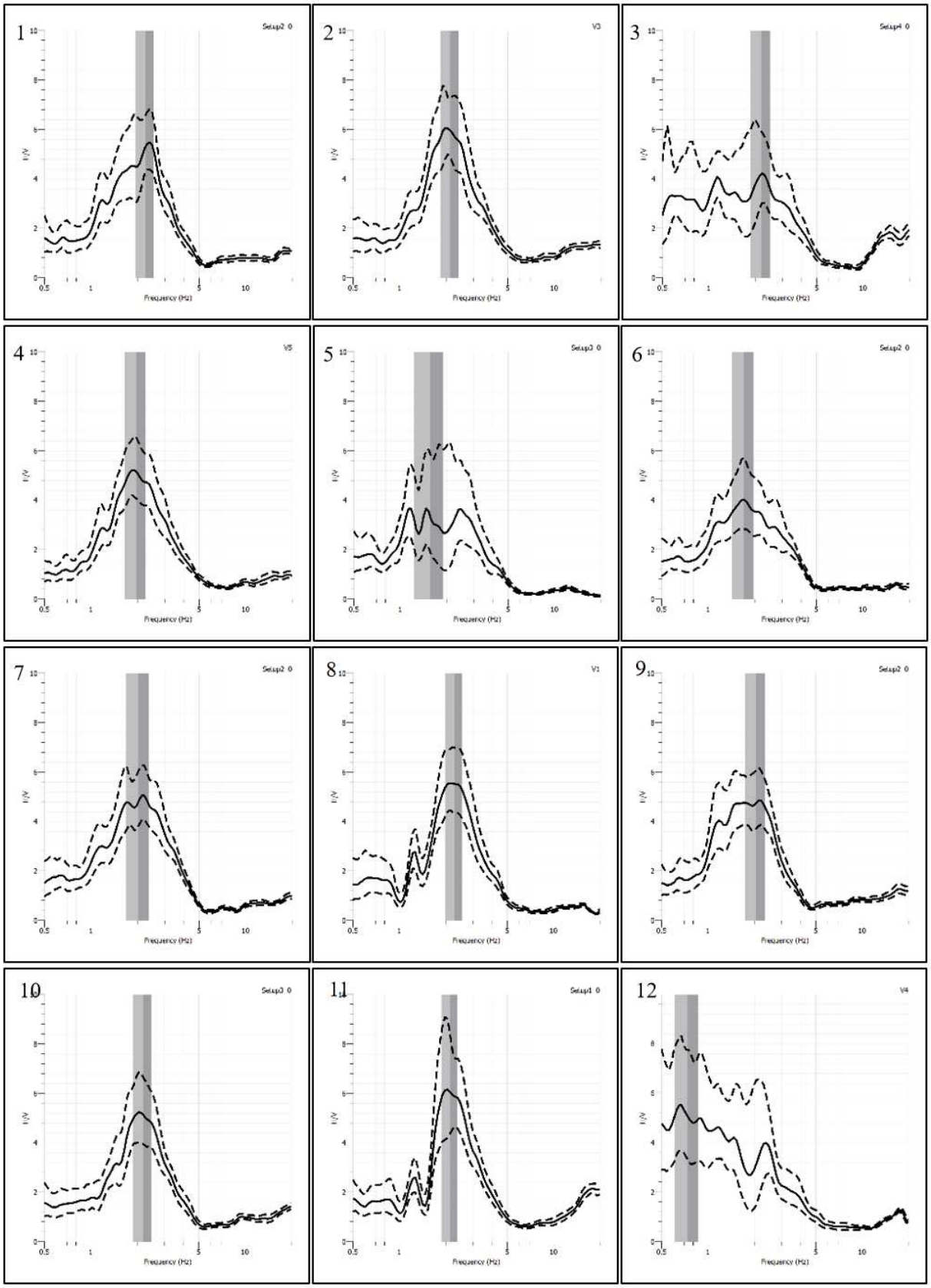
1
2
3
4
5
6
7
8
9
10
11
12
H/V
Frequency (Hz)

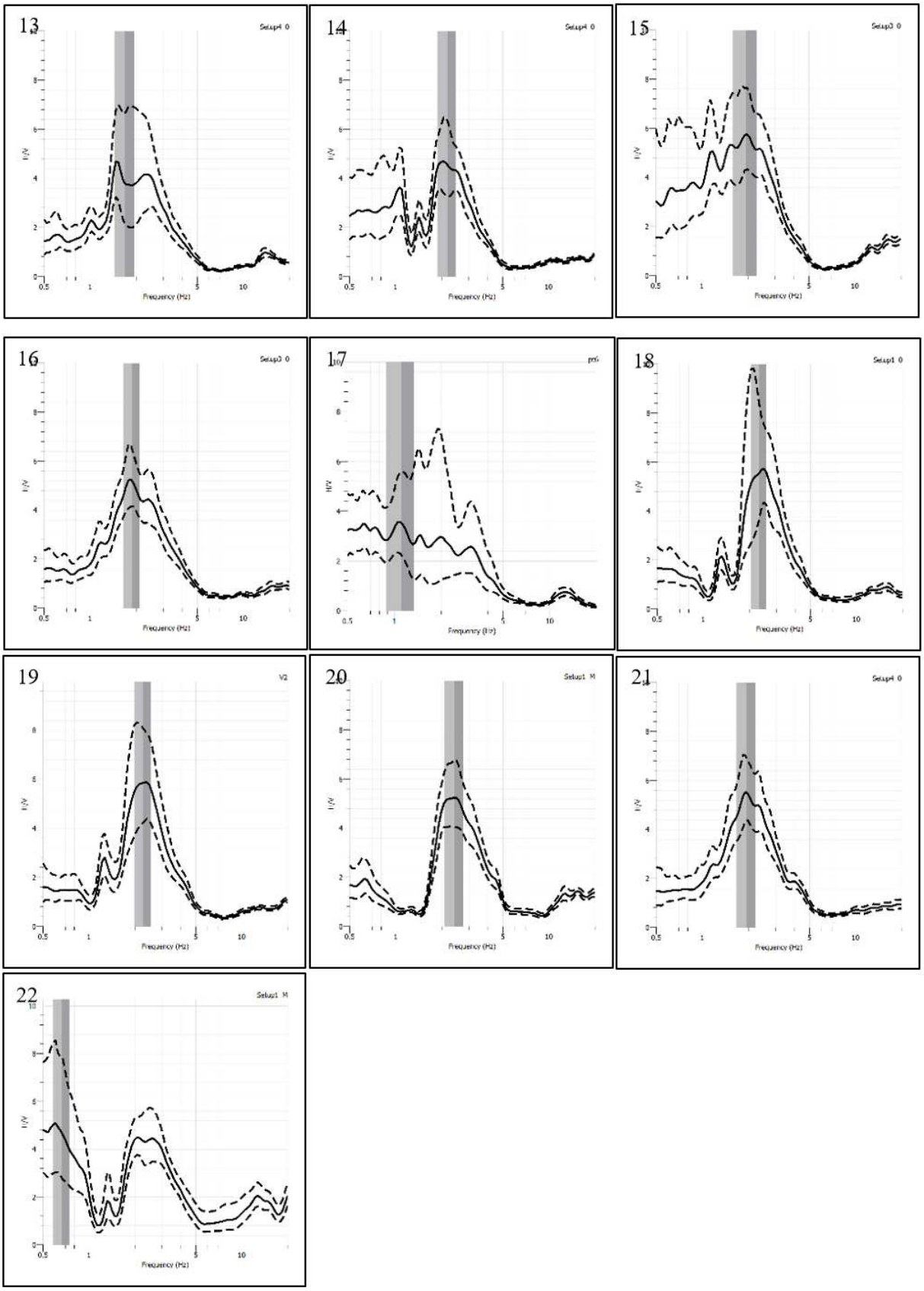
13
14
15
16
17
18
19
20
21
22
Frequency (Hz)

Appendix 3

Chapter IV. Earthquakes data used in SSR and earthquake HVSR computations

Time	Lat. (°)	Long. (°)	Mag.	Depth (km)	Catalog	Mag. Type	Location
07/08/2021 04:19	35.49	3.63	4.2	20	EMSC-RTS	mb	STRAIT OF GIBRALTAR
19/07/2021 19:21	36.77	5.52	4.3	10	EMSC-RTS	mb	NORTHERN ALGERIA
25/03/2021 02:37	36.94	5.25	4.4	10	EMSC-RTS	mb	NORTHERN ALGERIA
24/03/2021 23:23	36.90	5.37	4.2	10	EMSC-RTS	mb	NORTHERN ALGEERIA
18/03/2021 00:17	36.98	5.29	5.2	10	EMSC-RTS	mb	NORTHERN ALGERIA
18/03/2021 00:04	36.92	5.21	6	10	EMSC-RTS	Mw	NORTHERN ALGERIA
17/03/2021 21:49	36.50	6.74	4.7	10	EMSC-RTS	mb	NORTHERN ALGERIA
08/03/2021 18:00	39.64	22.22	4.3	10	USGS	mb	GREECE
06/03/2021 16:36	39.68	22.23	4.5	10	USGS	mb	GREECE
26/01/2021 21:54	37.18	3.73	4.4	10	EMSC-RTS	mb	SPAIN
26/01/2021 21:36	37.22	3.72	4.1	10	EMSC-RTS	mb	SPAIN
30/12/2020 05:15	45.44	16.18	4.8	10	EMSC-RTS	mb	CROATIA
29/12/2020 14:36	45.24	11.04	4.4	9	EMSC-RTS	ML	NORTHERN ITALY
29/12/2020 11:19	45.42	16.21	6.4	10	EMSC-RTS	Mw	CROATIA
05/11/2020 22:16	39.92	23.97	4.9	10	USGS	mb	GREECE
01/11/2020 13:15	44.36	15.45	4.6	10	EMSC-RTS	ML	CROATIA
25/10/2020 19:35	46.9	9.12	4.3	1	EMSC-RTS	ML	SWITZERLAND
30/09/2020 22:02	42.83	1.47	4.5	5	EMSC-RTS	mb	PYRENEES
24/09/2020 19:21	41.01	19.82	4	36	EMSC-RTS	ML	ALBANIA
07/08/2020 11:13	36.54	6.34	4.5	10	EMSC-RTS	mb	NORTHERN ALGERIA
07/08/2020 06:15	36.53	6.28	4.9	10	EMSC-RTS	Mw	NORTHERN ALGERIA
17/07/2020 08:10	36.4	6.34	4.5	10	EMSC-RTS	mb	NORTHERN ALGERIA
25/06/2020 17:30	44.67	22.40	4.3	11.2	USGS	mb	ROMANIA
20/05/2020 23:41	35.14	20.26	5.8	16	USGS	Mw	CENTRAL MEDITERRANEAN SEA
16/04/2020 09:42	44.65	9.41	4.2	3	EMSC-RTS	ML	NORTHERN ITALY
22/03/2020 05:22	45.87	16.02	5.4	10	EMSC-RTS	Mw	CROATIA
20/03/2020 21:38	39.24	20.45	4.6	10	USGS	mb	GREECE
21/02/2020 02:53	36.73	5.62	4.5	10	EMSC-RTS	mb	NORTHERN ALGERIA

24/01/2020 07:24	36.76	5.61	4.9	10	EMSC-RTS	Mw	NORTHERN ALGERIA
09/12/2019 03:37	44.00	11.31	4.8	9	EMSC-RTS	mb	NORTHERN ITALY
26/11/2019 06:06	41.58	19.33	5.4	10	EMSC-RTS	Mw	ADRIATIC SEA
11/11/2019 10:52	44.57	4.62	4.9	10	EMSC-RTS	Mw	FRANCE
21/09/2019 16:10	41.37	19.41	4.7	10	EMSC-RTS	mb	ADRIATIC SEA
13/08/2019 21:11	35.66	23.44	4.5	31.3	USGS	mb	GREECE
13/08/2019 11:17	44.47	9.82	4.1	7	EMSC-RTS	ML	NORTHERN ITALY
28/05/2019 08:48	46.37	6.75	4.2	2	EMSC-RTS	mb	FRANCE
17/01/2019 21:46	37.62	20.61	4.4	10	USGS	Mwr	GREECE
14/01/2019 23:03	44.37	12.32	4.5	25	EMSC-RTS	Mw	NORTHERN ITALY
25/12/2018 01:41	37.41	20.86	4.8	10	USGS	mb	GREECE
18/11/2018 12:48	44.07	12.49	4.2	43	EMSC-RTS	ML	NORTHERN ITALY
26/10/2018 02:17	37.36	20.59	4.7	10	USGS	mb	GREECE
26/10/2018 02:09	37.30	20.62	4.8	10	USGS	mb	GREECE
25/10/2018 22:54	37.52	20.55	6.8	14	USGS	Mw	IONIAN SEA
03/07/2018 19:38	51.61	16.22	4.3	10	EMSC-RTS	mb	POLAND
25/06/2018 08:21	40.66	23.31	4.1	10	USGS	Mwr	GREECE
25/06/2018 05:12	36.97	21.56	5.4	10	RENASS	mb	ATHENS
04/06/2018 22:09	32.56	4.55	4.3	10	EMSC-RTS	mb	MOROCCO
19/05/2018 16:41	44.85	9.69	4.2	10	EMSC-RTS [i]	ml	NORTHERN ITALY
19/11/2017 12:37	44.66	10.07	4.6	32	EMSC-RTS	mw	NORTHERN ITALY
10/11/2016 02:48	44.29	6.24	4.2	2	EMSC-RTS	ml	FRANCE
30/10/2016 06:40	42.84	13.11	6.5	10	EMSC-RTS	mw	CENTRAL ITALY
26/10/2016 19:18	42.92	13.13	6.1	8	EMSC-RTS	mw	CENTRAL ITALY
26/10/2016 17:10	42.88	13.13	5.5	9	EMSC-RTS	mw	CENTRAL ITALY
28/08/2016 16:42	42.96	12.93	4.1	10	RENASS [+]	mb	CENTRAL ITALY
24/08/2016 02:33	42.79	13.15	5.5	9	EMSC-RTS	mw	CENTRAL ITALY
24/08/2016 01:36	42.71	13.22	6.2	4	EMSC-RTS	mw	CENTRAL ITALY
30/07/2016 20:21	44.94	7.21	4.1	11	EMSC-RTS	mb	NORTHERN ITALY

23/06/2016 14:37	44.17	9.91	4.2	9	EMSC-RTS	mb	NORTHERN ITALY
06/11/2015 04:03	44.47	6.69	4.2	5	EMSC-RTS	ml	FRANCE
29/10/2015 00:37	42.24	3.18	4.4	10	EMSC-RTS	ml	PYRENEES
30/11/2014 09:34	44.59	9.38	4	2	EMSC-RTS	ml	NORTHERN ITALY
07/04/2014 19:26	44.51	6.71	5.2	8	EOST [n]	MLv	FRANCE
21/11/2013 10:36	44.90	9.23	4.2	0	EOST	MLv	FRANCE
30/06/2013 14:40	44.17	10.21	4.7	10	EMSC-RTS	mw	NORTHERN ITALY
21/06/2013 12:12	44.17	10.11	4.1	2	EMSC-RTS	ml	NORTHERN ITALY
21/06/2013 10:33	44.19	10.15	5.3	10	EMSC-RTS	mw	NORTHERN ITALY
25/02/2013 11:00	41.84	4.22	4.2	0	EOST	MLv	MEDITERRANEAN
25/01/2013 14:48	44.17	10.45	4.9	15	EMSC-RTS	mw	NORTHERN ITALY

[i] EMSC-RTS : European Mediterranean Seismological Centre Real Time Services
[+] RENASS : Réseau National de Surveillance Sismique
[n] EOST : Ecole et Observatoire des Sciences de la Terre

Appendix 4

Chapter IV. Velocity profiles of cross holes 2 and 3 used to estimate V_s values in the lithostratigraphic soil profile of the LVV

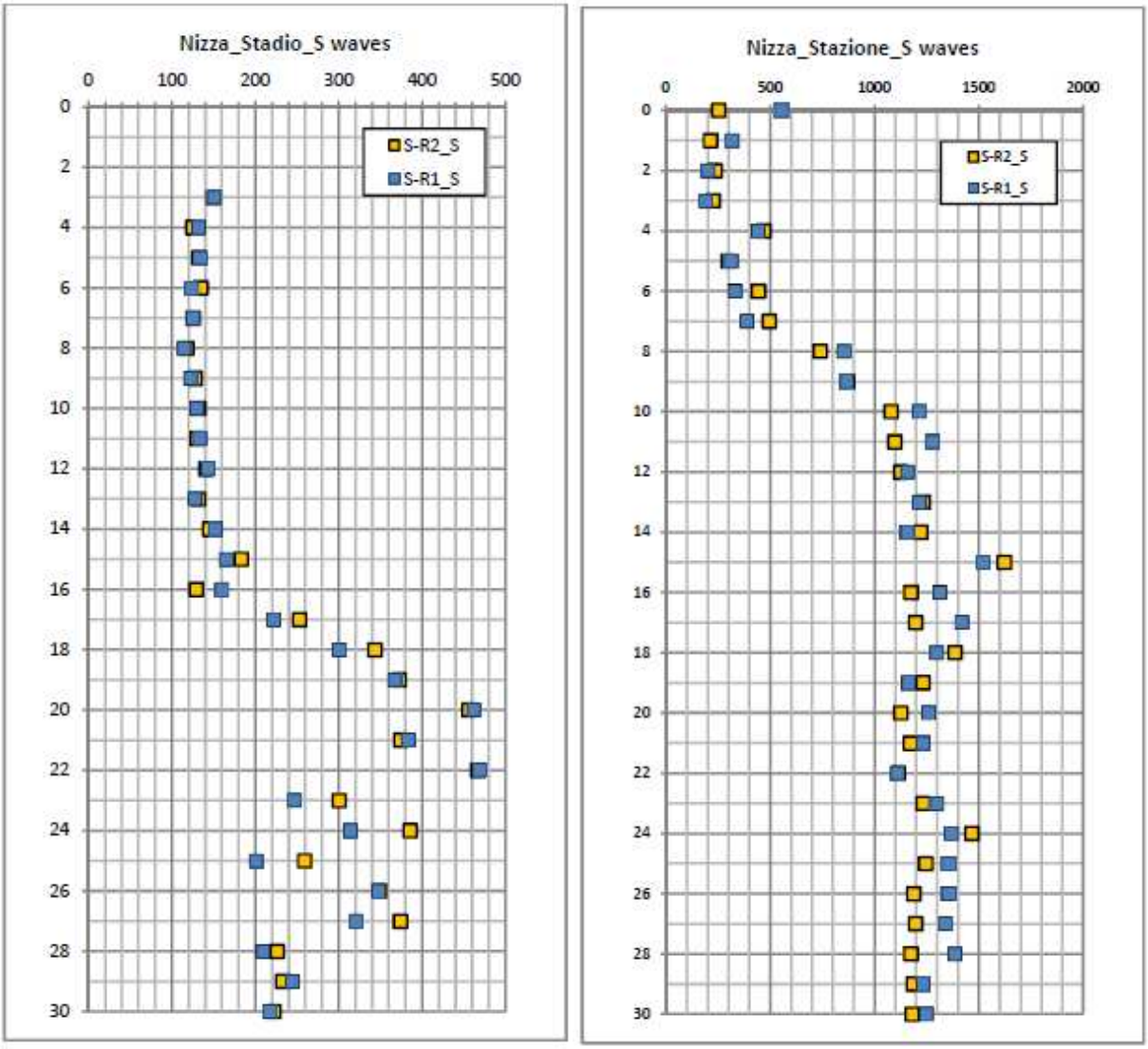

Velocity profiles of cross holes 2 (left) and 3 (right) available in the LVV provided by the city of Nice.

Appendix 5

Chapter IV. MASW measurements

- *Domain of validity*

Empirical criteria are used to estimate the maximal penetration depth and the vertical resolution of the MASW survey. A particular attention is paid on λ_{min} limit that defines the aliasing limit for each frequency (Stokoe et al., 1994; Rix and Leipski, 1991). This parameter is generally a fraction of the length of the seismic profile. The more the acquisition set up is long, the more accurate the mode spatial resolution is. In this campaign, the minimal in-between distance of geophone (dx) is 1.5 m, consequently, according to Asten and Henstridge (1984), the minimal wavelength (λ_{min}) that can be observed is 3 m (Eq. (95)) and the maximal wavelength (λ_{max}) is equivalent to the maximal length array (L). The maximal in-between distance of geophone is 3 m and permits to have a maximal length array of 69 m. According to Park et al. (1999), the maximal penetration depth (dp) is then equal to 34.5 m (Eq. (96)).

$$\lambda_{min} > 2 * dx \tag{95}$$

$$dp = \frac{L}{2} \approx \frac{\lambda_{max}}{2} \tag{96}$$

For each investigated site and each network length, five shots are performed. For each shot, seismic traces are summed up.

The MASW method (Foti et al., 2017; Park et al., 1999) is applied to the seismic data using the *Geopsy* software (Wathelet et al., 2020). For each studied site, dispersion curves are plotted, based on the results of the linear frequency-wavenumber (f-k) method (Aki, 1957). Regarding the ambient vibration data, for each site, data is analysed to identify their origin (natural or anthropic). The mHVSR method is applied to these data to extract mHVSR. The presentation of the data analysis will be made in the case of one investigated site but it is applicable for other sites.

- *Dispersion curves*

For one studied site, the number of f-k spectra computed correspond to the number of sources created during the data acquisition. f-k spectra are computed from the parameters presented in Table 41.

Table 41: Parameters for frequency-wavenumber spectrum computation in *Geopsy*.

PRE-PROCESSING WINDOW	
Normalization	$1/\sqrt{distance}$
Signal time limits	from T_0 to end
PROCESSING	
Frequency band width (ratio)	0.1
OUTPUT	
Frequency sampling	from 5 to 60 Hz
Step	Log
Sampling number	100
Velocity of the sampling	from 100 to 2000 or 3000 m.s^{-1} (as function of the geology of the site)
Step	Linear
Sampling number	100
Normalisation	By spectrum power
CURVES	
Wavelength limits	69 or 34.5m (as function of the network length)

f-k spectra are then summed up. Theoretical dispersion curves (TDC) are therefore plotted on the sum of the f-k spectra (or on particular spectrum if the dispersion curve is not well determined in the low frequencies). Finally, a mean of the TDC is computed. Below is presented an example of TDS at P1 site for the 69 m network (Figure 136).

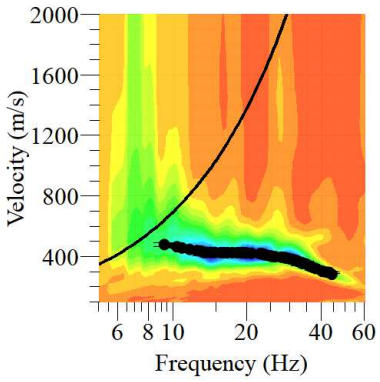

Figure 136: Stack of f-k spectra and theoretical dispersion curves at P1 site for the 69 m network.

Appendix 6

Chapter IV. Inversion parameters for rock sites investigation in the LVV

Table 42: Inversion parameters of seismic wave velocity.

TARGETS					
Targets	Dispersion curve			mHVSR ellipticity curve	
Weight of the standard deviation	1			1	
Minimal standard deviation	0			0	
RUNS					
Number of maximal iteration	500				
Ns0	50				
Ns	50				
Nr	50				
SITES PARAMETERS	**P1**	**P2**	**P3**	**P4**	
Inversed mode (0=fundamental, 1=higher)	0	0	0	1	For all sites = 0
Number of layers	2	2	3	4	

Ns0 = Number of models randomly generated before the 1st iteration
Ns = Number of models generated at each iteration
Nr = Number of best models to consider in the resampling

Table 43: Parameters for the inversion of V_s profiles.

	Value (fixed ?)	Behavior	Depth (fixed ?)
V_p	200 to 5000 m.s^{-1} (no)	Uniform	None
v	0.2 to 0.5 (no)	Uniform	None
V_s	150 to 3500 m.s^{-1} (No) (only for P2 : 100 to 1000 m.s^{-1} from 1 to 100 m (not fixed)	Uniform	1 to 100 m (No)
ρ	2000 kg.m^{-3} (yes)	Uniform	None

Appendix 7

Chapter IV. Building a 3D model using the *GDM* software

The geomodeler software : GDM MultiLayer 2018 ®

To elaborate the 3D model of the LVV, the *GDM* (Geological Data Modeling) software (*GDM MultiLayer 2018* 32 bits) developed by the BRGM is used. This software allows to interpolate punctual data using geostatistical methods based on several interpolation algorithms. File formats such as .xls, .txt, .csv, .mdb, .dbf among others can be integrated as the database in the software. More details about the software and its use can be found in the user's guide (Bourgine, 2018).

It is important to note the limits of the *GDM* software in the design of 3D model:

- It is not possible to visualize results as 3D graph, only the map or profile view is available.
- In the case of an update of the database, it is necessary to modify first the values in the database file (.xls, .txt, .csv, etc.) and then, to import the file in *GDM*. The modification made in the input file is not directly link to the database already present in the software.
- The update of data of one borehole implies to redo the complete interpolation process of all the model layers.

➢ *Building of the multi layers model*

A multi layers model is composed of the stacking of continuous or discontinuous field layers. These layers can be fractured and/or with variable thickness. Each layer is bounded between two surfaces: its floor at the bottom and its roof at the top. This is these surfaces that are modeled in the software. In our case, a rectangular mesh grid is generated for each geological formation based on the geotechnical and geophysical data available in the LVV. From punctual data and using interpolation process, the software computes the estimated altitude value of the limit between sedimentary layers at each node of the grid. The obtained different grids are then assembled to get the final model of the valley. After that, the *GDM* software is able to produce isovalue maps as vertical profiles.

➢ *GDM database*

To create the 3D multi sedimentary layers model of the LVV, three files are imported:

- The DEM of the studied area with a spatial resolution of 5 m.
- The file containing all altitude or thickness values of each sedimentary layer for each local constrain (geophysical and geotechnical data) with their respective coordinates.
- The file of the points of the interpolation contour of the model with coordinates.

We can note that *GDM* is able to manage different systems of coordinates in the same project. However the software cannot process coordinates in degree.

The input database file (.xls, .txt, .csv, etc.) is not sufficient to build rectangular mesh grid in the software. To begin, it is necessary to create a specific place in the software that is called a *GDM* base in order to import the input file. The *GDM* base helps the software to identify each column of the input file in terms of borehole ID, maximal depth, location, geological passes…

Special attention is paid to the homogenization of the interpretation of borehole log-stratigraphy. As explained in Chapter IV, each borehole is interpreted as function of the lithostratigraphic soil profile of the LVV. The homogenization process of the geological passes impacts the geometry of the sedimentary layering in the basin model. In that way, a subjective approach is applied to sort and to interpret each borehole passes (sometimes only a few of the sedimentary layers identified in the lithostratigraphic soil profile of the LVV are observed in the geotechnical data) leading to uncertainties in the sedimentary layering in the basin.

➢ *Interpolation limits*

To constrain the model, it is necessary to define interpolation limits. From the geological map of the LVV, it is possible to distinguish the limit between the basin and the bedrock. In this step, the interpolation is forced by using fictive boreholes. These data are aligned along the interpolation limits. The basin thickness is considered equal to zero at these points. It means that the altitude value of each floor of the sedimentary layer is equivalent to the altitude of the DEM. Therefore, the basin tends to have beveled edges.

➢ *Selection and wedging of boreholes*

Only boreholes located within the interpolation limits are taken into account in the model in order to avoid high computational costs. With the same mind, boreholes having inconsistent data are removed.

Sometimes a lag is observed between the altitude of the borehole top and the DEM altitude. This error can be induced either by a poor georeferencing or by the condition of the drilling (in excavation hole for example) or the absence of the DEM updating (addition of anthropogenic filling in some area). This lag between both altitudes needs to be corrected in the building of the model.

- *Removing last geological passes of borehole log-stratigraphy*

When a borehole does not reach the bedrock, it is not possible to determine the total thickness of the sediments at this point. Additionally, for the same borehole, the thickness of the last layer reached by the borehole cannot be known. This situation often appears in the geotechnical database of this study. In the interpolation process of the pass limits, *GDM* is not able to discriminate if one geological pass is continuous or not after the end of the borehole. If the altitude of a layer floor is attributed to the altitude of the end of the borehole, wrong results can be induced. A non-real thickness is then imposed. In front of this uncertainty, the only solution would be to neglect the last geological pass reached by the boreholes (if they are not reaching the bedrock). The scheme in Figure 137 describes the problem.

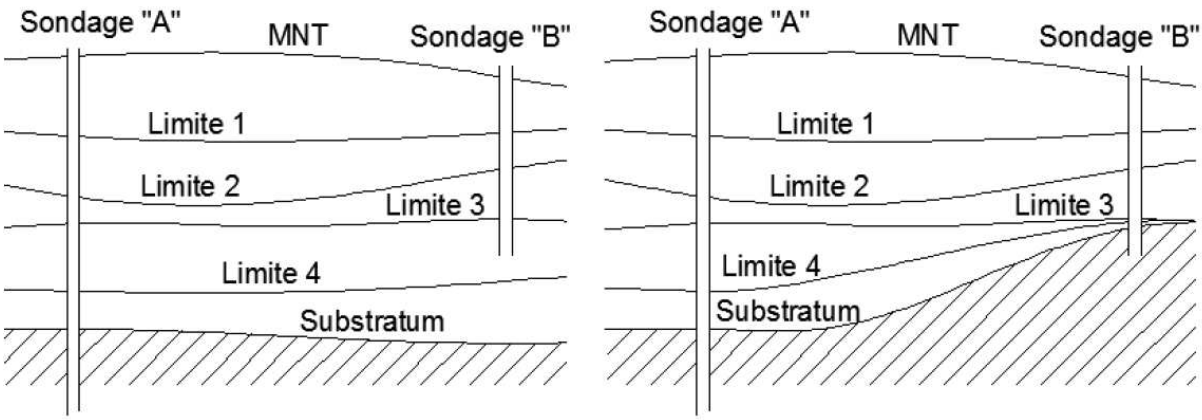

Figure 137: Scheme describing the situation of boreholes in reality (left) and the result of the model from *GDM* after removing the last passes.

In the Figure 137, all the layers are observed in the borehole « A » and are take into account in the model because the borehole reaches the bedrock. The position of all the layer limits is well known. On the contrary, the borehole « B » does not reach the bedrock. Therefore, the altitude of the floor of the layer 4 is not known. In this case, the thickness of this layer cannot be determined. The model only takes into account the altitude of the floor of the layer 3. Consequently, the interpolation process in the *GDM* software tends to go back up all the layer limits to the known limit.

- *Data interpolation*

First, to interpolate each layer limit, the method and the interpolation parameters should be defined. The *GDM* software proposes several interpolation methods which show different advantages and drawbacks (Table 44).

Table 44: Interpolation methods proposed in the *GDM* software.

Methods	Advantages	Drawbacks
Krigeage using a variogram model specified by the user	Providing better results. If the variable behavior is spatially homogeneous, this approach can give a standard deviation characterizing the result precision (interpolation error). Taking into account the drifting, the regularity of the interpolated variable, the maximal correlation distance and an anisotropic behavior.	Subjected to numerical instabilities (artefacts) if the data are spatially too unevenly distributed.
Local least square	Local fitting to a polynomial surface using least square method at each node of the grid. Convenient for phenomenon with large wavelength and measurement errors.	The spatial resolution is coarse.
Krigeage using a linear variogram of slope = 1 without drift (method proposed by default)	Generally it gives good results only if measurement errors are not important. Respecting the data points and takes into account the density of data.	Subjected to numerical instabilities (artefacts) if the data are spatially too unevenly distributed.
Krigeage using linear variogram and linear drift	Taking into account a drift of the interpolated data (if the drift is known). Same principle as the krigeage using linear variogram without drift.	Subjected to numerical instabilities (artefacts) if the data are spatially too unevenly distributed.
Local spline interpolation	Local fitting to a spline surface at each node of the grid. Convenient for regular phenomenon without measurement errors.	If there is measurement errors, interpolation artefacts can be appear. Subjected to numerical instabilities (artefacts) if the data are spatially too unevenly distributed.
Nearest neighbors/polygon of influence	Simple and fast way to visualize data without introducing interpretation. Assignment of the value of the closest data at each node of the grid. Using of a polygon of influence.	
Moving average	Simple and fast way to estimate data. Smoothing of the local variations and attenuation measurement errors.	
Inverse of distances	Convenient for spatially regular dataset without important measurement errors. Simple and fast estimation of data. Inducing concentric contour around the points.	Unconvenient for data in groupe or profile shape.

The interpolation method should be chosen as function of its ability and of the distribution of the input data of the model. In the case of the study of the LVV, even if ambient vibration measurements are regularly spatially distributed, geotechnical boreholes are not. Moreover, we

want that the model respects each local constraint. Therefore, we consider the krigeage approach proposed by default in the *GDM* software (Figure 138).

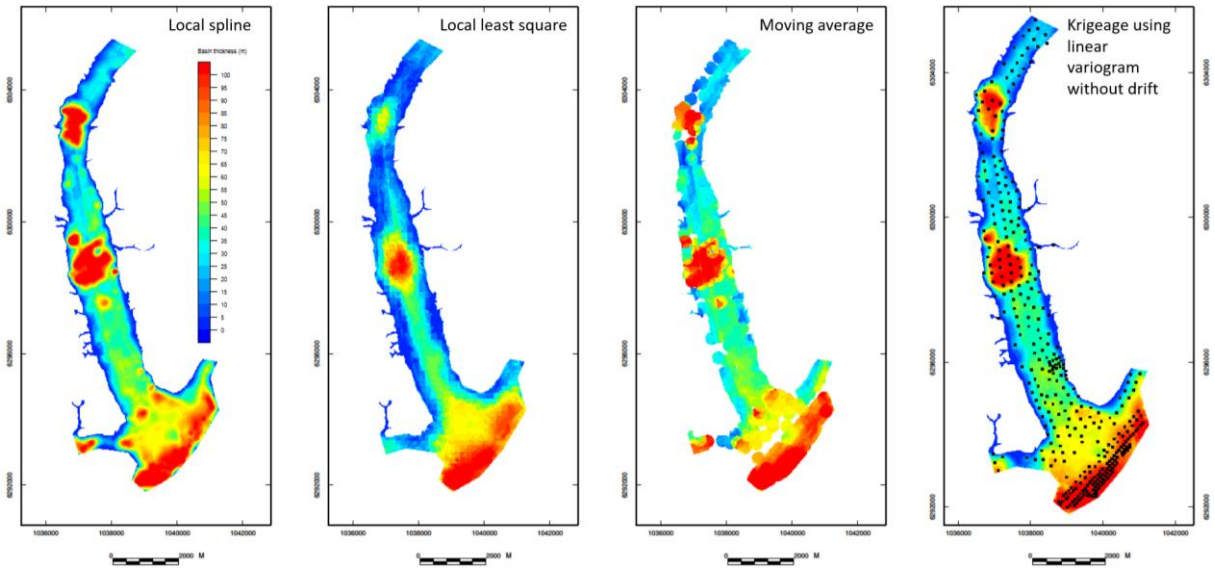

Figure 138: Example of the application of different interpolation methods to estimate the basin depth of the LVV (only from ambient vibration data indicated by the black dots). The krigeage method is used in the 3D model of the LVV.

Two important interpolation parameters require also attention: the type and the size of neighborhood. The software proposes two types of neighborhood presented in Table 45 and illustrated in Figure 139. It allows also to choose the number of points and the maximal size of the neighborhood research. By default, *GDM* computes a maximal size according to the data interpolation grid: maximal size = 20 * size of one interpolation mesh.

The size on the interpolation mesh needs to be defined at first if the sliding neighborhood by octant is selected. If not, the interpolation results may have errors.

Table 45: Type of neighborhood for the interpolation process in the *GDM* software.

Type of neighborhood	Action	Advantages	Drawbacks
Unique neighborhood	Interpolation from a set of data.	Stable for sets of a few of data. Smoothing of data.	Generation of instabilities if faults are present in the model (they are considered as "screen" during the neighborhood research). Global estimation.
Sliding neighborhood	Interpolation from a sub-set of data defined by: • Circular neighborhood (for closest neighbors algorithm and moving average method). • Rectangular neighborhood (estimated point is located in the center of the rectangle). • Neighborhood by octant (division of the space around the estimated point in 8 regular sectors, search for the maximum points in each sector up to a maximal distance).	Local estimation. No smoothing. Fast computing time. Less risk of numerical instabilities. For the rectangular neighborhood, the interpolation is performed by block. For the neighborhood by octant, the interpolation of irregular spatially distributed data.	Artefacts when irregular spatially distributed data. Parameters of neighborhood selection depending of data (induce a large variability).

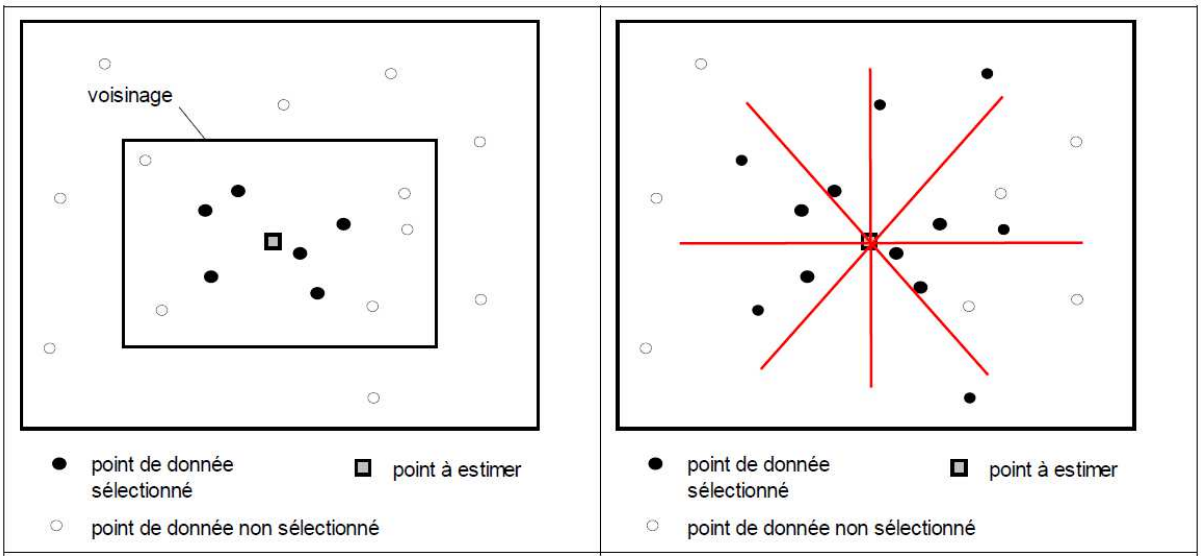

Figure 139: Type of neighborhood proposed by the *GDM* software: example of the rectangular neighborhood (left) and the neighborhood by octant with maximum 2 points per octant (right) from Bourgine (2018).

Table 46: Selection of the number of inteprolation points.

	Number of points
By default	100 (value to decrease if there is a lot of data).
For a sliding neighborhood by octant	Adding of the parameters "number of required points" (16 to 24 in simple cases, 32 to 48 in complex cases of data distribution), and "maximum number of points per octant" (necessary in the case of unevenly distributed data, by default = 1/4 of the number of required points, it means that the selection is performed among at least 4 octants).
If the database is large (>1000 points)	Increasing of the parameter value "maximum number of preselected points" (for sliding neighborhood), by defaults = 200, if a lot of data is heterogeneously distributed it is necessary to increase again this parameter (however the time cost increases too). For rectangular or circular neighborhood, the parameter “maximum number of neighbors" should be increased.

In the study of the LVV, the solution that gives best results to interpolate layers according to the distribution of data is the sliding neighborhood by octant with these parameters:

- a maximum number of preselected points equals to 200.
- a maximal number of neighbors equals to 100.
- a required number of points in the neighborhood equals to 12.
- a maximum number per octant equals to 3.

As result of the interpolation process, the software creates a grid file .grd for each layer containing altitude data.

- *Final model*

One important tool of the *GDM* software is the ability to merge several interpolation grids in order to elaborate a final model. To do that, the grids must have the same properties (type, origin, dimensions, etc…). Starting with the DEM interpolation grid, the layer grids is added one by one. Then, they are merged in one unique grid with the estimated altitudes of each layer, in the lithostratigraphic soil profile order.

- *Post processing*

During the stacking of the different layer grids, some errors can appear in the intersection of layer limits. To correct these errors, it is necessary to introduce mathematical corrections in the model. Thus following formula can be used to avoid that lower layer exceeds upper layer:

$$Z2 = \min (Z2 ; DEM)$$

$$Z3 = \min (Z3 ; Z2)$$

…

$$ZR = \min (ZR, Z9)$$

Where Z2 is the altitude of the floor of layer 2 which is older than the DEM layer and so, should be under this layer. The same description is applied for Z3 and ZR.

- *Additional computations*

It is now possible to perform computations between interpolated grids. From the stacking of the different grids, the thickness of each layer and the total thickness of the sediments can be computed at each node of the model using these formula:

$$TH1 = DEM - Z2$$

$$TH2 = Z2 - Z3$$

…

$$TH9 = Z9 - ZR$$

$$THT = DEM - ZR$$

And in order to verify the process: THT = Z1 + Z2 + Z3 + Z4 + Z5 + Z6 + Z7 + Z8 + Z9.

➢ *How to create a 3D model in the GDM MultiLayer 2018 software in a pratical way?*

- **Creation of a new project**:
  - *Projet* > *Nouveau*
    - Go to the model directory.
    - Name the file .gdm
    - Save.
    - Enter the author's name > OK
- **Loading of the DEM**:
  - *Données du projet* > Import *Grille Arc/Info Raster ASCII ESRI…*
    - Import a grid of points.
    - Import the DEM file.
- **Loading the interpolation limits of the model:**
  - *Données du projet* > *Etablir lien avec Base…*
    - Type of data: *Courbes*
    - Type of database: *Excel 2007*
    - Connection of the database file > OK
    - *Correspondance Base Externe – GDM* (depending of the database):
      - Curves : *Contours*
      - Key of curve : *ID*

Table 47: Example of the connection of the DEM file in the *GDM* software.

Champs Base externe	Long	=>	Champs GDM - Tête	=>	Champs GDM-Segment	Long GDM	Usage	Unité

1	ID	10000	=>	ID		xxxx	80	Indicatif complet	
2	X0		=>	X0		xxxx		Coordonnée X	m
3	Y0		=>	Y0		xxxx		Coordonnées Y	m
4	Z0		=>	Z0		xxxx		Coordonnées Z	m
5	X93				=>	X93		Coordonnées X	m
6	Y93				=>	Y93		Coordonnées Y	m
7	Z				=>	Z		Coordonnées Z	m

- OK
- Do not modify coordinates > OK

- Right click on the created data > Rename *Source de données* in *Contours* > OK

- **Save the project in *GDM*.**
- **Cutting the DEM as function of the interpolation limits of the model:**
  - Right click on the data *Grille MNT_5m.asc*
    - *Calculs* > *Estimer Grille 2D*

Table 48: Parameters for the cutting of the DEM.

Variables à interpoler	ALTI
Utiliser Modèle…	GRID1.GRD
Enveloppe	Polygones > Source de données : Contours > OK

- OK
- *Avertissement Estimation 2D* > *Oui*
- OK

- Right click on the created data > Rename *Source de données* in *DEM_Contours* > OK

- **Save the project in *GDM*.**
- **Extraction of a sub-grid of the *DEM_Contours* file:**
  - Right click on *DEM_Contours* > *Extraire sous-grille…*
    - Insert the coordinates of the sub-grid:

Table 49: Coordinates of the sub-grid used in the 3D model of the LVV.

X1 : 1035999	X2 : 1042505

Y1 : 6291500	Y2 : 6305946

- OK

- Right click on the created data > *Enregistrer Sous…*
  - *DEM_zone* > OK

- **Save the project in *GDM*.**
- **Loading the database:**
  - *Données du Projet* > *Etablir lien avec Base…*
    - Type of data: *Sondages*
    - Type of database: *Excel 2007*
    - Connexion of the database file > OK
    - *Correspondance Base Externe – GDM* (depending of the database):
      - Borehole : *MODELE*
      - Key of borehole: *HOLE*

Table 50: Example of the connection of the database file in the *GDM* software.

	Champs Base externe	Long	=>	Champs GDM - Tête	=>	Champs GDM-Segment	Long GDM	Usage	Unité
1	HOLE	10000	=>	HOLE		xxxx	80	Indicatif complet	
2	CODE BSS	10000	=>	Code BSS		xxxx	80	Texte/Code/Date	
3	X93		=>	X93		xxxx		Coordonnées X	m
4	Y93		=>	Y93		xxxx		Coordonnées Y	m
5	Z		=>	Z		xxxx		Coordonnées Z	m
6	TEXT	10000			=>	TEXT	80	Texte/Code/Date	
7	LITH	10000			=>	LITH	4	Code Palette	
8	TDEP				=>	TDEP		Profondeur de fin	m

- OK
- Do not modify coordinates > OK
- OK

- Right click on the created data > Rename *Source de données*

  in *MODELE_data* > OK

- **Save the project in *GDM*.**
- **Creation of altitude files for each type of layer:**

- Right click on *MODELE_data* > *Filtre* > *Filtrer…*
  - *Critères sur les passes de sondages* > *Nouveau*
  - Criteria on a field: *LITH*
  - Value list > double click on 1 > click on >> *LITH = *1** > OK
  - *Options…* > in output, the filter contains the list of boreholes having only selected borehole passes (they are therefore incomplete boreholes) > OK
  - OK
- Right click on the created data > Rename *Source de données* in *Z2* > OK
- Do the same with *Z3*, *Z4*, ect… Warning, after 3 filters, we can not filter anymore the database file. Then proceed as follow:
- Right click on *MODELE_data* > *Enregistrer Sous…*
  - OK
- Continue the filtering on the duplicated file and so on until the last layer.

- **Interpolation of the altitude file of each layer:**
  - Right click on the file *Z2* > *Calculs* > *Estimer Grille 2D…*
    - *Interpolation à partir des passes* > OK

Table 51: Parameter for the interpolation of the altitude of each layer.

Variables à interpoler	ZZZZ
Utiliser Modèle…	BASE1.GRD
Enveloppe	Polygones > Source de données : Contours > OK

    - OK
  - Right click on the created data > Rename *Source de données* in *GrilleZ2* > OK
  - Do the same with *Z3*, *Z4*, ect…

- **Creation of the *MODELE* file containing all the informations about the layers:**
  - Right click on the file *MNT_zone* > *Enregistrer Sous…*
    - *MODELE* > OK
  - Right click on the file *MODELE* > *Structure*
    - *Modifier…*

Table 52: Initialization of the variables of the model file.

Variables
DEM
Z2
Z3
Z4
…

ZN
EP1
EP2
EP3
EP4
…
EPT

- OK
- *Attribuer des champs…*

Table 53: Definition of the variable use and unit.

	Nom	Usage	Nom étendu	Descriptif	Unité
1	ALTI	ALTI	DEM	DEM	M
2	Z2	UNDF	Z2	Z2	M
3	Z3	UNDF	Z3	Z3	M
4	Z4	UNDF	Z4	Z4	M
5	…	…	…	…	…
6	ZN	…	…	…	…
7	EP1	UNDF	EP1	EP1	M
8	EP2	UNDF	EP2	EP2	M
9	EP3	UNDF	EP3	EP3	M
10	EP4	UNDF	EP4	EP4	M
11	…	…	…	…	…
12	EPT	…	…	…	…

- OK > OK

- Right click on the file *MODELE* > *Enregistrer…*
- Right click on the file *MODELE* > *Mise à jour de champs GDM…*
  - Source of input data : *GrilleZ2* > OK
    GDM field: *Z2*
  - OK > OK > OK
- Right click on the file *MODELE* > *Enregistrer…*

- Do the same with *Z3*, *Z4*, ect… and save every time.
- Right click on the file *MODELE* > *Calculs* > *Valoriser Champs Numériques*…
  - *Ajouter*…

Table 54: Correction of the layers altitude.

Z = min(X, Y)	Z2	=	min	Z2	DEM
…	…	…	…	…	…

  - OK
  - Do the same with the other layers.
  - *Appliquer* > *Oui*
  - Name of the parameter: *Correction des altitudes* > *Enregistrer* > OK
- Right click on the file *MODELE* > *Enregistrer*…
- Right click on the file *MODELE* > *Calculs* > *Valoriser Champs Numériques*…
  - *Ajouter*…

Table 55: Computation of the thickness of each layer.

Z = X-Y	EP1	=	DEM	-	Z2
…	…	…	…	…	…
Z = X-Y	EPT	=	DEM	-	ZR

  - OK
  - Do the same with the other layers
  - *Appliquer* > *Oui*
  - Name of the parameter: *Calcul des épaisseurs* > *Enregistrer* > OK
- Right click on the file *MODELE* > *Enregistrer*…

- **Creation of the color range:**
  - *Données du Projet* > *Nouvelle Palette*…
    - *Figurés pour un Code*
    - *Liste des valeurs de code… > MODELE_data* > *Codes de passes*: *LITH* > *Liste des valeurs* > *Ajouter dans la table une ligne par valeur de code* > OK
    - Select a picture for each value in *Num.*
    - Select a color for each value in *CLOR.*
    - OK
  - Right click on the created data > Rename *Palette*… in *Legende_profil*
- **Save the project in *GDM*.**
- **Export the model as a table:**
  - Right click on the file *MODELE* > *Exporter la Source de données*…
    - Choose the shapefile format .shp

- Open the QGIS software.
- In a new project, load a new vector layer.
  - Select the layer *MODELE.shp.*
- Open the attribut table of the shapefile layer.
  - *Sélectionner les données à partir d'une expression… > Z2 = 999.99000000000024*
  - Remove the selected lines.
  - Save the modifications.

- **You have now your 3D multi-layered model of the basin.**

Appendix 8

Chapter V. Borehole 10001X0458 from the BSS catalog localized at the eastern extremity of the sedimentary basin where profile modifications has been made

1000 - A - 458

CHANTIER : St AUGUSTIN Batiment :

FORAGE 3 Dossier : 1149_ 2